A COMPREHENSIVE FRAMEWORK FOR SYSTEMS IMMUNE MONITORING IN PATIENTS WITH CANCER

By

Allison Rae Greenplate

Dissertation

Submitted to the Faculty of the

Graduate School of Vanderbilt University

in partial fulfillment of the requirements

for the degree of

DOCTOR OF PHILOSOPHY

in

Microbiology and Immunology

May 11, 2018

Nashville, Tennessee

Approved:

Luc Van Kaer, Ph.D.

Jeffrey Rathmell, Ph.D.

Ann Richmond, Ph.D.

Earl Ruley, Ph.D.

Jonathan Irish, Ph.D.

To Jason, for joining me in this adventure. Wherever I've gone and whatever I've accomplished, it is only because of you.

ACKNOWLEDGEMENTS

There is neither enough room nor enough time for me to accurately and appropriately express my gratitude. To borrow from Tolkien, five and a half years is far too short a time to live among such excellent and admirable scientists. I am a different, and I hope better, person than I was when I started this journey. Here I do my best to acknowledge and thank those of you who shaped me, supported me, and promised me that there was a light at the end of this graduate school tunnel.

I must thank my mentor, Dr. Jonathan Irish, for allowing me to call your lab “home” for these 5 odd years. Thank you for the freedom to be creative and to direct my own project. Thank you for providing a space that encouraged deep, sometimes heretical, scientific conversations. Under your guidance, I have learned how to ask big questions and fine-tune small details. You have taught me how to defend my ideas, while still remaining open to criticism. Thank you for fostering independence and teaching me when it was ok to ask for help. I would not be the scientist I am today without your mentorship.

I would also like to thank my thesis committee, Dr. Luc Van Kaer, Dr. Jeffrey Rathmell, Dr. Ann Richmond, and Dr. Earl Ruley for their hard work and mentorship. You all provided guidance and encouragement while simultaneously pushing me to become the best scientist I could possibly be. I’d like to especially thank Earl for teaching me how to write grants and for always opening his door to me in my (many) moments of crisis. Earl, you helped me become a better scientist and a tougher person.

I am forever indebted to the members of the Irish and Ihrie labs. To Dr. Rebecca Ihrie, your thoughtful comments and keen eye for detail have helped me improve everything I’ve created. Thank you for the joint lab meetings. And thank you, Jonathan and Rebecca, for assembling two fantastic teams. In your labs, I have found best friends and for that I am forever

grateful. Justine Sinnaeve, Nalin Leelatin, and Caroline Roe, thank you for the 11am lunches, morning coffee, and the *endless* scientific and emotional support. The most important thing I have gained during my time at Vanderbilt is your friendship. Finally, I'd like to thank Dr. Brent Ferrell for the support, encouragement, and for helping me get my first paper published.

I must acknowledge my good friends who have helped me, at Vanderbilt and elsewhere. Thank you Lisa Poole, Bethany Carbonaeu, Becca Bluett, Theresa Barke, and Marilyn Holt for potlucks, happy hours, and loving support. To Sam Moxely and the members of Nashville Ultimate Machine, I wouldn't have survived my first few years as a graduate student without you. Thank you for providing an outlet and community that didn't involve science. Special thanks to Tim Noftzger who has been a friend for almost 10 years. Thank you for moving here and for always being excited about freezing cold camping trips. Zach Shunk, thank you for appearing when I needed a friend the most and for sticking around ever since. Thank you for being the company my misery needed. Finally, I'd like to thank Trey Fitch, Lacee Strickland, Allie Mikels, Jarrod Arnold, Matt Poppert, and all the members of CrossFit HDub. Without those early morning workouts, I would not have been motivated to make it in to lab during that last year.

None of my success would have been possible without the love and encouragement of my family. Mom, your support has been unwavering. Without your unconditional love and weekly phone calls, I would have never made it this far in life, let alone graduate school. You are selfless, wise, hilarious, beautiful, and inspiring. I am beyond lucky to be your daughter. Dad, thank you for always believing in me and encouraging me to "rock the ball". Thank you for raising me to embrace my weirdness. Most importantly, thank you for throwing me a life raft while I was drowning in science. Those months of working on EMD together were, by far, my favorite of graduate school. This PhD is only a reality because of you. Maddy, thank you for 4 years of sister dates. You made Nashville feel like home. Those runs and breakfasts made the hardest weeks not just bearable, but enjoyable. Your strength and drive pushed me to be better. Corrine, thank

you for loving me even when I was distant. You have understood me, always, and for the last 27 years I have considered you my very best friend. Your creativity and motivation inspire me daily. Thank you and Tom for bringing Dorothy Lucia into this world. I love her more than I can describe.

By far, the person I am most indebted to is my husband, Jason. You have made my life so inexplicably, undeservedly Good (with a capital G). Though I begrudgingly agreed to take your last name when we got married, I am so glad I did. Now, every grant, paper, and award will have your name attached as proof that none of it would be possible without you. Your patience and wisdom guided me through times of existential crisis. Your unconditional love reminded me that I am worthy and whole, even when I felt broken. Thank you for never giving up on me and always running out in the middle of the night to buy ice cream.

When I married Jason, I was lucky enough to marry into a second, wonderful family. To my in-laws, Cindy and Paul, thank you for your constant prayers and love. And to my siblings-in-law, Andrew, Bekah, Josh, Monique, Emily, Isaac, Melissa, Vito, and Soriya, thank you for accepting me and loving me like a sister. I have cherished our crazy adventures and look forward to a life time of more.

The work in this thesis has been made possible in part by grants F31 CA199993-01. Finally, I would like to thank all of the patients and their families who donated their biospecimens to make this work possible. Their sacrifice is what pushes science forward.

TABLE OF CONTENTS

Page

LIST OF TABLES

Page

LIST OF FIGURES

Page

LIST OF ABBREVIATIONS

ALCL	Anaplastic large-cell lymphoma
AML	Acute myeloid leukemia
APC	Antigen presenting cell
ATLL	Adult T-cell leukemia/lymphoma
Bcl-2	B-cell lymphoma 2
BTLA	B- and T-lymphocyte attenuator
CAR	Chimeric antigen receptor
CCL	C-C motif ligand
CCR	C-C chemokine receptor
CLP	Common lymphoid progenitor
CTCL	Cutaneous T-cell lymphoma
CTL	Cytotoxic T lymphocyte
CTLA-4	Cytotoxic T-lymphocyte associated protein 4
CXCR	CXC motif chemokine receptor
CyTOF	Cytometry by time of flight
DAMP	Danger associated molecular pattern
DC	Dendritic cell
DN	Double negative
DP	Double positive
EMD	Earth Mover’s Distance
Eomes	Eomesodermin
FACS	Fluorescence-activated cell sorting

FFPE	Formalin-fixed paraffin-embedded
FMI	Fluorescence median intensity
FoxP3	Forkhead box P3
GBM	Glioblastoma
HIV	Human immunodeficiency virus
HSC	Hematopoietic stem cell
ICAM-1	Intracellular adhesion molecule 1
ICP-MS	Inductively-coupled mass spectrometer
IFNα	Interferon alpha
IFNγ	Interferon gamma
IgG	Immunoglobulins of the G subclass
iNOS	Inducible nitric oxide synthase
ITAM	Immunoreceptor tyrosine-based activation motif
ITIM	Immunoreceptor tyrosine-based inhibitory motif
ITSM	Immunoreceptor tyrosine-based switch motif
JAK	Janus kinase
Lag3	Lymphocyte activation gene 3 protein
LCMV	Lymphocytic choriomeningitis virus
LFA-1	Lymphocyte function-associated antigen 1
mAb	monoclonal antibody
MDS	Myelodysplastic syndrome
MDSC	Myeloid derived suppressor cell
MEM	Marker Enrichment Modeling
MHC	Major histocompatibility complex
MLR	Mixed lymphocyte reaction

MMI	Media mass intensity
MMO	Mass minus one
MPP	Multipotent progenitors
NK	Natural killer
NKTL	NK/T-cell lymphoma
PAMP	Pathogen-associated molecular patterns
PBMC	Peripheral blood mononuclear cells
PD-1	Programmed cell death protein 1
PD-L1	Programmed death ligand 1
PD-L2	Programmed death ligand 2
PFA	Paraformaldehyde
RAG	Recombination activating genes
RCC	Renal cell carcinoma
ROS	reactive oxygen species
scRNAseq	Single cell ribonucleic acid sequencing
SEB	Staphylococcal enterotoxin B
SHP-1	SH2-domain containing tyrosine phosphatase 1
SHP-2	SH2-domain containing tyrosine phosphatase 2
SPADE	Spanning tree progression of density normalized events
STAT	Signal transducer and activator of transcription
T-ALL	T-cell lymphoblastic leukemia
T-bet	T-box transcription factor
TAM	Tumor-associate macrophage
T_{CM}	T central memory
TCR	T cell receptor

T_{EM}	T effector memory
T_{EMRA}	T effector memory cells, expressing CD45RA
T_{FH}	T follicular helper cell
TGFβ	Transforming growth factor beta
TIGIT	T cell immunoreceptor with Ig and ITIM domains
TIM-3	T cell immunoglobulin and mucin-domain containing-3
TNF	Tumor necrosis factor
T-NHL	T cell non-Hodgkin lymphoma
T-PLL	T cell prolymphocytic leukemia
T_{reg}	T regulatory cell
VEGF	Vascular endothelial growth factor

CHAPTER I

BACKGROUND AND RESEARCH OBJECTIVES

Introduction

The immune system is a complex network of cells spread throughout the body, spanning dozens of tissue types and locations. This network, functioning as individual cells and larger populations, protects the host from both external attack and internal mutiny of host cells that transform and become cancerous. T cells are a critical component of the immune response against cancer. Their generation, activation, and induction of effector function is an elegant, multi-step cycle that requires numerous cellular and molecular components (*1*). The immune system plays a major role in melanoma pathogenesis and understanding the interaction of the immune system with melanoma cells has paved the way for tumor immunology.

For decades, researchers have known that patients with melanoma generate an anti-tumor T cell response, evidenced by the existence of melanoma-antigen specific CD8 and CD4 T cells (*2, 3*). The presence of activated, memory T cells in the blood, lymph node, and tumors of patients with melanoma suggests that an anti-tumor T cell response has been generated, and yet tumors persist (*4*). This understanding that the human immune system mounted a response to the tumor resulted in the development of therapies, like vaccination and interleukins, designed to harness the immune system to better attack the tumor. However, these therapies resulted in meager response rates (*5*). In the early 1990's, immune checkpoint molecule cytotoxic T-lymphocyte-associated protein 4 (CTLA-4) was shown to attenuate T cell activity (*6*). The discovery of CTLA-4 and other immune checkpoints led to a new wave of melanoma therapeutics, known as immunotherapy. In 2011, a monoclonal antibody designed to block CTLA-4 became one of the first treatments to improve survival of late stage melanoma patients in decades (*7*). At

the beginning of this body of work, multiple monoclonal antibodies designed to block programmed cell death protein 1 (PD-1) was still in clinical trials (*8*).

Despite the success of immunotherapy in melanoma, it is still not known why some patients respond while others do not. Additionally, it is not known how immunotherapy impacts the immune system, as a whole, since immune checkpoints feature prominently at multiple key steps in the immune cycle (*1*). Compounding these unanswered questions is the complex, temporal nature of the anti-tumor immune response. A complete understanding of a systemic immune response, like those required for the regression of a melanoma tumor, requires the ability to monitor not only individual cellular populations with various phenotypes and functional states, but also the immune network as a whole. Furthermore, traditional, reductionist approaches that focus on one cell type or one protein of interest over look cells of unusual or unexpected phenotype.

High dimensional, systems immune monitoring is needed to fully understand the function and effects of immunotherapy. A high dimensional, single cell approach is needed in order to appropriately monitor and dissect the anti-cancer immune response. Recently, a new flow cytometry technique, known as mass cytometry, has been developed. Using monoclonal antibodies tagged with isotopically pure metals, mass cytometry allows for the simultaneous measurement of over 45 different parameters. This facilitates the characterization and quantification of numerous cell populations, phenotypes, and functional states within one sample (*9*). However, with this advance in bench science comes an unmet need for computational tools to analyze the resulting high dimensional data (*10*). Traditional bi-axial plots, used by immunologists for decades, become cumbersome and inefficient and fail to capture the complex multi-dimensional nature of mass cytometry data.

The combination of mass cytometry, computational analysis, and primary patient samples is needed to understand the clinical impact of immunotherapy in melanoma patients. Thus, the goal of this work is to develop a systems immune monitoring approach in order to dissect the mechanisms of immunotherapy in patients with melanoma (Figure 1.1).

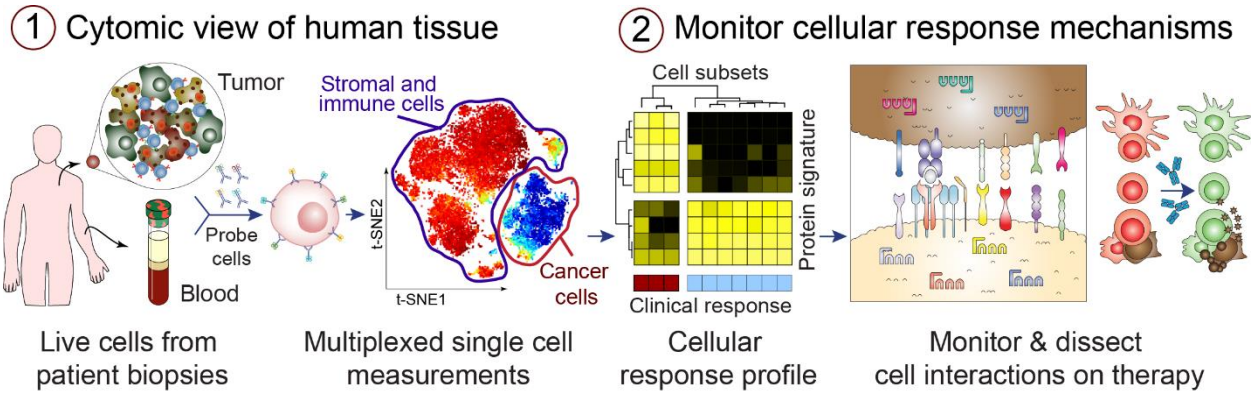

Figure 1.1. Systems immune monitoring in cancer therapy. The goal of this work is dissect response to immunotherapy using high dimensional, single cell biology and novel computational tools. 1) Acquisition of high quality tissue samples pre- and post-treatment is a critical element of human immune monitoring. Following processing into single cell suspension, and typically cryopreserved as aliquot. 2) Next, single cells must be detected using a quantitative technique. Critical to the analysis are software tools that cope with high dimensional data and provide human-readable single cell views. 3) Finally, statistical models are derived that correlate cell subsets and biomarkers with clinical outcomes. This information can be used to develop new mechanistic models of cell to cell interactions and the impact of treatment on signaling networks within and between cells.

T cell Development and Function

Generation of the T cell receptor

T cells are derived from multipotent hematopoietic stem cells (HSCs) which originate in the bone marrow. HSCs give rise multipotent progenitors (MPPs) before differentiating into common lymphoid progenitor (CLPs). CLPs that traffic from the bone marrow, through the bloodstream, to the thymus are poised to become T cells (*11*). Once in the thymus, CLPs interact with thymic epithelial cells, resulting in canonical Notch 1 signaling, committing these early thymic immigrant to the T cell lineage (*12*). Mature T cells are defined by expression of the T cell receptor

(TCR), a genetically rearranged antigen receptor composed of an α-chain and β-chain that binds to peptide fragments presented by major histocompatibility complex (MHC) molecules. The stages of T cell development correlate with the generation of the TCR, a process which involves somatic rearrangement of the variable (V), diversity (D), and joining (J) gene segments. In addition to lacking the TCR, the initial thymocytes lack expression of either T cell co-receptor CD4 or CD8 and are thus termed double negative (DN) thymocytes (*13*).

Thymocytes progress through four double negative stages, generating a functional TCR β-chain (*14, 15*). To generate a functional β-chain, thymocytes undergo recombination of the germline encoded V, D, and J segments by recombination activating genes (RAG) (*16*). If this β-chain is functional, it is able to pair with an invariant pre-TCR α-chain and CD3 molecule which is a functional pre-TCR that can traffic to the cell surface and transmit signals (*17*). After generation of a functional pre-TCR, thymocytes now enter the double positive (DP) phase, so called because of their dual expression of both co-receptors CD4 and CD8 (*15, 18*). The main focus of the DP phase is rearrangement of the TCR α-chain and production of a mature TCR complex. Like the β-chain, the α-chain undergoes rearrangement of the V and J loci; however, unlike the β-chain, there is no D segment. Once an α-chain is produced, it is paired with a β-chain, forming a TCR. Low levels of the TCR are expressed on the surface of the thymocyte, along with both CD4 and CD8. Thymocytes are now entering an antigen-dependent phase of maturation (*15*).

After producing a mature TCR, DP thymocytes migrate deeper into the thymus to undergo positive selection (*19*). A key feature of the TCR is the ability to recognize and bind to MHC containing a peptide fragment. Without this feature, T cells would not be able to identify and kill their targets. In order to survive positive selection, the TCR of DP thymocytes must bind, with appropriate strength, to MHC I or MHC II molecules (*20*). Thymocytes that bind too weakly or too strongly will die. It is during positive selection that DP thymocytes downregulate one co-receptor and become single positive (SP). If a survival signal is conferred through MHC I, the thymocyte

becomes CD8 single positive. Conversely, a survival signal given through MHC II results in CD4 single positive thymocytes (*19*).

Mature T cells are a potent effector cell with a great killing capacity. In order to prevent massive organism-wide destruction, thymocytes undergo a rigorous selection process to prevent the release of self-antigen-specific T cells into the periphery. In order to prevent wide-spread autoimmunity, SP thymocytes must also undergo negative selection (*20*). Thymocytes that bind with a strong affinity to MHC:self-peptide complex expressed in the thymus die by undergoing apoptosis (*19*). The outcome of thymocyte development and selection is a repertoire of mature T cells that recognize self MHC but are tolerant of MHC molecules presenting self-antigen peptides. Critically, mature T cells now proliferate in response to a strong TCR stimulus, as opposed to the thymocytes for whom a strong TCR stimulus results in apoptosis. Mature T cells then leave the thymus and traffic through the blood stream to peripheral lymphoid organs like the spleen and lymph nodes.

Antigen-specific T cell response

Generation of an antigen-specific T cell response requires precise orchestration of multiple cell types across multiple anatomical sites (*21*) (Figure 1.2). Antigen must first be processed and presented by antigen presenting cells (APCs) that then traffic to lymphoid tissues. These APCs must then attract naïve T cells from the blood into the lymphoid tissue (*22*). Here APCs and T cells with cognate MHC:peptide and TCR, respectively, must interact through multiple cell surface proteins in an inflammatory environment (*23*). Once T cells are primed and activated they must traffic to the site of infection where they migrate into the tissue and locate cells expressing cognate MHC:peptide. After engaging the TCR, the effector functions of the T cells are released and the target cell is killed (*21*).

Mature, naïve T cells travel through the blood and lymphatic system, entering into the lymphoid tissues where they come into contact with professional APCs, like dendritic cells (DCs). Migration from the blood stream to lymphoid tissues is orchestrated through chemokines (*22*). Chemokines, or chemotactic cytokines, are proteins secreted by cells that direct the migration of nearby cells with the appropriate receptors (*24, 25*). For example, lymph node resident DCs secrete C-C motif ligand 19 (CCL19) which binds receptor C-C chemokine receptor type 7 (CCR7), expressed by naïve T cells, attracting them to the lymph node (*26, 27*). Once T cells have migrated to the lymphoid tissue, they exit the blood stream and enter the tissue in a manner directed by cell:cell interactions (*28*). Selectins, like CD62L expressed on T cells binds to receptors on epithelial cells and initiate a signaling cascade that results in T cell extravasation into the lymphoid tissue (*29*).

Once inside the lymphoid tissue, T cells use their TCRs to sample MHC:peptide complexes presented on the surface of APCs. Adhesion molecules like lymphocyte function-associated antigen 1 (LFA-1) on T cells facilitate binding to APCs that express receptors, such as intracellular adhesion molecule 1 (ICAM-1) (*30*). This transient binding allows naïve T cells to sample a large number of MHC:peptide complexes as they travel through lymphoid organs. If a T cell recognizes its antigen, signaling through the TCR strengthens these transient binding interactions (*31, 32*). Those that do not come into contact with their cognate MHC:peptide complex travel through the tissue and reenter the blood stream. For those that come into contact with their antigen, multiple conditions must be met for productive priming and activation. The interaction of naïve T cells with mature, activated APCs in lymphoid organs is required for T cell activation and priming. T cells must receive three separate and distinct signals from their APC partner (*33*). The first of which is the signal sent through the TCR by the MHC:peptide complex. In addition to this signal, T cells must also receive a costimulation through tumor necrosis factor (TNF) family member, CD28 (*34*). B7 family members, expressed on activated APCs, bind to

CD28 on the surface of T cells and activate PI3K signaling (*35*). Importantly, upon activation, T cells upregulate CTLA-4 onto their surface. CTLA-4 binds with much higher affinity to B7 family members, out competing CD28 and preventing additional T cell activation (*36*). This makes already activated T cells less sensitive to antigens presented by APCs and limits the T cell response. The third and final signal required for productive T cell activation is provided in the form of cytokines (*37, 38*). If T cells receive all appropriate signals during activation, they undergo a period of rapid proliferation in the presence of IL-2 (*39*).

Although most self-reactive T cells are abolished during selection in the thymus, some escape to the periphery (*33*). T cells that react to self-antigens in the periphery either undergo peripheral tolerance or escape, remaining self-reactive. Peripheral tolerance and subsequent anergy arise when naïve T cells encounter MHC:peptide but don't receive a co-stimulation (*40, 41*). Co-stimulation from APCs is stronger in peripheral, non-lymphoid tissues or when the APCs have yet to be activated (*42*). If this occurs, these T cells are clonally deleted through activation-induced cell death or are rendered anergic.

There is a wide range of effector T cells, each with an important role in human health. Broadly, effector T cells fall into one of two categories defined by expression of their co-receptor, CD8 or CD4 (*33*). Effector T cells expressing CD8 are known as cytotoxic T cells (CTLs). CTLs function by killing target cells, often those infected by an intracellular pathogen or cells that have transformed and become malignant. In order to kill their target, CTLs release toxins perforin and granzymes (*43*). As the name indicates, perforin creates pores on the target cell and allows for the passage of granzymes (*44*). Granzymes, serine proteases, initiate programmed cell death, or apoptosis, by activating the caspase cascades (*45*). In addition to secreting cytotoxic granules, CTLs can also induce apoptosis in their target through binding of surface protein FAS ligand (CD95L) to protein Fas on the target cell (*46*).

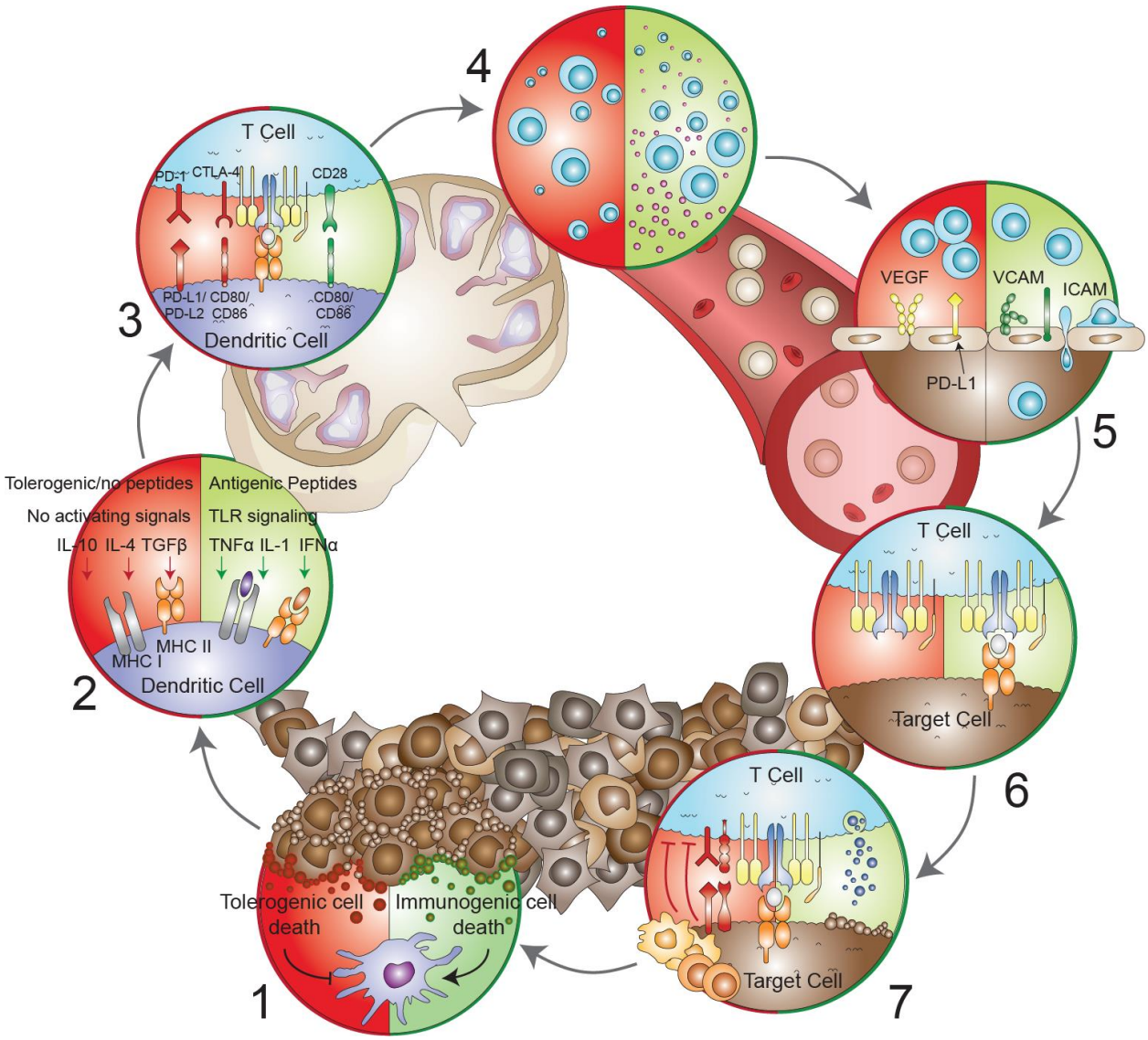

Figure 1.2. Generation, execution, and suppression of antigen specific T cell response. An antigen specific T cell response is needed for the clearance of external pathogens, like viruses and bacteria, and for transformed cells. The generation of immunity is a cyclical process with seven major stages. At each stage, factors promote a protective T cell response (green) or inhibit the immune response (red). Briefly, antigens are released from infected or transformed host cells (1), which are picked up and presented by antigen presenting cells (2). These antigen presenting cells traffic to the lymph node where they activate naïve T cells (3). After activation, T cell traffic through the blood and lymph following a chemical gradient (4) and enter into the area of inflammation (5). Once inside the inflamed tissue or tumor, T cells then recognize their target using their TCR (6) and exert their effector functions in order to promote cell death and begin the cycle again (7). *Adapted from Chen, et al. Immunity 2013*

In contrast to CD8 T cells, CD4 T cells differentiate into a multitude of effector subsets depending on the cytokine milieu present during activation (*33*). Type 1 helper T cells (T_H1 cells) are induced by IL-12 and IFNγ and go on to secrete IFNγ, activating macrophages to destroy intracellular pathogens (*47, 48*). The presence of IL-4 during activation results in generation T_H2 cells. This flavor of helper T cell produces anti-inflammatory cytokines like IL-4, are responsible for clearing parasitic infections, and are key players in the humoral immune response (*47, 49*). T follicular helper (T_{FH}) cells are also crucial for strong humoral immune response. They are located in the B-cell follicles of lymph nodes and secrete IL-21 to activate B cells to produce immunoglobulins of the G subclass (IgG) (*50*). T_H17, T_H22, and T_H9 cells are named after their effector cytokine (e.g. T_H17 are so named because they secrete IL-17) and are responsible for neutrophil recruitment, mucosal immune response, and humoral immunity respectively (*51-53*). Finally, induced T regulatory (T_{reg}) cells are marked by their expression of transcription factor FoxP3 and cell-surface proteins CD25 and CD4. Although highly heterogeneous, T_{regs} as a subpopulation of T cells are known to regulate the immune response, maintain tolerance, and prevent autoimmune disease (*54*).

In order for effector T cells to exert their effector function, they must first recognize their target and convey this message through the TCR. The TCR, comprised of the alpha and beta chain discussed earlier, is not sufficient to transmit signal from the immune synapse to the nucleus (*55*). Instead, it is a part of the TCR complex, together with CD3γ, CD3δ, CD3ε, and intracellular signaling domains CD3ζ (*56*). The first requirement of TCR signaling is recognition of cognate MHC:peptide. Binding of the TCR to its MHC:peptide initiated phosphorylation of the immunoreceptor tyrosine-based activation motifs (ITAMs) in the CD3 accessory proteins (*57*). This signaling is initiated by binding of CD4 or CD8 binding to cognate MHC. Src family kinase LCK is constitutively associates with CD4/ CD8 and phosphorylate the CD3 complex (*58*). After phosphorylation of CD3, SYK family member, ZAP-70, associates with the phosphorylated CD3ζ

through its SH2 domains to carry on the signal (*59*). After recruitment to the CD3 complex, ZAP-70 targets adaptor proteins LAT and SLP-76 (*60, 61*). SLP-76 binds adapter protein GADS and PLCγ to continue the phosphorylation cascade (*62, 63*). Complete activation of PLCγ in naïve T cells requires co-stimulation through CD28. Engagement of CD28 results in phosphorylation of Itk and subsequent activation of PLCγ (*64*). From here, the TCR signaling pathway splits into three arms, each resulting in the activation of unique transcription factors. In the RAS pathway, RAS is recruited by DAG where it is phorsphorylated by PKCθ and RAS, in turn, regulates the Map kinase (MAPK) pathway (*65*). The PKCθ pathway activates the NFkB signaling pathway (*66*). In the third arm, entry of calcium (Ca^{2+}) activates transcription factor NFAT. Signaling through the TCR induces activated T cells to proliferate and exert effector functions (Figure 1.3).

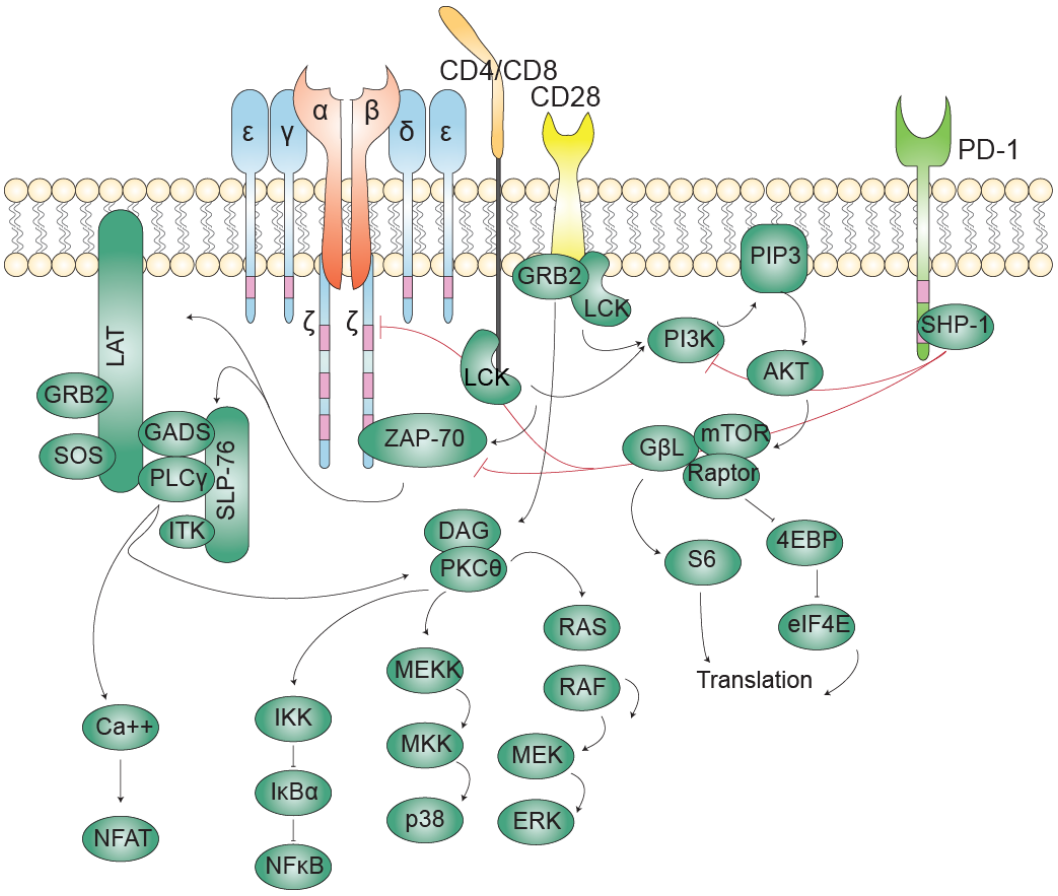

Figure 1.3 T cell Receptor Signaling and Inhibition by PD-1. Engagement of the TCR by MHC molecules results in a phosphorylation cascade. The binding of PD-1 to its ligands can recruit SHP-1, resulting in dephosphorylation of key signaling proteins in the TCR signaling cascade.

Chronic antigen stimulation and T cell exhaustion

The complex development and activation of T cells, as described above, results in a host capable of defending itself against “non-self” entities, such as viruses and bacteria. During viral infection of an immune-competent host, the virus enters the host and begins to replicate, activating the innate immune system through various mechanisms, including (but not limited to) expression of pathogen-associated molecular patterns (PAMPs) and down regulation of MHC molecules (*67*). Dendritic cells in the lymph node present viral antigen on MHC II and MHC I to T cells. In the presence of appropriate co-stimulation, T cells with cognate TCR for the specific viral peptide being presented are activated, clonally expand, and produce effector cells. These effector cells secrete proteases and cytokines, capable of killing infected target cells (*21*). In acute infections, viral antigen is cleared and effector cells and inflammatory cytokines recede, returning the immune system to its pre-infection, homeostatic state (*68*). A successful immune response also generates long lived memory T cells, capable of persisting without the presence of antigen (*69*). However, not all viral infections are cleared by the immune system. Through a variety of immune evasion mechanisms (*68, 70*), some viruses persist in the host despite a mounted immune response. In this case, instead of antigen clearance, the host will experience continuous or intermittent antigen exposure. If left unchecked, continuous attack of infected host cells by antigen specific T cells would result in severe immunopathology. Resulting immunopathology can often be of greater detriment to the host than constant habitation by the virus itself (*71*). It thus becomes necessary for the host to downregulate the inflammatory immune response, reducing the ability of CTLs to proliferate and kill their target. This dampening of the immune response results in CTLs that are unable to exert effector function in response to chronic antigen stimulation and are thus termed “exhausted” (*72*). T cell exhaustion was first described in 1998 by Rafi Ahmed’s group, who showed silencing of suppression of CD8 T cell effector function in mice with

chronic lymphocytic choriomeningitis virus (LCMV) (*73*). It was later shown that chronic antigen stimulation is sufficient to induce CD8 T cell exhaustion in mice (*74*).

There are several mechanisms by which the immune system regulates itself to prevent immunopathology during chronic viral infection, resulting in T cell exhaustion (Figure 1.2). Expression of inhibitory surface proteins, anti-inflammatory cytokines, regulatory immune cells, and altered antigen presentation by APCs all contribute to suppression of the antigen-specific T cell response. Expression of inhibitory surface proteins by T cells is perhaps the most well-known mechanism of immunoregulation. PD-1, is a key inhibitory protein that regulates T cell effector function, both preventing autoimmunity and promoting exhaustion (*75*). Mice lacking *Pdcd1*, the gene encoding PD-1, experience low levels of autoimmunity and those mice already predisposed to autoimmune disease see acclerated pathology (*76, 77*). Seminal work by Barber *et al.* showed that PD-1 was upregulated on T cells in mice during chronic LCMV infection and blockade of PD-1 with antibodies rescued T cell effector function and enhanced viral control, suggesting that PD-1 played a key role in T cell exhaustion (*78*).

The expressin of PD-1 is tightly regulated. Only when T cells are activated through their antigen receptors is PD-1 expressed on their cell surface (*79*). PD-1 has two known ligands, PD-L1 and PD-L2, expressed on both lymphoid and non-lymphoid cells (*80, 81*). The binding of PD-1 to a ligand interfere with the TCR signaling, dampening effector functions usually initiated through antigen receptor signaling (*75*). Upon ligation, the intracellular tyrosine residues that are part of the immunoreceptor typrosine-based inhibitory- and switch- motifs (ITIM, ITSM) are phosphorylated. These phosphorylation events provide docking sites for two phosphatases, SH2-domain containing tyrosine phosphatase 1 and 2 (SHP-1 and SHP-2) (*82, 83*). These phosphatases act by inhibiting phosphorylation of CD3ζ and ZAP70, as well as preventing activation of PI3K in response to CD28 costimulation (*84, 85*). It is also thought that PD-1 inhibits the RAS pathway, including downstream molecules ERK1 and EKR2 (*86*) (Figure 1.3). PD-1 isn't

the only inhibitory receptor expressed by activated T cells. CTLA-4, lymphocyte activation gene 3 protein (Lag3), T cell immunoglobulin and mucin-domain containing-3 (TIM-3), and B- and T-lymphocyte attenuator (BTLA) are just a few of the many inhibitory molecules whose ligation dampens the effect of antigen-specific T cells. Each molecule has a unique mechanism of action and blockade of multiple pathways simultaneously results in a synergistic recovery of effector function (*87-90*). These inhibitory receptors, along with many others, are heterogenously expressed across cell subsets and within different tissue compartments, creating a complex environment of lymphocyte regulation (*87*). Although expansive, inhibitory receptors are not the only mechanism of T cell regulation in situations of chronic antigen stimulation.

Extrinsic factors also contribute to T cell exhaustion. Small proteins, known as cytokines, are key factors in T cell exhaustion. Transforming growth factor beta (TGFβ) is a key immunoregulatory cytokine. It is produced primarily by certain subsets of T cells and macrophages, explored further in the next paragraph, and works by suppressing T cell activation and proliferation. Activated TGFβ binds to the TGFβ receptor, inducing a signaling cascade through the SMAD pathway, and resulting in SMAD proteins that translocate to the nucleus to regulate transcription and inhibit progression into the cell cycle (*91, 92*). Virus-specific CD8 T cells in mice with chronic LCMV displayed increased SMAD2 phosphorylation, pro-apoptotic protein Bim, and overall apoptosis. CD8 T cells from mice genetically engineered to have attenuated TGFβ signaling were increased in number and functionality compared to those from wild type mice (*93*). TGFβ has also been shown to induce immunosuppression of virus-specific CD8 T cells in humans with Hepatitis C virus (HCV) and human immunodeficiency virus (HIV) (*94, 95*). Another cytokine responsible for regulating T cell effector function is interleukin 10 (IL-10). Like TGFβ, IL-10 is produced by subsets of monocytes and T cells (*96*). IL-10 signaling inhibits cytokine production and diminishes the ability of APCs to present antigen (*97*). Antibody blockade of IL-10 in mice results in enhanced T cell effector function and concominant viral control (*98*). As

mentioned previously, these inhibitory cytokines are largely produced by subsets of regulatory monocytes and T cells. These regulatory cells make up the third mechanism by which exhaustion is induced.

Regulatory T cells (T_{regs}) are the most well known regulatory cell type. T_{regs} that control antigen-specific T cells are converted in the periphery from naïve CD4 T cells. Canonically, they express surface proteins CD4 and CD25 and transcription facter forkhead box p3 (FoxP3), although a subset of CD8 expressing $CD25^{+}FoxP3^{+}$ regulatory cells exist and regulate immune function (*99, 100*). T_{regs} act suppress activated, effector T cells through the secretion of inhibitory cytokines, consumption of growth factors, like IL-2, and induction of apoptosis or cell cycle arrest through cell-cell contact (*101*). In human patients, suppression of virus-specific T cells by T_{regs} has been demonstrated in many chronic infections, including HIV and HCV (*102-104*). Cells of the myeloid lineage are also able to induce dysfunction in T cells during periods of chronice viral stimulation. Myeloid derived suppressor cells (MDSCs) are a heterogenous group of immature myeloid cells, first described in a model of mouse lung cancer (*105*). MDSCs found in humans are less well defined than those in mice, but generally classified as $CD14^{+/-}CD33^{+}CD11b^{+}$HLA-DRlo (*106*). Secretion of three key mediators by MDSCs results in the suppression of T cells. These three mediators include arginase-1, inducible nitric oxide synthase (iNOS), and reactive oxygen species (ROS) (*106-108*). While not a comprehensive list of regulatory cells or strategies, this section provides a brief glance at the complexity and depth of immune regulation both in health and in chronic antigen stimulation.

Exhaustion is thought to be a hierarchical process, with the loss of effector functions occuring at different stages (*109*). The first phases of exhaustion usually include the loss of ability to proliferate rapidly, secrete IL-2 or kill the intended target (*72*). At intermediate stages, effector cells loose the ability to secrete other effector cytokines. Severe exhaustion is thought to occur when cells are no longer able to degranulate or secrete IFNγ. In the final and most extreme

versions of exhaustion, antigen-specific T cells are deleted from the repertoire (*110-112*). As T cells progress through exhaustion, they upregulate multliple, diverse inhibitory receptors, beginning with PD-1. Loss of effector function and subsequent exhaustion occurs for both CD8 and CD4 antigen-specific T cells (*109, 113, 114*). Viral load increases with exhaustion and loss of effector function. While this loss of effector function and eventual deletion resembles both T cell anergy and senescence, exhausted T cells develop in different environments and have very different molecular profiles. The largest difference being the expression of PD-1 in exhausted T cells, but not in anergic or senescent cells (*115*). Unlike senescent T cells, it is possible to "rescue" exhausted T cells, restoring their effector function and ability to rapidly replicate. Exhaustion can be reversed by blocking the PD-1 pathway if CD8 T cells have not progressed too far through the exhaustion heirarchy (*78, 116*).

While T cell exhaustion and dysfunction were first described in the context of chronic antigen stimulation during viral infection, these ideas were later used to understand the emerging field of tumor immunology. Chronic inflammation and immune evasion, including the induction of T cell exhaustion, are key characteristics of malignancies (*117*). With is high antigenic load and robust anti-tumor T cell response, melanoma has been at the forefront of tumor immunology and T cell exhaustion (*118*). In the following section, I will disucss the T cell response to tumors, T cell dysfunction in the tumor microenvironment, and development of immunotherapies with a focus on the role of melanoma.

Melanoma and Tumor Immunity

Immune surveillance in cancer

In the early 20th century, Paul Ehrlich first postulated that the immune system might play a role in controlling cancer (*119*). It was decades before this hypothesis had any experimental backing, first gaining traction after a great increase in the understanding of the immune system

and the subsequent discovery of cancer antigens (*120*). These data provided the foundation for the original immune surveillance hypothesis, in which researchers once again considered that the immune system was responsible for surveilling and controlling the growth of malignant cells. However, confounding experiments and dissent of the community at large once again caused the immune surveillance hypothesis to fall out of favor (*121*). Definitive evidence for the roll of immune surveillance was published in 1998 and 2000 by Dr. Robert Schreiber's group. Genetically engineered mice, insensitive to IFNγ developed tumors more rapidly and with greater frequency than their wildtype counterparts after treatment with carcinogenic chemicals (*122*). A few years later, the same group showed that both IFNγ and lymphocytes protect the host against development of cancer. In addition to this ground breaking finding, Shankaran, et al also showed that the process of tumor cell clearance by lymphocytes resulted in a selective pressure that lead to development of less immunogenic tumor cells. Tumor cells grown in immunocompetent mice were less able to establish and grow when transferred into naïve, wild type recipients as compared to those originally grown in immune deficient mice (*123*). This discovery shifted the immunosurveillance hypothesis, now suggesting that the immune system is responsible not only for the control and elimination, but also responsible for the escape and expansion of transformed cells.

To reflect this paradoxical role of the immune system in cancer development and progression, Schreiber's group went on to establish a new immune surveillance hypothesis, which he called the immunoediting hypothesis. The immunoediting process is a sequential progression comprised of "elimination", "equilibrium", and "escape" phases (*119*). The first phase, elimination, describes complete immunological deletion of the transformed cells prior to pathology in the host. If all cancerous cells are killed, the immunoediting process ends here; however, cells that persist elimination go on to enter equilibrium. During this second phase, the immune system prevents pathological growth of and alters the immunogenicity of the cancer cells. Like the elimination

phase, the host is unaware of this phase as pathology does not occur. It is possible for this phase to last for the lifespan of the host, without proceeding to the escape phase. In the final phase, escape, tumor cells acquire the ability to circumvent the immune system, either through change in the tumor cells themselves or through suppression of the immune cells. It is during this phase that the host experiences pathology due to tumor outgrowth (*124*). To better understand the role of the immune system in cancer and the development of anti-cancer therapies, each phase will be discussed in more detail below.

Complete elimination of tumor cells and possible progression into the next two phases is a cyclical process, often referred to as the "cancer-immunity cycle" (*1*). First, transformed cells must be "seen" by the immune system as non-self. This can occur through expression of mutational antigens, testes antigens, over expression of cellular antigens, viral antigens, or differentiation antigens (*125*). In melanoma, tumor associated antigens are usually either testes antigens, like MAGE and NY-ESO-1, or differentiation antigens, such as gp100 and tyrosinase (*126*). Immature dendritic cells must encounter these antigenic cells in the presence of inflammatory stimuli, like the expression of damage associated molecular patterns (DAMPs) or IFNγ (*127-129*). Activated DCs must then travel to the lymph node where they present their antigen to naïve T cells for activation. For activation of T cells and elimination of the tumor, it is important that DCs are fully mature upon reaching the lymph node, expressing key co-stimulatory molecules like CD80 and CD86 (*130*). Once activated, the tumor antigen specific T cells must traffic through the lymphatic system or blood to stream to enter into the tumor (*4, 131*). Tumor antigen specific T cells now must recognize their MHC:peptide expressing target, using their TCR before exerting their effector functions in the same way that virally infected cells are recognized by effector T cells (*1*). If this cycle completes and all cancer cells are killed, the elimination phase is complete and the host remains pathology, and cancer free. In melanoma, as well as other cancers, there are much data to suggest that this cancer:immunity cycle results in the generation

of tumor antigen specific T cells and the elimination of cancer cells. Memory and effector tumor-antigen specific T cells have been characterized in the blood and lymph nodes of human patients with melanoma and there have been multiple accounts of spontaneous regression of melanoma tumors (*4, 132, 133*). If tumor cells persist despite an immune response, the system progresses into the equilibrium phase.

During the equilibrium phase, tumor cells are kept from causing pathology by cells of the adaptive immune system. Clinical scenarios have often been used as support for the equilibrium phase of the immunoediting hypothesis. For example, two allograft, kidney transplant recipients were each diagnosed with metastatic melanoma two years after transplantation and subsequent immunosuppressive drugs. Investigators discovered that the kidney donor had been diagnosed with melanoma over a decade prior to her death and was considered cancer free at the time of donation (*134*). This suggests that the cancer was held in check, at equilibrium, by the original host's immune system but was able to grow in the presence of immunosuppressive drugs. Later, mouse models provided more definitive and mechanistic evidence for the equilibrium state. Koebel, et al. treated mice with low doses of a carcinogen, inducing occult tumors. Mice remained untreated for over 200 days to ensure that the cancer was indeed occult before being treated with a control monoclonal antibody (mAbs) or anti-CD4/anti-CD8/anti-IFNγ mAbs to deplete the T cell response. Mice with depleted T cells quickly developed large tumors at the site of the previous carcinogen injection, while the mice receiving control mAb did not (*135*). While this phase of immunoediting can occur undetected for the duration of the host's life, the constant immune pressure on genetically unstable cells can result in changes that allow the cancer cells to escape from immune control.

The third phase of the immunoediting hypothesis, escape, where their growth is no longer controled by immunological pressures. Cancer cells can escape immune control either through changing themselves to be less immunogenic or direct suppression of the immune cells (*119*). As

discussed in previous paragraphs, elimination of cancer cells requires the completion of a multi-step cancer:immunity cycle. In the following paragraphs, I will elaborate on different immune evasion mechanisms present at each stage of the cancer:immunity cycle that promote tumor cell escape (Figure 1.2).

Immune evasion and T cell dysfunction in the tumor microenvironment

In the first stage of the cancer:immunity cycle, tumor-associated antigens are picked up by local DCs (Figure 1.2, 1). A method that halts the cycle at its first stage is immunoselection of poorly immunogenic cancers during the equilibrium phase. Thus, cancer cells that do not generate a strong adaptive immune response are able to outlive strongly immunogenic cells (*136*). In order for a successful first stage of the cycle, DCs must encounter antigen in the proper context. Cells that die and release antigen following necrosis release DAMPs, along with antigen, activating the DC and causing maturation. However, if cancer cells die via apoptosis, no such danger signals accompany antigen release and the DCs become tolerogenic (*129*). Tolerogenic DCs are unable to properly activate CTLs in the lymph nodes, cutting the cancer:immunity cycle short. As in chronic viral infections, immunosuppressive cytokines like IL-10 can downregulate the ability of DCs to present antigen (*97, 137*) (Figure 1.2, 2). This is a mechanism by which tumors can induce tolerance in tumor-antigen specific T cells, thus rendering them nonresponsive.

Because the cancer:immunity cycle is, as its name suggests, cyclical, defects in the first stages intimately affect the following stages. For example, in mouse models of melanoma, β-catenin signaling from the cancer cells blocks production of chemokine CCL4, preventing dendritic cells from entering the tumor microenvironment. Without DCs, there is no presentation of antigen to T cells in the lymph node, and thus naïve T cells are not primed and activated for killing their target (*138*). Even when DCs are recruited to the tumor microenvironment and are able to pick up tumor-antigen, the tumor microenvironment can induce expression of inhibitory ligands on their

surface. Vascular endothelial growth factor (VEGF) is able to induce expression of PD-L1 on the surface of APCs in the tumor microenvironment. This PD-L1 can then interact with PD-1, expressed on the surface of recently activated T cells, to inhibit proliferation or cytokine secretion (*139*). Similarly, recently activated T cells express CTLA-4 on their surface. CTLA-4 is able to outcompete CD28 for binding to CD80 and CD86, expressed on DCs, and through doing so, suppress T cell function (*36*). Antibody blockade of CTLA-4 enhances the priming of tumor-specific T cells and can lead to tumor clearance in both mice and people (*6, 7, 140*) (Figure 1.2, 3).

If tumor antigen-specific T cells are able to be activated and primed, they must then traffic to the site of the tumor. In an optimal immune response, the cells located at the tumor site will produce CCL3, CCL5, CCL20, and CXCL10 in order to recruit CD8 T cells (*131*). However, posttranslational modifications of chemokines, like proteolysis or nyosylation, can reduce their ability to recruit T cells to the tumor (*141*) (Figure 1.2, 4). Beyond migrating through the blood and lymphatic systems to reach the site of the tumor, the activated tumor-specific T cells must cross the vascular epithelium to reach their target. Entrance into the tumor, through the epithelium is a multistep process involving rolling and adhesion of the T cell to the epithelium. Molecules, like VEGF, can inhibit this process and prevent the T cells from entering into the tumor microenvironment (*141, 142*). Additionally, endothelium associated with the tumor microenvironment can express PD-L1 and PD-L2 which can suppress T cell activity (*143*) (Figure 1.2, 5).

Once inside the tumor microenvironment, the activated tumor specific T cells must recognize their target. However, some tumor cells acquire the ability to downregulate MHC I, thereby becoming invisible to the T cells (*144*). Tumor cells also can have defects in the machinery needed to properly process and present antigen, preventing the formation or presentation of antigenic peptides in the MHC I groove (*145*). Additionally, selective pressure during the

equilibrium phase can result in an outcropping of tumor cells that don't express antigens seen as "non-self" by the immune system (*146*) (Figure 1.2, 6). The final stage of the cancer:immunity cycle occurs when CTLs recognize their target and exert their effector function, eliminating the cancer cell. There are multiple mechanisms within the tumor microenvironment that allow tumor cells to evade killing by tumor specific T cells. Tumor cells express a variety of proteins on their surfaces, many of which are detrimental to T cell immunity (*1*). Molecules in the TNF family, like FAS-L can directly kill T cells who express cognate receptor, FAS (*147*). As in systems of chronic viral infection, expression of inhibitory receptor ligands by the target cell can result in suppression of T cell function. A wide variety of inhibitory receptors and their ligands are known to play a role in the tumor microenvironment, especially in melanoma. PD-1 and its ligands PD-L1 and –L2 are perhaps the most well-known inhibitory pathways. As discussed previously in this text, ligation of PD-1 results in dampening of the TCR signaling pathway and subsequent loss of effector function (*148-150*). Inhibitory molecules TIM-3, LAG-3, BTLA, TIGIT, and CTLA-4, among others, have all shown a role in cancer cell survival (*151*). Flow cytometry analysis of tumor infiltrating T cells has shown co-expression of multiple inhibitory receptors, highlighting the complexity of immune suppression in the tumor microenvironment (*151-153*). Secreted factors like TGFβ and IL-10 also contribute to poor T cell function, just as in chronic viral infection (*154, 155*). Similar to environments of chronic antigen stimulation, regulatory cells like MDSCs and T_{regs} play a crucial role in promoting tumor growth and survival by suppressing T cell effector function (Figure 1.2, 7) (*156*).

Development and success of checkpoint blockade

Melanoma is a major human health problem with nearly 90,000 new cases and 10,000 deaths each year in the USA alone. Despite the fact that advanced melanoma responds poorly to both chemotherapy and radiotherapy, these treatments remained the best options for patients for over 30 years. During this time, patients diagnosed with late stage melanoma had a median

survival of less than one year (*157*). With so many stages of the cancer:immunity cycle vulnerable to suppression by cancer cells, it's not surprising that a multitude of anti-cancer drugs aimed at boosting the immune system have been developed. With a high mutational burden and extensive immune infiltrate into tumors, melanoma has been a model system for cancer immunotherapy. Additionally, it is the disease at the center of this thesis. For that reason, I will focus on the development of immune boosting therapies in the context of melanoma during the following section.

The Alkylating agent dacarbazine was approved for the treatment of metastatic melanoma in 1975. With dacarbazine, median survival ranged from 5-11 months, with an overall 1-year survival of 27% (*158*). Despite the dismal prognosis, this remained the only treatment option for nearly 30 years. In 1992, IL-2 was approved for use in melanoma (*159*). The goal of treatment with IL-2 was to stimulate the cytotoxic function of both CTLs and NK cells in the tumor microenvironment. Approximately 6% of patients treated with IL-2 had a complete response with 16-20% of patients undergoing partial responses. Despite improved survival compared to dacarbazine and even complete cures for a small fraction of patients, IL-2 had to be administered in the hospital, under close supervision due to its high toxicity (*5*). Another cytokine used to treat melanoma is interferon alpha (IFNα). In addition to its anti-proliferative and apoptotic effects on melanoma cells, IFNα was intended to increase the immunogenicity of the tumor cells and increase clonal expansion of tumor-specific CD8 T cells (*160-162*). Response rates reached as high as 23% with IFNα (*5*). These cytokine therapies, along with others, were designed to bolster the cancer:immunity cycle at various stages, including antigen presentation and T cell activation. The small cohort of patients who responded robustly indicated that the immune system was indeed being strengthened, however that majority of the patients failed to respond.

A key step in generating anti-tumor immunity is the presentation of antigen by DCs. Melanoma is well known for expressing antigens recognized by the immune system, however

suboptimal antigen presentation has been observed (*2*). Vaccination to induce immune recognition of tumor cells was thus proposed as a possible anti-cancer therapy. A variety of vaccines were developed and tested in the context of melanoma. Rosenberg, et al treated melanoma patients with a vaccine derived from the gp100 melanoma associated antigen with resulting response rates over 40% (*163*). Using DC vaccines, Thurner, et al achieved objective responses in 6/11 patients with metastatic melanoma (*164*). Despite success by these physician scientists, the majority of patients treated with any of a large number of cancer vaccines did not show clinical response. Indeed, a lack of clinical response was often seen even in patients who developed high levels of tumor antigen-specific CD8 T cells (*5, 165*). Although cancer vaccines did not improve outcome for the majority of melanoma patients, they provided additional biological insight into the biology at the heart of the disease. Primarily, they revealed that even if anti-tumor T cells are appropriately generated, tumor regression does not occur.

Adoptive transfer of lymphocytes is another key development in melanoma immunotherapy. Tumor reactive T cells were isolated from autologous tumors, expanded ex vivo, and then returned to the patient following lymphodepletion. In clinical trials, adoptive T cell transfer resulted in complete responses in 8% of patients and partial responses in 50% of patients (*166*). In addition to cancer vaccines, the Rosenberg group pioneered adoptive chimeric antigen receptor (CAR) T cell therapy for patients with melanoma. In these studies, T cells were engineered to express T cell receptors specific for tumor antigens. With partial response rates of 13%, CAR T cell therapy did not perform as well as autologous T cells (*167*).

In the final phase of the cancer:immunity cycle, tumor antigen specific T cells recognize and kill their intended target. Despite generation or adoptive transfer of activated, tumor-specific T cells, the majority of patients continued to see tumor progression. Inhibitory receptors and their ligands are major suppressive elements present at multiple stages of the cancer:immunity cycle. As mentioned earlier, inhibitory molecule CTLA-4, expressed on activated T cells, outcompetes

CD28 for binding with CD80 and CD86. This interaction suppresses T cell activity during periods of chronic antigen stimulation (*36*). Preclinical mouse models showed tumor clearance in mice treated with an antibody that blocked CTLA-4 from binding to CD80 and CD86 (*6*). This response was only seen in mice that had generated an anti-melanoma tumor response. However, by combining CTLA-4 blockade with granulocyte/macrophage colony-stimulating factor (GM-CSF), Allison and colleagues were able to rescue those mice with poorly immunogenic tumors (*168*). These preclinical findings launched the production and subsequent clinical trial of fully humanized monoclonal antibody designed to block CTLA-4, ipilimumab. Ipilimumab performed well throughout the phases of clinical testing and in the final, randomized, three-arm clinical trial, metastatic melanoma patients who were treated with ipilimumab had a survival increase of 3.5 months beyond the group who did not receive the drug (*7*). In addition to increased survival, 18% of patients treated with ipiliumumab survived greater than 18%. This was more than 10% higher than those treated with the gp100 vaccine alone (*7*). Ipilumumab became the first drug to improve survival for patients with metastatic melanoma (*151*). A unique feature of CTLA-4 blockade, not seen in chemotherapy or small molecule inhibitors, was delayed response time. In many patients, response to ipilimumab took up to 6 months, far longer than the response time of weeks seen for patients treated with chemotherapy (*151*). The success of CTLA-4 blockade in melanoma patients has paved the way for other immunotherapies designed to block immune checkpoints.

A key immune checkpoint in the anti-cancer immune response is PD-1. Discussed earlier, PD-1 is largely relegated to the peripheral tissues at the time of antigen-induced inflammation (*169*). When PD-1, expressed on the surface of T cells, is engaged by its ligands, T cells are suppressed and unable to exert their effector functions (*80*). Intratumoral, melanoma-specific T cells have been shown to express high levels of PD-1 and to be functionally impaired (*149*). Together with high expression of ligand PD-L1 on cancer cells, pre-clinical models have been tested for monoclonal antibody blockade of PD-1 (*148, 170*). As of 2012, antibodies designed to

block PD-1 were still undergoing clinical trial. Results appear promising with several patients experiencing tumor regression and significant increases in lymphocyte infiltration into metastatic tumors (*171*). Follow up studies show that the response is both durable and that side effects are remarkably low compared to treatment with ipilimumab (*151*).

Systems Immune Monitoring

The immune system is a complex network comprised of localized and specialized tissue sites connected by circulating immune cells. Traditional immunological techniques and approaches have provided a depth of knowledge within each compartment, but struggle to comprehensively dissect the network and its interactions as a whole. In addition to system-wide complexity, each cell subset is itself a “system within a system”, possessing its own hierarchies and heterogeneity. As cancer and immune system cells compete in a complex and continuously evolving cycle (*1*), understanding the complex rules governing anti-cancer immune responses poses a challenge. Multiple subsets of immune cells are implicated as promoters or inhibitors of the anti-tumor immune responses (*172, 173*). To dissect and predict anti-cancer immune responses, it is crucial to not only monitor the cellular milieu of peripheral blood, tumor sites, and draining lymph nodes, but also to monitor the cell surface molecules responsible for cell:cell interactions, the deep immunophenotype of cell subsets of special interest, and intracellular signaling events including post translational protein modifications, proliferation, cytokine production, and other functional capabilities (Figure 1.4).

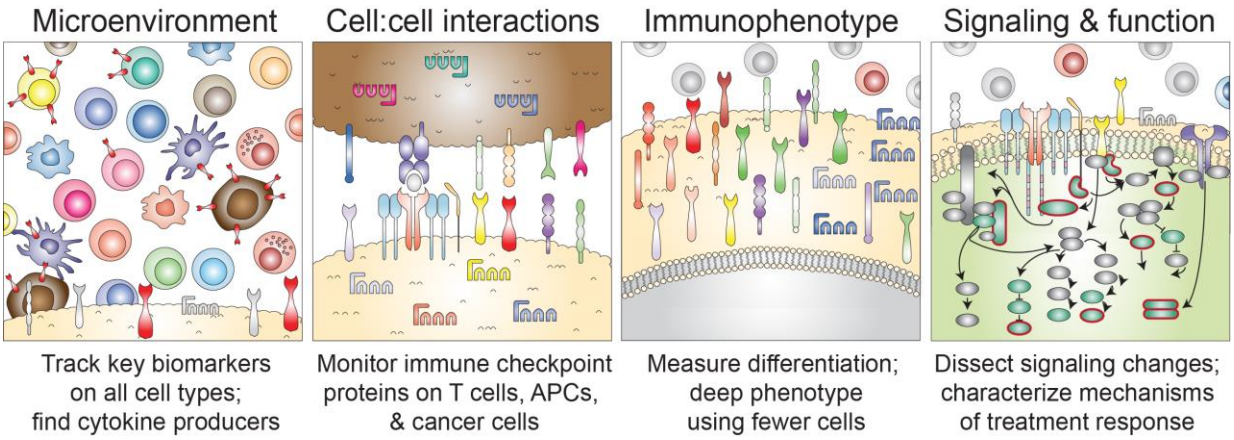

Figure 1.4. Focal single cell areas in systems cancer immunology. Mass cytometry and other multidimensional single cell tools can be focused to resolve key biomarkers and mechanisms at different layers of cellular interaction. Most commonly, mass cytometry is used to provide cytomic resolution, meaning that all the different cell types present in a tissue are quantified and phenotyped. As this can generally be achieved with 10 markers on a typical mass cytometry panel, this leaves at least 25 mass channels available for detection of cell interaction markers, immunophenotype, and intracellular signaling (*174*). As nearly any cellular property can now be quantified at the single cell level (*175*), multidimensional cytometry enables biomarkers with complex expression patterns that can vary with cell type and activation state – such as PD-L1 (*176*) – to be broadly monitored. Another advantage of cytomic approaches is that cells with unusual and unexpected phenotypes present in a patient's tissue sample do not escape detection due to expert bias or overly focused analysis strategies. These advantages of mass cytometry address ongoing needs in cancer and immune biomarker development (*177*).

Rationale and techniques

Each step of the cancer-immunity cycle includes the potential for competition between effector and regulatory cells, and nearly every immune cell subset has been implicated in the anti-cancer immune response (*178*). Dendritic cells presenting tumor antigen are required to activate a specific anti-cancer adaptive immune response (*1, 179*). Effectors like $CD8^+$ and $CD4^+$ T cells, NK cells, and tumor specific antibodies participate in direct killing of tumor cells (*123, 180-182*). Controlling these effectors are cells and signaling mechanisms that can check or attenuate immune responses, including regulatory and suppressive cells arising from the T cell (*183*), myeloid (*184*), and B cell lineages (*185*). These effector and regulatory cells are diverse in phenotype and variable in abundance (*186*). While some cell subsets comprise a substantial proportion of the total leukocyte pool (e.g. ~2-11% cytotoxic T cells), others, such as T_{regs} or

memory B cells, can contain critical information while comprising <5% of total leukocytes (*187-190*). Although small in number, regulatory cell subsets can drastically impact the anti-tumor immune response. Thus, the ability of mass cytometry to characterize rare cells comprising as few as 1 in 10,000 cells is a key advantage for evaluating the state of a patient's immune system (*191*).

In addition to detecting rare cellular subsets, high dimensional single cell technologies are also capable of revealing cells with unusual or unexpected phenotypes. With single cell analysis, it is possible to not only resolve rare cell subsets or subtle changes in phenotype, but also to distinguish cancer cells from healthy non-hematopoietic cells, and immune cells (*175, 192*). Small phenotypic shifts, such as the slight downregulation of antigen receptors by activated T cells (*193*), may provide important information about the state of a patient's immune system. At present, the effort is to track the status of cells and identify markers and mechanisms that indicate status can cell type, including "poised to attack cancer cells", "in need of priming", "held in check by regulation", or "lacking key effector subsets". Given sufficient examples, it may be possible to discern the signaling rules that govern cell identity and to use this information to precisely modulate the *in vivo* activity of target cell subsets.

The behavior of effector immune cells is directly affected by the engagement of cell surface receptors. While some ligands are soluble, like many cytokines and chemokines, many are bound to the surface of APCs and even cancer cells themselves. A long list of cancer cell bound ligands are known to modulate and suppress the behavior of cytotoxic T cells within the tumor microenvironment (*151*). Although it is well known that cancer cells express molecules like PD-L1 that modulate the immune response, the surface phenotype of cancer cells is less well characterized than immune cells. Including key markers of cancer cell type in immune classification panels makes it possible to localize biomarker and cytokine expression to cancer

and immune cells, which is especially important given how cancer cells aberrantly express molecules from outside their lineage of origin.

Distinguishing “cancer” versus “healthy” cells and then attributing genotype and phenotype characteristics is especially critical when developing novel therapeutics expected to have selective activity on cancer cells. Analysis of non-cancer cells can provide information on off-target effects of therapeutics. For example, small molecule inhibitors have varied functional impacts across immune cell populations (*9, 194*). Preserving viability and effector function of healthy immune cells during cancer therapy is crucial for maintaining an effective anti-tumor response (*195*).

Single-cell biology in clinical practice

The immune system is constantly in flux with cells undergoing stimulation, suppression, expansion and death resulting in phenotypic changes (*196*). Static snapshots of tissue and tumor resident or peripheral immune cells provide a wealth of information about overall immune function and tumor immune response, although lack key information about dynamic changes. Serial acquisition of healthy donor peripheral blood revealed low intra-donor variability but high inter-donor variability (*197*). With the combination of high, single-cell resolution and primary patient samples over the course of therapy, it is possible to create an in-depth picture of the immune network as therapy progresses. By connecting this detailed picture with the clinical outcome of the patients, it may be possible to 1) identify a marker that predicts whether patients will respond to therapy and 2) identify a specific cell type or group of cells that are responsible for successful therapy.

Multidimensional flow cytometry has been a gold standard of single cell biology, both within basic research labs and the clinic. Flow cytometry is routinely used in the clinic for analysis and diagnosis of leukemia and lymphoma, identification of lymphocyte subsets in HIV infection,

monitoring solid organ transplantation matches, and detection of immunodeficiency. In traditional flow cytometry, single cell suspensions are stained with a cocktail of antibodies tagged with different fluorophores (*198*). Stained cells are then run through a flow cytometer in a single cell stream, passing by lasers that excite the fluorophores conjugated to the antibodies bound to the cell surface. The emissions of the excited fluorophores are then recorded by the machine's detector (*199*).

Like fluorescence flow cytometry, mass cytometry utilizes single cell suspensions stained with antibody cocktails. However, instead of fluorophores, antibodies used in mass cytometry are coupled to pure metal isotopes rarely found in nature. Stained single cells are atomized and ionized by argon plasma. The resulting ion clouds are then resolved and quantified by time-of-flight mass spectrometry. Mass cytometry largely eliminates spectral overlap issues that can confound quantitative fluorescence cytometry and has been used to measure over 40 parameters simultaneously at the single cell level (*200*). The use of metal isotopes and inductively-coupled mass spectrometer (ICP-MS) allows for precise quantitation (*201*). The capacity to measure so many features per cell allows combined detection of surface proteins, intracellular phospho-proteins, transcription factors, and functional markers, such as cleaved caspases, within a single panel. While monitoring of these features in live cells is not possible, by fixing cells at multiple times following stimulation, a kinetic analysis of specific populations within a heterogeneous sample is obtained (*9, 192, 194*).

While mass cytometry is not the only quantitative, high-dimensional technique, it is especially effective for monitoring immune responses in patients undergoing immunotherapy. In particular, mass cytometry allows for high-dimensional, single cell analysis at a relatively high throughput of around 500 cells per second. Other multidimensional techniques may play a role in immune monitoring as well. Polychromatic fluorescence flow cytometry has contributed immensely to the field of tumor immunology and, unlike CyTOF, can be utilized for fluorescence

associated cell sorting (FACS). Multidimensional fluorescence and mass based imaging techniques can provide information about cellular positioning and cell-cell contacts (*194, 202, 203*), but typically measure several orders of magnitude fewer cells per sample than either fluorescence or mass cytometry. These techniques make excellent use of widely-available formalin-fixed paraffin-embedded (FFPE) blocks of tumor tissue. Recent work indicates that fixed cells can be released for analysis by mass cytometry (*204*).

In addition to protein, it is possible to measure RNA transcripts at the single cell level. Single cell RNA sequencing (scRNAseq) measures the transcriptome quantitatively at the single cell level (*205*). Despite the high dimensional, single-cell capabilities, scRNAseq typically measures only tens to hundreds of cells per sample and detection of transcripts can be confounded by issues including cell size, cell cycle changes, cell death, and allele dropout (*206*). Additionally, scRNAseq is restricted to measuring RNA transcripts and does not provide information about which genetic material is ultimately translated into protein or how these proteins are post-translationally modified. Quantitative PCR can also measure DNA, but is generally focused on hundreds of targets. Polychromatic fluorescence cytometry, imaging cytometry, scRNAseq, qPCR, and many other high dimensional technologies have produced great advances in the field of tumor immunology and will continue to play key roles in discoveries aimed to improve patient care. However, mass cytometry's ability to measure surface protein expression, post-translational modifications, transcription factors, and functional outcomes (e.g. cytokine production, apoptosis, cell cycle) for millions of cells at the single cell level (*175*) makes it uniquely adapted for monitoring immune responses in cancer patients undergoing immunotherapy.

Machine learning for human immunology

The increasing dimensionality of mass and fluorescence cytometry has dramatically increased the robustness and complexity of cytometry data (*207*). Analysis of data from a single

mass cytometry panel containing 30 antibodies would require hundreds of traditional, biaxial plots (*174*). The use of hundreds of biaxial plots to analyze high dimensional, single cell data is not only impractical, but also insufficient in its ability to characterize complex cellular phenotypes and overly reliant on prior knowledge of the cell of interest. Thus, the growing use of high-dimensional cytometry has necessitated the development of novel data analysis tools. These advances have ushered in an 'information age' of single cell biology (*208*) by providing researchers with access to machine learning tools for dimensionality reduction, clustering, and model building. Machine learning algorithms can be designed to learn and improve performance based on previous experience (*209*). Algorithms are needed to facilitate interpretation of highly complex, multidimensional data.

Machine learning and computational analysis make it possible to analyze large data sets in a reasonable amount of time. The technological advances in flow cytometry have enabled the field to measure over 30 parameters simultaneously, either through mass cytometry or polychromatic fluorescence cytometry. Analysis via traditional biaxial gates would result in hundreds of biaxial gates, and these gates would still fail to show high-dimensional co-expression of measured proteins (*174*). Computational analysis tools like SPADE reduce multi-dimensional data into two dimensions while retaining high dimensional phenotype (*210*). This allows the user to comprehensively analyze co-expression of all measured proteins. In addition to comprehensively analyzing and displaying data, computational methods are able to reduce bias. Analyzing all the data allows for the identification of cells with unusual or novel phenotypes that might have been overlooked otherwise (*208*).

Ultimately, it may be possible to bring cytomic profiling into the clinical setting such that a rapid assessment of cellular biomarkers could guide treatment. However, the current data analysis workflow remains driven by human experts and accounts for nearly half of the time spent going from sample to useful data. Expert driven manual analysis, the current gold standard, of

high dimensional data is much too time consuming for practical clinical use. Computational analysis tools are not only able to dramatically speed up analysis, but also reduce bias and facilitate the discovery of unexpected cell types or phenotypes. By using an unsupervised computational workflow (*207*), it is now possible to automatically analyze cellular populations, subsets, and single-cell phenotype for millions of cells within minutes of data collection. In time, computational tools are expected to play an increasing role in guiding diagnosis and treatment selection.

Mass cytometry could play several potential roles in cancer therapy. First, identifying markers that predict response to immune checkpoint inhibitors is a major unmet need. Pre-treatment or early-on-treatment peripheral blood or tumor biopsies could be profiled to identify immune cell subsets that correlate with response to treatment or even severe toxicities. Second, with the advent of immune therapy combinations, dissecting the individual and collective effects of each agent will be critical. For example, a combination partner with immune therapy that dampens cytotoxic T cell proliferation or signaling may compromise rather than enhance the anti-tumor immune response. Mass cytometry could be used, therefore, in clinical trials or even in a high-throughput fashion to screen novel combinations. Particular cellular populations may herald durable responses, or conversely, impending relapses. Studies by our group and others are addressing these clinical challenges.

A critical element is the acquisition of high quality samples of human tissue. As a field, there is a need for standardized procedures and consistent support for sample acquisition as part of clinical trials, especially early phase trials. Still missing, however, are studies testing the impact of sample acquisition and preparation conditions on a wide number of endpoint assays and standard protocols for data quality assessment that include protocols for data analysis. This problem is especially significant in the realm of multi-center trials, where differences in capacity and experience among the centers leads to inconsistent practices that jeopardize data integrity.

However, publication and agreement on standards of practice can ameliorate these inconsistencies. As mass cytometry and other single cell immune monitoring techniques become more widely adopted, it will be valuable for the field to further develop and implement standardized procedures for immune monitoring, from sample collection to cytometric protocols to data analysis.

Research Objectives and Preface

The purpose of this thesis is to dissect mechanisms of response to anti-cancer therapy in patients with melanoma using a systems immune monitoring strategy that characterizes and quantifies changes in the individual populations and immune system, as a whole. For those diagnosed with late stage melanoma, prognosis remains poor, with median survival ranging from 6-9 months (*211*). Despite the presence of melanoma-specific T cells in the blood and tumor of patients with advanced disease, immune-mediated tumor rejection is rare (*212*). Recently, two therapies aimed at boosting T cell function have been FDA approved or begun clinical trials. Ipilimumab and pembrolizumab block immune checkpoint molecules CTLA-4 and PD-1 respectively from binding their ligands. While both therapies have increased efficacy compared to chemotherapy, most patients ultimately relapse and die from their disease (*213-215*). There are currently no clinical biomarkers to predict which patients will respond to immunotherapy. Additionally, the effects of these immune checkpoint inhibitors on the systemic immune system are unclear. Understanding the mechanisms of response to immunotherapy is critical for improving treatment. The work described in this thesis describes the development of experimental and computational tools designed to dissect a systems biology response to therapy, over the course of time. When applied to clinical samples, this frame work reveals a novel population of T cells that lack CD4 and CD8 and are common across multiple types of human cancer.

In Chapter II, I describe work performed with Katherine Vowell (nee Nicholas), Ph.D. to evaluate a new technology, mass cytometry, to best characterize and dissect the human immune

system under stimulated conditions. Mass cytometry is an antibody-based technology that provides the unprecedented ability to monitor dozens of proteins at the single cell level, without the limitations of spectral overlap seen in fluorescence flow cytometry. Our work revealed that a single, mass cytometry panel comparably reflected results from five fluorescence flow cytometry panels in the ability to quantify and characterized stimulated, human immune cells. Additionally, I found that high dimensional data combined with data analysis tool viSNE allowed for the quantification and characterization of stimulated T cells, lacking canonical T cell marker CD3. This work reveals the importance of high dimensional, single cell biology for identifying and tracking immune cells in the context of chronic stimulation, similar to that seen in the tumor microenvironment.

In Chapter III, I summarize work done closely with Dr. Utpal Davé to characterize genomics and cytomics of T cell neoplasms. In this body of work, I use high-dimensional, single cell biology to characterize the phenotype and dissect signaling responses in a patient with T cell pro-lymphocytic leukemia (T-PLL) before and after treatment. Next generation sequencing was used to profile diverse T cell neoplasms from over 90 patients. One third of patients harbored mutations in the JAK-STAT pathway. Ruxolitinib, a JAK inhibitor, was used to treat an index patient. Mass cytometry and phospho-flow cytometry was used to characterize phenotype and signaling before and after therapy and revealed downregulation of phosphatase CD45, JAK pathway hyperactivation, and common-gamma chain cytokine hypersensitivity. This work provides compelling evidence for improved patient care and increased mechanistic understanding of anti-cancer therapy through the use of systems immune monitoring in the clinic.

In Chapter IV, I detail my work applying systems immune monitoring to a case study of a melanoma patient receiving anti-PD-1 who develops myelodysplastic syndrome unexpectedly. By using mass cytometry, I was able to simultaneously track and characterize myelodysplastic blasts and non-blast immune cells. This patient had a slightly elevated frequency of PD-1^{+}PD-L1^{-}

myeloid cells prior to treatment and displayed an increase in activated ($CD45RA^+$) non-blast myeloid cells as anti-PD-1 therapy progressed. Additionally, the large phenotypic shift of the peripheral blasts was effectively captured. This work builds on the clinical impact of high dimensional, systems immune monitoring shown in the previous chapter. Additionally, this work provides evidence for use of mass cytometry for identifying cells of unusual and unexpected phenotype while revealing a need for unbiased cell identification and tracking.

In Chapter V, I describe my part in developing Marker Enrichment Modeling (MEM), a novel tool for quantifying cellular heterogeneity in human tissues. The MEM algorithm automatically calculates a label for cellular populations, providing a quantitative list of population-specific features. Using this label, it is possible to directly compare cell population identity across experiments and even platforms. My role in this work was to generate a high-dimensional data set of clinical, human samples including peripheral blood, tonsil, and melanoma tumors. I then applied the MEM algorithm and similarity score, developed by Dr. Kirsten Diggins, to the CD4 T cell compartment of the human samples. MEM was able to identify key features of CD4 T cell subsets, like expression of CD45RO on memory cells. The similarity score, based only on MEM labels, was able to correctly cluster known CD4 populations from across patients and tissue types. This work provides a first step towards automated identification of cellular populations and leads the way for a data base of cell identity.

In Chapter VI, I detail my work in dissecting systems immune response of melanoma patients receiving anti-PD-1 therapy and small molecular inhibitor therapy using an ensemble of tools I developed. This ensemble of tools includes Earth Mover's Distance (EMD) combined with tSNE, a tool developed for mass cytometry during my time in graduate school, population quantification, and population characterization using MEM. Combining these tools revealed stability in the peripheral blood of melanoma patients receiving anti-PD-1 therapy, with the exception of a patient who developed myelodysplastic syndrome (described in Chapter IV).

Further analysis revealed a loss of detection of PD-1^{+} T cells in the periphery. These PD-1^{+} T cells were phenotypically distinct from PD-1^{+} T cells found in the tumor, specifically lacking activation markers but expressing trafficking proteins. In contrast to the stable immune system of patients receiving immunotherapy, the ensemble system analysis platform revealed plasticity in the T cell compartment of melanoma tumors receiving small molecular inhibitor therapy. An increased frequency of CD3^{+} CD4^{-}CD8^{-} (DN) T cells was seen in human melanoma tumors serially biopsied after MEK and BRAF inhibitor therapy. These DN T cells were phenotypically distinct from DN T cells from healthy tissue but similar to DN T cells found in glioblastoma and renal cell carcinoma. This work develops a novel, automated work flow for immunologists and clinicians using high dimensional technology to monitor patients undergoing therapy. When applied to a clinical scenario, the ensemble analysis process reveals a novel T cell, shared across cancers.

In Chapter VII, I summarize my findings of systems immune monitoring in patients with melanoma and their significance. My future directions diverge into two paths--biological and computational. Biologically, I propose that future studies should focus on in-depth characterization of phenotype, function, and development of double negative T cells in healthy and malignant human tissue. This can primarily be accomplished through sequencing RNA, measuring intracellular effector molecules in response to stimulation, and developing ex vivo culture models to track development. Computationally, I will discuss the future of automated data analysis for the clinic and discuss the roll of machine learning in human health.

CHAPTER II

MULTIPARAMETER ANALYSIS OF STIMULATED HUMAN PERIPHAL BLOOD MONONUCLEAR CELLS: A COMPARISON OF MASS AND FLUORESCENCE CYTOMETRY

Authors: Katherine J. Nicholas, Allison R. Greenplate, David K. Flaherty, Brittany K. Matlock, Juan San Juan, Rita M. Smith, Jonathan M. Irish, Spyros A. Kalams

This work is adapted from the manuscript published in *Cytometry Part A* 2016 (Nicholas, et al. 2016).
http://onlinelibrary.wiley.com/doi/10.1002/cyto.a.22799/full
License 4275960274774, Issued January 25, 2018

Introduction

Fluorescence cytometry has driven forward our understanding of cell biology in human immune monitoring and disease studies for decades by quantitatively characterizing single cells based on cell surface and intracellular features (*174, 175, 199, 216, 217*). Mass cytometry is a new quantitative single cell flow cytometry approach that employs antibodies conjugated to stable isotopes of metals and time of flight mass spectrometry as a detection technology (*201, 218*). Due to the precision of mass resolution, hundreds of features can theoretically be measured on each cell simultaneously using a mass cytometer. Recently mass cytometry has emerged as a powerful tool for high dimensional single cell analysis that has been used to characterize diverse populations of immune cells (*9, 186, 200, 219-223*).

While several studies have highlighted the potential of mass cytometry for describing cellular subsets in great detail (*9, 186, 200, 219-222*), only a few of these studies have directly compared mass cytometry with traditional fluorescence cytometry for evaluating human cell populations (*9, 174, 223, 224*). Furthermore, despite its promise, mass cytometry is still a

relatively new technology, and extensive optimization of panel design, protocols, and analysis workflows will be required to acquire and appropriately analyze the vast amount of data generated (*207, 225, 226*). Here a direct comparison of mass cytometry and traditional fluorescence cytometry is described in detail for human subjects. A panel of 20 well-established surface markers of lymphocytes was used to assess whether mass cytometry provided equivalent per-marker and per-subset information on a one-to-one basis with traditional fluorescence cytometry. Unstimulated and stimulated human PBMC from six donors were analyzed with five established fluorescence cytometry panels in our laboratory and one newly optimized mass cytometry panel. The results of the two platforms were highly concordant, suggesting that mass and fluorescence cytometry will be complementary technologies used for characterizing the complex, dynamic cellular phenotypes that exemplify immune responses.

Materials and Methods

Cell isolation and culture

Peripheral blood mononuclear cells (PBMC) from healthy donors (N = 6) were isolated using density gradient separation (Ficoll-Paque™ Plus, GE Healthcare, Piscataway, NJ, USA). PBMC were pelleted by low speed centrifugation (400 x *g*), resuspended in media composed of 90% fetal bovine serum (Atlanta Biologicals, Norcross, GA, USA) containing 10% DMSO (Sigma-Aldrich, St. Louis, MO, USA), frozen slowly in the vapor phase of liquid nitrogen in multiple cryotubes, and stored in liquid nitrogen, as previously described (*227*). The Vanderbilt University's Institutional Review Board approved this study, and all individuals provided written informed consent.

Individual PBMC cryotubes were thawed in 2 mL of warm phosphate buffered saline (PBS, Gibco, Life Technologies, Grand Island, NY, USA), pelleted by centrifugation (650 x *g*), divided for immediate *ex vivo* phenotyping or phenotyping following 16 hours of *in vitro* SEB (EMD

Millipore, Billerica, MA) stimulation, and then pelleted again before resuspension in room temperature PBS (*ex vivo*) or R10 media (*in vitro*) at 10 x 10^6 cells/mL. R10 media contained RPMI 1640 Medium (Gibco), 2 mM L-glutamine (Gibco), 50 µg/mL penicillin (Gibco), 50 µg/mL streptomycin (Gibco), 10% FBS, and 10 mM HEPES buffer (Thermo Fisher Scientific, Waltham, MA, USA). Cells for *ex vivo* staining were further divided among flow cytometry tubes (Falcon 2052, BD-Biosciences, San Jose, CA) for fluorescence or mass cytometry staining, described below. Cells for *in vitro* culture were stimulated by addition of SEB to achieve a final concentration of 1 µg/mL in 200uL of 10 x 10^6 cells/mL in 48-well flat bottom culture plates (Costar, Corning Incorporated, Corning, NY, USA). After 16 hours of incubation at 37°C in a 5% CO_2 incubator, cells were removed from the plate, washed twice in PBS, and stained as described below.

Fluorescence cytometry

For each healthy donor, 2 x 10^6 PBMC were stained in 200µL PBS. PBMC were incubated first with a viability dye for 10 minutes (LIVE/DEAD Aqua, Life Technologies), washed once in PBS, and then stained with combinations of fluorescently-tagged antibodies (Table 2.1). For *ex vivo* phenotyping, cells were stained with Panels 1-5 from Table 2.1 (for antibody information see Table S2.1). For phenotyping following *in vitro* stimulation, cells were stained with Panels 3-5 from Table 2.1 at 16 hours after addition of SEB. After staining, all cells were washed twice in PBS and fixed with 2% paraformaldehyde (PFA, Electron Microscopy Services, Fort Washington, PA, USA) and refrigerated up to 24 hours until analysis on the Special Order Research Product (SORP) BD LSRFortessa (BD Biosciences, San Jose, CA) at the Vanderbilt Flow Cytometry Shared Resource.

Mass Cytometry

For each healthy donor, 2 x 10^6 PBMC were stained in 50 µL PBS. PBMC were incubated first with a viability reagent (50 µM cisplatin, Enzo Life Sciences, Farmingdale, NY, USA) in 1 mL serum-free RPMI for 3 minutes. Cisplatin was quenched by washing once with RPMI containing

10% FBS followed by two washes in PBS. A master mix containing 21 antibody-metal conjugates (Table 2.2, Table S2.1) was added to each sample (50 µL total staining volume) and incubated at room temperature for 25 minutes. Cells were then washed twice with PBS, fixed for 10 minutes

Table 2.1 - Fluorescence cytometry instrument and antibody panel information

Instrument characteristics			Reagent panels				
Laser emission and output power	Bandwidth transmitted to PMT	Fluorochrome	1	2	3	4	5
639nm (40mW)	750 - 810	APC-Cy7, APC-A750	HLA-DR	CD8	HLA-DR	HLA-DR	CD8
	663 - 677	APC		CD3	CD3	CD20	CD3
488nm (50mW)	505 - 550	FITC	CD57	CD45RO	CD25	CD27	
561nm (150mW)	685 - 735	PE-Cy5.5		CD127			
	600 - 620	PETR	CD14				CD45RO
	750 - 810	PE-Cy7			CD38	CD38	
	655 - 685	PE-Cy5			CD62L		CD4
	575 - 590	PE	CD16	CD27	CD69	CD86	CD40L
404nm (100mW)	430 - 470	PB, BV421, V450	CD3	CCR7	CD8		PD-1
	685 - 735	BV711	CD19			CD19	
	595 - 620	BV605		CD4	CD4		
	505 - 550	Aqua	Live/dead	Live/dead	Live/dead	Live/dead	Live/dead

Five fluorescence cytometry panels were designed to measure PBMC populations with 21 parameters comparable to those measured in mass cytometry: 20 fluorophore-labeled antibodies and 1 viability marker. Panel 1: PBMC subsets; Panel 2: T cell memory subsets; Panel 3: T cell activation; Panel 4: B cell activation; Panel 5: T cell activation and exhaustion.

with 1.6% PFA at room temperature, washed once with PBS, and then permeabilized at -20°C in 1 mL 100% cold methanol for 20 minutes. Following permeabilization, cells were washed at 800 x *g*, stained with 250 nM Iridium intercalator (*228*) (Fluidigm/DVS Sciences, Sunnyvale, CA) for 16 hours at 4°C, washed twice in PBS, washed once with ddH_2O, and then re-suspended in 500 µL ddH_2O for mass cytometry analysis that day. Cells were filtered immediately before injection into the mass cytometr using a 35µm nylon mesh cell-strainer cap (BD Biosciences).

Samples were analyzed using a CyTOF 1.0 (Fluidigm Sciences, Sunnyvale, CA) and CyTOF software version 5.1.615 (Fluidigm) at the Vanderbilt Flow Cytometry Shared Resource. Dual count calibration (on the "data") and noise reduction (cell length 10-75, lower convolution threshold 10) were applied during acquisition.

Data processing and statistical analysis

All fluorescence and mass cytometry FCS files were uploaded and evaluated using Cytobank software and established methods (*207, 229*). Data were transformed to arcsinh scales with varying cofactors: mass cytometry cofactors ranged from 15 to 50 while fluorescence cytometry cofactors ranged from 150 to 3,000. Software compensation was applied to all fluorescence cytometry FCS files. For viSNE analysis in Figure 2-3, 150,000 total cells were analyzed and equal cell numbers were sampled from each FCS file. 8-parameter viSNE maps were created using the 8 antibodies listed in Panel 3 of Table 2.1. GraphPad Prism software (GraphPad, La Jolla, CA, USA) was used to determine Spearman's rank correlation coefficient rho (ρ) between fluorescence and mass cytometry values (Table 2.3).

Results

Fluorescence and mass cytometry panels to track T cell identity-panel design

Five fluorescence cytometry panels currently in use in our laboratory were used to measure 20 well-established cell surface markers chosen to provide a systematic view of T cell activation after SEB stimulation (Table 2.1). Fluorochrome and antibody conjugates were chosen based upon current availability in the laboratory and their compatibility with the BD LSRFortessa at the Vanderbilt Flow Cytometry Shared Resource.

A single mass cytometry panel was developed to measure the same set of 20 surface markers captured by the five fluorescence cytometry panels (Table 2.2). While mass cytometry

Table 2.2 - Mass cytometry panel to identify PBMC populations

	Target	Metal	Mass	Cell type
1	CD19*	Neodymium (Nd)	142	B cells
2	**CD40L***	Neodymium (Nd)	143	Activated T cells
3	CD4	Neodymium (Nd)	145	T helper cells
4	CD8*	Neodymium (Nd)	146	Cytotoxic T cells
5	CD20*	Samarium (Sm)	147	B cells
6	**CD38**	Neodymium (Nd)	148	Activated lymphocytes
7	CD62L	Europium (Eu)	153	Activated lymphocytes
8	CD86*	Gadolinium (Gd)	156	Activated lymphocytes
9	CCR7*	Terbium (Tb)	159	T cell memory subsets
10	CD14*	Gadolinium (Gd)	160	Monocytes
11	CD69	Dysprosium (Dy)	162	Activated lymphocytes
12	**HLA-DR**	Dysprosium (Dy)	163	APCs; activated T cells
13	CD45RO	Dysprosium (Dy)	164	T cell memory subsets
14	CD16*	Holmium (Ho)	165	NK cells
15	CD27*	Erbium (Er)	167	T cell memory subsets
16	CD25	Thulium (Tm)	169	Activated lymphocytes
17	CD3	Erbium (Er)	170	T cells
18	CD57*	Ytterbium (Yb)	172	T cell memory subsets
19	**PD-1**	Ytterbium (Yb)	174	Exhausted T cells
20	CD127*	Ytterbium (Yb)	176	T cell memory subsets
21	CD45	Samarium (Sm)	154	White blood cells
22	Nuc acid --Ir	Iridium (Ir)	191/193	DNA+ Cells
23	Cisplatin	Platinum	195	Viable cells

One panel was used to measure 23 parameters using mass cytometry: 21 metal-conjugated antibodies, 1 DNA marker, and 1 viability marker (cisplatin). Bolded antibodies were custom conjugated using MaxPar Metal Conjugation Kits. “Cell type” indicates the type of cell that was identified for correlative purposes with fluorescence cytometry data. Asterisks (*) denote when different clones were used in mass and fluorescence cytometry. Bolded antibodies were custom conjugated to metals using purified antibodies from BioLegend and metal-labeling kits from Fluidigm. Markers #21-23 were not used in direct comparison to similar fluorescence parameters. Conjugates were chosen to minimize crosstalk.

avoids the severity of channel overlap that affects fluorescence cytometry, ‘crosstalk’ between channels exists. Crosstalk leads to false signals and must be taken into consideration when designing a panel for mass cytometry and gating cellular populations. The three sources of crosstalk result from variations in abundance sensitivity, isotope purity, and oxide formation (Fluidigm.com “Maxpar Panel Designer User Guide”). These types of crosstalk can contribute to signal in the M±1 and M+16 masses from the dominant signal at mass M. To minimize crosstalk

within this panel, four of the 20 antibodies were custom conjugated to metals (Table 2.2, bolded).

Single antibody titrations were performed for all fluorochrome-conjugated antibodies (FCAs) and metal-conjugated antibodies (MCAs) as needed. As an example, Figure S2.1 shows the titration of CD4-Nd^{145} and CD4-PETR (PE-Texas Red). CD4-Nd^{145} was titrated from 0uL to 0.5uL (recommended amount) with DNA intercalator to identify single cells for analysis (Figure S2.1A). The mean mass intensity (MMI) of the CD4-Nd^{145}+ population shifted from 6.63 to 264.48 while the MMI of the CD4-Nd^{145}- population stayed between -0.40 and -0.19 (Figure S2.1A and S2-1C). The standard deviation of the CD4-Nd^{145}- population was always below 1 (Figure S2.1A and S1C). With increasing antibody concentrations the frequencies of the CD4-Nd^{145}+ populations increased from 0.18% to 60.73% and stain index values increased from 11.78 to 149.16 (Figure S2.1A and S2-1C).

A single antibody titration was also performed with CD4-PETR from 0uL to 2uL and FSC and SSA properties were used to identify single cells for analysis (Figure S2.1B). The mean fluorescence intensity (MFI) of the CD4-PETR+ population increased from 715.13 to 57736.25 while the CD4-PETR- population shifted from 113.71 to 898.64 (Figure S2.1B and S2.1C). The standard deviation of the CD4-PETR- population ranged

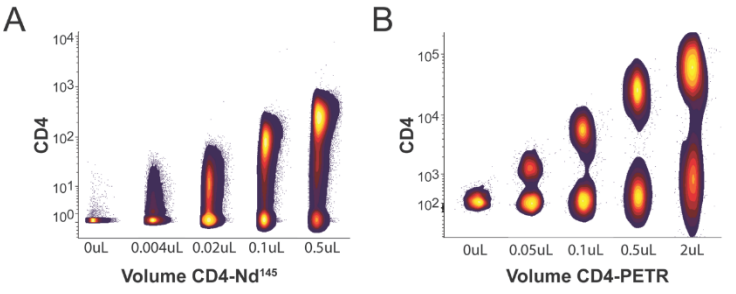

C

Conjugate	Volume (µL)	% CD4+ cells	MMI/MFI (-)	MMI/MFI (+)	SD (-)	Stain index
CD4-Nd^{145}	0	0.18	-0.49	6.63	0.30	11.78
	0.004	13.41	-0.37	7.78	0.53	7.62
	0.02	49.69	-0.27	15.42	0.60	13.04
	0.1	60.46	-0.32	82.97	0.59	70.56
	0.5	60.73	-0.19	264.48	0.89	149.16
CD4-PETR	0	0.56	113.71	715.13	102.95	2.92
	0.05	44.83	128.30	1429.07	106.38	6.11
	0.1	49.78	185.01	5646.98	177.43	15.39
	0.5	51.92	357.86	24078.51	381.68	31.07
	2	55.42	898.64	57736.25	1080.30	26.31

Figure S2.1. Titration of anti-CD4 by mass and fluorescence cytometry. (A) PBMC were stained with Intercalator and different volumes of CD4-Nd^{145}. CD4 staining on single cells (as identified in Figure 2.2B) is shown as detected by mass cytometry. (**B)** PBMC were stained only with CD4-PETR at indicated volumes. Singlets (identified as in Figure 2.2A) were analyzed for CD4 expression using fluorescence cytometry. **(C)** The mean mass intensity (MMI) and mean fluorescence intensity (MFI) of cells within CD4- or CD4+ gates are reported. The standard deviation of CD4 intensity in the CD4- gate was also calculated (SD (-)). Stain index was calculated using the following equation: $\frac{MFI(+)-MFI(-)}{2\times SD}$ (or MMI where appropriate).

between 100-1100 (Figure S2.1B and S2-1C). The frequencies of CD4-PETR detected ranged from 0.56% to 55.42% and the stain index of CD4-PETR ranged from 2.92% up to 31.07% (Figure S2.1B and S2.1C). The highest stain index was achieved at the 0.5uL concentration (Figure S2.1B and S2.1C).

The remaining MCAs and FCAs were conjugated and titrated in a similar manner (Table 2(1-2) and Table S2.1). For fluorescence cytometry, single antibody titrations were performed

Table 2.3 - Correlations of fluorescent and mass cytometry analysis of percent positive cells for proteins measured on healthy human PBMC

			Spearman rank		Pearson		Frequency detected (fluorescent)				Frequency detected (mass)			
Antibody	Gated off of	n	ρ (rho)	p	r	p	Range	Mean (*ex vivo)*	Mean (+ SEB)	Average MFI	Range	Mean (*ex vivo)*	Mean (+ SEB)	Average MMI
CD57*	Live CD16+	6	1.00	0.003	0.99	<0.0001	16.15-58.52	33.28	n/a	10178	17.83-51.91	31.18	n/a	290
CD27	Live CD3+	6	1.00	0.003	1.00	<0.0001	53.14-89.51	75.05	n/a	13995	52.27-85.02	71.25	n/a	54
CD45RO	Live CD3+	6	0.94	0.017	0.94	0.005	31.98-59.18	46.98	n/a	5811	30.71-64.83	48.64	n/a	861
CD3	Singlets	12	0.92	<0.0001	0.92	<0.0001	24.36-74.87	62.24	39.28	5759	30.36-71.58	62.36	36.81	262
CD62L	Live CD3+	12	0.90	0.0002	0.93	<0.0001	32.79-79.58	48.60	55.24	18435	28.93-79.03	41.18	53.16	62
HLA-DR	Live CD20+	12	0.88	0.0003	0.87	0.0002	31.22-98.89	72.74	97.59	20843	56.50-97.07	74.18	91.46	1225
CD69	Live CD4+CD3+	12	0.86	0.0006	0.95	<0.0001	0.15-38.46	1.51	29.84	2650	0.26-57.98	0.87	36.27	178
PD-1	Singlets	12	0.85	0.008	0.72	0.007	6.1-19.16	9.39	13.72	1915	11.65-19.55	16.73	14.69	19
CCR7*	Live CD3+	6	0.83	0.058	0.96	0.002	35.47-88.22	59.32	n/a	1946	34.41-80.48	59.12	n/a	72
CD38	Live CD8+CD3+	12	0.83	0.001	0.96	<0.0001	1.62-86.03	37.64	39.72	8987	3.62-57.63	24.89	22.67	37
CD40L*	Singlets	12	0.81	0.002	0.83	0.0008	0.01-33.58	0.52	18.47	1286	1.47-22.37	4.84	18.13	14
CD25	Live CD4+CD3+	12	0.80	0.003	0.92	<0.0001	5.21-30.94	8.58	22.72	1402	0.33-62.31	3.22	33.93	180
CD20*	Singlets	12	0.78	0.004	0.80	0.002	4.15-13.21	7.33	7.82	10756	2.54-11.8	6.91	7.29	145
CD16*	Singlets	6	0.77	0.100	0.67	0.14	4.31-16.92	11.22	n/a	10133	6.55-16.47	9.86	n/a	283
CD86*	Live CD19+	12	0.76	0.006	0.97	<0.0001	1.87-88.30	3.20	77.48	21763	9.42-80.56	13.06	68.29	54
CD19*	Singlets	12	0.73	0.009	0.78	0.0030	4.07-12.24	6.66	7.46	7264	3.42-13.8	6.15	9.29	307
CD4	Live CD3+	12	0.72	0.01	0.74	0.006	51.40-90.09	75.31	73.92	3685	47.41-78.39	63.10	57.25	255
CD8*	Live CD3+	12	0.72	0.01	0.79	0.002	9.17-21.49	15.35	13.55	4467	4.28-16.23	16.73	12.85	485
CD27*	Live CD20+	12	0.69	0.016	0.50	0.09	7.23-38.34	21.67	11.73	1607	5.51-27.04	18.17	11.44	26
CD127*	Live CD3+	6	0.60	0.240	0.75	0.08	79.16-93.92	86.05	n/a	2130	33.90-61.20	50.81	n/a	8
CD14*	Singlets	6	0.43	0.420	0.23	0.66	2.23-17.69	10.51	n/a	16727	3.42-16.47	11.04	n/a	122

Antibodies are listed in order of decreasing Spearman's rank correlation coefficient rho (ρ). Asterisks (*) denote when different clones were used in mass and fluorescent cytometry. Bolded antibodies were custom conjugated to metals using purified antibodies from BioLegend and metal-labeling kits from Fluidigm. The starting population of cells was used to determine the percent positive of cells for each protein. N indicates the number of values used in the Spearman rank and Pearson analysis: N was 6 when only *ex vivo* data was used (antibodies solely used in Panel 1 or 2, Table 2.1); N was 12 when an *ex vivo* and *in vitro* value were used from each subject.

for all FCAs and final volumes were chosen based on stain index. For markers not typically expressed on resting T cells (e.g. CD69), antibody titrations were performed on cells stimulated *in vitro* with SEB. To optimally titrate antibodies in the mass cytometry panel, final concentrations were chosen based on the frequency of detected populations (considering their fluorescence counterparts), stain index, and crosstalk of each MCA into their M+1, M-1, and M+16 channels. For mass cytometry, custom conjugates were titrated in groups as they were created. PBMC were then stained with the full mass cytometry panel (Table 2.2) at recommended volumes and adjustments were made as needed for each antibody. Further titrations were done in groups that never included masses within 1 or 16 masses of each other. As needed for antibodies with non-bimodal distributions additional antibodies were included to determine optimal staining volumes. For example, final adjustments of PD-1 staining volumes were made after plotting PD-1 versus CD45RO on CD4+ T cells (Figure S2.2).

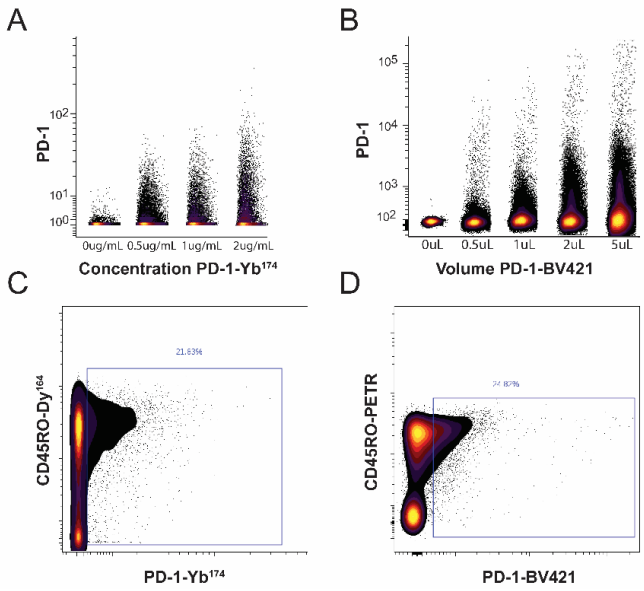

Figure S2.2. Titration of anti-PD-1 by mass and fluorescence cytometry. (A) PD-1-Yb^{174} staining on single cells (as identified in Figure 2A). **(B)** PD-1-BV421 staining on singlets (as identified in Figure 2.2B). (**C-D**) Since CD45RO helps to gate PD-1+ cells, PBMC were stained with CD3, CD4, CD45RO, and various volumes of PD-1. Optimal staining volumes of PD-1 were chosen based on staining patterns of PD-1 on CD4+ T cells (identified as in Figure 2.2A and 2.2B) using mass (C) and fluorescence (D) cytometry.

Values derived from fluorescence and mass cytometry were closely correlated

Several factors were taken into consideration when setting gates on mass cytometry data to ensure that only true signal was being reported. In the absence of background signal, the gate for a particular metal could theoretically be set at 10^0. However, sources of background including nonspecific binding of antibodies and crosstalk from other channels require gates to be set at least at 10^1 since the abundance sensitivity for our instrument is 1% and the MMIs of the antibodies ranged up to 1000 (data not shown, Table 2.3). To help determine where a gate should be set, mass minus one (MMO) controls can be used to ensure that only signal from a single antibody is being detected within a gate. High-density antigens with bimodal staining patterns (MMIs between 10^2 and 10^3) did not require MMOs since the mass intensity of the signal was significantly beyond 10^1. MMOs were especially important, however, when the MCA had a non-bimodal staining pattern, was a dim antigen, and was at the M+1, M-1, or M+16 position of a MCA with an intense, abundant signal.

Figure 2.1 illustrates how gates were set for such an antibody, CD25-Tm^{169}, using a mass minus one (MMO) control. The frequency of Tm^{169}+ events when PBMC were only stained with DNA intercalator and CD4-Nd^{145} was 0.02% when the gate was set at 10^1 (dashed line gate) and 0% when the gate was set at 22 (solid line gate) which represents the actual gate used to identify CD25+ cells (Figure 2.1A). When PBMC were stained with the full mass cytometry panel (Table 2.2) except CD25-Tm^{169} –an MMO control—the frequency of Tm^{169}+ events when the gate was set at 10^1 was 2.63% (Figure 2.1B, dashed line gate). This signal results from crosstalk into Tm^{169} by the rest of the panel: most likely M-1 crosstalk from CD3-Er^{170} and M+16 crosstalk from CD62L-Eu^{153}. When the gate was set at 22, however, the frequency of non-specific signal was reduced to 0.19% (Figure 2.1B, solid line gate). This gate, which avoided analyzing artifact signals, was then used in the full panel to detect true CD25+ events (Figure 2.1C).

Final decisions for gating took into consideration many factors including crosstalk,

fluorescence/mass counterpart staining, company and literature staining pattern data and frequencies, and staining patterns off of multiple cell populations (e.g. markers present on certain cell types and absent on others). The staining pattern for CD27 illustrates how gates were set for antibodies that were not at the M±1 or M+16 position of another antibody. Alternatively, the staining pattern for CD45RO-Dy^{164} illustrates gating when considering M+16 crosstalk from CD38-Nd^{148} and M±1 crosstalk from HLA-DR-Dy^{163} and CD16-Ho^{165}. An MMO was not required here, however, since the antigen was highly-expressed and displayed a bimodal staining pattern. This example further demonstrates the need for careful panel design.

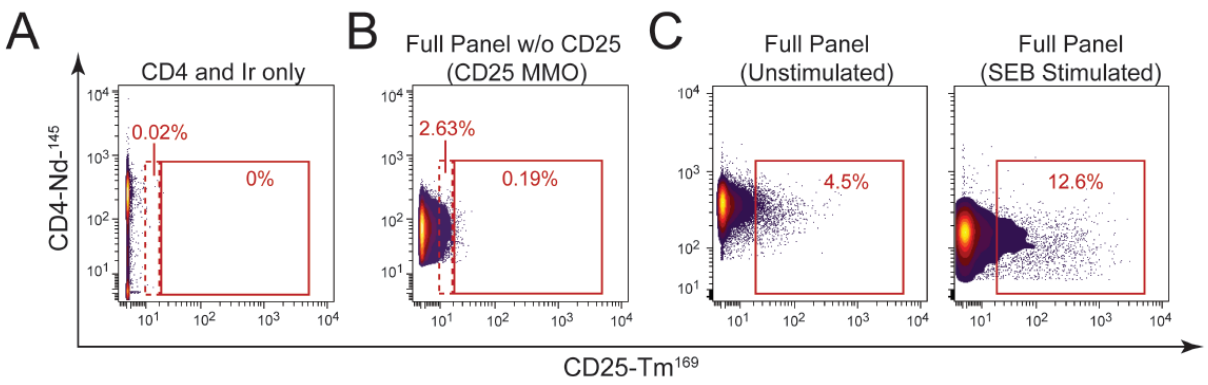

Figure 2.1. MMOs guided gating for CD25 expression on live single CD4+ T cells. (A) PBMC were stained only with DNA intercalator and CD4-Nd^{145}. Single cells were analyzed for CD25 expression. The gate with the dashed red line is set at 10, the same as in (B). The gate with the solid red line is set at 22, the same place as in (B-C) and Figure 2.2. **(B)** PBMC were stained with all the MCAs (Table 2.2) *except* CD25-Tm^{169} (termed a mass minus one (MMO) control). Gates are set the same as in (A), and frequencies inside each gate represent non-specific signal in the Tm^{169} channel. **(C)** PBMC were stained with all the MCAs (Table 2.2) with or without SEB stimulation (the same plots from Fig. 2-2 are shown).

Identification of live single cells

To directly compare mass and fluorescence cytometry, an equivalent starting population of live single cells was identified in healthy human PBMC (Figure 2.2). In fluorescence cytometry (Figure 2.2A), forward and side light scatter signal properties were used to identify intact single cells and exclusion of the LIVE/DEAD Aqua dye identified live single cells. In mass cytometry (Figure 2.2B), event length and intercalator uptake were used to identify intact single cells and

exclusion of cisplatin (*230*) identified live single cells. Although PBMC were stained with CD45-Sm^{154} it was not included in analysis since we did not have a comparable marker fluorescently and correlations improved between the two technologies when identical phenotypic gating strategies were used. After single cells were identified, live CD3+ cells and CD4+ and CD8+ T cells were gated by mass and fluorescence cytometry (Figure 2.2A-B). Both mass and fluorescence cytometry measured comparable increases in CD25 expression following SEB stimulation (Figure 2.2C-D).

Correlation between fluorescence and mass cytometry data

Statistical correlation between fluorescence and mass cytometry was determined using Spearman's rank (Table 2.3) for all 20 measured proteins. Samples analyzed in parallel by mass and fluorescence cytometry included 12 populations of PBMC from 6 individual healthy donors under 2 conditions (unstimulated *ex vivo* and 16 hours after *in vitro* SEB stimulation). Frequencies of cellular populations identified by 20 MCAs and FCAs were directly compared using biaxial gating plots (as in Figure 2.2). The frequency of each antibody was gated from the same starting population, which is indicated in the "gated on" column (Table 2.3). The range of frequencies detected, mean frequencies of unstimulated and stimulated populations, and average intensity of each marker by fluorescence and mass cytometry is indicated (Table 2.3).

Statistically significant correlations were observed for all 9 proteins detected using the same antibody clones (custom or commercially conjugated). Eleven of the metal conjugated antibodies in the mass cytometry panel did not match the FCAs in our existing panels, (Table 2.3, asterisks) but 9 out of 11 of these antibodies still identified similar frequencies of populations by both technologies.

CD14 and CD127 were the only two antibodies that did not provide consistent values between the two technologies. We compared the two CD14 clones (Tük4-PETR and M5E2-FITC) using fluorescence cytometry and found that despite showing bimodal staining patterns they did

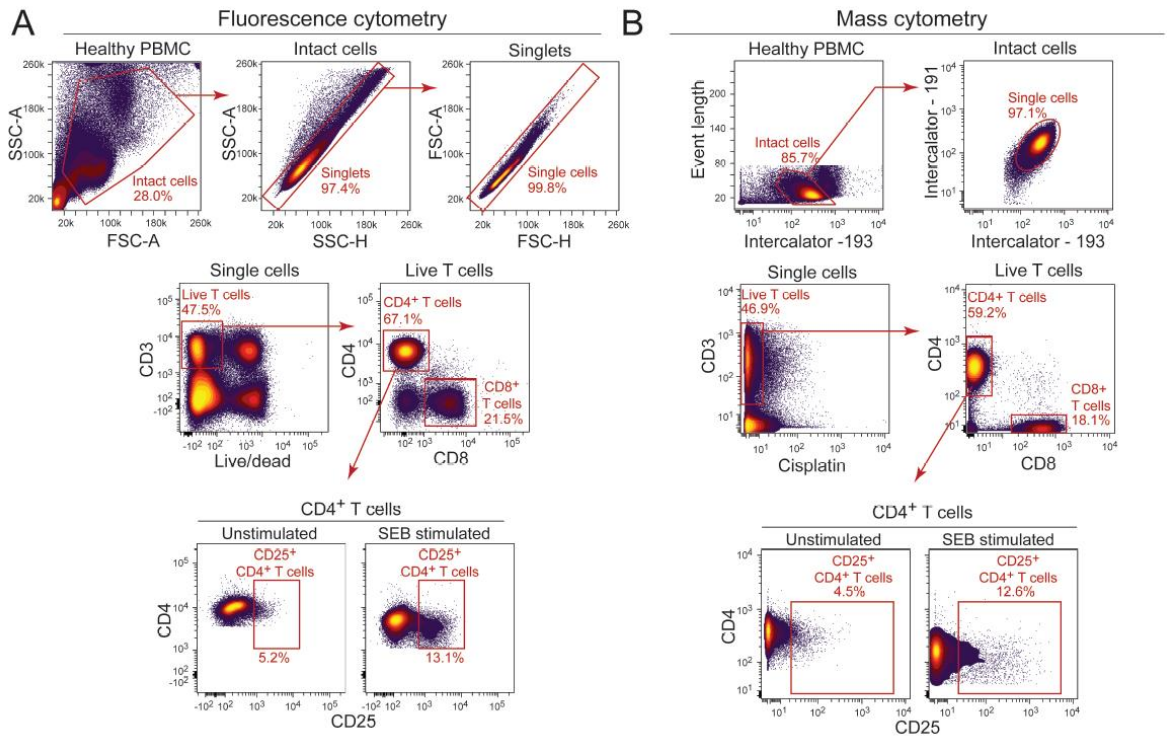

Figure 2.2. Gating schemes for fluorescence and mass cytometry. Plots show PBMC from a single healthy human donor. (**A**) Representative biaxial plots show the gating scheme for fluorescence flow cytometry. Intact single cells were gated using forward and side scatter area and height properties. Single cells were then assessed for viability and expression of CD3. This population was further gated as $CD8^+$ and $CD4^+$ T cells. CD25 expression on $CD4^+$ T cells was compared in PBMC from an individual healthy donor with or without SEB stimulation. (**B**) Representative biaxial plots show the gating scheme for mass cytometry. Single cells were identified using event length and intercalator uptake and then gated and compared as for fluorescence cytometry.

not detect similar frequencies of CD14+ singlets (N=6, p=0.36, rho=0.49). When we compared the two CD127 clones using fluorescence cytometry (R34.34-PECy5.5 and A019D5-PECy7) we found they did in fact detect similar frequencies of CD127+ T cells. Staining improved dramatically with a new lot of CD127-Yb^{176}: the MMI increased from 8 to 65. Comparison with six new subjects with truncated panels demonstrated the frequency of CD127+ T cells detected was highly correlative between the two technologies (N=6, p=0.002, r=0.96). These additional experiments suggest the two discrepancies we found in Table 2.3 were not due to differences in mass and fluorescence cytometry, but far more likely to be due to differences in the particular antibody clone, or particular lot of antibody used.

viSNE identified similar frequencies of activated CD4+ T cell populations

Large data sets resulting from mass cytometry have resulted in the development of new computational approaches to analyzing complex single cell data. Having found a high degree of correlation between the two technologies, we next compared the ability of an unsupervised high-dimensional analysis program, viSNE, to analyze data sets derived from both mass and fluorescence cytometry. viSNE was developed for mass cytometry data and approximates high dimensional relationships using a two dimensional scatter plot, or map, where each dot represents a single cell (*231*). To read a viSNE map, one can visually identify an 'island' of cells and then determine the cellular identity based on marker expression. To determine whether viSNE could identify similar populations using mass and fluorescence cytometry data sets we chose to study frequencies of activated CD4+ T cells. The viSNE map in Figure 2.3 was generated with an equal number of cells from the FCS files of each healthy donor before and after stimulation. The viSNE analysis was restricted to eight markers of T cell activation and analyzed FCS files stained either with Panel 3 (Table 2.1) or the identical eight markers in the mass cytometry panel (Table 2.2). While cells identified by mass cytometry were tagged with greater than eight antibodies, only the same eight antibodies from the fluorescence T cell activation panel were considered when creating the viSNE maps with mass cytometry data (Figure 2.3B).

When applied to fluorescence and mass cytometry data, viSNE created similar maps that demonstrated patterns of T cell activation. One fluorescence cytometry viSNE map (Figure 2.3A) and one mass cytometry viSNE map (Figure 2.3B) is each shown ten times highlighting the intensity of CD3, CD4, CD8, CD69 and CD25 on SEB stimulated (top rows) or unstimulated (bottom rows) PBMC. A gate was drawn (black outline) to highlight the population of activated CD4+ T cells. Cells within this island displayed characteristics of activated $CD4^+$ T cells that included little or no CD3, no CD8, moderate CD4, and high expression of CD69 and CD25 (Figure 2.3A-B). The activated cells are not present in the unstimulated condition (Figure 2.3A-B) and

this is further highlighted both by the frequency and density of cells within the gate on the viSNE maps (Figure 2.3C). viSNE identified similar frequencies of activated CD4+ T cells analyzed by mass and fluorescence cytometry (p=0.007, ρ=0.74) and all subjects had cells that fell within this gate after stimulation (Figure 2.3D).

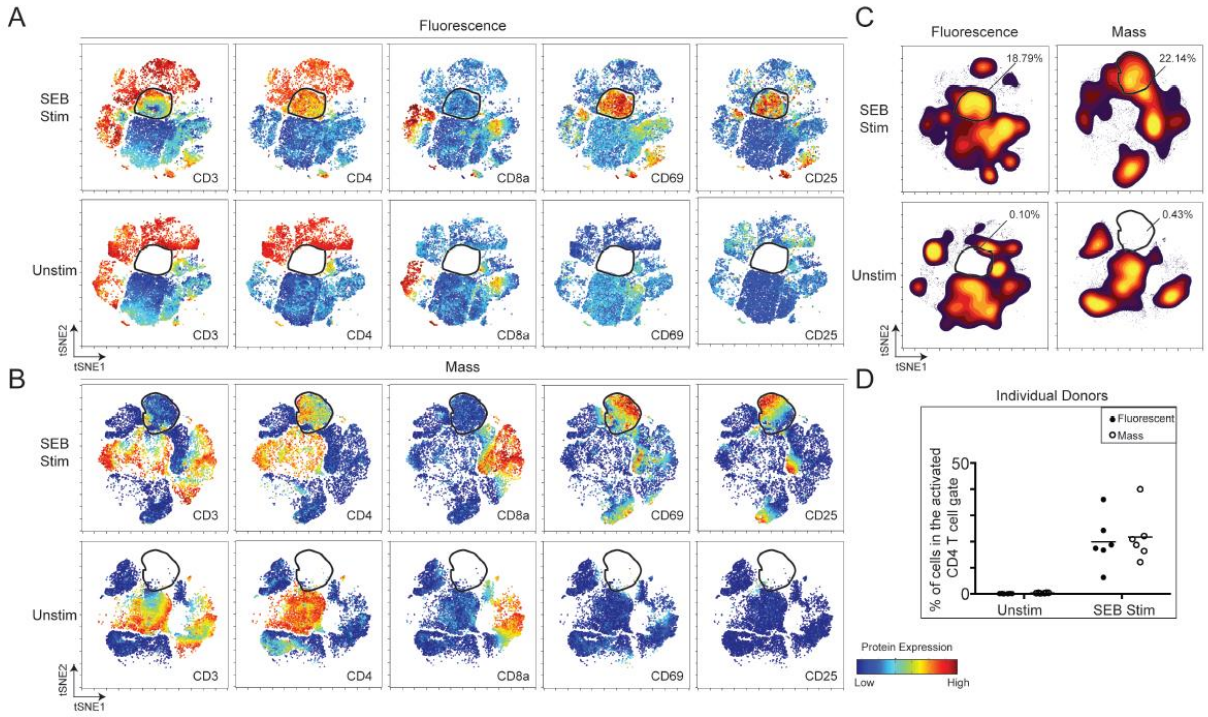

Figure 2.3. viSNE identified activated T cells in 8-dimensional analysis of fluorescence and mass cytometry. (A-B) viSNE plots show unstimulated and SEB stimulated PBMC compared according to 8 proteins (Table 2.2, Panel 3) detected by fluorescence cytometry (A) or mass (B) cytometry. For each cell, color indicates the intensity of the labeled protein on a rainbow heat scale (arcsinh scales). Activated $CD4^{+}$ T cells ($CD3^{lo/-}CD4^{med}CD8^{-}CD69^{hi}CD25^{hi}$) are outlined in black. Maps from one representative donor are shown. (C) Maps displaying density of cells from the same donor by fluorescence and mass cytometry highlight the absence of activated cells in the unstimulated condition. (D) SEB induced T cell activation in all 6 individuals, with similar percentages measured by fluorescence and mass cytometry (Wilcoxen matched pairs t-tests p=n.s).

Dimensionality reduction tools identify cells with non-canonical phenotype

To determine whether tools other than viSNE would also effectively characterize activated T cells, a spanning-tree progression analysis of density-normalized events (SPADE) (*210*) analysis was performed (Figure 2.4) using the same population of cells as in the viSNE analysis.

SPADE was applied to live CD45$^+$ PBMC from 6 healthy donors and included both unstimulated and SEB stimulated cells (Figure 2.4). While viSNE analysis showed individual cells, SPADE analysis clustered cells based on their similarity in high-dimensional space into various nodes (22). Clusters of cells identified by SPADE were based on expression of the 21 markers used in the SPADE analysis (Figure 2-4A). Two different clusters of CD8$^+$ T cells (termed P1 and P2, outlined in green and blue, respectively) and CD4$^+$ T cells (P3 and P4, outlined in dark and light pink, respectively) were identified by SPADE (Figure 2-4A). To determine whether these CD4$^+$ and CD8$^+$ T cell populations were similar to the cells we found in the viSNE islands, expression of CD3 and activation markers was evaluated (Figure 2-4B-C). Figure 5B shows evaluation of these cells for CD3 and the activation marker CD69. These plots illustrate that populations P2 and P4 on the SPADE plots displayed an activated phenotype with downregulated CD3 (Figure 2-4B). Further, populations P1 and P3 had a resting phenotype with high expression of CD3. In the unstimulated condition, the P2 population made up only 0.4% of total CD8$^+$ T cells, whereas in the SEB stimulated condition, P2 comprised 32.7% of the CD8$^+$ population. Likewise, P4 made up 0.2% of CD4$^+$ T cells in the unstimulated condition and 51.9% of CD4$^+$ T cells in the SEB stimulated condition. These results indicate that T cells with an activated phenotype were rare prior to stimulation and greatly expanded in the SEB stimulated condition. A heat map of median expression of all 21 proteins along with CD45 showed that the identified cells also expressed activation markers in addition to CD69 and contained cells with various memory statuses (Figure 2-4C). Thus, both SPADE and viSNE effectively identified T cells lacking the canonical marker, CD3, following SEB stimulation.

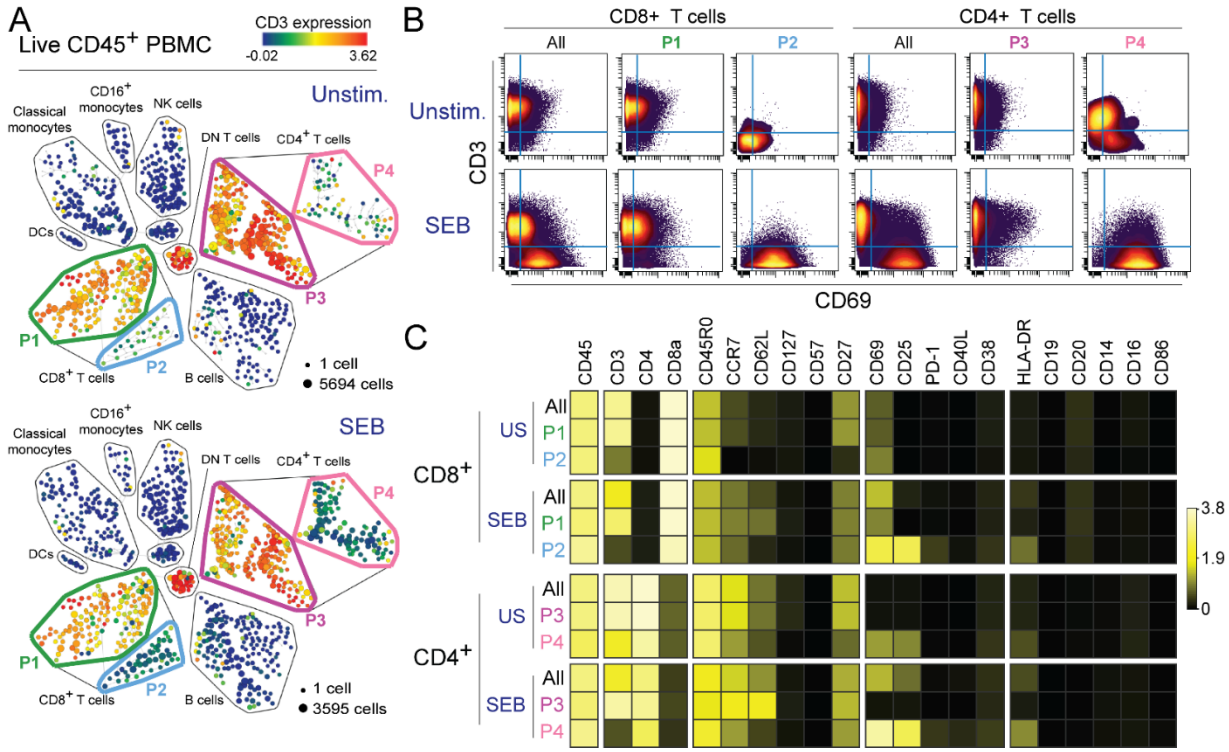

Figure 2.4. SPADE characterized T cells with down regulated CD3.
(A) Live CD45⁺ PBMC were analyzed by the dimensionality reduction and clustering tool SPADE. Unstimulated (top) and SEB stimulated (bottom) cells from six healthy donors were grouped according to expression of 20 proteins (Table 2.1). Circle size indicates the number of cells in each cluster and color indicates CD3 expression on the population of cells clustered in the circle (arcsinh scale). Populations of CD4⁺ and CD8⁺ formed distinct groups and were labeled P1-P4. (B) Biaxial plots show the expression of CD3 and CD69 on cells from P1-P4 of the SPADE tree as well as all CD8⁺ or CD4⁺ T cells. (C) A heatmap displays the median intensity of all 20 measured proteins for CD4⁺ and CD8⁺ T cell populations identified by SPADE. US = unstimulated. Populations P1 (green) and P2 (blue) were CD8⁺ T cells with a resting or activated phenotype, respectively (arcsinh scale). Populations P3 (dark pink) and P4 (light pink) were CD4+ T cells with a resting or activated phenotype, respectively.

Discussion

The ability to combine high-dimensional single cell biology with unsupervised analysis approaches is powering a new era of systems immunology. Here, a high-dimensional mass cytometry panel was developed to track human T cell responses after *in vitro* stimulation with superantigen. The frequencies of markers detected with 20 antibodies within the mass cytometry panel were compared on a one-to-one basis with antibodies from five fluorescence cytometry panels. The resulting data indicate that mass and fluorescence cytometry data are highly comparable. We also show that unsupervised viSNE analysis provides valuable insight into single cell data, regardless of the instrumentation used to collect that data. The 20 antibody T cell panel developed and validated in this study is expected to be particularly useful for detailed characterization of human T cell populations in a variety of settings such as longitudinal immune monitoring of viral infections, immune disorders, and cancer.

Mass cytometry has the potential to greatly expand the number of observable features on small populations of cells (*191*). Recent studies achieved 38- and 44-parameter single cell analysis using mass cytometry (*200, 219*). Alternatively, the number of measurable parameters using polychromatic fluorescence cytometry has increased to 20 and is growing still with the advent of new instruments and fluorochromes (*232*). We previously used multiparameter fluorescence flow cytometry with many of the same markers used in this study to evaluate the activation status of subpopulations of virus-specific T cells in memory compartments of peripheral blood (*233-236*) and cerebrospinal fluid (*237, 238*). Here, we used previously established panels in our laboratory that focused on T cell memory and markers of immune activation to provide a detailed comparison of mass and fluorescence cytometry.

A high dimensional mass cytometry approach provided equivalent per-marker and per-subset information when compared directly with traditional fluorescence cytometry (Figure 2-2, Table 2.3). For example, the average difference in CD3+ cells detected by both technologies was

4.8% even though healthy variation before and after stimulation spanned a range of 25-75%. The findings in this study align well with published comparisons of mass and fluorescence cytometry (*9, 174, 224*). Other than expected differences due to using different antibody clones, the minor discrepancies observed between the two technologies (Table 2.3) likely resulted from differences in gating for 'live single cells'. Prior to viability gating, fluorescence cytometry employed forward and side scatter while mass cytometry employed DNA content and cell length (Figure 2.2). Overall, these results provide further support for the concordance between the two technologies.

We demonstrate that the high-dimensional visualization tool, viSNE, was still effective even in a 'low-dimensional' 8-parameter analysis. Amir and colleagues demonstrated previously that viSNE successfully identifies blood cell populations even when using non-canonical markers (*231*). This ability to detect obscure or unexpected cells is one of the most powerful attributes of new unsupervised analysis programs (*208*). In this study, viSNE identified activated CD4+ T cells based on their multidimensional phenotypes without requiring cells to express CD3. Additionally, viSNE returned comparable results with mass and fluorescence cytometry data considering 8 parameters, further strengthening the correlations of antibody detection between the two platforms. Going forward, familiarity with these tools, and learning their strengths and weaknesses, is likely to become a core skill for immunologists, especially since they apply well to any type 'event list' format data, such as single cell cytometry data from flow and imaging instruments.

The dynamic, biological changes that characterize signaling responses can create analysis challenges for both humans and machines. An important aspect of this study was the resolution of T cell responses to SEB superantigen stimulation. This type of study provides a model for studies where immune cells are stimulated *in vivo* by therapies or chronic inflammation and *ex vivo* in laboratory analysis. Induced changes in protein markers typically considered 'core identity markers', such as CD3 downregulation on T cells, are common following leukocyte

activation. Loss of 'standard' markers might complicate traditional analysis workflows that are dependent on univariate or bivariate gating. Bivariate gating is particularly susceptible to this issue as lack of one marker can exclude a cell from further downstream analysis. For example, one recent mass cytometry study of T cells stimulated by PMA/ionomycin or anti-CD3 focused on $CD3^{+}$ cells and did not include $CD3^{lo/-}$ cells from biaxial and SPADE analysis (*239*). Here, a multidimensional analysis strategy robustly identified cell populations, including $CD3^{lo/-}$ T cells, whose phenotype had shifted following stimulation (Figure 2-3, 4). In this case, results confirmed an expression pattern of activated T cells whose phenotype has been well understood for some time (*193, 240-242*). Similarly, a recent study used SPADE to determine the phenotype of human tonsillar T cells actively infected with varicella zoster virus (VZV) (*222*). In that study, cells infected with VZV showed decreased expression of CD3 while other markers, such as PD-1 and CD69 were increased. This study along with ours highlight the importance of analysis approaches that characterize all cells, even those with novel, unexpected, and poorly understood phenotypes (*208*). Furthermore, our results indicated that high-dimensional analysis tools were valuable for both fluorescent and mass cytometry data analysis (Figure 2-3).

One disadvantage to mass cytometry is that the samples must be destroyed for analysis, so this technology is not suitable for cell sorting. Hence, these should be viewed as complementary technologies. After identification of cell populations of interest with an extensive mass cytometry panel and high dimensional analysis with unsupervised algorithms, more focused fluorescence cytometry panels can be designed to sort cells for further analysis (*226, 234, 235, 243*). For this approach to work, however, it will be necessary to have matched panels of antibodies that can reliably detect the same markers with each technology, and we demonstrate that this is feasible.

This combination of single-cell measurements and computational analysis provides a framework for systematic characterization of the complex, dynamic phenotypes that

exemplify immune responses. The ability of viSNE and SPADE to detect shifts in populations as a result of stimulation suggests they will be indispensable analysis tools for going forward in detecting perturbations in protein expression in both health and disease. This rigorous comparison of mass and fluorescence cytometry suggests that the technologies are highly comparable. Traditional biaxial gating and an unsupervised high-dimensional analysis approach, viSNE, identified similar patterns of protein expression and frequencies of cellular populations in superantigen stimulated human blood. These results demonstrate that multidimensional analysis using either platform will be particularly useful for the comprehensive characterization of cells, including cells with dynamic or unexpected cell phenotypes in health and disease.

Table S2.1 - Antibody-metal and antibody-fluorophore information

Target	Conjugate	Clone	Source	Unitless Dilution Used	Final Concentration (ng/mL)
CD19	142Nd	HIB19	DVS	1:100	12.5
CD40L	143Nd	24-31	BioLegend	1:100	2000
CD4	145Nd	RPA-T4	DVS	1:100	20
CD8a	146Nd	RPA-T8	DVS	1:1000	2
CD20	147Sm	2H7	DVS	1:100	30
CD38	148Nd	HIT2	BioLegend	1:100	4000
CD62L	153Eu	DREG-56	DVS	1:200	3.75
CD45	154Sm	HI30	DVS	1:2000	1.25
CD86	156Gd	IT2.2	DVS	1:200	1500
CCR7	159Tb	G043H7	DVS	1:200	25
CD14	160Gd	M5E2	DVS	1:67	30
CD69	162Dy	FN50	DVS	1:1000	2.5
HLA-DR	163Dy	L243	BioLegend	1:100	2000
CD45RO	164Dy	UCHL1	DVS	1:200	25
CD16	165Ho	3G8	DVS	1:200	3.75
CD27	167Er	L128	DVS	1:50	15
CD25	169Tm	2A3	DVS	1:400	1.5
CD3	170Er	UCHT1	DVS	1:133	5.625
CD57	172Yb	HCD57	DVS	1:400	1.875
PD-1	174Yb	EH12.2H7	BioLegend	1:100	1000
CD127	176Yb	A019D5	DVS	1:50	12
Nucleic Acid	191/193Ir	n/a	DVS	1:50	250nM
Live/dead	195Pt	n/a	Enzo Life Sciences	1:500	50uM
CD19	BV711	SJ25C1	BD	1/40	300
CD40L	PE	Trap1	BD	1/200	62.5
CD4	BV605	RPA-T4	BD	1/100	500
CD4	PECy5	RPA-T4	BD	1/200	15
CD8	APCA750	3B5	Invitrogen	1/400	1000
CD8	V450	RPA-T8	BD	1/200	250
CD20	APC	L27	BD	1/200	200
CD38	PE-Cy7	HIT2	eBioScience	1/800	250
CD62-L	PE-Cy5	DREG-56	BD	1/100	60
CD86	PE	2331 (FUN-1)	BD	1/40	250
CCR7	BV421	150503	BD	1/40	625
CD14	PETR	TüK4	Invitrogen	1/4000	25
CD69	PE	FN50	BD	1/100	30
HLA-DR	APCy7	L243	BioLegend	1/100	2000
CD45RO	FITC	UCHL1	BD	1/20	2500
CD45RO	PETR	UCHL1	Beckman Coulter	1/400	50
CD16	PE	B73.1	BD	1/2000	50
CD27	PE	M-T271	BD	1/40	625
CD27	FITC	M-T271	BD	1/400	1250
CD25	FITC	2A3	BD	1/400	25
CD3	PB	UCHT1	BD	1/100	2000
CD3	APC	UCHT1	BioLegend	1/800	600
CD57	FITC	NK-1	BD	1/40	312.5
PD-1	BV421	EH12.2H7	BioLegend	1/100	500
CD127	PE-Cy5.5	R34.34	Beckman Coulter	1/400	1000

Viability	V500	n/a	Invitrogen	1/2000	proprietary

Information for all staining reagents. Unitless dilutions were chosen based on the highest stain index (fluorescently) for each antibody determined by single antibody titrations. Final concentrations were calculated using the concentration of each reagent (specific to Lot #) provided by each source.

CHAPTER III

GENOMIC PROFILING OF T CELL NEOPLASMS REVEALS FREQUENT *JAK1* AND *JAK3* MUTATIONS WITH CLONAL EVASION FROM TARGETED THERAPIES

Authors: Allison Greenplate*, Kai Wang*,Rati M. Tripathi, Norma Palma, Siraj M. Ali, Phil J. Stephens, Vincent A. Miller, Yu Shyr, Yan Guo, Nishitha M. Reddy, Lina Kozhaya, Derya Unutmaz, Xueyan Chen, Jonathan M. Irish, Utpal P. Davé

*These authors contributed equally to this work

This work is presented as it appears in manuscript form in *JCO Precision Oncology*, Accepted November 2017 (Greenplate and Wang, et al. 2016).

Introduction

In Chapter II, I developed a mass cytometry panel that faithfully recapitulated 5 fluorescence flow cytometry panels for a high-dimensional view of stimulated, human T cells. Combined with dimensionality reduction tools SPADE and viSNE, I was able to identify stimulated T cells, even though they had lost canonical marker of T cell identity, CD3. With experimental evidence that this work flow could capture stimulated T cells, I next wanted to test it in a clinical setting where T cells were stimulated *in vivo*. To do this, mass cytometry, viSNE, and phospho-flow were used to characterize the cellular phenotype and dissect mechanism of response of a T cell neoplasm to a small molecule inhibitor.

T-cell neoplasms are known for their clinically aggressive behavior and for their high risk of relapse and resistance to conventional cytotoxic regimens. Adult patients with precursor

neoplasms such as acute T-cell lymphoblastic leukemia (T-ALL) or with mature neoplasms such as T-cell non-Hodgkin lymphoma (T-NHL) have 5-year 20-30% survival even after intensive multi-agent chemotherapy (*244-249*). There are rare exceptions to these dismal outcomes such as children and adolescent T-ALL and anaplastic large cell lymphoma (ALCL) with unique gene rearrangements (i.e. ALK^+ or $DUSP22^+$) where 5-year survival rates are over 70-80% with similar chemotherapy regimens (*248, 250, 251*). However, relapsed disease is very challenging to cure. Clearly, novel therapeutic approaches are needed and the development of commercially available next generation sequencing has raised the possibility of genomically-directed therapy that may be applied to T-cell leukemias and lymphomas. Genomic profiling has been performed on several histopathologic subtypes of T-cell leukemias and lymphomas to better characterize the molecular genetics (*252-256*). Interestingly, recent genomic profiling has discovered frequent aberrations within the JAK-STAT pathway in both precursor (T-ALL) and mature T-cell neoplasms (T-NHL) suggesting JAK kinase inhibition may be important therapeutically(*257*).

Janus Kinases are encoded by 4 paralogous genes, *JAK1-3 and TYK2*. These tyrosine kinases are recruited to cytokine receptors where they transduce signals by phosphorylation of key substrates, most importantly, Signal Transducer and Activator of Transcription (STAT) proteins that bind DNA and regulate gene expression. *JAK1* mutations have been found in 10% of childhood T-ALL (*258*). Our lab and others have found *JAK3* mutations in cutaneous T-cell lymphoma (CTCL), adult T-cell leukemia/lymphoma (ATLL), T-cell prolymphocytic leukemia (T-PLL), and NK/T-cell lymphoma (NKTL) (*259-263*). Analyses of human leukemia lines and mouse models show that JAK mutations are typically activating, causing constitutive signal transduction, which may be blocked by tyrosine kinase inhibitors. Two such ATP-competitive inhibitors have been approved by the U.S. FDA for human use. Ruxolitinb is approved for use in myeloproliferative neoplasms and tofacitinib is approved for rheumatoid arthritis (*264, 265*).

In this study, we deployed a commercially available hybrid-capture/next generation

sequencing platform to characterize major recurrent oncogene and tumor suppressor aberrations in 91 T-cell neoplasms. This targeted approach found 33% of cases had JAK-STAT abnormalities including missense mutations in *JAK1*, *JAK3*, rearrangements in *JAK2* and *JAK3*, and missense mutations and amplifications of *STAT3* and *STAT5*. We analyzed an index case of T-cell prolymphocytic leukemia (T-PLL), a deadly mature T-cell neoplasm with both *JAK1* and *JAK3* gain of function missense mutations (*266*). This patient's T-PLL had progressed on multiple lines of chemotherapy but responded to ruxolitinib, a JAK1/2 inhibitor. The patient eventually relapsed due to clonal expansion of T-PLL cells with gain of function of JAK3 and downregulation of CD45. Our study is the first to demonstrate an *in vivo* response to ruxolitinib in a T-cell neoplasm, which underscores the importance of the IL2RG/JAK1/JAK3 cytokine pathway in the pathogenesis of T-cell neoplasms, and supports inhibition of JAK enzymes as therapy.

Materials and Methods

Patient samples, processing, sequencing. Patient peripheral blood or bone marrow was banked after informed consent under a protocol approved by the Vanderbilt Institutional Review Board. Workflows have been described as the commercially available FoundationOne® and FoundationOne® Heme assays. DNA and RNA were extracted from fresh liquid specimens (blood or bone marrow aspirate). Adaptor-ligated libraries were created from DNA and cDNA as described (*267*). Libraries were sequenced on Illumina HiSeq2500 to >500x coverage depth for DNA and >3M unique pairs for cDNA. DNA and RNA sequence data were processed using a customized analysis pipeline designed to accurately detect multiple classes of genomic alterations, specifically base substitutions, indels, focal gene amplifications, homozygous gene deletions, gene fusions, and genomic rearrangements (*267*).

Gene expression. Our RNA-seq workflow has been previously described and is also detailed in the supplement (*268*). Whole RNA was prepared from T-PLL cells with Trizol (Invitrogen). Total

RNA quality was analyzed on a 2100 Bioanalyzer (Agilent); 200 ng of DNase-treated total RNA with a RNA integrity number greater than 7 was used to generate polyA-enriched mRNA libraries using TruSeq Stranded mRNA sample kits with indexed adaptors (Illumina). Library quality was assessed using the Bioanalyzer and libraries were quantitated using KAPA Library Quantification Kits (KAPA Biosystems). Pooled libraries were subjected to 50 bp single-end sequencing using manufacturer's protocol (Illumina HiSeq2500). De-multiplexed Fastq files containing purity-filtered reads were generated with CASAVA software (Illumina). Construction of indexed bam files and alignment were done as described (*268*). Differential gene expression was analyzed using 3 different statistical methods as described (*269*).

Antibodies and staining. See supplemental Tables S3.1 and S3.2 for list of antibodies used in this study. Cell staining is described in supplement.

Table S3.1. List of select antibodies used in flow cytometry in this study.

Antigen/Antibody	Fluorescent conjugate	Vendor	Cat No.
CD3/ UCHT1	PE-Cy7	BD Pharmingen	555333
CD4/ RPA-T4	BV605	BD Horizon	562659
CD45/ HI30	BV395	BD Horizon	563791
P-STAT1/ KIKSI0803	eFluor 660	eBioscience	50-9008-41
P-STAT5/ 47	PE	BD Phosflow	612567
P-STAT6/ 18/P-Stat6	PerCP-Cy5.5	BD Phosflow	561195

Mass Cytometry and phospho-flow. Immediately prior to running on the mass cytometer, cells were resuspended at approximately $0.8x10^6$ cells/mL in EQ™ Four Element Calibration Beads (Fluidigm Sciences). Calibration beads were used to correct signal fluctuation as previously described (*270*). All data were analyzed with Cytobank software (www.Cytobank.com). ViSNE analyses were performed as described (*231*). All surface markers were used to create the viSNE map with the exception of CD107a. Protein expression on the viSNE maps is shown with an arcsinh transformation. Stimulation and detection of phospho-protein signaling was performed as previously described (*271*). After staining, cells were washed twice in PBS and run on a 5-laser

LSRII (Becton Dickinson). Data were analyzed with Cytobank software. Median fluorescent intensities were arcsinh-transformed and fold change calculated by the table's minimum value (*272*).

Table S3.2. List of conjugated antibodies and their target antigens used in mass cytometry.

Conjugate	Antigen	Antibody clone	Vendor	Cat no.
141Pr	CCR6 (CD196)	G034E3	Fluidigm	3141003A
142Nd	CD19	HIB19	Fluidigm	3142001B
143Nd	CD117 (c-Kit)	104D2	Fluidigm	3143001B
144Nd	CCR5	NP-6G4	Fluidigm	3144007A
145Nd	CD4	RPA-T4	Fluidigm	3145001B
146Nd	CD8a	RPA-T8	Fluidigm	3146001B
147Sm	CD20	2H7	Fluidigm	3147001B
148Nd	CD34	581	Fluidigm	3148001B
149Sm	CCR4 (CD194)	205410	Fluidigm	3149003A
150Nd	CD43	84-3C1	Fluidigm	3150006B
151Eu	CD107a	H4A3	Fluidigm	3151002B
152Sm	TCRgd	11F2	Fluidigm	3152008B
153Eu	CD45RA	HI100	Fluidigm	3153001B
154Sm	CD45	HI30	Fluidigm	3154001B
156Gd	CXCR3 (CD183)	G025H7	Fluidigm	3156004B
158Gd	CD33	WM53	Fluidigm	3158001B
159Tb	CCR7	G043H7	Fluidigm	3159003A
160Gd	CD14	M5E2	Fluidigm	3160001B
162Dy	CD69	FN50	Fluidigm	3162001B
164Dy	CD45RO	UCHL1	Fluidigm	3164007B
165Ho	CD16	3G8	Fluidigm	3165001B
166Er	CD44	BJ18	Fluidigm	3166001B
167Er	CD27	O323	Fluidigm	3167002B
168Er				
169Tm	CD25	2A3	Fluidigm	3169003B
170Er	CD3	SP34-2	Fluidigm	3170007B
171Yb				
172Yb	CD57	HCD57	Fluidigm	3176019B
174Yb	HLA-DR	L243	Fluidigm	3174001B
175Lu	CXCR4	12G5	Fluidigm	3175001B
176Yb	CD127	A019D5	Fluidigm	3176004B

Briefly, samples were thawed and $2x10^6$ were removed for immunophenotyping by mass cytometry and remainder of the sample was used for phospho-flow cytometry. Cells rested for 30 minutes at 37 °C prior to stimulation. Cells were aliquoted into FACs tubes and allowed to rest for 5 additional minutes. Signaling was activated by stimulation with 20 ng/mL (final concentration) of IL-2, IL-4, IL-7, IL-9, IL-21, or IFNγ for 15 minutes at 37 °C. Signaling was stopped by fixation with the addition of a final concentration of 1.6% paraformaldehyde (Electron Microscopy Sciences) and incubation for 15 minutes at room temperature. Cells were washed twice with PBS/1% BSA and permeabilized with >90% ice-cold methanol. Cells were rehydrated in PBS and washed once in PBS/1%BSA. Cells were stained with 50 µL PBS/1% BSA containing antibody cocktail for 30 minutes at room temperature (protected from light). See supplemental Table below for list of antibodies used in this study.

*Phosphatase enzyme assay and inhibitor studies***.** Frozen pre- and post-treatment T-PLL cells and Jurkat cells were lysed in hypotonic buffer and cytosol prepared as described (*273*). Ruxolitinib and tofacitinib were purchased from Selleck Chemicals and working solutions prepared in DMSO. T-PLL cells were plated in RPMI/10%FCS and treated with DMSO alone or varying concentrations of drug. Cell viability was quantified by CyQuant assay as described (*260, 273*). Statistical analyses were performed with GraphPad Prism.

Results

Genomic profiling of T-cell leukemias and lymphomas

We analyzed 91 cases of diverse T-cell leukemias and lymphomas for alterations in 405 cancer-causing genes by comprehensive hybrid capture of genomic DNA followed by next generation sequencing. Based on WHO's classification scheme, our cohort was comprised of 25 precursor T-cell neoplasms (i.e. T-ALL, acute lymphoblastic leukemias) and 66 mature T-cell neoplasms: angioimmunoblastic lymphoma (AITL, n=8), anaplastic large cell lymphoma (ALCL,

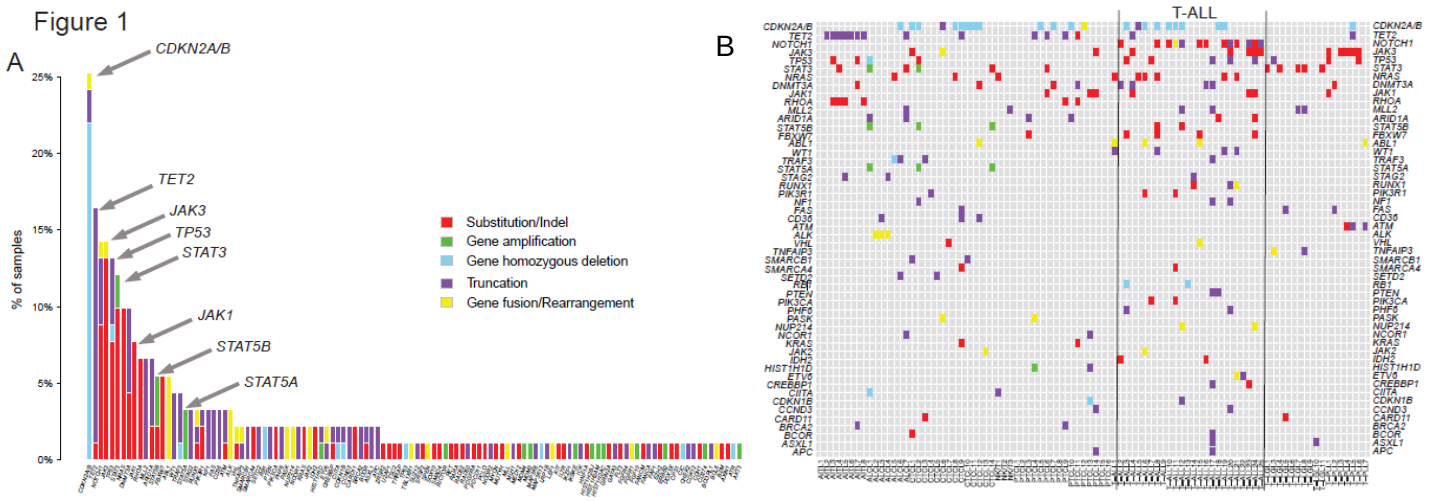

Figure 3.1. Targeted next generation sequencing of T-cell neoplasms. A, bar graph shows the frequency of genetic aberrations (color coded) in 91 samples of T-cell leukemias or lymphomas. Y-axis shows percent of total samples. **B**, tile plot shows recurrent genetic aberrations in all 91 cases. Lines bracket immature T-cell neoplasms that are T-cell acute lymphoblastic leukemias (T-ALL). X-axis shows T-cell neoplasm subtype of each individual case: AITL: angioimmunoblastic T-cell lymphoma; ALCL: anaplastic large cell lymphoma; CTCL: cutaneous T-cell lymphoma; NKT: NK/T-cell lymphoma; PTCL: peripheral T-cell lymphoma; T-ALL; T-LGL: T-cell large granular leukemia; T-PLL: T-cell prolymphocytic leukemia. Y-axis shows genes with boxes colored red for substitution/Indels (insertions or deletions), green for gene amplifications, blue for homozygous deletion, purple for truncation, and yellow for gene fusion or rearrangement as noted in panel A.

n=7), cutaneous T-cell lymphoma (CTCL, n=14), peripheral T-cell lymphoma (PTCL, n=16), T-cell large granular leukemia (T-LGL, n=11), T-cell prolymphocytic leukemia (T-PLL, n=7), and NK/T-cell lymphoma (NK/T, n=3). Our cohort showed a marked male predominance for both immature and mature T-cell neoplasm consistent with the epidemiology of these cancers (*274, 275*). Samples were sequenced at a mean exon depth of 489x by Illumina HiSeq. As shown in Figure 3.1, the most common gene alterations were *CDKN2A/B* followed by *TET2*, *NOTCH1*, *JAK3, TP53, STAT3, NRAS, DNMT3A, JAK1, RHOA, MLL2,* and others.

We compared the frequencies of gene alterations between immature (T-ALLs) and mature T-cell neoplasms. *NOTCH1* (48% v. 3%, P=0.0001), *FBXW7* (16% v. 1.5%, P=0.0191), and *NRAS* (24% v. 4.5%, P=0.0117) mutations were more frequent among T-ALL cases compared to mature T-cell neoplasms. *STAT3* mutations (0 v. 18%, P=0.032) were more common in mature T-cell neoplasms; 31.8% (29/91) of our cases had alterations in the JAK-STAT pathway. *JAK3*

was the most commonly mutated kinase in our cohort, involving 13% (12/91) of cases, followed by *JAK1,* which was mutated in 7.7% (7/91). We found 2 cases of *JAK2* rearrangement (CTCL, T-ALL cases) and 5 cases of *ABL1* rearrangements (1 CTCL, 1 T-PLL, 4 T-ALLs). *JAK3* mutations were present in similar frequency in T-ALL compared to mature T-cell neoplasms (Fisher exact test, P=0.19) but were highly frequent in certain mature T-cell neoplasms such as T-PLL (5/7, 71% cases). Interestingly, all 5 cases of T-PLL had the M511I *JAK3* mutation; all of the *JAK3* and *JAK1* mutations were in the COSMIC database, frequently within the pseudokinase domains of the proteins (Figure 3.2)(*276*). We had previously identified *JAK3* missense mutations in CTCL and ATL(*259*). Focal *STAT3*, *STAT5A*, and *STAT5B* amplifications were identified in 2 cases (CTCL and ALCL), in addition to missense mutations within the SH2 domains of STAT3 and STAT5B, such as *STAT3* D661Y/V in T-LGL (Figure 3.2). *STAT5* and *STAT3* gene alterations were mutually exclusive with *JAK1* or *JAK3* mutations. PTCL6 had mutations in *STAT3* and *JAK1* at 7% allele frequencies, respectively, and were likely separate clones. *JAK1* and *JAK3* mutations were observed in the same tumor in 5

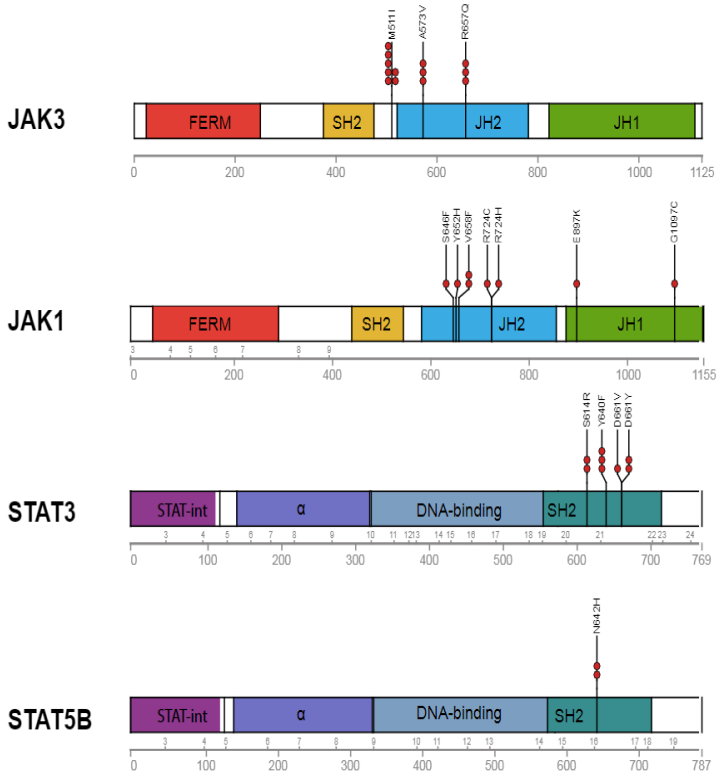

Figure 3.2. Frequent missense mutations in *JAK1*, *JAK3*, *STAT5B*, and *STAT3*. Schematic shows protein domain structures of JAK3, JAK1, STAT5B, and STAT3. Gray lines under the schematics show exon numbers above and amino acid numbers below; JAK3's exons are not shown due to differential splicing. Missense mutations are denoted by red circles with codon changes as shown. For JAK proteins, FERM denotes the conserved domain named for its founding members (Band 4.2, Ezrin, Radixin, and Moesin); SH2 stands for Src Homology domain 2, JH2 denotes JAK Homology domain 2 (also known as the pseudokinase domain), followed by JH1 for JAK Homology domain 1, the functional kinase domain. For STAT proteins, STAT-int denotes STAT interaction domain, α, alpha-helical domain, DNA-binding domain, followed by SH2 or Src Homology domain 2.

cases but concordant mutations in the same cell could not be confirmed. *JAK3* mutations were concordant with mutations in *TP53* in 4 cases, *NOTCH1* mutations in 4 cases, and *CDKN2A* deletion in 3 cases.

Exceptional response of a JAK1 mutant T-cell prolymphocytic leukemia

We evaluated a 62-year-old woman in our clinic with relapsed T-PLL. She presented with constitutional symptoms, splenomegaly, and leukemic blood counts that had risen over 150,000/µl progressing through alemtuzumab, CHOP (cyclophosphamide, doxorubicin, vincristine, prednisone), romidepsin, and pralatrexate. The T-PLL cells were $CD2^+CD3^+CD4^+CD7^+CD8^-CD56^-CD57^-$ **(**Figure 3.3A), had clonal T-cell receptor rearrangement (data not shown), and infiltration of bone marrow (Figure 3.3B-E). We analyzed the T-PLL cells (90% of PBMC) by hybrid capture followed by next generation sequencing. As shown in Figure 3.3F, the T-PLL cells had a *JAK1* V658F mutation at 40% allele frequency and a *JAK3* M511I mutation at 5%. Other notable mutations were in *ATM* and *TP53* at allele frequencies of 92% and 78%, respectively, suggesting loss of heterozygosity. Both *JAK1* and *JAK3* mutations had been described in hematologic malignancies and proven to be oncogenic in various assays (*263, 276-278*). The clonal *JAK1* mutation could be targeted by ruxolitinib, a kinase inhibitor with activity against JAK1/2(*264*). The patient was agreeable to this off-label therapy and started on 20 milligrams twice daily; her peripheral count (90% T-PLL) declined from 142,000 to 85,000 within 5 days. By 7 days her spleen, which was 4 cm below the costal margin prior to therapy, was no longer palpable. She experienced no adverse effects from ruxolitinib and her leukocyte count stabilized to ~60,000 for over 110 days. For the 100 days prior to ruxolitinib therapy, she required 10 apheresis units of platelets and 7 units of packed red blood cells whereas on ruxolitinib therapy, she received 3 apheresis units of platelets and 2 units of PRBCs. Unfortunately, by day 116, her leukemic blood count increased to 116,000 and a bone marrow biopsy confirmed relapsed disease (Figure 3.3G). The patient developed worsening thrombocytopenia that did not respond

Figure 3

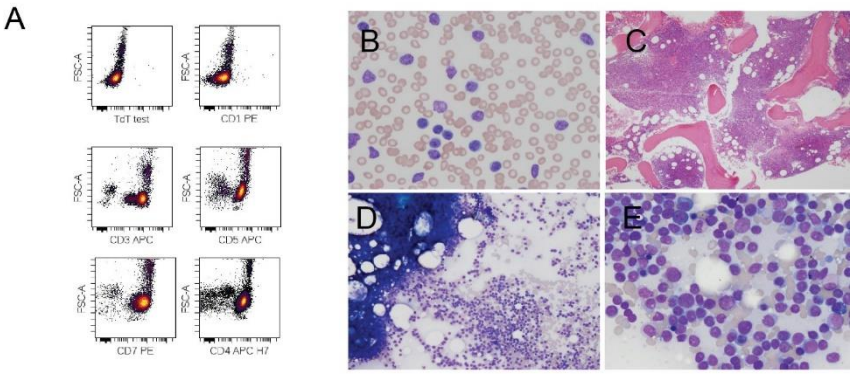

F

Gene name	mutation	MAF, pre-rx	MAF, post-rx
JAK1,	c.1972G>T, p.V658F	0.40, 772	0.18., 458
JAK3,	c.1533G>A, p.M511I	0.05, 850	0.28, 444
ATM	c.2941C>T, p.R981C	0.92.507	0.97, 197
TP53	c.526T>G, p.C176G	0.78, 374	0.97, 220

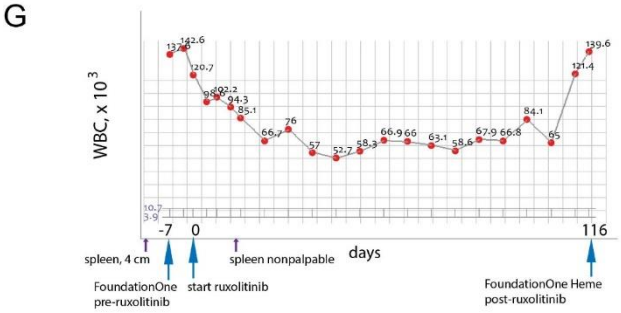

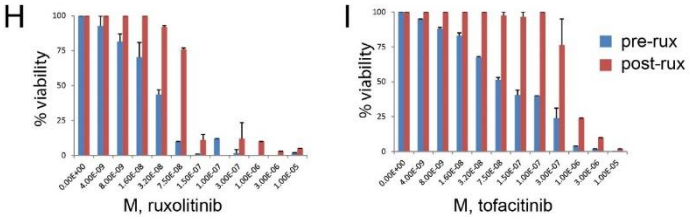

Figure 3.3. A remarkable case of T-cell prolymphocytic leukemia (T-PLL) that responded to specific JAK1 inhibitor, ruxolitinib. A, dot plots show the immunophenotype of the patient's T-PLL cells at presentation as analyzed by flow cytometry; T-PLL cells were interpreted as TdT^- $CD1^-$ CD3+ $CD5^+$ $CD7^+$ $CD4^+$. **B**, photomicrograph of patient's peripheral blood smear. **C**, photomicrograph of the patient's bone marrow biopsy showing marked hypercellularity. **D**, shows bone marrow aspirate with homogeneous cells. **E**, bone marrow aspirate at high power shows neoplastic cells with fine chromatin and prominent nucleoli. **F**, table shows Foundation One panel analysis of patient's T-PLL cells before (pre-rx) and after (post-rx) ruxolitinib treatment. Major gene mutations are shown with their MAF, major allele frequencies and the number of reads. For example, JAK1 V658F was present in the pre-ruxolitinib sample at 40% supported by 772 reads. **G**, shows a plot of the total leukocytes for the patient; y-axis shows cells number ($x10^3$); gray brackets show the normal range of peripheral leukocyte number. X-axis shows time in days with some clinical features highlighted. Purple arrows time points of physical exams showing palpable spleen 4 cm below costal margin prior to ruxolitinib therapy, which was not palpable after treatment. Blue arrows show the time of first FoundationOne analysis, start of ruxolitinib therapy, and FoundationOneHeme panel analysis at relapse. **H**, shows bar graphs of patient's T-PLL cells treated in vitro with varying concentrations of ruxolitinib (left panel) or tofacitinib (right panel) shown in molar, M. Y-axis shows cell viability; blue bars show pre-ruxolitinib and red bars show post-ruxolitinib/relapse samples. Error bars are SEM of three independent experiments.

to cytotoxic chemotherapy, and succumbed to her disease. Acquired resistance to ruxolitinib and the pan-JAK inhibitor, tofacitinib, was cell-intrinsic since it was observed *ex vivo*. Pre-treatment T-PLL cells were more sensitive to ruxolitinib ($IC50=3.85x10^{-8}$ M) and tofacitinib ($IC50=8.64x10^{-8}$ M) compared to post-treatment cells ($IC50_{rux}=4.21x10^{-7}$ M; $IC50_{tof}=2.86x10^{-6}$ M, $P<0.0001$) (Figure 3.3H).

Genetic and immunophenotypic analysis of resistance to ruxolitinib therapy

At relapse, the *JAK3* M511I allele frequency had increased from 5% to 28%, whereas the allele frequency of *JAK1* V658F had decreased from 40% to 18% in the T-PLL cells (Figure 3.3F). *TP53*, *ATM*, and other mutational frequencies did not change. We analyzed the pre- and post-ruxolitinib T-PLL cells by RNA-seq where the steady state abundance of mutant mRNAs approximated the allele frequencies. We analyzed the patient's pre- and post-ruxolitinib/relapse T-PLL cells for 28 cell surface antigens by mass cytometry. We analyzed the multidimensional staining pattern by viSNE, an algorithm that maps cells on to a 2-dimensional plot (*231*). PBMCs from healthy donors stratified into distinct cell populations corresponding to specific lineages: $CD4^+$/$CD8^+$ T cells, NK cells, macrophages, and B cells (Figure 3.4A). Our patient's T-PLL cells clustered into a unique island, comprised of 95.3% total peripheral cells with few non-malignant cell types (Figure 3.4A). The relapsed sample showed two distinct leukemic populations, one resembling the pre-ruxolitinib sample (46.1%) and a new island emerging with drug resistance (50.6%). CD45 protein expression was the major feature discriminating the two relapsed cell populations (Figure 3.4C-D). The $CD45^+$ population resembled the pre-treatment cells except for reduced expression of CD127 (IL7R). The $CD45^{lo/-}$ population showed increased CD27 (TNFRSF7), CD44 (H-CAM), CCR4, CCR7 and reduced CD43 (Leukosialin) in comparison to pre-treatment or post-treatment $CD45^+$ cells (Figure 3.4C-D). CD45 is a receptor tyrosine phosphatase encoded by the *PTPRC* gene that negatively regulates JAK-STAT and T-cell receptor signaling (*279, 280*). CD45 downregulation coincident with clinical relapse on ruxolitinib

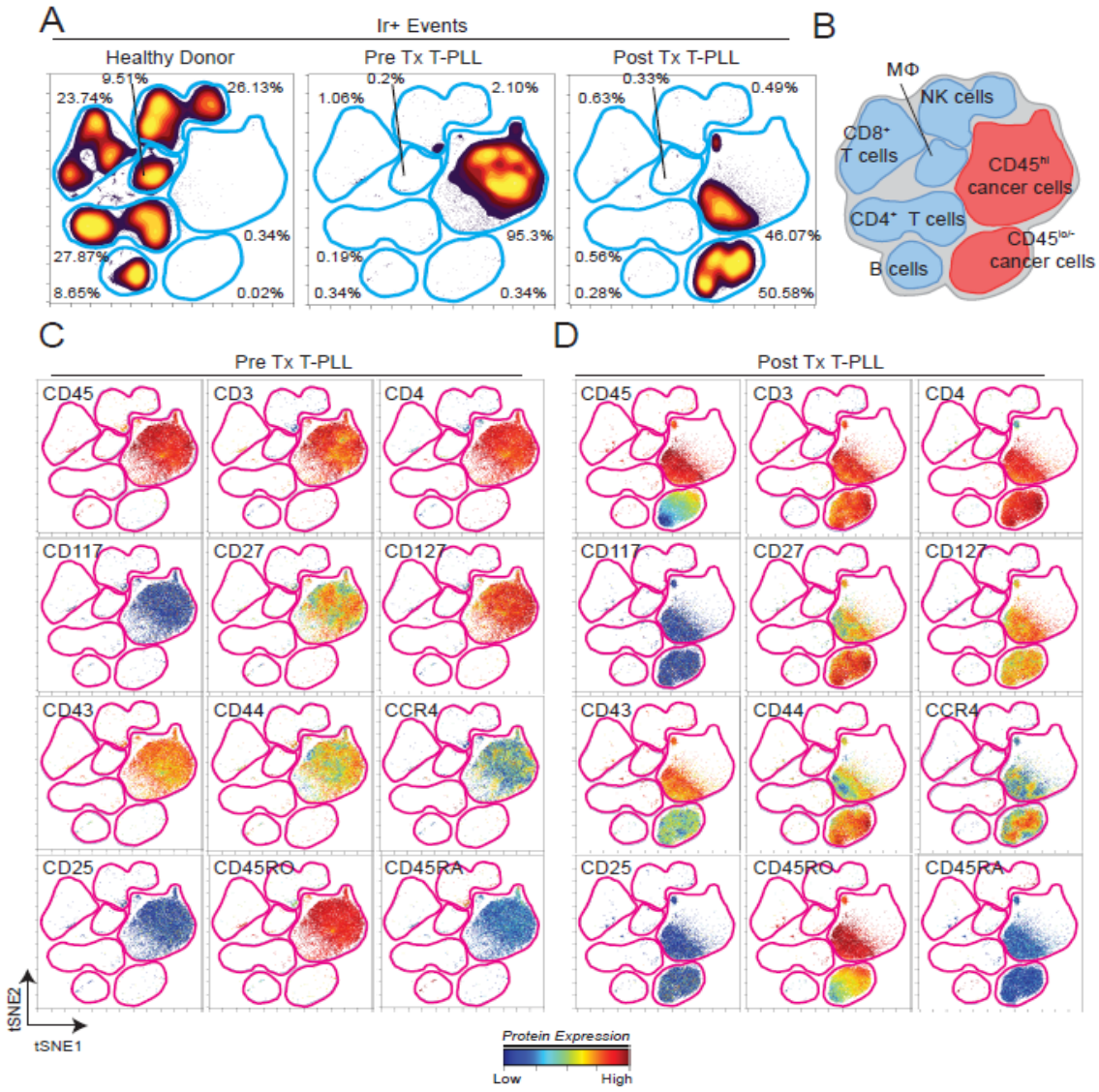

Figure 3.4. CyTOF analysis shows marked change in immunophenotype of T-PLL cells after relapse from ruxolitinib. Peripheral blood samples from healthy donor and the T-PLL patient, pre-ruxolitinib (Pre-tx) and at relapse (Post-Tx) were analyzed by mass cytometry after staining for 28 cell surface markers. **A**, shows viSNE analysis performed on the data allowing grouping of peripheral leukocytes into distinct islands corresponding to cell lineages (see **B**); Iridium (DNA intercalator) positive events (Ir^+) show those cells that were intact. **C**, shows the level of expression of 12 cell surface markers in the distinct islands. **D**, shows the same 12 markers but in the relapsed sample, post-ruxolitinib/relapse (Post-Tx). High dimensional, single-cell immunophenotype was measured using a 28-marker mass cytometry panel. A, viSNE map shows cell density for all Iridium-positive (nucleic DNA intercalator) cells from a healthy donor, pre-ruxolinitib T-PLL (Pre Tx, and post-ruxolitinib/relapse relapse (Post Tx). (B) Cellular identity of each island was identified using expression of all 28 measured proteins. Protein expression is shown on a common viSNE map for (C) pre-ruxolitinib T-PLL (Pre Tx) and (D) post-ruxolitinib/relapse relapse T-PLL (Post Tx). For (C-D) color indicates the intensity of the labeled protein on a rainbow heat scale (arcsinh scales).

implied that it may be a mechanism for ruxolitinib resistance. The *JAK1* mutation was not

detectable by Sanger sequencing but the *JAK3* mutation was clonal and present in $CD45^{hi}$, $CD45^{int}$, and $CD45^{-}$ cells (Figure 3.5A-B). CD45RO and CD45RB were the mRNA isoforms expressed by the T-PLL cells (RNA-seq and FACS). Whole transcriptome analysis on pre-treatment and post-treatment samples found that *PTPRC* mRNA abundance was significantly reduced in the relapsed sample by 1.95-fold (Figure 3.5D, p=3.18E-74), approximating the 50% reduction in protein levels observed by flow cytometry. *JAK1*, *JAK2*, and *JAK3* mRNAs were also significantly downregulated (Figure 3.5D). JAK1 and JAK3 were probed by Western analysis of whole cell lysates and showed lower protein abundance in the relapsed sample compared to lysates before ruxolitinib treatment (Figure 3.5C).

Next, we analyzed the tyrosine phosphatase activity in lysates prepared from T-PLL cells pre- and post-ruxolitinib/relapse therapy. Immunodepletion with specific antibody against CD45 reduced total tyrosine phosphatase activity to 20-22% of normal, confirming that CD45 was the major enzyme contributing to this enzyme activity in T-PLL cells (Figure 3.5E). The specific activity of tyrosine phosphatase in pre-ruxolitinib lysates was 3.40 µmol/min/mg (95% CI: 3.10-3.70), which was decreased 54% to 1.85 µmol/min/mg (95% CI: 1.58-2.12) in the post-ruxolitinib/relapse sample (P<0.0001) (Figure 3.5F). Thus, the cellular phosphatase activity reflected the decreased CD45 protein levels which paralleled the decrease in *PTPRC* mRNA abundance. Interestingly, we found another T-PLL case with *JAK3* M511I mutation that had downregulated CD45 at the time of relapse from CHOP chemotherapy.

Enhanced phosphorylations downstream of JAK1/3 at relapse

CD45 was previously shown to directly dephosphorylate JAK1 and JAK3 suggesting that its loss of function should show increased activity of JAK3 or JAK1. To analyze JAK activity, we probed the intracellular phosphorylation of key substrates in T-PLL cells pre- and post-ruxolitinib/relapse treatment by flow cytometry. The percentage of T cells expressing basal levels

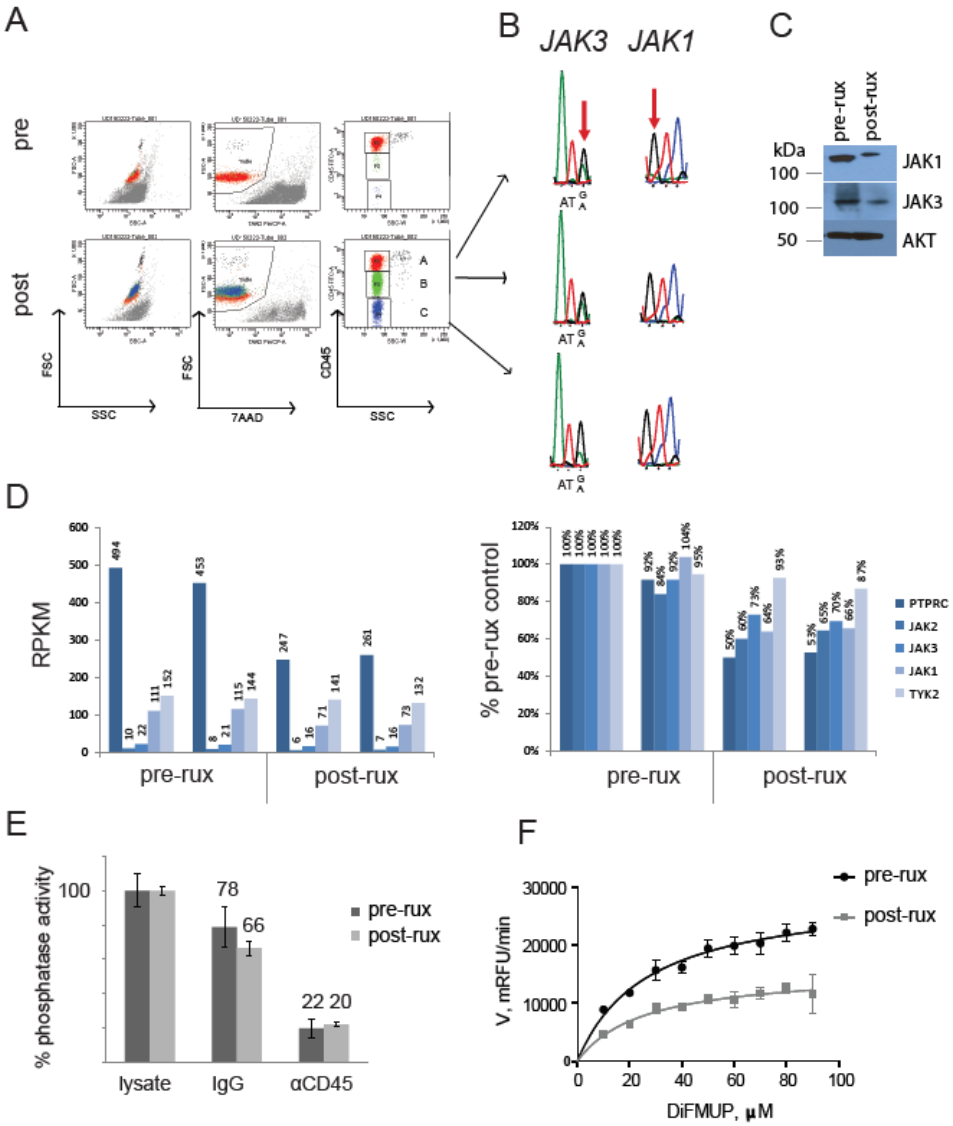

Figure 3.5. Clinical resistance correlates with downregulation of CD45 protein, mRNA, and phosphatase activity. A, flow cytometry dot plots show staining patterns of T-PLL cells pre- and post-ruxolitinib/relapse for forward and side scatter (FSC, SSC), 7-aminoactinomycin D (7-AAD), and anti-CD45. Three distinct populations were noted based on CD45 expression (A, B, C); cells were flow sorted, extracted for genomic DNA, subjected to PCR for relevant exons, and sequenced in panel **B**. **C**, shows Western blot analysis of pre-ruxolitinib and post-ruxolitinib/relapse/relapse T-PLL cells for total JAK1, JAK3, and AKT proteins. **D**, shows RNA-seq results for *PTPRC, JAK2, JAK3, JAK1*, and *TYK2*. Vertical line separate pre-ruxolitinib and post-ruxolitinib/relapse samples; both were analyzed in duplicate. Left panel shows RPKM for T-PLL, reads per kilobase of gene per million reads; right panel shows RPKM normalized to pre-ruxolitinib reads (set at 100%). **E**, bar graphs show measured in vitro phosphatase activity from cytosolic lysates prepared from T-PLL cells, before (dark gray) and after (light gray) ruxolitinib. Second set of assays were done after pull down with isotype control IgG/Protein A/G. Third set of assays were done after incubation with anti-CD45/Protein A/G; values were normalized to cytosolic lysates prior to immunodepletion (set at 100%); error bars show SEM from quadruplicates. **F**, graph shows a kinetic phosphatase assay of cytosolic lysates prepared from pre-ruxolitinib and post-ruxolitinib/relapse T-PLL cells. X-axis shows varying concentrations of phosphatase substrate, DiFMUP, in micromolar; y-axis shows velocity of product formation in mRFU/min.

of p-STAT1 and p-STAT5 were increased in pre-ruxolitinib cells and in post-ruxolitinib/relapse cells compared to healthy T cells (22.72% and 21.24% v. 0.79%; 57.52% and 54.84% v. 2.21%) whereas no cells in any condition expressed basal phosphorylation of p-STAT6, which served as a control (Figure 3.6B). T-PLL cells with the lowest expression of CD45 had the highest proportion of p-STAT5^{+} cells at baseline prior to any stimulation (Figure 3.6C). To assess whether T-PLL cells had increased sensitivity to cytokine stimulation in addition to increased basal signaling, we stimulated each sample with 20 ng/mL cytokine for 15 minutes. Signaling was quantified as previously described (*272, 281*), using median fluorescence intensity of per-cell phospho-protein to create a fold-change. Increased phosphorylation of STAT5 was seen after in vitro stimulation with IL-2, IL-4, IL-7, IL-21, and IFN-γ but not IL-9 in both pre- and post-ruxolitinib/relapse treated samples as compared to healthy T cells (Figure 3.6D). A comparison between pre- and post-ruxolitinib/relapse T-PLL cells showed similar p-STAT5 levels at baseline and after stimulation by cytokines (Figure 3.6D). For example, IL-2-induced 1.49-fold change in p-STAT5 for pre-ruxolitinib samples and 1.44 in post-ruxolitinib/relapse samples. To understand the effects of CD45 expression we gated on CD45^{hi}, CD45^{lo}, and CD45^{-} post-ruxolitinib/relapse T-PLL cells and analyzed p-STAT5 and p-STAT6 basally and in response to stimuli. CD45^{hi} had the lowest p-STAT5 response to IL-2 (0.23), followed by CD45^{lo} (0.61); and, CD45^{-} (1.24) (Figure 3.6D); this pattern was seen for all common gamma chain cytokines in contrast to control, p-STAT6 (Figure 3.6D-E). In summary, T-PLL cells were hyper-responsive to common gamma chain cytokines and CD45 expression was negatively correlated with p-STAT5 at relapse.

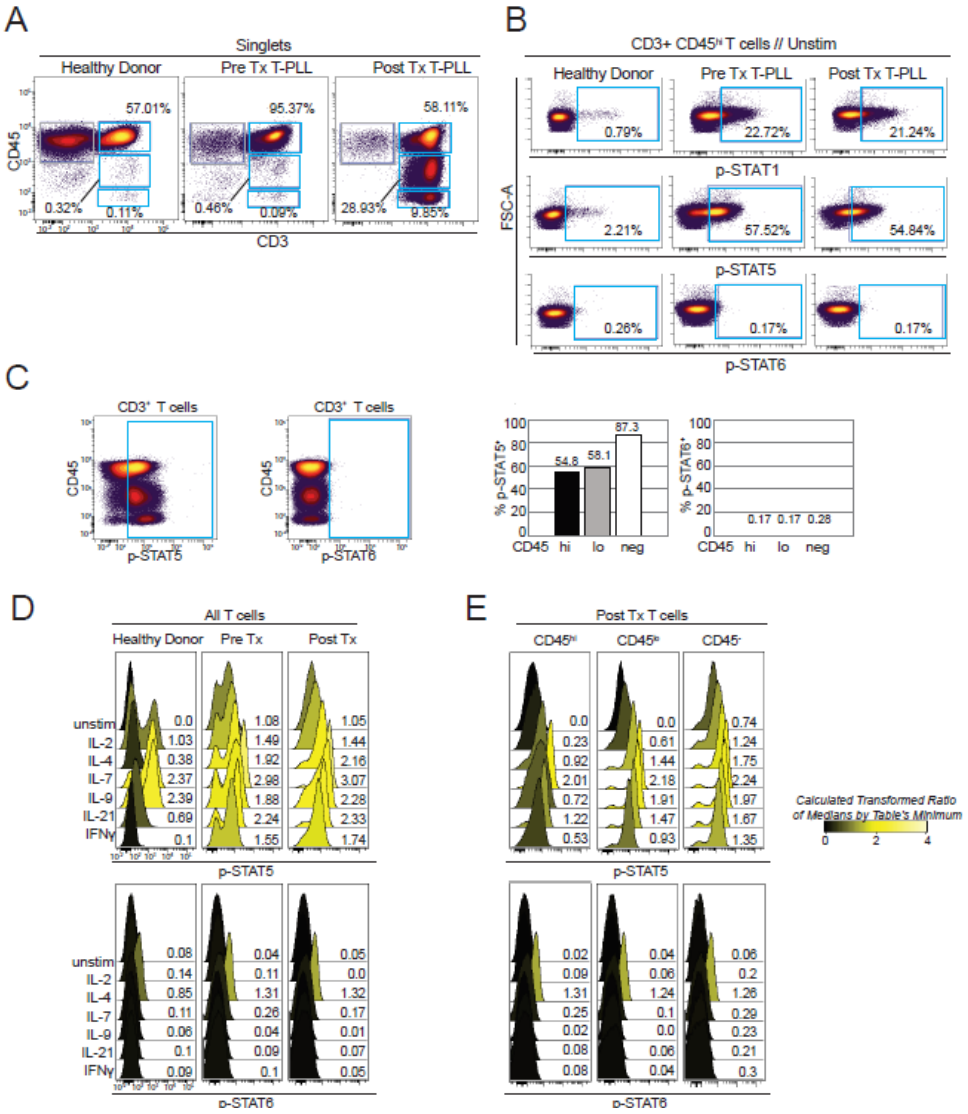

Figure 3.6. T-PLL cells have constitutive phospho-STAT1 and phospho-STAT5. Intracellular signaling responses of PBMCs from healthy donor, and our T-PLL patient before (pre-Tx) and after (post-Tx) relapse from ruxolitinib treatment were monitored using phospho-flow cytometry. **A**, biaxial plots show expression of CD45 and CD3 on healthy donor and T-PLL samples. Blue gates indicate populations defined by expression of CD45 (hi, lo, and negative). $CD3^+$ included peripheral T cells in health donor and all T-PLL cells. **B**, biaxial plots show basal p-STAT-1, p-STAT5, and p-STAT6 in $CD3^+$ $CD45^{hi}$ cells. **C**, biaxial plot shows CD45 v. p-STAT5 and p-STAT6 at the time of relapse. Right panel shows bar graph of percent cells with p-STAT5 or p-STAT6 for cells expressing CD45hi, CD45lo, and $CD45^{neg}$. **D**, graphs show p-STAT5 and p-STAT6 for health donor T cells, pre-Tx T-PLL, and post-Tx T-PLL unstimulated or after 15 minutes of cytokine stimulation at 20 ng/mL. **E**, similar graphs of cytokine stimulated p-STAT5 and p-STAT6 for post-Tx T-PLL cells gating on $CD45^{hi}$, $CD45^{lo}$, or CD45neg. Values are from median fluorescent intensities that were arcsinh transformed and expressed as fold change from the table's minimum value. Graphs are shaded from black to yellow to reflect ratios from 0-4, as shown by the scale.

Discussion

In this study, we profiled diverse T-cell neoplasms by targeted next generation sequencing of the exomes from ~400 known tumor suppressors and oncogenes. Among oncogenic mutations, *JAK-STAT* (33%) alterations were the most common. Our cohort was comprised of cases submitted to Foundation Medicine due to relapsed or resistant disease, so the observed genetic alterations may be specific to advanced stage or therapeutic resistance. Nevertheless, our mutation frequencies for *JAK3* (13% of cases) and for *JAK1* (8.7%) were consistent with genomic profiling studies focused on specific disease subtypes T-ALL, ATLL, T-PLL, and CTCL (*258-262*) and less common in AITL and PTCL (*282, 283*). The JAK mutations in our study were mutually exclusive with *STAT3* and *STAT5* gene alterations, as expected since STAT3 and STAT5 proteins are downstream of IL2RG/JAK1/3-restricted cytokines. Interestingly, recent data in cell lines and mouse models suggest that JAK1 enzyme activity is required for mutant JAK3's effects (*284-286*). However, as in the index case, the mutations were co-occurring but not present in the same cell since we never found allele frequencies approaching 50% for *JAK1* and *JAK3* mutations in the same tumor.

Most importantly, the *JAK1* and *JAK3* mutations were functionally significant since they induced constitutive phosphorylations of downstream STAT5 proteins. Phospho-STAT3 was not observed in the T-PLL cells (data not shown) even though it is an important downstream substrate in other T-cell neoplasms such as ALCL (*287*). Thus, signaling patterns downstream of JAK1/3 may be unique to disease subtype. STAT1 and STAT5 phosphorylations in T-PLL could be inhibited by specific JAK inhibitors, ruxolitinib and tofacitinib (*288*). In the index case, treatment with ruxolitinib induced an impressive clinical response. These compelling data argue for oncogene dependence upon the JAK-STAT pathway in T-PLL, results that may extend to other T-cell neoplasms with *JAK* mutations. Furthermore, this oral drug worked where intensive parenteral therapies had failed to control the disease.

Our studies showed two cell-intrinsic mechanisms accounting for resistance to ruxolitinib: expansion of the mutant JAK3 T-PLL clone and downregulation of CD45. Ruxolitinib's IC50 for JAK1 is 3.3 nM and for JAK2 is 2.8 nM in *in vitro* studies (*289*) ; its IC50 for JAK3 is 428 nM (*289*). This diminished potency against JAK3 probably accounted for the expansion of the mutant *JAK3* clone from 10% pre-ruxolitinib to 56% at relapse. The T-PLL cells showed cross-resistance to tofacitinib, which has nanomolar IC50 for JAK3 (*290, 291*). The downregulation of CD45 protein appears to be an additional resistance mechanism at relapse. Reduced CD45 proteins reduced the total tyrosine phosphatase activity in the T-PLL cells, which correlated with increased p-STAT5. *PTPRC* mRNA abundance was decreased suggesting either enhanced mRNA degradation or transcriptional repression. The expression pattern of CD45 in a clonal T-PLL population resembles position effect variegation, an epigenetic phenomenon (*292, 293*). Since the primary leukemia samples were consumed, we were unable to directly transduce *PTPRC* cDNA to test if JAK inhibitor sensitivity could be restored. Thus, a cooperative genetic interaction between PTPRC loss of function and *JAK3* M511I remains speculative. We observed an additional case of T-PLL with a clonal *JAK3* M511I mutation that had similarly downregulated CD45 after relapse from CHOP chemotherapy, suggesting that downregulation of CD45 protein may play a role in chemotherapy resistance. Notably, Porcu et al discovered deletion, missense, and nonsense mutations in *PTPRC in T-cell ALL, evidence that supports a tumor suppressor role for PTPRC in this disease* (*294*). Furthermore, Porcu et al also showed concordant loss of function in *PTPRC* and gain of function in *JAK1* or *IL7R*, suggesting that these two hits cooperate in T-ALL pathogenesis. In fact, they described augmented P-STAT5 when *PTPRC* was knocked down by siRNA. Our studies on the index case are similar to these findings since we also observed an inverse correlation between CD45 levels and P-STAT5 albeit in T-cell PLL. Our studies do suggest that PTPRC may be a tumor suppressor in more mature T-cell neoplasms in addition to precursor T-ALL, and its loss of function may be an important resistance mechanism to ruxolitinib.

Finally, the data presented in this study support the design of larger phase I/II clinical trials testing ruxolitinib on its own or in combination with cytotoxic therapies in T-cell neoplasms. A basket design where patients with rare T-cell subtypes may be enrolled based on the presence of *JAK1* or *JAK3* mutations may be most informative.

CHAPTER IV

SYSTEMS IMMUNOLOGY OF CHECKPOINT INHIBITOR THERAPY: A CASE STUDY OF MYELODYSPLASTIC SYNDROME REVEALED IN A MELANOMA PATIENT UNDERGOING ANTI-PD-1 THERAPY

Authors: Allison R. Greenplate, Douglas B. Johnson, Mikael Roussel, Michael R. Savona, Jeffrey A. Sosman, Igor Puzanov, Paul Brent Ferrell*, Jonathan Michael Irish*

*Equal contribution

This work appears as published in manuscript form in *Cancer Immunology Research* (Greenplate, et al. 2016)

Introduction

I was able to fully characterize T cells of unusual phenotype from *ex vivo* stimulation (Chapter II) and *in vivo* transformation (Chapter III). The work from Chapter III revealed the clinical impact of mass cytometry and high dimensional data analysis. Given the impact and functionality of this work flow both in the lab and in the clinic, I next decided to use it to dissect the impact of immunotherapy on both T cells and the immune system as a whole in patients with melanoma.

Antibodies targeting the programmed cell death-1 (PD-1) receptor and its ligand (PD-L1) have demonstrated remarkable activity in a variety of solid tumor malignancies and Hodgkin disease (*295-299*). Agents such as nivolumab and pembrolizumab block this key immune checkpoint to generate effective CD8 T-cell mediated anti-tumor immune responses (*1*). Although generally well-tolerated, anti-PD-1/PD-L1 agents have also induced grade 3-4 immune-mediated adverse events (~5% of patients) (*295, 297, 300*). The ability to monitor the immune system as a whole is needed in clinical settings where therapies are designed to alter the interaction between multiple cell types, such as the blockade of the PD-1/PD-L1 interaction. Mass cytometry has emerged as an important platform for comprehensive and minimally biased immune profiling (*208*). This approach has been applied effectively in the context of healthy human bone marrow,

blood, and tonsil tissue (*9, 222, 223, 301*). An important element of high dimensional mass cytometry is the use of unsupervised computational data analysis tools that reveal and characterize cells with unusual phenotypes (*207, 219, 231*).

To examine the effects of immune checkpoint inhibition on peripheral blood cell subsets, we performed serial blood acquisition in patients with advanced melanoma being treated with pembrolizumab. Multiplexed mass cytometry analysis of peripheral blood characterized the phenotypic evolution of all major immune cell and blast populations. Here, we present a case report of a single patient from this study who experienced clinical emergence and progression of MDS while undergoing treatment with pembrolizumab.

Materials, & Methods

Subject

The subject was consented to an IRB-approved research protocol to collect serial blood prior to treatment (baseline) and following pembrolizumab (at 3 weeks, 6 weeks, 12 weeks, and 24 weeks). Peripheral blood was obtained during regularly scheduled laboratory blood draws in accordance with the Declaration of Helsinki following protocols approved by Vanderbilt University Medical Center (VUMC) Institutional Review Board.

PBMC preparation

Peripheral blood mononuclear cells (PBMCs) were isolated from 20 mL of freshly drawn blood using sodium heparin anticoagulant and Ficoll-Paque PLUS (GE Healthcare Bio-sciences, Uppsala, Sweden) centrifugation. Freshly isolated PBMCs were immediately cryopreserved in FBS (Life Technologies, Grand Island, NY, USA) containing 12% DMSO (Fischer Scientific, Fair Lawn, NJ, USA).

Mass cytometry

Purified antibodies from Biolegend (San Diego, CA, USA) were labeled using MaxPar DN3 kits (Fluidigm Sciences, Toronto, Canada) and stored at 4°C in antibody stabilization buffer (Candor Bioscience GmbH, Wangen, Germany). PBMC were first incubated with a viability reagent (25 µM cisplatin, Enzo Life Sciences, Farmingdale, NY, USA) as previously described (*230*). For staining, 2 x 10^6 cells were washed in PBS containing 1% BSA and stained in 50 µL PBS/1% BSA containing antibody cocktail. Cells were stained for 30 minutes at room temperature using antibodies listed (Supplementary Table 4.1). Cells were washed twice in PBS/1% BSA and then fixed with 1.6% paraformaldehyde (PFA, Electron Microscopy Sciences, Hatfield, PA, USA). Cells were washed once in PBS and permeabilized by resuspending in ice cold methanol. After incubating overnight at -20°C, cells were washed twice with PBS/1% BSA and stained with iridium DNA intercalator (Fluidigm Sciences,) for 30 minutes at room temperature. Finally, cells were washed twice with PBS and twice with diH_2O before being resuspended in 1x EQ™ Four Element Calibration Beads (Fluidigm Sciences) and collected on a CyTOF 1.0 mass cytometer (Fluidigm Sciences) at the Vanderbilt Flow Cytometry Shared Resource. Events were normalized as previously described (*270*).

Cytometry data analysis

Analysis was performed on Cytobank using published techniques including viSNE (*229, 231*). Each file was pre-gated on $CD45^{lo}$ events. All $CD45^{lo}$ events were used and BTLA, CD69, HLA-DR, CD45RO, CD44, CD27, CD3, CD45RA, CXCR3, CD33, CD16, PD-L1, CD4, CD8a, CD43, ICOS, CD20, CD38, CCR4, CD45, CCR7, CD25, CXCR5, CD57, PD-1, and CD56 were used to create the t-SNE axes of the viSNE map.

Results

Medical case report

A 72-year old female patient with a past medical history of breast cancer treated with mastectomy and chemotherapy (24 years prior) developed swelling in her thigh. CT scan showed a 2x4x3 cm complex, cystic mass in the soft tissues of the thigh. She underwent a resection that revealed melanoma with involved lateral margins. No primary site was identified, and she received 2800 cGy via external beam therapy to the resection margin in the thigh (American Joint Committee on Cancer [AJCC] stage TxNxM1a). A surveillance PET-CT scan performed 18 months later demonstrated multiple new pulmonary nodules, and she received ipilimumab 3mg/kg for four doses. Repeat CT scan showed disease progression in the lungs, and she was started on pembrolizumab 2mg/kg every 3 weeks (pembrolizumab expanded access program). Her initial surveillance scans in 3 months showed a mixed response in lung nodules but overall stable disease. Her subsequent CT scan 6 months into therapy showed disease progression, primarily in two lung nodules (Figure 4.1A). She underwent radiation to those nodules and has continued pembrolizumab.

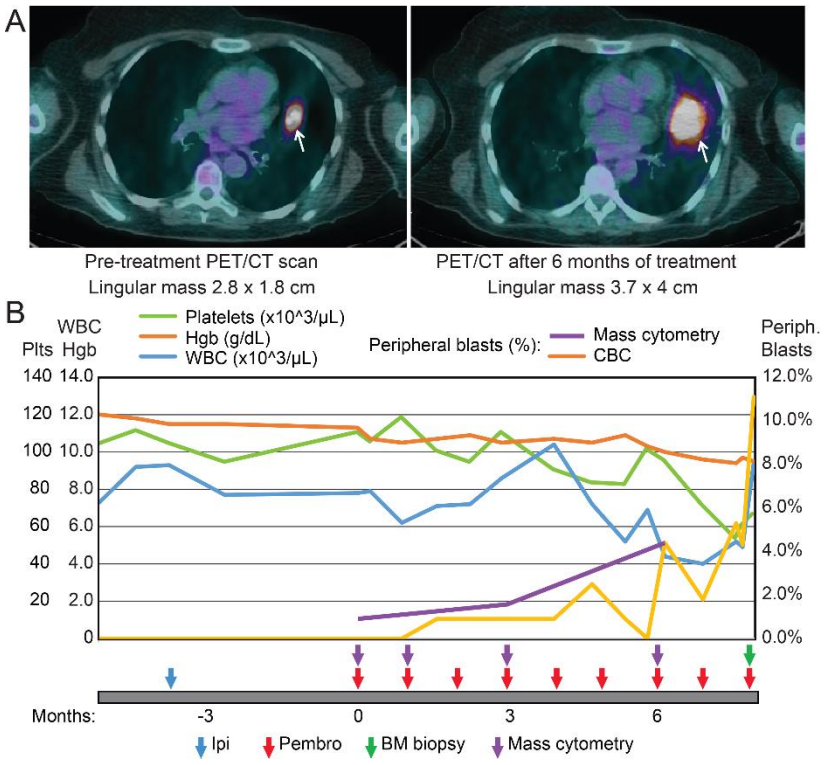

Figure 4.1. Clinical Imaging and Blood Counts. A) Pre-therapy and post-therapy PET/CT scans are shown that highlight a lingular metastasis that increases in size during the course of therapy. B) Select peripheral blood counts and blast cells by manual differential are shown prior to and during therapy. The patient had a pre-existing thrombocytopenia (green line) that worsened over time. After therapy initiation, blasts (yellow) are seen to increase as hemoglobin (Hgb, orange line) drops and white blood cells (blue line, same scale as Hgb) remain in the normal range.

Prior to starting pembrolizumab, the patient was noted to have mild thrombocytopenia (platelet count $95x10^9$/L), which had been present but stable for the previous 18 months, and normal white blood cell count and hemoglobin. Her monocyte count was slightly elevated ($1.27x10^9$/L), but otherwise she had a normal differential. One month after starting pembrolizumab, she developed a clinically detectable but small circulating myeloid blast population on her CBC differential which remained at <1% for the next two months (Figure 4.1B). Blasts were not detected in her pre-treatment sample on her CBC differential, but were detected pre-treatment by CyTOF analysis (Figure 4.2). After treatment, her peripheral blast percentage rose to 4.4% and her platelets and hemoglobin fell to $72x10^9$/L and 9.4g/dL, respectively, prompting a bone marrow biopsy. This revealed refractory anemia with excess blasts-2 (RAEB-2) with 8.5% blasts. During this workup, her peripheral blast percentage ranged from 7-11% and she began decitabine treatment. Since initiating decitabine, she has felt well and her peripheral blast count has stabilized.

High dimensional cytometry revealed peripheral blasts

Samples of peripheral blood from prior to anti-PD-1 therapy, 3 weeks, 12, and 6 months following the initiation of therapy were analyzed by a 33-parameter mass cytometry panel. Major cell populations were revealed using traditional biaxial plots (Figure 4.2). As a subset of peripheral blood mononuclear cells (PBMCs), blasts ranged in abundance from 1.16% pre-therapy to 4.65% at six months after the start of treatment (Figure 4.2A and Figure 4.2C, left). In comparison to mature myeloid and monocyte cell populations, the majority of peripheral blasts expressed lower CD45 and CD33, higher CD38, and comparable HLA-DR (Figure 4.2B). Four additional cell populations were monitored using mass cytometry over the course of anti-PD-1 therapy (Figure 4.2C, right). Myeloid cells ($HLA\text{-}DR^{pos}CD19^{neg}CD3^{neg}CD16^{neg}$) increased over the course of anti-

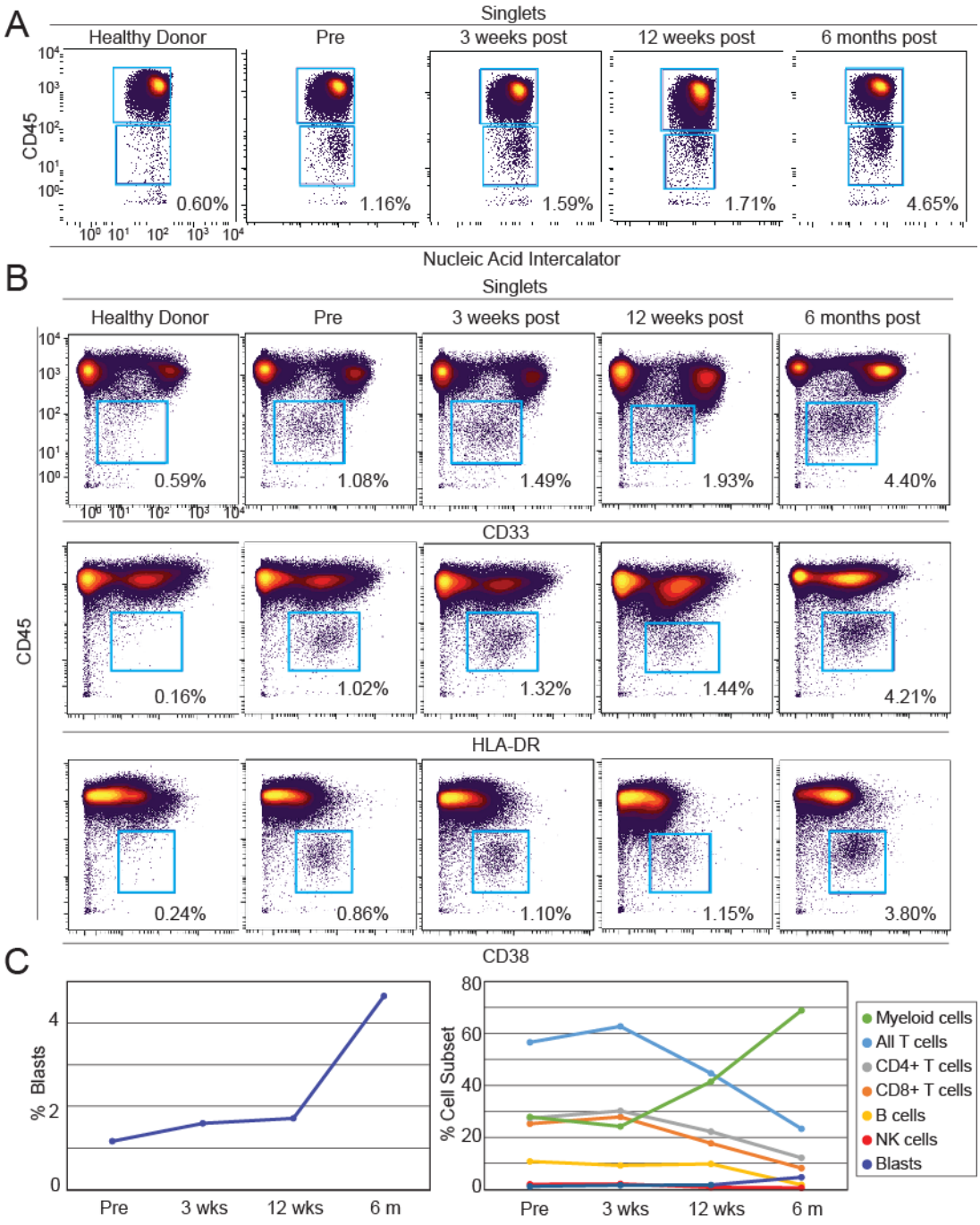

Figure 4.2. Identification of peripheral blasts by mass cytometry in a melanoma patient undergoing anti-PD-1 therapy. A 33 parameter mass cytometry panel was used to immunophenotype peripheral blood from a melanoma patient over the course of anti-PD-1 therapy. A) Cells positive for nucleic acid intercalator, a marker of nuclear DNA, and low for CD45 were identified over the course of therapy, but not in a healthy donor. B) The majority of CD45^{lo} events (blue gate) from the patient expressed intermediate levels of CD33 and high levels of both HLA-DR and CD38 compared to non-blasts, consistent with peripheral myeloblast phenotype. C) Peripheral blasts increased from 1.16% to 4.65% of all PBMC (left). The percentage of T (light blue), B (yellow), and NK (red) cells declined over the course of therapy while the percentage of myeloid cells (green) increased (right).

PD-1 therapy, while T cells ($CD3^{pos}CD19^{neg}$), B cells ($CD19^{pos}CD3^{neg}$), and NK cells ($CD16^{pos}CD3^{neg}CD19^{neg}$HLA-$DR^{neg}$) decreased.

Increased percent of PD-1 positive monocytes during therapy

To determine which cells could be modulated by pembrolizumab, mass cytometry was used to monitor PD-1 protein expression on all major peripheral blood subsets. In the blood of healthy donors, 1.8% ± 0.68% of HLA-$DR^{pos}CD19^{neg}CD3^{neg}CD16^{neg}$ myeloid lineage PBMCs expressed PD-1 (n=5). In contrast, elevated levels PD-1^{pos} myeloid cells were seen in all pre- and post-treatment samples collected from the melanoma patient (Figure 4.3A). PD-1^{pos} myeloid cells decreased over therapy from 4.04% pre-treatment to 2.81% at 6 months after the start of pembrolizumab. The percentage of PD-1^{pos} $CD4^{+}$ T cells in PBMC was high prior to therapy (4.93% in the patient prior to therapy *vs* 3.31% ± 1.28% in healthy donors, n=5). However, by week 3 post therapy, the frequency of both PD-1^{pos} CD8 and CD4 T cells in PBMC decreased below normal (1.94% and 2.29% respectively in patient 6 months after start of therapy *vs* 4.44% ± 2.15% and 3.31% ± 1.28% respectively in healthy donors, n=5). B cells, NK cells, and blasts were very rarely PD-1^{pos} (Figure 4.3A, <2% PD-1^{pos} at all observed times).

Mass cytometry was also used to monitor expression of PD-L1, a key ligand for PD-1 and potential biomarker of anti-PD-1 treatment response (*302*). PD-L1 expression was largely absent; no cell subset was observed to express PD-L1 on >1.5% of cells (data not shown). Monocytes were the only peripheral cell subset to exhibit increased PD-1 expression and a large increase in activation marker CD45RA was seen on monocytes over the course of therapy (Figure 4.3B) (*303*). These results highlight monocytes as an important target population that could be activated by pembrolizumab.

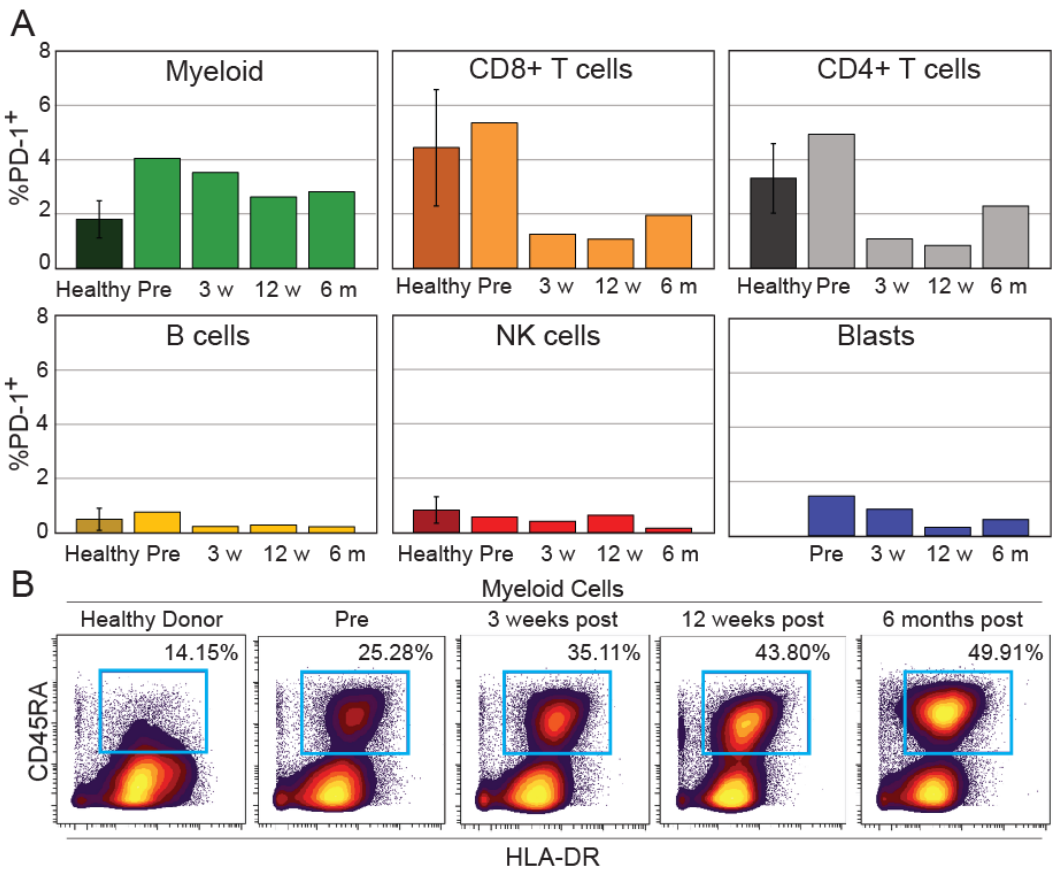

Figure 4.3. An increased percent of PD-1 positive monocytes was seen in the patient over the course of therapy. A) The percentage of PD-1^{pos} cells was determined for blasts, CD8 T cells, CD4 T cells, myeloid cells, NK cells, and B cells. For healthy, n=5. B) Biaxial plots show the increase of activated monocytes through dual expression of CD45RA and HLA-DR on non-lymphoid cells from a healthy donor and from the patient over the course of anti-PD-1 therapy.

Blast Phenotype Was Significantly Altered After Three Weeks of anti-PD-1 Therapy

To assess phenotypic change of the blasts over the course of anti-PD-1 therapy, blast cells from each time point were gated based on immunophenotype and analyzed in a single viSNE plot (Figure 4.4A). viSNE approximates high dimensional relationships using a two dimensional (2D) scatter plot, or map, where each dot represents a single cell (*231*). Cells close together on a viSNE map are phenotypically similar across all parameters used to make the map. Gates were used to assess the percentage of cells in the densest regions of the viSNE map and the fold change in population frequency was compared over therapy (Figure 4.4B). Pre-therapy, blasts

fell mostly within population 1, defined by high expression of HLA-DR, CD33, CD38, CD43, and CD44 and intermediate expression of CD45RA. By 6 months post-start of therapy the cells had shifted phenotype and largely fell into population 7, defined by expression of CXCR3 in addition to the phenotypic characteristics of population 1. Each population was distinguished by key phenotypic differences (Figure 4.4C).Populations 3 and 5 were distinguished by a lack of HLA-DR and CD33 expression along with high expression of the T cell costimulatory molecule CD28 and the chemokine trafficking marker CXCR3, respectively. Additionally, population 6 expressed both myeloid markers (HLA-DR and CD33) and neural cell adhesion molecule (NCAM/CD56), a marker expressed on NK and neural lineage cells, as well blasts in MDS and AML (*304*).

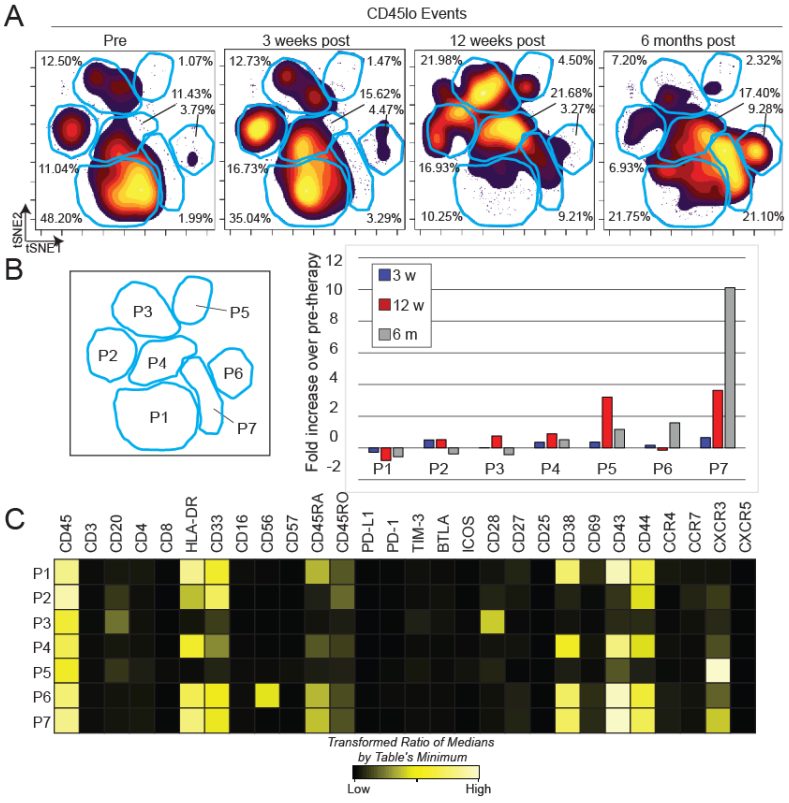

Figure 4.4. Peripheral blast phenotype shifts dramatically over the course of anti-PD-1 therapy. A) CD45lo events from the patient were gated and used to create a viSNE map. Blue gates identify major islands of cell density over all four time points. Each population denoted by the letter P followed by a number. B) Increase in cell density within each population (P, right) is shown as fold change over percentage of cells within sectors from the pre-therapy sample (left). C) A heatmap displays intensities of 28 measured proteins for each population identified on the viSNE map. Intensity is shown as heat, calculated as a transformed ratio of medians by the table's minimum.

Discussion

We report here a case study of a patient who experienced progression of MDS while undergoing anti-PD-1 therapy for advanced melanoma. Subclinical MDS was detected by mass cytometry prior to treatment and blasts became clinically apparent and progressed during treatment. Given the importance of the immune checkpoint inhibitor treatment class for melanoma and other malignancies and the unexpected nature of the emergence and progression of MDS, we described the clinical features and immune evolution of this case. As anti-PD-1 directed therapies are expected to be approved and tested in numerous malignancies, it is important to explore cellular response profiles of the immune system as a whole. When paired with unsupervised computational analysis tools (*231*), mass cytometry provides a complete platform for immune monitoring that effectively addresses the heterogeneity and complexity of primary tissue biopsies by revealing and characterizing known and novel cell populations.

In this case study, a population of myeloid peripheral blasts became apparent and was readily detected by both computational and human expert analysis. Both complete blood counts and mass cytometry were able to identify these cells, ranging from approximately 1% to 5% of PBMC. Of interest, while no peripheral blasts were identified prior to treatment on clinical analysis, a clear population was detected by mass cytometry. Lymphocytes decreased while myeloid cells increased, indicative of disrupted hematopoiesis. Additionally, mass cytometry effectively characterized PD-1 and PD-L1 expression on all major peripheral blood immune subsets. Phenotypes of immune cells and blasts were tracked over the course of therapy, revealing an increase in PD-1^{pos} monocytes and the emergence of a CXCR3^{pos} blast population, respectively. This phenotypic evolution of peripheral blasts may be shaped by the presence of anti-PD-1, or may simply reflect the natural history of MDS.

Peripheral blasts were largely negative for PD-1 and PD-L1 protein expression underscoring the premise that if anti-PD-1 is used to treat MDS or myeloid leukemia in the future, additional treatments may be needed to augment therapy in cases where a PD-L1 negative peripheral blast population is present (*305*). Notably, the frequency of PD-1 positive T cells decreased following anti-PD-1 treatment, perhaps due to receptor occupation by pembrolizumab or their accumulation in tumors. The presence of myeloid blasts may alter the outcome of immune checkpoint inhibitors for PD-1 expressing T cells.

In this case, it is unclear whether pembrolizumab contributed to MDS progression. Increasingly, the role of the immune system in the development and progression of MDS is being elucidated. Recent data shows that inflammatory cytokines and Th17-cell subsets are predominant in low risk disease, but in high risk MDS (as in our patient) regulatory subsets begin to dominate, giving rise to an overall suppressive immune microenvironment (*306, 307*). Furthermore, myeloid-derived suppressor cells (MDSCs) and associated suppressive cytokines TGF-β and IL-10 have been found at increased levels in MDS bone marrow and may promote progression of disease and suppress normal hematopoiesis through immune suppression and dysregulation (*308*). From these data, it is clear that multiple immune regulatory processes are involved in advanced MDS and rescue of exhausted T-cells through PD-1 blockade may only solve part of the problem. Perhaps inhibition of the MDSCs or cytokine responses could serve as a synergistic approach together with PD-1 blockade.

This patient is the second reported case of the development and progression of MDS while undergoing anti-PD-1 therapy (*309*). Interestingly, the other reported case occurred in a patient with Hodgkin lymphoma who had received multiple prior chemotherapies. Our patient had also received both chemotherapy and radiation therapy. Although MDS was likely precipitated by these other risk factors, anti-PD-1 may have contributed to disease progression in her case, and should be a consideration in other high-risk patients exposed to anti-PD-1 therapy.

This case study highlights both the complexity of immune monitoring in the context of cancer treatment and the power of high dimensional tools to provide a comprehensive and minimally biased view of dynamic cellular systems. It is clear that high dimensional immune monitoring will be of significant value in cases where immune checkpoint inhibitors are used in the context of MDS, myeloid leukemia, or other myeloid bone marrow failure syndromes. These results also underscore the critical need to characterize mechanisms of response to immune checkpoint inhibitors, as these mechanisms may depend greatly on the disease context in which they are applied.

Chapter V

CHARACTERIZING CELL SUBSETS IN HETEROGENOUS TISSUES USING MARKER ENRICHMENT MODELING

Authors: K. E. Diggins, A. R. Greenplate, N. Leelatian, C. E. Wogsland, and J. M. Irish

This work is adapted from a manuscript published in *Nature Methods* (Diggins, et al. 2017)

Introduction

Quantitative cytometry workflows have developed diverse approaches to grouping cells into populations and visualizing results in graphs that arrange populations based on phenotype (*207, 310*). Important features of populations are typically assumed to be those most highly or differentially expressed. This approach works well when feature variability is low and cells match established types, but computational analysis of single cell data routinely reveals novel cells with non-canonical phenotypes (*219, 311, 312*). This is especially common in diseases where abnormal expression profiles and signaling responses distinguish clinically significant cell subsets (*272, 313-316*). Existing statistical approaches can be used to characterize a population's degree of difference from a reference, but may be limited to a normal distribution or may not account for intra- and inter-population variability in a single metric.

The MEM equation (Eq. 1) produces a signed value for each population feature by quantifying positive and negative, population-specific, contextual feature enrichment relative to a reference cell population (Supplementary Note 1).

MEM score = $|MAG_{POP} - MAG_{REF}| + \left(\frac{IQR_{REF}}{IQR_{POP}}\right) - 1$, ($MAG_{POP}$-$MAG_{REF}$) <0 → MEM = -MEM

(Eq. 1)

In Eq. 1, POP denotes the population of interest, REF denotes the reference population to which POP will be compared, MAG is feature magnitude (here, median protein expression detected by mass or fluorescence flow cytometry), and IQR indicates the interquartile range. A reference population (REF) is chosen based on a biological comparison of interest (Supplementary Figure 5.1). MEM was designed to quantify enrichment, whereas other metrics used in cytometry, such as Kolmogorov-Smirnov (K-S)(*317*), area under the ROC curve (AUC)(*318*), and Earth Mover's Distance (EMD) (*319*), capture other differences between frequency distributions. In datasets including healthy human blood, bone marrow, and tonsil, murine tissues, and human tumors, MEM identified key proteins used by experts to distinguish rare and novel cell subsets.

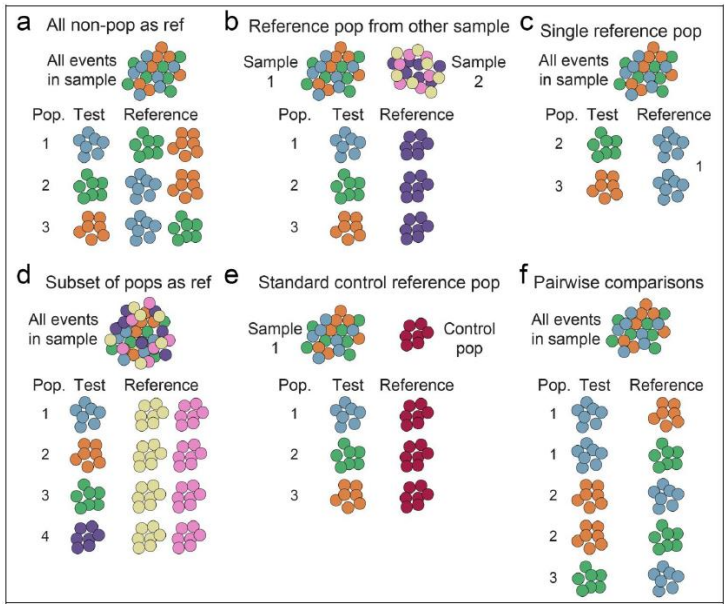

Supplementary Figure 5.1. Examples of MEM reference population selection to capture different contexts. Alternative reference populations (REF) can be used to capture how features of the test population (POP) are enriched in different contexts. Reference comparisons include a) all non-population cells in the sample or experiment (default), b) a population from another sample in the same study, c) a population from the same sample, d) multiple subsets of non-population cells from the same sample, e) a standard control population, and f) pairwise comparison between all populations in a sample.

Results and Discussion

Four cytometry studies, Dataset A (*320*), Dataset B(*9*), Dataset C(*219*), and Dataset D, collected as described by Leelatian and Doxie, et al.(*321*), were used to evaluate the ability of MEM to

identify biological features of expert and machine identified cell subsets. For datasets A, B, and C, populations had been previously identified by experts and by computational tools including viSNE(*231*) and SPADE(*210*), which are used in mass cytometry for dimensionality reduction and cell clustering(*207*), respectively.

Dataset A was mass cytometry data quantifying expression of 25 proteins on healthy human peripheral blood mononuclear cells (PBMC) (*320*). This dataset was chosen for two reasons: 1) the 7 cell subsets present are well-established, phenotypically distinct populations that served as a gold standard of biological 'truth' and 2) the cells in each of the 7 subsets were characterized for 25 proteins that displayed varying homogeneous and heterogeneous expression patterns. Populations were expert gated following viSNE analysis and each population was compared to the other cells in the sample (Figure 5.1). MEM returned labels that matched prior expert analysis(*320*) and correctly assigned high positive enrichment values to canonical protein features of each subset (Figure 5.1b), including CD4 on $CD4^+$ T cells (▲$CD4^{+6}$ $CD3^{+5}$ ▼$CD8a^{-4}$ $CD16^{-3}$), IgM on IgM^+ B cells (▲MHC II^{+8} IgM^{+6} $CD19^{+5}$ ▼$CD4^{-6}$ $CD3^{-5}$), CD11c and MHC II on monocytes (▲$CD11c^{+8}$ $CD33^{+7}$ $CD14^{+6}$ $CD61^{+6}$ MHC II^{+4} $CD44^{+3}$ ▼$CD3^{-5}$ $CD4^{-4}$), and CD16 on NK cells (▲$CD16^{+9}$ $CD56^{+2}$ $CD11c^{+2}$ ▼$CD4^{-7}$ $CD3^{-4}$ $CD44^{-3}$). Proteins that were not significantly enriched on any of the 7 subsets of mature human blood mononuclear cells were correctly assigned near-zero MEM scores (e.g. CD34 and CD117 proteins expressed on hematopoietic stem cells, Figure 5.1b). Similarly, proteins with little variability across cell subsets were assigned low, near-zero MEM scores, even for highly expressed proteins (e.g. CD45 on all subsets, CD45RA on non-T cells, Figure 5.1b). Incorporating information about feature variability allowed MEM to capture negative enrichment that was not reflected in magnitude difference (MAG_{DIFF}). Highly enriched proteins were more

important to accurate population identification than proteins characterized by high median expression alone (Figure 5.1c; Supplementary Figure 5.2).

To test the hypothesis that features with high MEM scores would be important for computational cluster formation, the 25 proteins measured in Dataset A (Figure 5.1b) were sorted in six ways: 1) high to low MEM score, 2) high to low median value, 3) high to low MAG_{DIFF}, 4) high to low z-score, 5) high to low K-S statistic, and 6) randomly (Supplementary Table 3). Z-score and K-S statistic values are shown in Supplementary Table 4. The proteins were then sequentially, cumulatively excluded from use in k-means clustering and f-measure was calculated to measure clustering accuracy (Figure 5.1c and Supplementary Figure 5.2). Random exclusion was performed 15 times and the average result is shown (Figure 5.1c). Clustering accuracy was

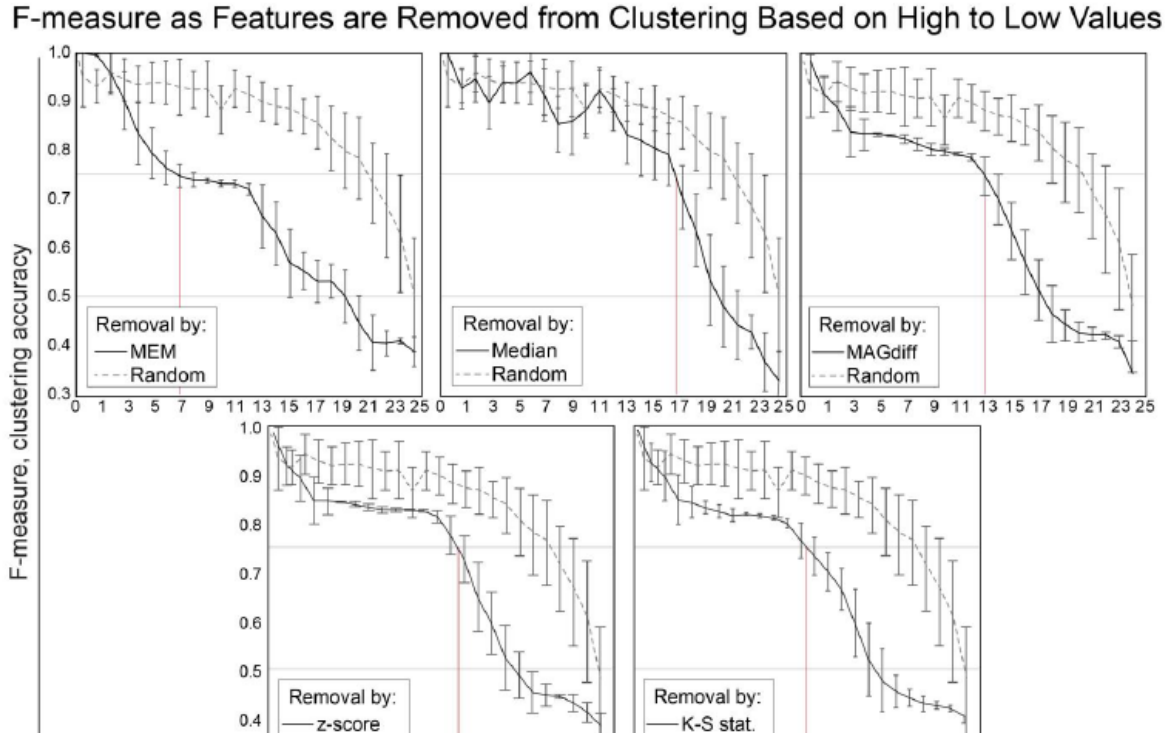

Supplementary Figure 5.2. MEM highly scores markers that are important to clustering accuracy. Markers were sequentially and cumulatively excluded from k-means cluster analysis of Dataset A, from high to low, sorted based on 5 different statistics or scores (marker order shown in Supplementary Table 3): MEM, median, median difference (MAGDIFF), z-score, and Kolmogorov-Smirnov (K-S) statistic. Clustering accuracy was quantified as the f-measure where true cluster identity was assumed to be the clusters formed by clustering on all 25 markers in the dataset. The moving average of the f-measure is shown. Error bars represent the standard error. The vertical red line indicates the number of excluded features at which the f-measure reached 0.75.

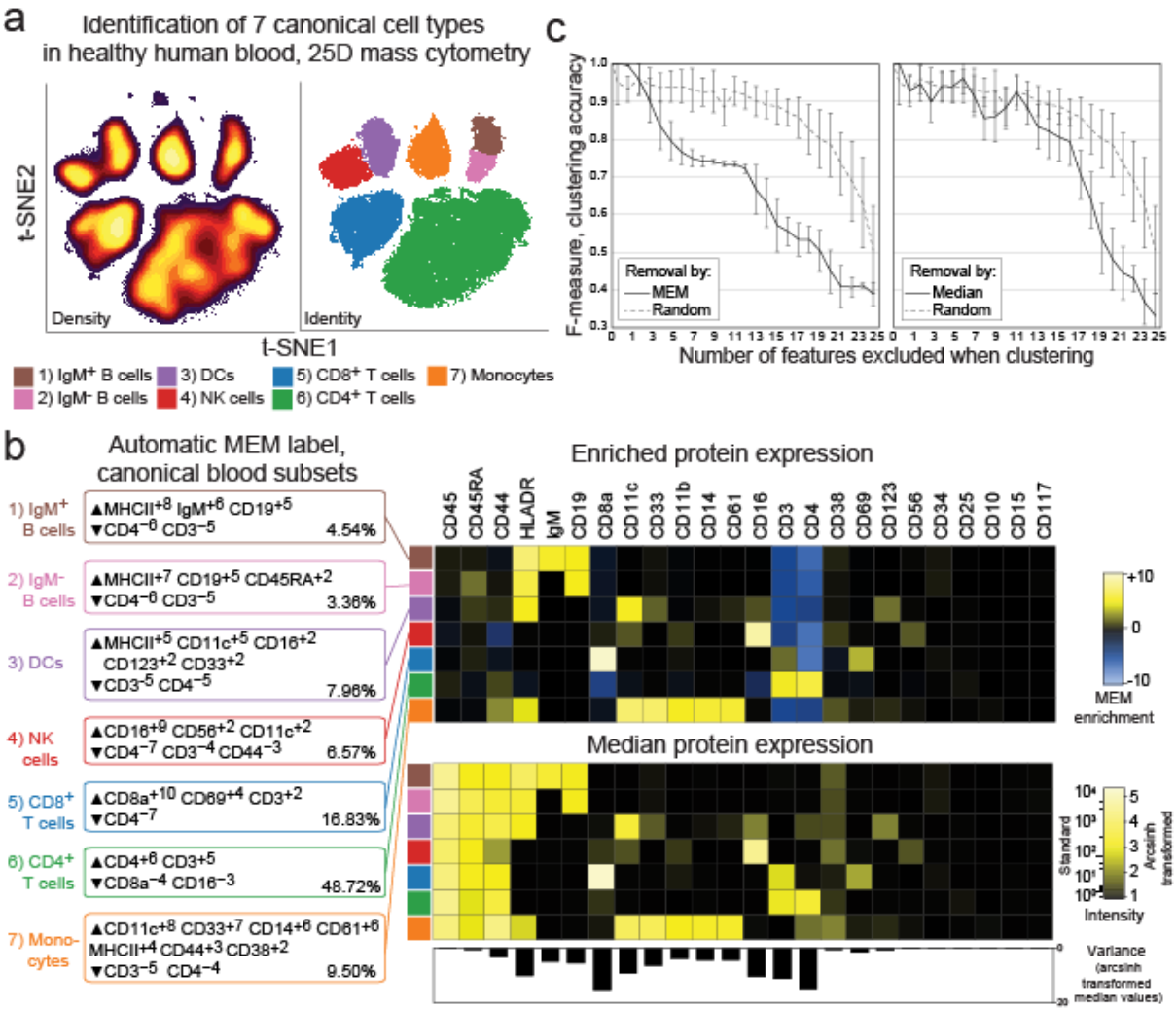

Figure 5.1: Marker enrichment modeling (MEM) automatically labels human blood cell populations in Dataset A. a) Cells from normal human blood grouped into 7 canonical populations using viSNE analysis and expert review of 25D mass cytometry data. b) MEM labels computationally generated for each canonical cell subset. Heatmaps show protein enrichment values used to generate MEM labels and the median protein expression values for each protein on each cell subset. Variability in protein expression across the 7 canonical cell populations is shown below to highlight proteins that were expressed homogeneously (low variability, e.g. CD45) and those that were expressed heterogeneously (high variability, e.g. CD8a, CD4). c) Graphs show decreasing f-measure (clustering accuracy) as markers were excluded from k-means cluster analysis based on high to low absolute MEM or median values, compared to random exclusion.

most impacted by excluding proteins based on MEM score. F-measure dropped to 0.75 after removing the proteins with the top 6 MEM scores, whereas a comparable F-measure decrease was only observed after removing the 14 highest markers based on MAG_{DIFF}, the 13 highest markers based on z-score, and the 12 highest markers based on K-S statistic values

(Supplementary Figure 5.2). Removing markers based on median was not significantly different from removing markers randomly until the 15 markers with the highest median signal intensity were excluded (Supplementary Figure 5.2). The same analysis was performed with viSNE in place of k-means clustering to visualize loss of population resolution (Supplementary Figure 5.3c). In this case, loss of accuracy was reflected in the viSNE map as a loss of separation between "islands" of cells. These results indicated that MEM enrichment scores captured markers that were important to cell identity better than traditional comparisons based solely on median protein expression.

Dataset B was mass cytometry data quantifying expression of 31 proteins on healthy human bone marrow (*9*). Computational and expert analysis had previously identified 23 populations of cells that were analyzed here by MEM (Supplementary Note 3). For example, the cell subset labeled as HSCs was highly enriched for CD34 ($CD34^{+6}$) and negatively enriched for CD45 ($CD45^{-5}$). Dataset B also illustrated the general rule that MEM scores will approach median values as feature variability within populations decreases (Supplementary Figure 5.4). MEM

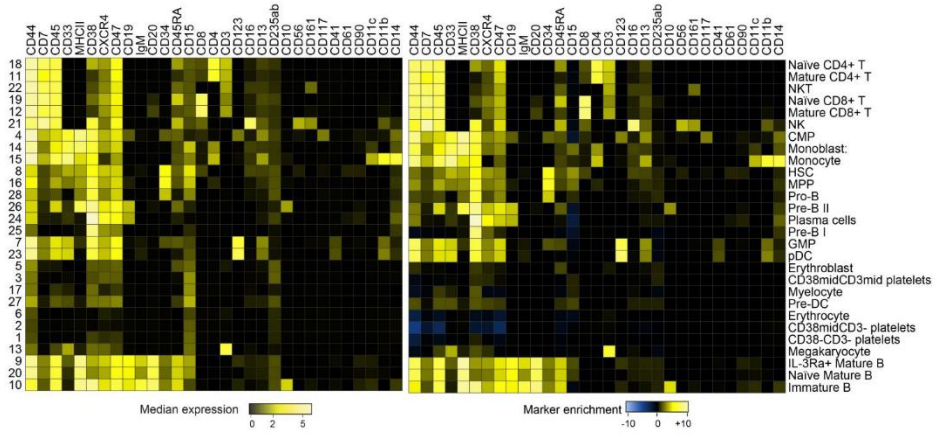

Supplementary Figure 5.4. MEM scores largely reflect median expression values for relatively homogenous populations. Heatmaps show median intensity of protein expression (left) and protein enrichment by MEM (right) for measured proteins in 28 populations characterized as relatively homogeneous for established cell types by expert analysis (rows). Each population was compared to the other 27 subsets for the MEM analysis. MEM scores approach median expression values in homogeneous populations because the contribution of variance approaches zero.

captured feature enrichment and heterogeneity better than median in diverse populations, as in Figure 5.1c.

Dataset C was mass cytometry data quantifying expression of 38 proteins on murine cells from eight tissues(*219*) (Supplementary Note 4). In this dataset, "cluster 28" was a novel population identified as CD11b^{int} NK cells. The MEM label for cluster 28 within ILCs was ▲CD11b^{+5} CD62L^{+3} ▼CD4^{-7} CD103^{-4} Terr119^{-3} (Supplementary Figure 5.5). This MEM label captured the key feature of this novel innate lymphoid cell subset (CD11b^{int}) and highlighted additional features that can be used to match this subset to cells identified by others (i.e., to cytotype the population). These results indicate that MEM labels complement unbiased population discovery and effectively characterize *cyto incognito*(*208*) by providing unbiased descriptions that correctly capture key features of novel cell types.

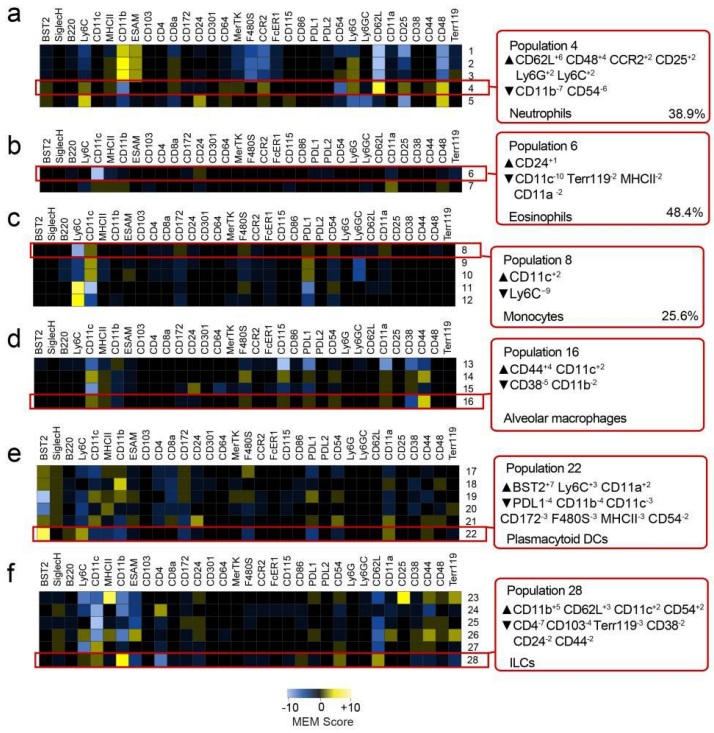

Supplementary Figure 5.5. Focused MEM analysis quantifies feature enrichment within phenotypically similar groups of cells. a-f) Focused MEM analysis on murine myeloid cell subsets. A MEM label for one population within each group is shown as an example. Groups were defined as the 6 major murine subgroups identified by t-SNE and DensVM by Becher et al.

An important aspect of MEM is generation of machine-readable quantitative labels that can be used to register population identities across samples and studies. A MEM label for a newly discovered population can be compared quantitatively against a reference set of established MEM labels or a MEM label reported in a paper. To illustrate this idea, the pairwise, normalized root-mean-squared distance (RMSD) of MEM scores was calculated as a measure of similarity between 80 populations of cells from 7 different studies including healthy $CD4^+$ T cell and B cell (Figure 5.2). Cells had highly similar MEM scores within each major cell type, regardless of platform (mass or fluorescence flow cytometry), study, or tissue source. For example, T cells run on mass cytometry from different blood donors were 97% ± 1.3 similar to each other, 85% ± 1.9 similar to T cells from blood run on fluorescence flow cytometry, and 87% ± 2.1 similar to T cells from tonsil run on mass cytometry (Figure 5.2, Supplementary Table 5). However, these cells were 66.9% ± 13 similar to any B cell population. In addition to differentiating between subsets that are well known to be different, MEM is also able to distinguish the subtle differences between subsets that are known to have similar phenotype by median expression. To test the ability of MEM to differentiate between these types of cell subsets, a similarity score was calculated for T effector memory (T_{EM}), T central memory (T_{CM}), naïve T cells, and T effector memory cells that express RA (T_{EMRA}) (Figure 5.3). In this analysis, T_{CM} and T_{EM} formed a separate cluster, apart from naïve and T_{EMRA} cells. This indicates that MEM scores provide a way to communicate cell identity and to quantify similarities of cell types from the text label alone.

Dataset D included 52 populations of tumor infiltrating APCs, tumor infiltrating T cells, and non-immune malignant tumor cells identified in human glioma tumors (*321*). To obtain these populations, each tumor was analyzed by viSNE and cell subsets were expert gated solely on t-SNE cluster density. To determine whether MEM could distinguish immune cell subsets from other tumor cell types with limited information, MEM scores were calculated using only 9 markers that were expected to be expressed on cancer cells (S100B, TUJ1, GFAP, Nestin, MET,

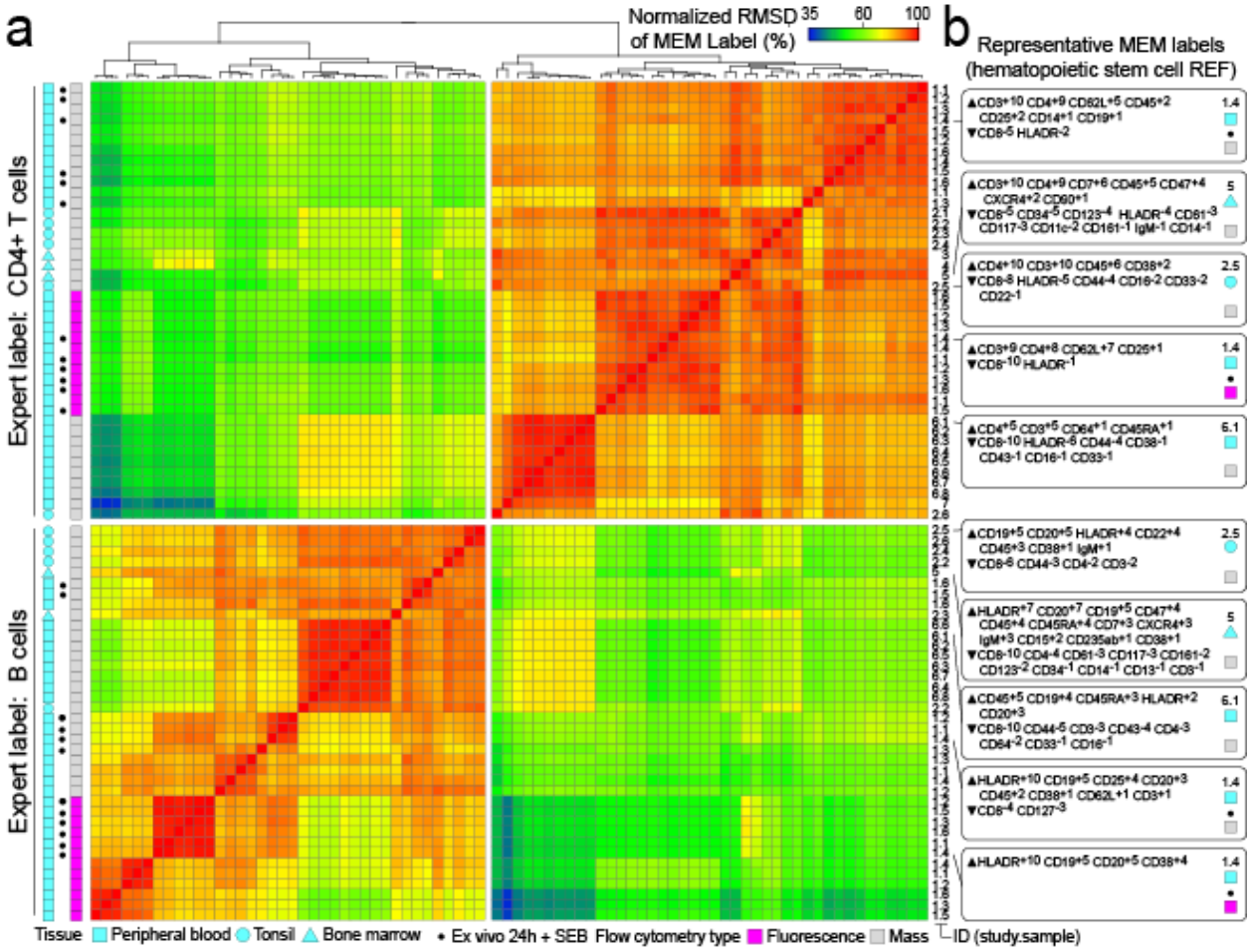

Figure 5.2. Hierarchical clustering based solely on MEM **label groups T cells and B cells measured in diverse studies using different cytometry platforms.** A) MEM label values were compared for each of 80 populations (CD4+ T cells and B cells) from 3 human tissues representing 6 mass cytometry studies and 1 fluorescence flow cytometry study. Populations are shown clustered according to MEM label percent similarity. Tissue type, source study (numbered 1-7 and referenced in online methods), and individual sample IDs are indicated to the right. *indicates samples stimulated by bacterial superantigen *Staphlococcus* enterotoxin B (SEB). B) Representative MEM labels for CD4+ T cells (top) and B cells (bottom) from SEB-stimulated normal human blood (1.4, top, mass cytometry), normal human bone marrow (5, mass cytometry), normal human tonsil (2.5, mass cytometry), SEB-stimulated normal human blood (1.4, bottom, fluorescence flow cytometry), and normal human blood (6.1, mass cytometry).

PDGFRα, EGFR, HLA-DR, and CD44, Figure 5.4a). The 52 populations were grouped into 13 major cell types based on MEM enrichment of 9 analyzed proteins, and these groups were interpreted as tumor infiltrating APCs (Figure 5.4b, blue), tumor infiltrating T cells (Figure 5.4b, green), or non-immune tumor cells (Figure 5.4b, red). To confirm cell identity, four protein features that had been excluded from MEM analysis were assessed (Figure 5.4c, CD45, CD3, CD45RO,

and CD64). CD45 and CD3 were used to confirm T cell identity and CD45 and CD64 were used to confirm APC identity. MEM correctly identified both immune cell subsets from all tumor types without using key immune lineage markers and without using healthy populations (e.g. APCs from blood or tonsil) to guide the clustering. Thus, MEM labels distinguished populations of cells based on non-traditional features and in a disease context.

MEM labels provided a quantitative language to objectively communicate characteristics of new and established cell types observed in complex tissue microenvironments. Algorithmic comparison of MEM labels correctly identified 80 cell populations from 7 studies of 3 human tissues measured using different instrumentation and distinguished tumor-infiltrating immune cell subsets and malignant cell populations from human glioma tumors. Following additional validation in other cell types, tissues, and instrumentation platforms, it may be possible for machines and humans to use MEM labels to learn and clearly communicate cell identity (cytotype). Given widespread adoption and reporting, MEM labels could be used to communicate

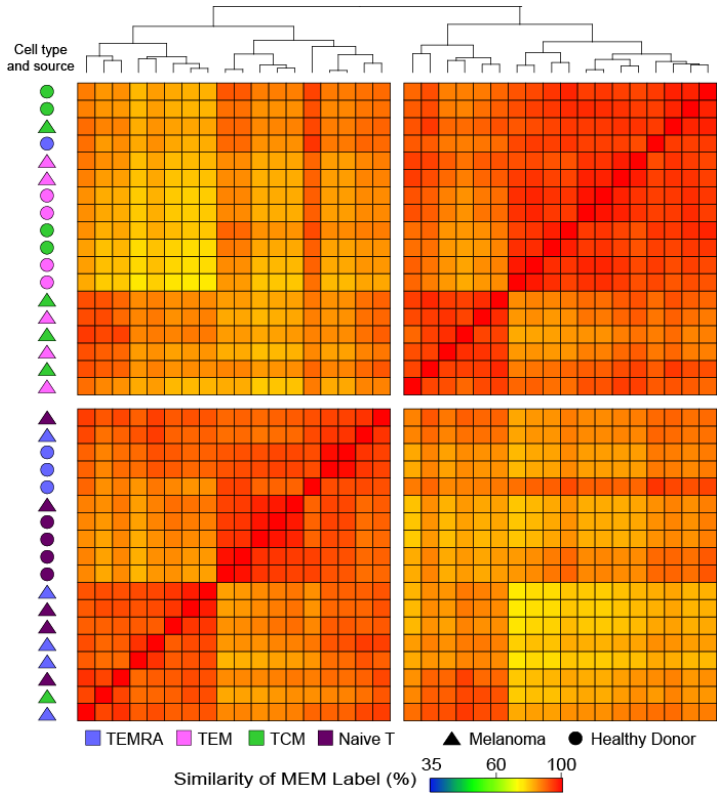

Figure 5.3. Hierarchical clustering based solely on MEM **label groups T cell subsets characterized by mass cytometry.** MEM label values were compared for each of 36 populations from 2 human tissues, healthy donor peripheral blood and melanoma tumor. Populations are shown clustered according to MEM label percent similarity. Tissue type, and individual population IDs are indicated to the left.

cytotypes in a manner analogous to cluster of differentiation (CD) naming of antigen targets of antibodies (*322*). MEM can compare populations against a common reference (Supplementary Note 5) and guide feature selection for computational and experimental analysis. MEM can also be used to monitor changes in tissues over time during treatment. Deviation from a stable MEM score for peripheral blood cell subsets would be expected in the case of emerging malignant cells (*315*), and lack of change towards a healthy set of MEM scores for blood or bone marrow cell subsets might indicate a lack of response to chemotherapy for a leukemia patient. MEM is expected to assist in machine learning applications by providing quantitative text descriptions of cytotype that can be algorithmically parsed and used to classify newly identified cell subpopulations.

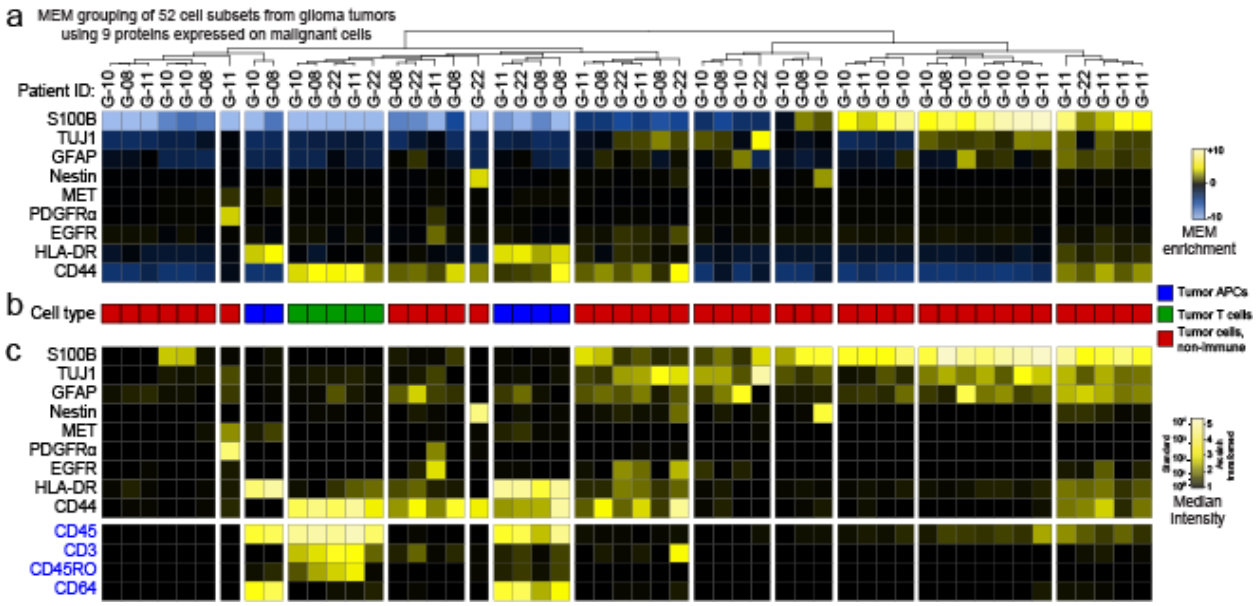

Figure 5.4. MEM correctly grouped immune and cancer cell populations from glioma tumors using nine proteins expressed on cancer cells in Dataset D. (A) A heatmap of MEM enrichment scores is shown for 52 populations of cells identified in tumors from 4 glioblastoma patients (G-08, G-10, G-11, G22) in an unsupervised manner using viSNE. (B) Each population was annotated for a cell type based on review of the MEM label and classified as tumor infiltrating APCs (blue), tumor infiltrating T cells (green), or non-immune tumor cells (red). (C) A heatmap of median intensity values is shown for the 13 measured proteins from each of the 52 tumor cell populations.

Materials and Methods

Data Availability Statement

The normal human PBMC dataset (Figure 5.1) were generated by CyTOF analysis as described by Leelatian, et al.(*320*) and is available as an FCS file in Flow Repository (https://flowrepository.org/experiments/1043).

The normal human bone marrow data set from Bendall and Simonds, et al(*9*) (Dataset B) was downloaded from Cytobank (*229*) as FCS files that included the cell population IDs defined by Bendall and Simonds, et al.(*9*) (https://reports.cytobank.org/1/v1). MEM enrichment scores from Dataset B were compared to the authors' analysis and prior studies of proteins marking stem cells, progenitor cells, and mature cells (*323, 324*)

The murine myeloid CyTOF dataset from Becher, et al(*219*) (Dataset C, Supplementary Note 4) was downloaded from Cytobank as FCS files that contained gated cell events and cluster IDs as designated by automated analysis conducted by Becher et al(*219*). MEM enrichment scores from Dataset C were compared to the authors' analysis and prior studies of neutrophils (*325, 326*).

Datasets for Figure 2 were generated in 7 separate fluorescence and mass cytometry studies by 1) Nicholas et al. (*327*), 2) Polikowsky et al.(*223*), 3) Ferrell et al. (*328*), 4) Amir et al.(*231*), 5) Bendall and Simonds et al.(*9*), 6) Greenplate et al., previously unpublished data, and 7) Leelatian et al (*320*).

The phospho-flow AML data set generated by Irish et al.(*313*) (Supplementary Note 5-Fig.2) was downloaded from Cytobank as FCS files.

The human GBM mass cytometry dataset (Figure 5.3) was generated and analyzed as described by Leelatian and Doxie et al.(*321*) and are available on Flow Repository as text files (https://flowrepository.org/experiments/1044/).

Code Availability

Software for generating MEM scores is available as Supplementary Software.

CyTOF data pre-processing and analysis

Data analysis was performed using the online analysis platform Cytobank(*229*) and the statistical programming environment R. Raw median intensity (MI) values were transformed to a hyperbolic arcsine scale. A cofactor of 15 was used for the PBMC dataset (Figure 5.1), and 5 was used for the normal human bone marrow data set and for the murine myeloid data set. Single, intact cells were gated based on cell length (30-60) and nucleic acid intercalator (iridium). Major PBMC subsets were gated based on CD45 expression (leukocytes) and on canonical lineage marker expression to identify major blood cell subsets.

FCS files were exported from Cytobank as FCS or tab-delimited text files that were parsed for expression intensity information using the R package flowCore (*329*). MEM was calculated using the arcsinh transformed MI values, as described above. Heatmaps were generated using the heatmap.2 function in the gplots R package(*330*).

Fluorescence Phospho-Flow AML Data Analysis

Data were downloaded from Cytobank as FCS files and processed in R as described above. MFI values were transformed to a log normal scale. For each AML patient, a median value and an IQR value was calculated for each marker in the unstimulated condition and for the stimulated conditions. The unstimulated median values were subtracted from the stimulated median values, and likewise for the IQR values. MEM was then calculated by comparing each

patient's subtracted median and IQR values to those of the other patients. This enabled a comparison of fold change signaling values rather than raw values.

Marker Enrichment Modeling (MEM)

MEM analysis begins after populations have been identified and aims to provide a simple way to compare findings from experts working with different platforms or performing analysis using different computational tools for population discovery (*210, 331-334*) and graphical visualization (*9, 200, 313, 314, 335*). These tools have differing strengths that depend greatly on the structure of the datasets and controls, the biological goals of the study, and the quality of the existing knowledge in the field (*207, 216, 310*).

MEM equation

The MEM equation is implemented as an R package (Supplementary Software). Currently, MEM uses medians as the magnitude value; however, depending on the data type, mean may be a more appropriate magnitude statistic and mean could be substituted for median in the equation. Similarly, other statistics, such as variance, might be substituted for IQR. The MEM equation was developed with the intention of capturing and quantifying population-specific feature enrichment in a simple equation that avoids over-fitting or unnecessary computation. The primary goal of this equation is to scale magnitude differences depending on distribution spread. While other distribution features such as skew or shape could be informative, incorporating only two pieces of information – magnitude and spread – into the equation captured enough information to be useful in quantifying both positive and negative population-specific feature enrichment.

MEM output and score scaling

The MEM R script outputs a heatmap of MEM values with a text label summary of feature enrichment as the population (row) names. The + or - value provided along with the marker name

is converted to a -10 to +10 scale and rounded to the nearest integer. As implemented here, the maximum of the scale was set using the highest absolute value MEM score observed across all markers and populations. All values in the matrix are divided by this maximum value and multiplied by 10 to achieve the -10 to +10 scaling. After scaling, the original sign value is reapplied to each MEM score. Scaling the output this way is intended to generate MEM values and labels that are intuitive to human readers and to facilitate comparison of feature enrichment across experiments, samples, batches, time points, and data types.

IQR Threshold

Because MEM uses a ratio of IQR values, near zero values in the denominator, IQR_{POP}, will greatly increase MEM scores. For each measurement type, it is important to identify a minimum significant IQR value so that small IQR values below the platform's ability to distinguish signal from noise do not inappropriately increase MEM scores. To automatically determine a minimum threshold for IQR_{POP}, the algorithm here calculated the average of the IQR values that were associated with the lowest quartile of population and reference medians. For the mass and fluorescence cytometry datasets used, the automatically calculated IQR threshold was on average 0.5 ± X and so the IQR threshold for all studies here was set to 0.5. The default IQR threshold in the algorithm is also set to 0.5. To have the IQR threshold re-calculated, investigators should specify the "auto" option for the IQR.thresh argument in the MEM function. It is recommended that investigators applying MEM to datasets from different instruments or who are testing MEM for the first time determine whether a change in the IQR threshold is needed.

Reference population selection

MEM scores are contextual; a population's MEM score depends on the reference population(s) to which it is compared. Selection of a reference population should be made deliberately depending on the biological question being addressed. When populations in a MEM analysis arise

from different experimental sources, it may be necessary in some cases to normalize measurements prior to MEM analysis to avoid artifacts from experimental variation.

PBMC processing and mass cytometry

PBMC were isolated and cryopreserved as described by Greenplate, et al(*312*). PBMC were stained with metal conjugated antibodies and prepared for the mass cytometry as previously described (*312*). The following antibodies were used in the staining panel: CD19-142, CCR5-144, CD4-145, CD64-146, CD20-147, CCR4-149, CD43-150, CD14-151, TCRγδ-152, CD45RA-153, CD45-154, CXCR3-156, CD33-158, CCR7-159, CD28-169, CD29-162, CD45RO-164, CD16-165, CD44-166, CD27-167, CD8-168, CD25-169, CD3-170, CD57-172, PD-L1-175, and CD56-176 (Fluidigm Sciences). In addition, the following purified antibodies from Biolegend were labeled using MaxPar DN3 kits (Fludigm Sciences), stored at 4°C in antibody stabilization buffer (Candor Bioscience GmbH) and used in the same panel: ICOS-141, TIM-143, CD38-148, CD32-161, HLA-DR-163, CXCR5-171, and PD-1-174.

Cell subpopulation MEM Score Similarity Calculations

Comparison of $CD4^+$ T cells to B cells in Figure 2

In order to assess the robustness of MEM across tissue sample types, donors, experimental runs, and flow cytometry platforms (fluorescence and mass cytometry), MEM scores were calculated for cell subsets from 7 different experiments that included 3 healthy human bone marrow samples(*9, 231, 328*), 9 healthy human PBMC samples(*320, 327*), and 6 healthy human tonsil samples(*223*). MEM scores were calculated for each population using as the reference population a combination of hematopoietic stem cells gated as $CD34^+$ $CD38^{lo/-}$ from two studies of healthy human bone marrow (*9, 328*). Population similarity was calculated using root mean squared distance (RMSD) calculated on all population MEM scores in a pairwise fashion. MEM scores were calculated using all markers in common between each dataset and the HSC reference.

RMSD was calculated here as the square root of the average in squared distance between all MEM values in common for each pair of populations and then converted into percent maximum possible RMSD. Given the -10 to 10 MEM scale, an RMSD of 20 was the maximum possible difference and corresponded to 0% similarity, whereas an RMSD of 0 between MEM labels indicated 100% similarity. This approach emphasized differences in marker expression when comparing populations. Calculated statistics for $CD4^+$ T cell comparisons included average MEM value +/- standard deviation and p-value calculated using an unpaired, two-tailed Student's t-test.

Human Glioma and Normal Immune Cell MEM Analysis

Glioblastoma data (G-08, G-10, G-11, and G-22) were collected following a published protocol (*321*). Cells were stained with isotope-tagged antibodies to detect surface and intracellular targets following established protocols (*321, 336*). MEM analysis of glioblastoma patient samples was performed with 9 markers (S100B, TUJ1, GFAP, Nestin, MET, PDGFRα, EGFR, HLA-DR, and CD44), using arcsinh transformation of original median intensity values with a cofactor of 5. Each cell subset was the POP, and the remaining cell subsets were the REF in the analysis.

Z-score and K-S statistic calculations

Z-score was calculated between POP and REF as (MEANpop-MEANref)/STDEVref for each marker.

The K-S statistic(*317, 337*) was calculated comparing the distribution for each marker on POP and REF using the function ks.test() in R.

F-measure Analysis

PBMC populations were defined by expert human gating on canonical markers. For f-measure analysis (Figure 5.1c and Supplementary Figure 5.2), the 25 measured markers from the CyTOF analysis of healthy PBMC were sorted based on absolute MEM scores, median

values, median difference, z-score, and K-S statistic (shown in Supplementary Figure 5.2), or randomly across all PBMC populations and the 25 measured proteins. The 5x25 matrix was converted into an ordered vector (length 25X5) and then sorted by absolute value. The first occurrence of each marker in the list was kept and subsequent occurrences of that marker in the list (i.e. that marker's scores on other populations) were discarded. The order of markers excluded by MEM, median, median difference, z-score, and K-S statistic are shown in Supplementary Table 3. Markers were then sequentially, cumulatively excluded from k-means clustering of cells from high to low absolute for each statistic or score. F-measure was calculated as:

Sensitivity = True Positives/ (True Positives + False Negatives)

Specificity = True Negatives/ (True Negatives + False Positives)

F-measure = 2*(sensitivity*specificity)/ (sensitivity + specificity) An F-measure was calculated for each round of clustering, where truth was the cell cluster ID resulting from clustering on all 25 markers. The moving average of f-measure with an interval of 3 was calculated in Microsoft Excel. The F-measures for random marker exclusion are the average at each point of 15 different rounds of random marker exclusion from clustering.

Chapter VI

COMPUTATIONAL IMMUNE MONITORING REVEALS ABNORMAL DOUBLE NEGATIVE T CELLS PRESENT ACROSS HUMAN TUMOR TYPES

Authors: Allison R. Greenplate, Daniel D. McClanahan, Brian K. Oberholtzer, Deon B. Doxie, Caroline E. Roe, Kirsten E. Diggins, Nalin Leelatian, Megan L. Rasmussen, Mark C. Kelley, Vivian Gama, P. Brent Ferrell, Douglas B. Johnson, Jonathan M. Irish

Introduction

The immune system is a complex network of cells and tissue types, and it is increasingly important to simultaneously track cell subsets and understand the system as a whole. Longitudinal monitoring of changes in the immune system has provided insight into drug response and disease progression (*301, 312, 338*). Differences in response to perturbation can stratify clinical outcome (*316, 339*) and indicate mechanism of action (*340*). Challenges to the immune system, such as vaccination, infection, surgical intervention, or the emergence of a malignancy, can elicit detectable changes above the relatively stable basal state of each individual. Vaccination-induced immune remodeling has been shown to be acute and quickly followed by a return to the individual's basal "steady state" signature (*197, 341*). Cytomic approaches that can characterize all the cells in a system are an area of active development in immunology (*207, 208, 310*). A common framework for data analysis will allow researchers using these cytomic approaches to compare and contrast immune systems from diverse research areas, including tumor immunology and treatment response (*316, 342, 343*), blood cancer (*272, 313, 314, 328, 344*), bone marrow failure (*312, 345*), and human immune variation and autoimmunity (*197, 216, 301, 346, 347*).

Across these studies, four dynamic elements stand out as key features of cellular systems: 1) plasticity or stability of the system as a whole, 2) changes in abundance of known cell subsets, 3) emergence of unexpected features on cell subsets, and 4) emergence of novel or unexpected cell types. The central goal here was to simultaneously employ distinct tools focused on these different data types as an ensemble and to organize this copious information into an automated "first pass" analysis that could be easily interpretable by an immunologist and that would highlight cell subsets for in-depth review. Systematically monitoring the cells of the immune system and their features is especially powered when serial samples from an individual can be used as comparison points. However, this approach generates vast amounts of data. Simultaneously tracking entire systems and the parts that comprise them can become overwhelming in the context of clinical research, where cells of interest can be rare (*316, 342*) and where the entire system can change quickly in unanticipated ways (*312*). Thus, in cytomic, system-level studies, the data analysis strategy is as important as the experiment design (*207, 310, 316*), and it is vital to track known reference populations and place new observations in the context of prior knowledge (*335, 348*). Tools exist for visualizing and gating (*210, 231, 314, 334*), supervised population and biomarker analysis (*333, 349*), and describing cell population identity (*348*) within high dimensional data sets. In contrast, there is a great need for automated analysis for the steps immediately after population identification (gating). Tools for cellular clustering are especially numerous, specific for each data type, and have been extensively addressed in prior work (*350*). The components selected for the ensemble toolkit here included the Earth Mover's Distance algorithm (*319*), t-distributed stochastic neighbor embedding (t-SNE) (*231*), and Marker Enrichment Modeling (MEM) (*348*). The growth and success of high dimensional single cell technologies relies on ongoing development of data analysis tools needed to parse the large amounts of data and place results in context (*310, 335, 348*). It remains relatively rare for researchers to choose data analysis approaches that explicitly incorporate time or other changes.

To validate and challenge computational analysis tools it is valuable to explore immunology problems representing differing levels of prior knowledge, amounts of change, and abundances of target cell types. Here, the first challenge (Dataset 1) comprised data from melanoma patients undergoing anti-PD-1 therapy with pembrolizumab. Dataset 1 was chosen for the relevance of this therapeutic strategy and because the dataset includes an unusual case from a patient with a distinct, unexpected immune system trajectory (*312*). This example was chosen to include an important outlier case that should not be missed, but which is unusual enough that training datasets would not normally include an example of it. Dataset 2 comprised a previously published data set of peripheral blood from acute myeloid leukemia (AML) patients undergoing chemotherapy (*328*). Dataset 2 was chosen as an example of dynamic cellular populations shifting dramatically over therapy. This dataset was also included to represent the challenge of tracking and characterizing treatment-refractory leukemic blasts, which did not converge on a single phenotype and instead shifted into different phenotypic compartments, none of which matched the phenotype of healthy cells (*328*). Dataset 3 includes serial melanoma tumor biopsies from patients treated with dabrafenib, a $BRAF^{V600}$ inhibitor (BRAFi), and trametinib, a MEK inhibitor (MEKi). A challenge of Dataset 3 is to apply multiple tools in a system that is relatively less well studied and includes a diverse set of individuals and mass cytometry panels. By providing both high level and detailed views of cellular systems changing over time in human patients, the ensemble approach revealed new knowledge about immune system interactions in these three study types with contrasting changes and challenges.

Results

Earth Mover's Distance evaluated phenotypic plasticity in the peripheral immune system during therapy

To monitor the response of peripheral immune system to anti-PD-1 therapy (Dataset 1), blood was drawn from melanoma patients immediately prior to therapy, and 3 weeks, 12 weeks, and 6 months after the start of therapy. Mass cytometry was used to characterize peripheral blood mononuclear cells (PBMCs) from each patient at each time point (Tables S6.1 and S6.2). In order to monitor and quantify the phenotypic plasticity of the peripheral immune system as a whole, a workflow was developed in which the Earth Mover's Distance (EMD) algorithm was used to quantify differences between viSNE maps (*231, 319, 351*). One viSNE map was created for eight patients analyzed at four clinical timepoints and eight healthy controls (Figure 6.1A, Table S6.1). EMD was then used to quantify the differences between each viSNE map and the numerical results were displayed in a heat map (Figure 6.1B). Low EMD scores indicated that the maps were similar, whereas larger EMD scores indicated divergent maps. To determine whether the peripheral immune systems of each patient remained stable or had increased phenotypic plasticity over the course of anti-PD-1 therapy, intra-patient EMD values were compared to inter-patient EMD values. In 7 out of 8 melanoma patients receiving anti-PD-1 therapy, the intra-patient EMD score was lower than the inter-patient EMD score, indicating that each patient's peripheral blood immune system was more similar to itself than to that of any of any other patient, regardless of any ongoing therapy response (Figure 6.1C). The exceptional patient, MB-009, did not conform to this pattern (median intra-patient EMD value ± standard deviation, 4.22±2.69 v median inter-patient EMD value, 3.99±2.48). This patient was diagnosed with myeloid dysplastic syndrome 8 months after starting anti-PD-1 therapy and was known to have an expansion of mature and blasting myeloid cells and a decrease in all other major cell types in the periphery (*312*). For a detailed report of this patient, see Chapter IV. Thus, combining EMD and viSNE allowed for an automated approach to quantify stability and plasticity of a system over the course of therapy.

Ensemble analysis revealed decreases in PD-1$^+$ T cells during anti-PD-1 therapy

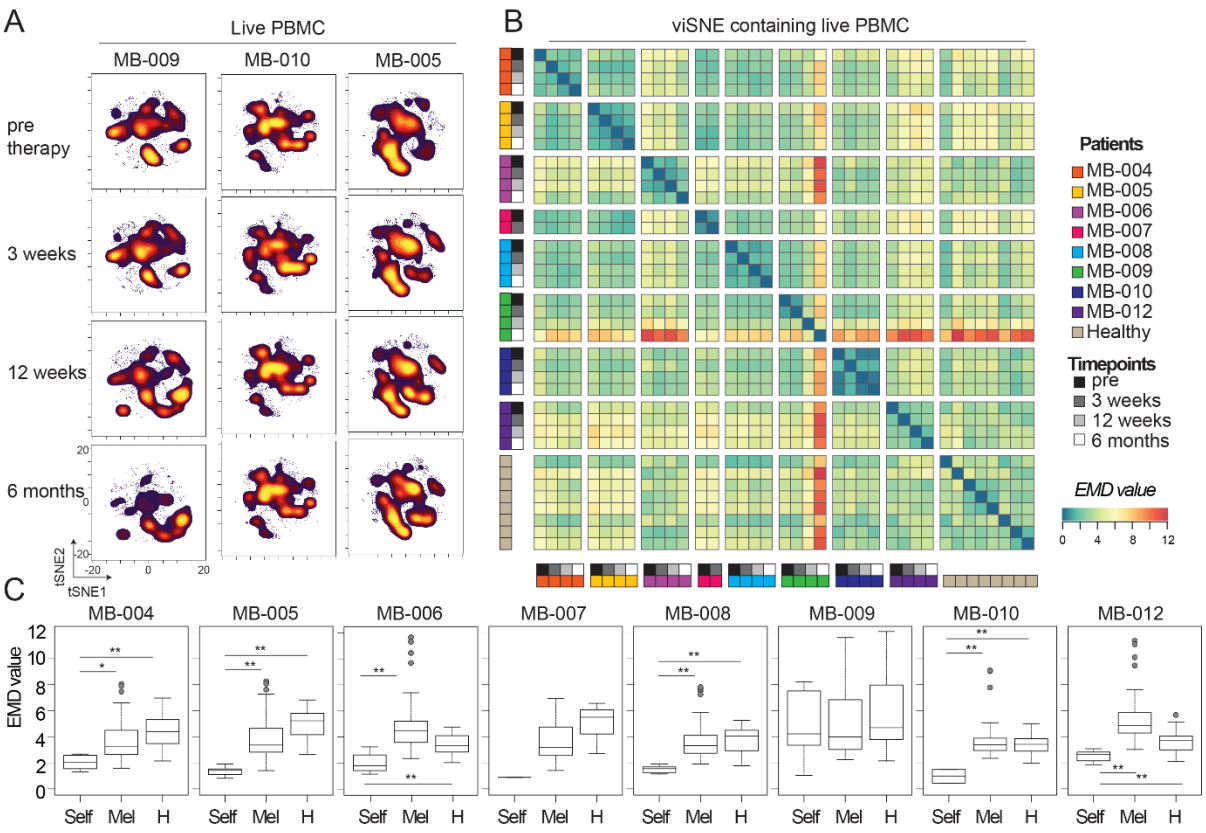

Figure 6.1. Earth Mover's Distance quantifies phenotypic plasticity of the system over therapy and identifies outlier patient. Peripheral blood mononuclear cells (PBMC) from melanoma patients undergoing anti-PD-1 therapy and healthy donors were characterized by mass cytometry. Equal numbers of live events from each sample were run together on a viSNE map. (A) Representative live leukocyte viSNE plots are shown for three patients at all collection points during therapy. (B) EMD was calculated, pairwise, for all samples. Heat indicates magnitude of EMD value. (C) Median EMD was calculated for each patient from pairwise EMD between samples from that same patient (light grey), between that patient and all other pembrolizumab samples (white), and between that patient and all healthy donors (dark grey). N=6, 104, and 32 respectively (with exception of MB-007 where N=1, 52, and 16 respectively). *p<0.001, **p<0.0001. The whiskers of the boxplot extend to the most extreme data point which is no more than 1.5x the interquartile range from the box. "Self" represents intra-patient EMD values, "Mel" represents inter-patient EMD values, and "H" represents EMD values of indicated patient compared to healthy donor.

While viSNE and EMD provided a quantitative, first-glance at system stability, it is possible that shifts in abundance or phenotype of small, biologically relevant populations may be over-looked. To avoid missing small but crucial cell subsets, the system was split into classical immune populations using traditional, biaxial gating (Figure S6.1). Twenty-eight cell populations were identified and the change in frequency of those populations, compared to the pre-therapy time point, was calculated (Figure 6.2A-B). Two populations showed significant changes in frequency.

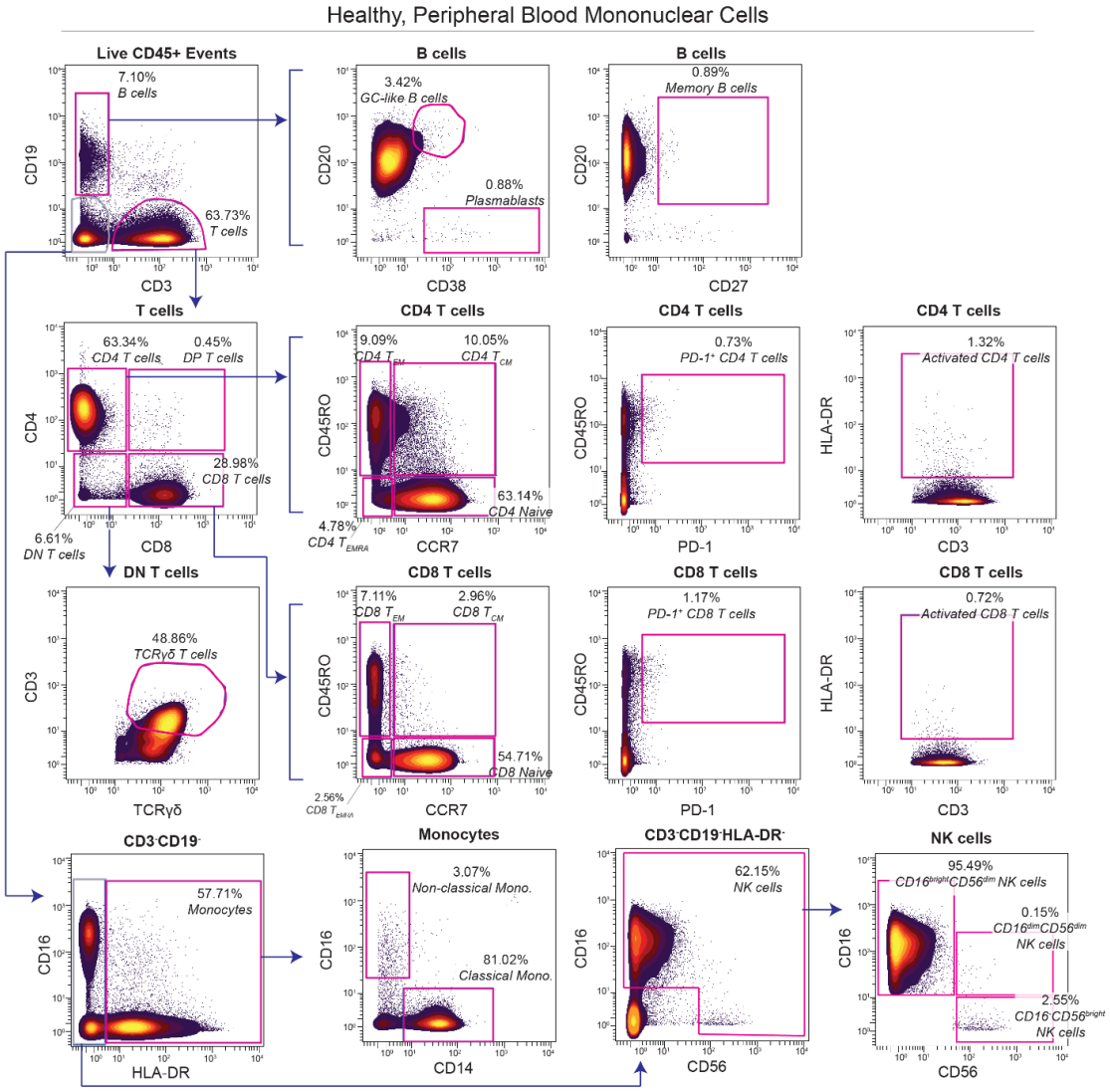

Supplemental Figure 6.1. Identification of immune populations in the peripheral blood (Related to Figure 6.2). PBMC isolated from the peripheral blood of melanoma patients undergoing αPD-1 therapy and healthy donors was analyzed by mass cytometry. Biaxial mass cytometry plots show the gating scheme for populations in the peripheral blood. Shown here are representative plots of the gating scheme with an example healthy donor.

$CD4^+$ $PD\text{-}1^+$ and $CD8^+$ $PD\text{-}1^+$ T cells had a significant change in frequency [N=10, p <0.0001 (pre vs 3 weeks) and p =0.0011 (pre vs 12 weeks) for $CD4^+$ $PD\text{-}1^+$ T cells, and p = 0.00057 (pre vs 12 weeks), for $CD8^+$ $PD\text{-}1^+$ T cells] over the course of therapy, both decreasing (Figure 6.2A-C). Increased frequencies of $CD4^+$ T effector memory (T_{EM}) cells at 6 months post therapy and activated $CD4^+$ T cells at three weeks post therapy were also analyzed (Figure S6.2).

Marker Enrichment Modeling identified signature features of PD-1⁺ T cells in tumor and blood

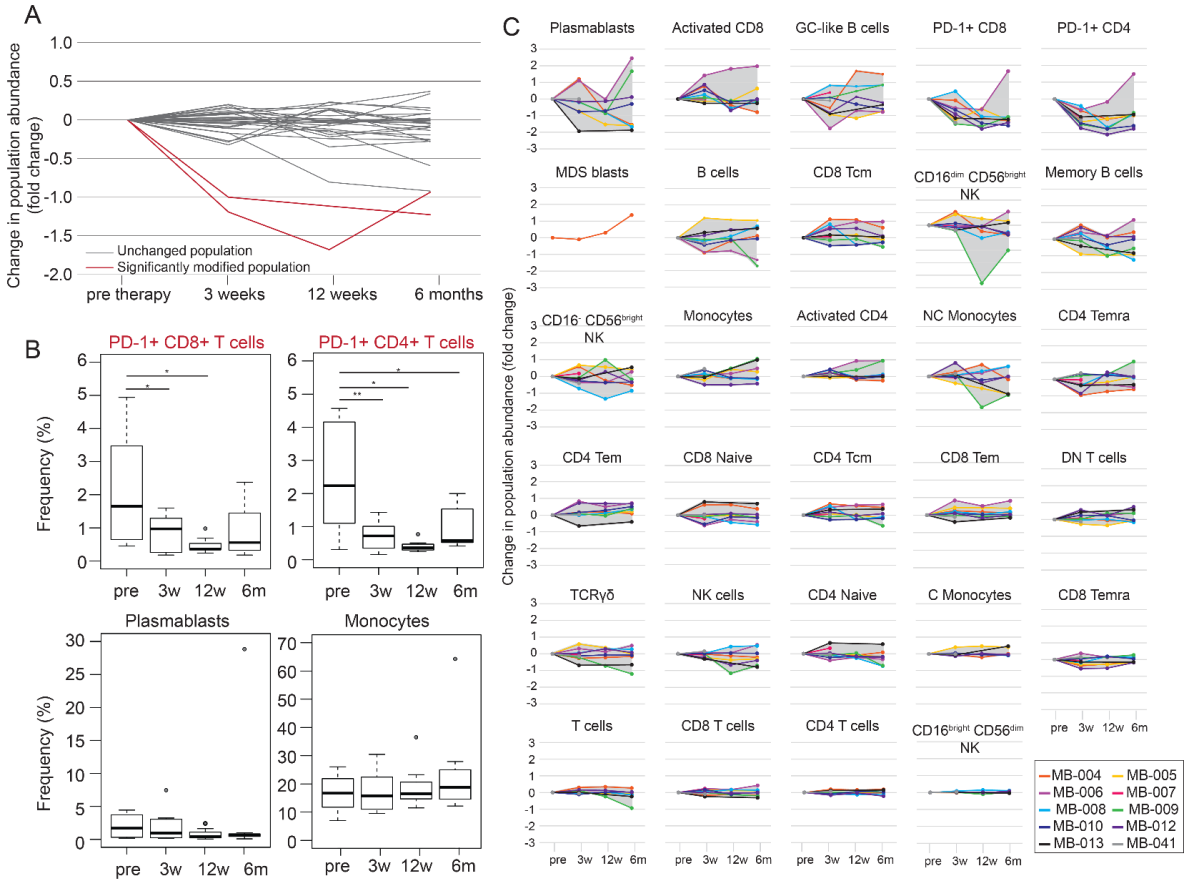

Figure 6.2. Frequency tracking of populations identifies a loss of detectable PD-1⁺ T cells. Established immune populations were manually gated and population frequencies were determined over the course of anti-PD-1 therapy. (A) Population frequencies at 3 weeks, 12 weeks, and 6 months post start of anti-PD-1 therapy were normalized to the pre therapy frequency. Each line represents a change in frequency for one population. Significantly changing populations, compared to pre-therapy, are shown in red. (B) Change in population frequency is shown for individual patients for each population median shown in (A). Each time point after the start of therapy was compared to the pre-therapy time point using a two tailed, paired t-test. With a Bonferroni correction, significantly different populations had a p value < 0.0018. P values are indicated for populations with significant changes. (C) Boxplots of population frequency are shown for each significantly changing population (top) and for two populations that did not significantly change (bottom). *P* values were derived from an uncorrected, two tailed, paired t-test. *p<0.05, **p<0.01. See also **Figures S1** and **S2, Tables S1** and **S2**.

The next step in the ensemble systems immune analysis pipeline was to automatically quantify enrichment of measured parameters and determine how those enriched parameters changed during treatment. MEM was used here to identify signature features of each population at each

time point following established methods (*348*). MEM scores can range from +10 (maximum

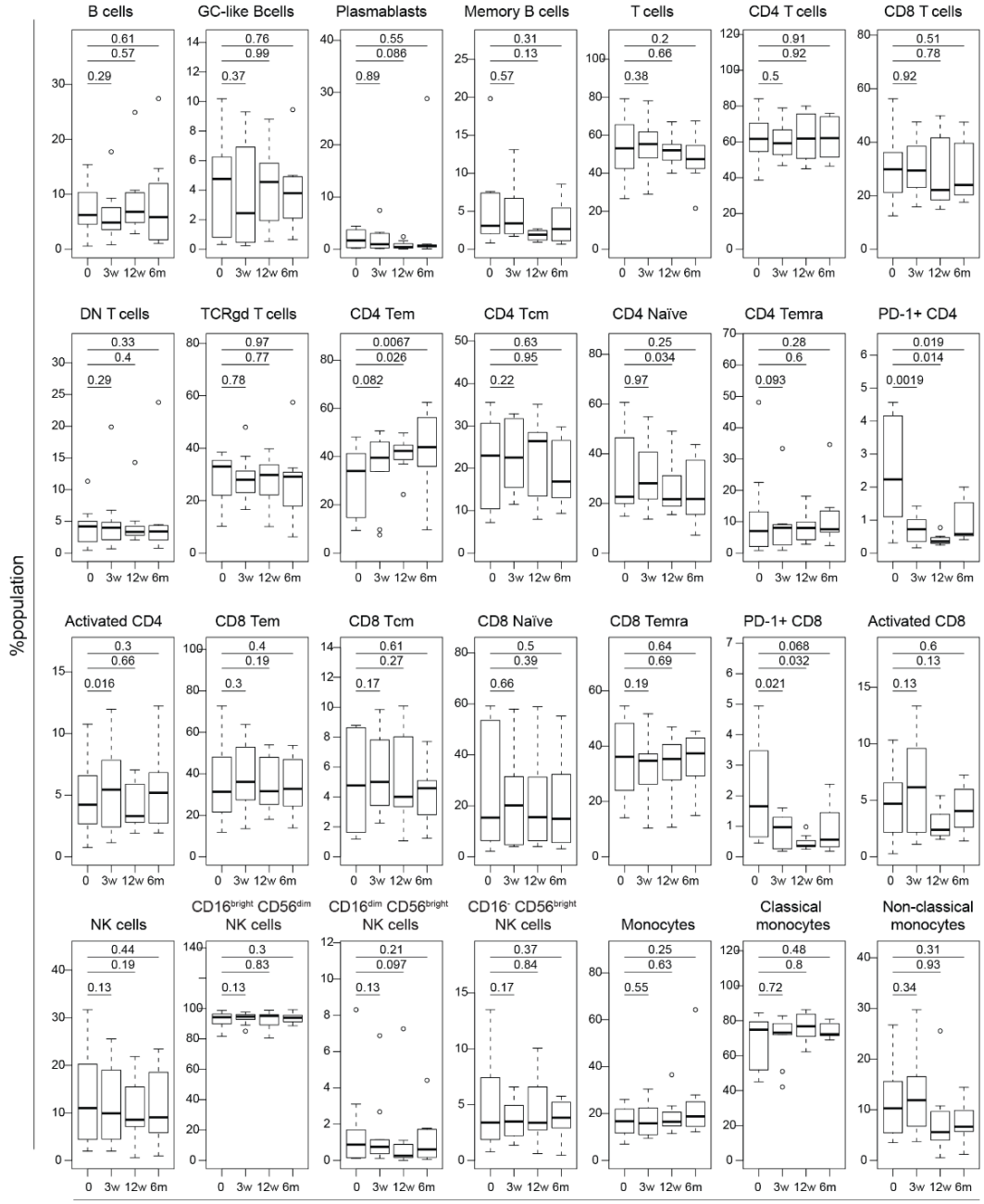

Supplemental Figure 6.2. Melanoma patient population frequency (Related to Figure 6.2). In the Pembrolizumab treated cohort, 10 individuals were samples prior to the start of treatment, with sample of peripheral blood at 3 weeks (3w), 12 weeks (12w), and 6 months (6m) post-start of therapy. The frequency of each population is plotted as a boxplot for melanoma patients over the course of therapy. Each population is labeled on the graph and the *P* value from an uncorrected, two tailed, paired t-test is shown. The whiskers of the boxplot extend to the most extreme data point which is no more than 1.5x the interquartile range from the box.

enrichment) through 0 (no enrichment) to -10 (maximum lack) and here are reported as the median +/- standard deviation in MEM value for the cell population. As expected, PD-1^{+} CD8 and CD4 T cells from pre-therapy samples were enriched for canonical identity makers CD3 and CD8 and CD4, respectively (Figure 6.3A-B**,** top). To indicate changes in enrichment patterns, change in MEM score (∆MEM) was calculated by subtracting the median MEM score for each parameter

at the pre-therapy time point from the indicated time point after the start of therapy. After 3 weeks and 6 months of anti-PD-1 therapy, PD-1^{+} CD8 T cells lost enrichment, but not expression, for CD3 (ΔMEM of -5; median ± standard deviation, CD3 MMI 40.9±11 (3 weeks) and 48.3±14.1 (6 months)) (Figure 6.3A, bottom, Figure 6.3C). This was not the case for PD-1^{+} CD4 T cells (Figure 6.3B, bottom). Given a loss of enrichment of the CD3 subunit of the T cell antigen receptor, a

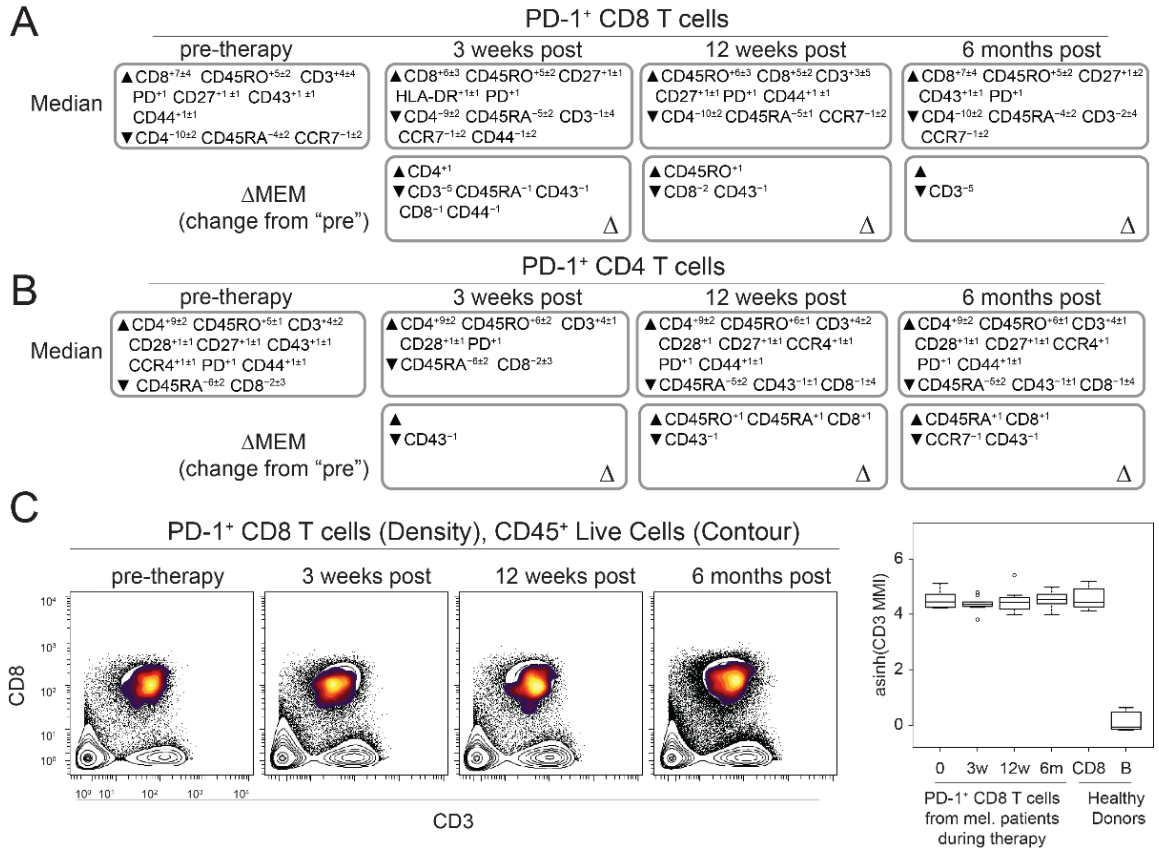

Figure 6.3. Marker enrichment modeling identifies signature features of populations over the course of therapy. Tissue-specific MEM labels were created for each cell population, from each patient, at each time point. (A) Median MEM labels are shown for PD-1^{+} CD8 T cells at each time point during therapy (top). ΔMEM labels were calculated by subtracting the median pre-therapy MEM scores from the median MEM scores at each time point. ΔMEM labels indicate the change in MEM value compared to pre-therapy (bottom). (B) Median MEM labels are shown for PD-1^{+} CD4 T cells at each time point during therapy (top). ΔMEM labels are shown for PD-1^{+} CD4 T cells from each time point during therapy (bottom). MEM values are represented as the median MEM value ± standard deviation. (C) Biaxial plots of CD3 and CD8 are shown for PD-1^{+} CD8 T cells from representative melanoma patients (MB-004) undergoing anti-PD-1 therapy (left). Density: PD-1^{+} CD8 T cells, Contour: live CD45^{+} cells. Transformed ($arcsinh_5$) CD3 median metal intensity (MMI) is shown for PD-1^{+} CD8 T cells at each time point during therapy [pre-therapy (0), n=10; 3 weeks (3w), n=10; 12 weeks (12w), n=7; 6 month (6m), n=8 healthy, n=8];. Healthy PBMC donor CD8 T B cells are shown for reference. See also **Tables S1** and **S2**.

canonically expressed and enriched T cell marker, on these peripheral blood PD-1$^+$ CD8 T cells, it was important to determine their novelty by comparing them to other subsets, including PD-1$^+$ CD8 T cells from tumors or healthy donors. To assess the novelty of this population, MEM labels were created for PD-1$^+$ CD4 and PD-1$^+$ CD8 T cell gated from (1) blood from melanoma patients during anti-PD-1 therapy, (2) human melanoma tumors, (3) blood from healthy donors, and (4) tonsil or adenoid from healthy donors. Induced pluripotent stem cells, analyzed by mass cytometry, were used as a control cell reference for MEM calculations. Similarity in MEM labels was then compared using root-mean-square deviation (RMSD) (*348*) (Figure 6.4A-B). B cells gated from healthy donor blood and tonsil were also included for contrast because of their distinctly different enrichment profiles. As expected, these B cells clustered separately from the T cell populations. PD-1$^+$ CD4 T cells from blood of healthy donors and melanoma patients receiving anti-PD-1 therapy clustered together, whereas PD-1$^+$ CD4 T cells from melanoma tumors and healthy donor tonsils formed a different cluster (Figure 6.4A). Similarly, PD-1$^+$ CD8 T cells from melanoma tumors clustered with those from healthy donor tonsils, while PD-1$^+$ CD8 T cells from healthy donor blood and melanoma blood formed two, intermixed clusters. These results indicated PD-1$^+$ T cells found in the blood were distinct from those found in the tumor or healthy tonsil. Median MEM labels, which display enrichment scores for each measured feature, are shown for each tissue's PD-1$^+$ T cell populations (Figure 6.4B). PD-1$^+$ CD8 T cells from the blood of melanoma patients were enriched for CD43 protein expression and trafficking markers like CCR4 and CXCR3 and specifically lacked activation markers CD38 and CD69, as compared to PD-1$^+$ CD8 T cells in melanoma tumors (Figure 6.4C, left). PD-1$^+$ CD4 T cells were enriched for CD4 (+3), as compared to their melanoma tumor counterparts. There was no difference in enrichment

between PD-1+ CD4 T cells in the peripheral blood of melanoma patients and healthy donors (Figure 6.4C, right). PD-1$^+$ T cells from the blood of melanoma patients and healthy donors were therefore phenotypically similar. Thus, MEM, as part of this ensemble, automated quantitative comparisons of high-dimensional data from different tumor and donor types.

Ensemble systems analysis revealed increased CD4 T cell frequency following chemotherapy in AML patients

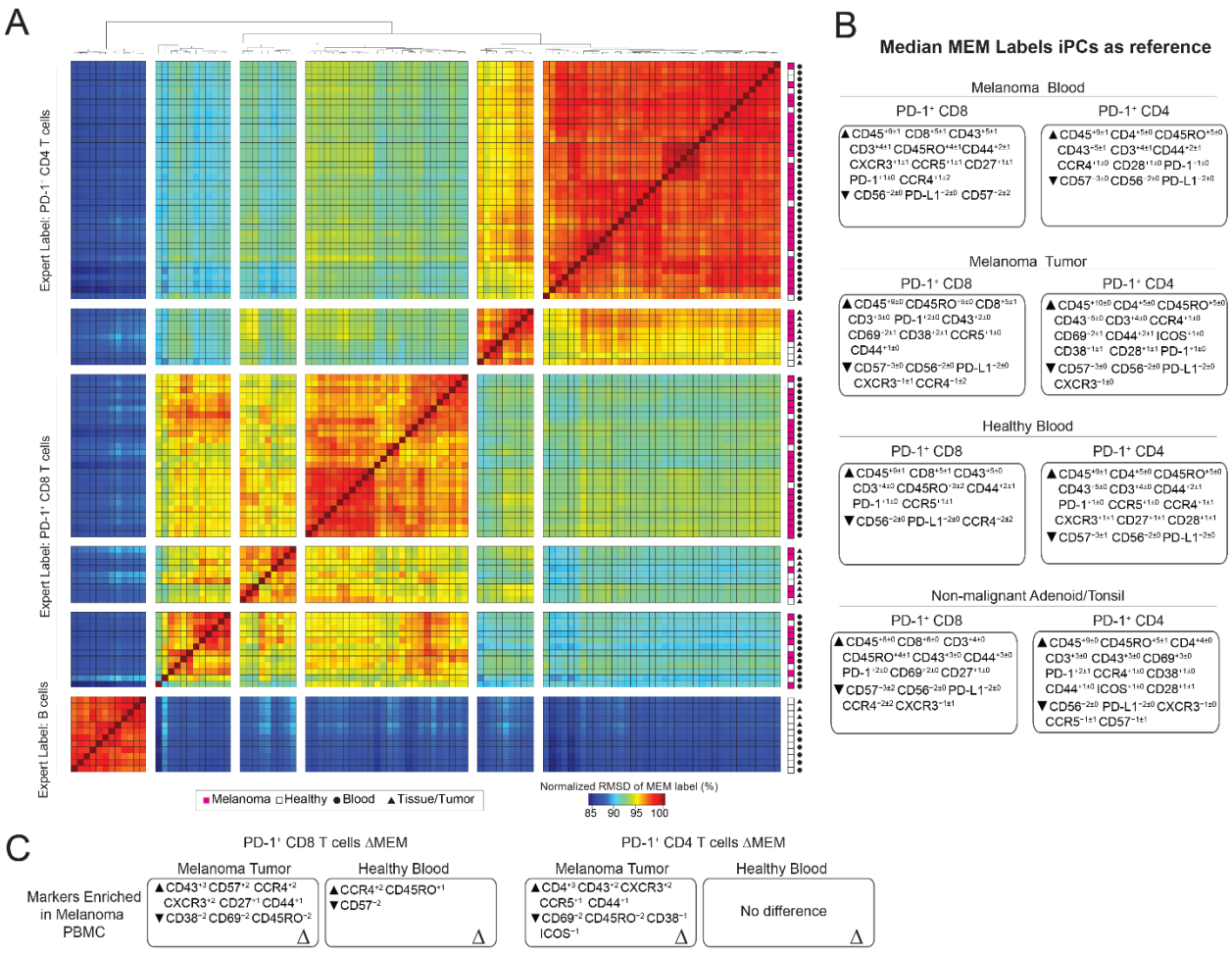

Figure 6.4. MEM reveals that PD-1$^+$ T cells from blood differ from those in the tumor. (A) MEM labels were compared for each of the 112 populations (PD-1$^+$ CD4 and CD8 T cells and B cells) from three human tissues. Populations were defined using traditional biaxial gates as in **Figure S1**. Tissue type and source are indicated in the bottom left. (B) Median MEM labels are shown for PD-1$^+$ CD4 and CD8 T cells from each tissue type. MEM values are shown ± standard deviation. (C) ΔMEM scores show the difference in median MEM scores between PD-1$^+$ CD8 T cells (left) or PD-1$^+$ CD4 T cells (right) in the peripheral blood and those found in the tumor or blood of healthy donors. See also **Tables S1** and **S2**.

The ensemble systems immune monitoring pipeline was applied to a previously published data set of peripheral blood from acute myeloid leukemia patients undergoing chemotherapy (Dataset 2, (*328*)) in order to describe and dissect system wide changes. All peripheral blood mononuclear cells, including blasts and non-blasts, were identified using the gating scheme published by Ferrell et al. EMD on t-SNE revealed lack of intra-patient stability in 3 of 5 patients, as seen by no significant difference between intra- and inter-patient EMD values (Figure 6.5A, Figure S3). The remaining two patients showed intra-patient stability, most likely due to the presence of leukemic blasts throughout treatment. Fifteen populations were defined automatically using the SPADE algorithm to cluster on t-SNE axes (Figure 6.5B), as previously described (*207, 334*).

Of the 15 populations identified, 7 showed significant changes in at some point during chemotherapy (Figure 6.5C). MEM was used to label the automatically identified populations (Figure 6.5D, Figure S4). Two populations of blasts were defined by HLA-DR enrichment and observed to decrease over the course of chemotherapy. In contrast, $CD4^-$ T cells and two subsets of $CD4^+$ T cells were observed to expand following chemotherapy. Population 13 was enriched for CD4 (+5), CD7 (+4), and CD45 (+2) while specifically lacking expression of HLA-DR (-3) and CD123 (-2), indicating that this is likely a population of CD4 T cell. To assess whether population 13 was similar to CD4 T cells of healthy donors, RMSD on MEM labels, created using hematopoietic stem cells as a common reference, was calculated, and published data from healthy donor CD4 T cells and B cells was used as prior knowledge (*348*). Population 13 clustered with CD4 T cells from healthy donors (Figure 6.5E). Taken together, these results suggest that chemotherapy allowed emergence of a non-malignant population of CD4 T cells.

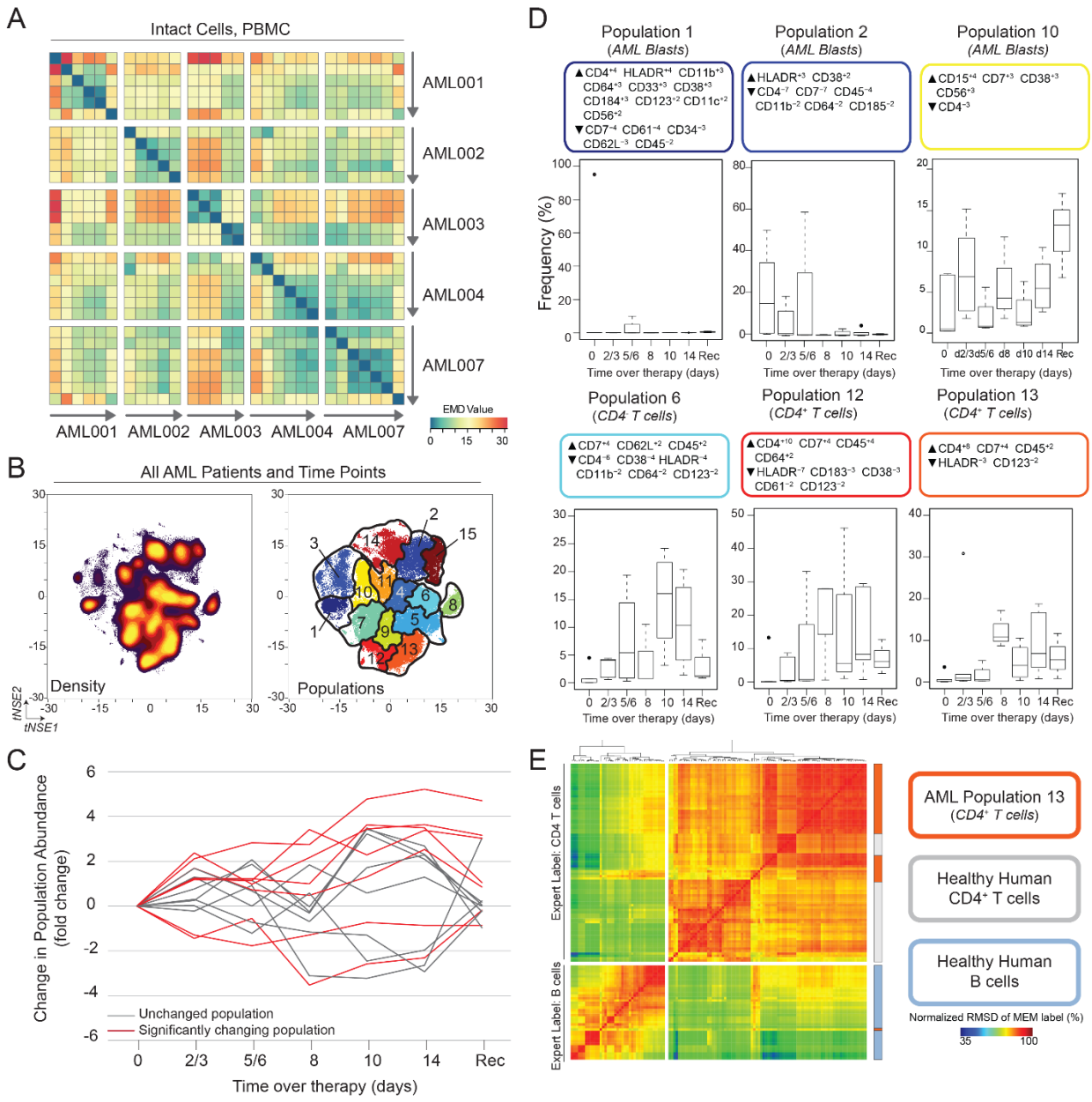

Figure 6.5. Ensemble immune analysis and automated gating identifies loss of peripheral blasts and increase in non-malignant immune cells in AML patients undergoing chemotherapy. PBMCs from AML patients undergoing chemotherapy were characterized by mass cytometry. Equal numbers of live events from each sample were run together on a viSNE map. (A) EMD was calculated, pairwise, for all samples. Heat indicates magnitude of EMD value. (B) Populations were identified (right) by SPADE of cell density on t-SNE axes (left). (C) Frequency of populations identified in (B) was normalized to the pre therapy frequency and compared using a paired t test. Populations with time points that significantly change from pre-therapy are shown in red. (D) Boxplots are shown for each significantly changing populations. Each population is labeled with a MEM label and an expert given name derived from the MEM label. (E) MEM labels from Population 13 were compared with the 80 populations (CD4 T cells and B cells) from Diggins, et al using RMSD. See also **Figures S3** and **S4**.

Loss of activated T cells and expansion of CD4$^-$CD8$^-$ T cells in tumors of melanoma patients treated with MEKi and BRAFi

Samples from a cohort of melanoma patients with *BRAF*^{V600E} mutations treated with targeted therapies dabrafenib and trametinib (n = 11) (Dataset 3), were characterized by mass cytometry and the data analyzed by the ensemble systems immune monitoring pipeline. Combining EMD and viSNE to quantify stability of the immune compartment showed that each patient remained more similar to itself than to other melanoma tumors or healthy tonsils over the course of therapy. However, EMD run on t-SNE axes created from analysis of T cells revealed that the T cell compartment did not have lower intra-patient EMD values, as compared to inter-patient EMD values (Figure 6.6A). Thus, significant immune plasticity followed therapy. Immune populations were defined using traditional biaxial gates and the change in frequency for those populations was calculated. After 4 weeks of treatment, there was a statistically significant change in frequency of 5 immune populations was observed. One population of interest included unexpected double-negative T cells lacking expression of CD4 or CD8 (DN T cells) that comprised 7.23±17.18% in pre-therapy tumors, 26.27±16.36% in tumors 4 weeks post-therapy, and 3.57±1.52% of a healthy lymph node ((median ± standard deviation) **F**igure 6.6B, Figure S6.3, Figure S6.4). Pre-therapy MEM labels showed that DN T cells were enriched for CD3 (+2), CD45 (+2), CD45RO (+1), CD4 (+1), and CD28 (+1) but specifically lacked CD8 (-3) and CD45RA (-2) when compared to all cells found within the melanoma tumors. ΔMEM scores indicated that, over the course of therapy, DN T cells became more enriched for CD45RO (+1) and CD44 (+1) but lost enrichment of CD69 (-1), CD43 (-1), CD27 (-1), and HLA-DR (-1) (Figure 6.6C). Given that T cells can down regulate expression of CD4 or CD8 if highly activated (*352*), DN T cells from melanoma tumors, glioblastoma (GBM), renal cell carcinoma (RCC), and healthy tonsils were

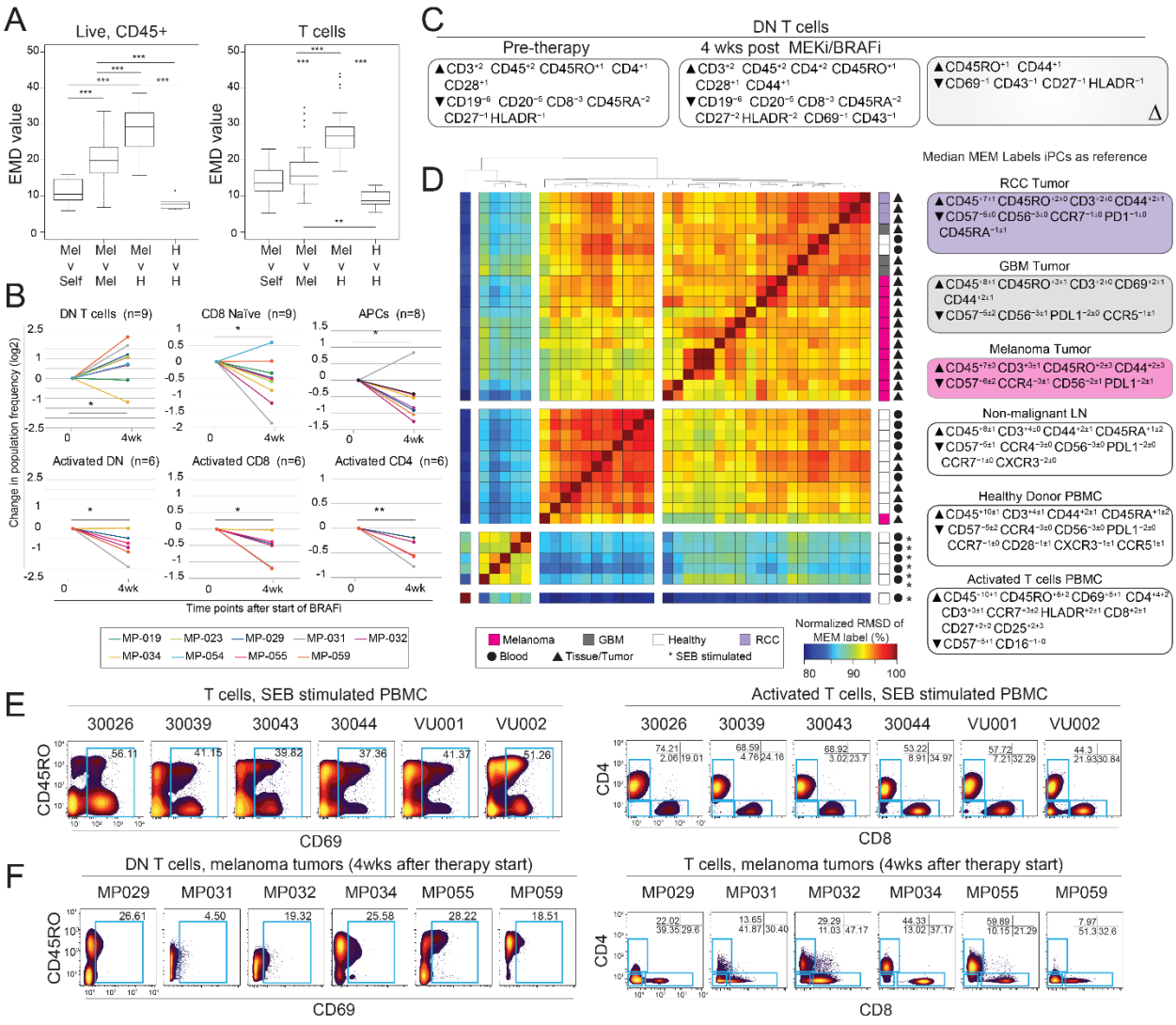

Figure 6.6. Ensemble immune analysis identifies expansion of CD8 and CD4 double negative T cells in tumors from patients treated with BRAF and MEK inhibitors. Single cell suspensions of melanoma tumor biopsies from before and after treatment with BRAF and MEK inhibitors were characterized by mass cytometry. (A) Equal numbers of live events (left) or T cells (right) from each sample were run together on a viSNE map. EMD was calculated, pairwise, for all samples. Boxplots show median, pairwise EMD values for listed comparisons. Unpaired student t test. *p<0.05. **p<0.01, ***p<0.001. (B) Change in population frequency is shown for individual patients for each significantly changing population. Each time point after the start of therapy was compared to the pre-therapy time point using a two tailed, paired t-test. *p<0.05. **p<0.01. (C) Median MEM labels are shown for double negative (DN) pre therapy and 4 weeks after therapy. A ΔMEM score shows the difference in median MEM scores DN T cells before and after the start of therapy. (D) MEM labels from tumor resident DN T cells were compared with SEB stimulated T cells from peripheral blood using RMSD. Median MEM scores for each tissue are shown on the right. (E) Biaxial plots of all T cells from SEB stimulated PBMC (left) and activated T cells (CD69+, plots on right). (F) Biaxial plots of DN T cells from tumors of patients treated for 4 weeks with BRAFi and MEKi (left) and all T cells from (right). See also **Figures S5** and **S6**, **Tables S1** and **S2**.

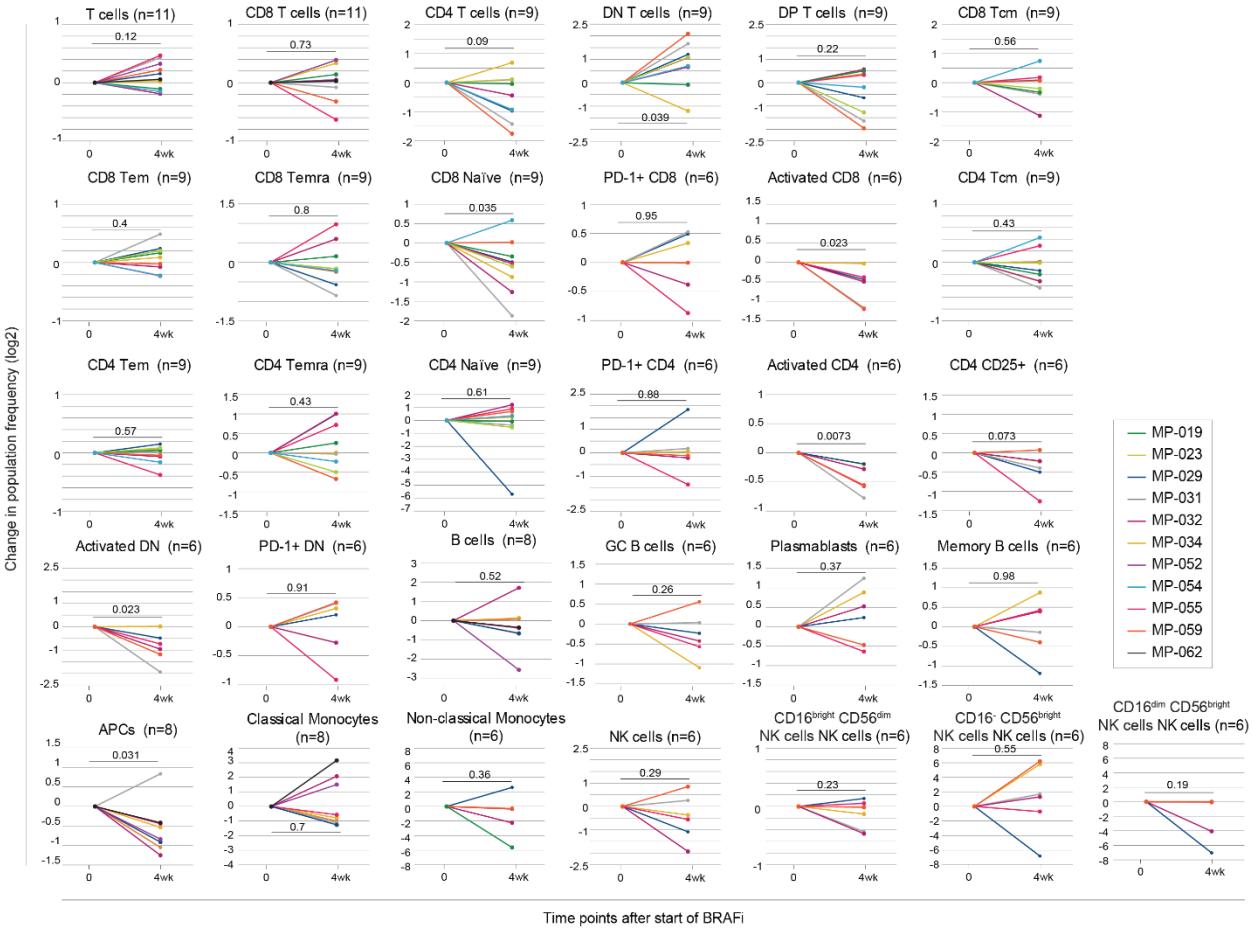

Supplemental Figure 6.3. Change in frequency of populations identified by biaxial gating in melanoma patient tumors treated with MEKi and BRAFi (Related to Figure 6). Melanoma patients had a tumor biopsied before the start of therapy. For two weeks, patients were treated with a BRAFi and at the two week mark, a MEKi was added. At 4 weeks, the tumor was removed. Immune populations (31) were gated using biaxial plots. Population frequencies at all time points of therapy were normalized to the pre chemotherapy frequency and compared using a student's t test (uncorrected *P* value shown). The number of matched pairs of melanoma tumors shown in boxplots is shown to the left (or below) the population name.

compared to classical activated peripheral blood T cells stimulated through the T cell receptor by Staphylococcal enterotoxin B (SEB) (*327*) (Fig 6.6D). SEB stimulated T cells formed their own cluster, apart from all other DN T cells and shared 87.2% (±2.88%, n=78 comparisons) similarity with DN T cells from melanoma tumors. In contrast, DN T cells from melanoma, GBM, and RCC clustered together, with a similarity scores of 93.6% (±1.06%, n=78 comparisons). Of T cells

activated by SEB, close to half were $CD69^+$ (41.26±7.41%) and nearly all retained CD4 or CD8 co-receptor expression (Figure 6.6E). In contrast, DN T cells from post-treatment melanoma tumors contained fewer $CD69^+$ cells (22.45±8.76%) (Figure 6.6F). Thus, DN T cells from melanoma, GBM, and RCC consisted of a phenotypically distinct population of DN T cells unlike any observed in healthy tissue. Taken together, these data suggest that an unusual population of T cells emerged in tumors from melanoma patients treated with BRAFi and MEKi, and that this DN T cell population occurs in multiple types of tumors.

Discussion

The manuscript describes an analysis suite designed to be a common starting point for immunologists tracking cells over time, provides three reference datasets for testing tools designed to discover and characterize cell subsets, and reveals unexpected cells in the context of cancer therapies. While we expect the algorithms in the ensemble will change and improve over time, the four cellular properties identified should be considered essential features for immune monitoring with any single cell platform. This ensemble data analysis strategy was designed specifically for systems immune monitoring in longitudinal, clinical studies, but it could be applied for any system with change. For example, we envision adapting it to study experimental perturbations to map signaling networks and drug responses (*194, 353*). This ensemble approach was robust across multiple, contrasting studies in quantifying change and stability in immune system cells. Additionally, this approach provided a detailed analysis of the abundance and tractable quantitative phenotype of populations that comprised each system. One of the most

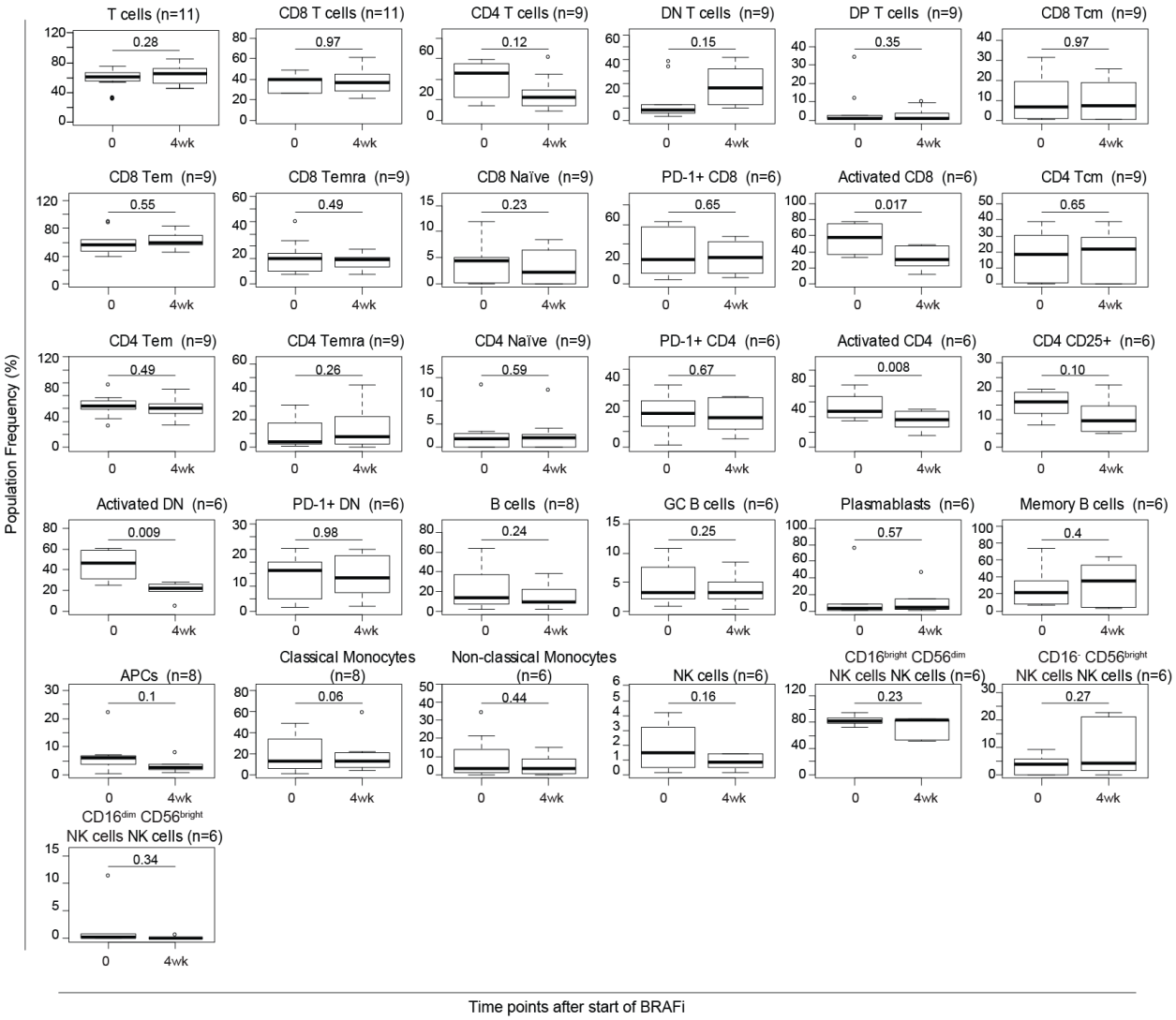

Supplemental Figure 6.4 Melanoma tumor population frequency before and after MEKi and BRAFi treatment (Related to Figure 6.6). The frequency of each population is plotted using boxplots. Uncorrected *P* values are shown for each time point compared to pre-therapy (paired, t-test). The number of matched pairs of melanoma tumors shown in boxplots is shown to the left (or below) the population name. The whiskers of the boxplot extend to the most extreme data point which is no more than 1.5x the interquartile range from the box.

striking findings was a population of $CD4^-$ $CD8^-$ DN T cells observed to have a common phenotype in three human tumor types, melanoma, renal cell carcinoma, and glioblastoma that had a phenotype distinct from that of resting $CD4^-$ $CD8^-$ DN and SEB activated T cells from healthy individuals. This result is consistent with recent reports characterizing the striking phenotypic

similarity of T cells infiltrating melanoma and colon cancer mouse tumor models (*354*) and provides new evidence that common changes to immune cell mechanisms are shared across human tumor types and play a role in response to targeted therapy.

Overall, the peripheral immune system was remarkably stable in melanoma patients over the course of anti-PD-1 therapy, similar to the stability seen in healthy individuals over time (*197, 301*). However, by combining viSNE with EMD, one patient was identified as having a highly plastic immune system. This patient was previously diagnosed with MDS as described in Chapter IV of this thesis (*312*). It may be common in cancer immune monitoring to observe outcomes that are, individually, rare (*355*). An analysis strategy must expect the unexpected and may struggle if tailored too closely to examples (*356*). Caveats exist for using EMD to quantify differences between viSNE maps. All samples must be embedded on the same viSNE map in order to be appropriately compared and precautions, like barcoding and bead normalization, must be taken to ensure that differences in viSNE maps are attributed to biological differences and not batch effects. Identification of cells into groups can be accomplished in whichever way is most appropriate to a system, or in multiple ways, prior to ensemble analysis (*210, 314, 334, 350*). Because the ensemble toolkit does not rely on known populations, it remains independent from methods of automated population identification (*207, 350*) and can be used to compare and communicate analysis results from teams relying on computational approaches, immunologists, and bioinformatics experts.

The ensemble approach was especially adept at capturing shifts over time and was able to identify a shift in relative abundance of a subset of T lymphocytes, their phenotype and intra-patient recovery of these phenotypes, all of which could have significant implications for maintenance of remission and clinical outcomes (*357, 358*). A human immune monitoring strategy using this ensemble toolkit might therefore provide new insight into the immune system's interaction with leukemia remission and relapse.

The ensemble toolkit was able to detect known biological occurrences, as well as identify novel potential mechanisms for further study. The ensemble toolkit detected an overall loss of PD-1$^+$ T cells in the peripheral blood over the course of therapy. This has previously been described and attributed to receptor occupancy by the drug itself (*295, 359*). Previous work revealed an expanded population of Ki67$^+$ CD4 T cells in the peripheral blood during immunotherapy (*342, 343*). While our comparable study did not measure Ki67 in the blood and thus could not be compared directly, we did observe a trend towards increased activated CD4 T cells, as defined by expression of HLA-DR, at 3 weeks after the start of therapy and CD4 T_{EM} cells at all time points after the start of therapy (Figure S6.2). In addition to capturing known clinical events, the ensemble tool kit identified a novel population of DN T cells present in unexpectedly high frequencies in melanoma tumors before and after treatment with BRAFi and MEKi as compared to healthy lymphoid tissue. Expanded DN T cell populations have previously been reported in metastatic lymph nodes of melanoma patients (*360*), however their deep phenotype or frequency in response to inhibitor therapy has not yet been described. Previous work has described the expansion of a regulatory CD3$^+$ T cell population lacking both CD4 and CD8 after T cell receptor (TCR) and cytokine (*361-364*). Further, MEK inhibitors can support anti-tumor T cell function by blunting TCR-induced apoptosis (*365*). Therefore, it is possible that high frequencies of DN T cells after treatment with MEKi and BRAFi indicate an accumulation of T cells derived from tumor resident T cells, although additional mechanistic studies are required.

Overall, the melanoma tumor dataset (Dataset 3) highlights the complexity of tumor-associated T cells in human malignancies and provides further evidence that phenotypically diverse populations of tumor resident T cells can be found across multiple, distinct tumor types (*354*). The data presented here will join a common immunology reference set (*348, 366-368*) that can be mined further to characterize and understand changes in immune and cancer cell populations diverse disease settings and build a reference of cellular identity.

Materials and Methods

Study Design

In the case of peripheral blood collected from melanoma patients receiving pembrolizumab, the purpose of the study was to identify biological characteristics of melanoma occurring prior to treatment and at different time points following therapy for patients being treated with immune based therapies. To be included in this study, patients met the following inclusion criteria: 1) pathologically proven diagnosis of melanoma, 2) 18 years of age or older, 3) treated with immune-based therapies, and 4) willing to have several serial blood draws. Patients not receiving immune-based therapy or unwilling or unable to provide consent were not included. There was no blinding or randomization process in this study. Blood specimens were obtained from patients during the time of scheduled phlebotomy for routine clinical laboratory analysis. Peripheral blood draws were done on the day of therapy start and 21 days (±10 days), 84 days (±21 days), and 180 days (±21 days) following initiation of therapy.

In the case of tumors sampled sequentially from melanoma patients treated with targeted therapy, the objective was to identify biomarkers of response and resistance to B-RAF and MEK targeted therapy in melanoma. Patients with advanced, operable BRAF mutation-positive melanoma will received GSK-2118436 (BRAF inhibitor) for two weeks, followed by the combination of GSK-2118436 and GSK-1120212 (MEK inhibitor) for two weeks, followed by surgical resection of the disease. Tumor biopsies were obtained prior to start of therapy and 2 weeks after combined GSK-2118436 and GSK-1120212 (*369*). To be included in this study, patients met the following inclusion criteria: 1) signed written, informed consent, 2) between the ages of 18 and 90, 3) patients with locally or regionally advanced melanoma being considered for resection of the lesion(s) for local-regional control and potential cure, 4) BRAF V-600 mutation positive by snapshot molecular analysis, 5) measurable disease, 6) all prior treatment related toxicities

CTCAE ≤ Grade 1 at the time of enrollment, 6) adequate baseline organ function, 8) women of childbearing potential with a negative serum pregnancy test within 14 days of first dose of study or men with female partner of childbearing potential must have had either had a prior vasectomy or agree to use effective contraception, and 9) able to swallow and retain oral medication. There was no blinding or randomization process in this study.

Human Tissue Sample Collection and Preservation

All human samples were obtained in accordance with the Declaration of Helsinki following protocols approved by Vanderbilt University Medical Center Institutional Review Board (IRB). The patient information for unpublished samples can be found in Supplemental Table 6.1. Healthy donor tonsil, adenoid, and blood were collected as “non-human subjects”, without gender or age information. Upon single cell isolation, all cells were cryopreserved in 88% fetal calf serum + 12% DMSO. Cells from human samples were collected and isolated as follows:

Peripheral Blood

Peripheral blood mononuclear cells (PBMCs) were collected, isolated, and cryopreserved from approximately 20 mL of freshly drawn blood as previously described (*312*). Briefly, peripheral blood was drawn into sodium heparin anticoagulant and PBMC were isolated by centrifugation after layering on top of a Ficoll-Paque PLUS (GE Healthcare Bio-Sciences) gradient.

Solid Tissue.

Melanoma tumors, glioblastoma tumors, and non-malignant human adenoid and tonsil tissue were resected from patients with consent and in accordance with the Declaration of Helsinki. All solid tissue samples were dissociated into live, single cell suspension and samples were cryopreserved using a previously documented protocol (*370, 371*). Solid tissue samples were first manually dissociated using a scalpel. The minced tissue was then incubated in RPMI 1640

(Corning/Mediatech, Corning, NY) plus 10% FBS in a final concentration of 1 mg/mL collagenase II (Sigma Aldrich; Darmstadt, Germany) and 0.25 mg/mL DNase (Sigma Aldrich) for 1 hour in a 37° C incubator with 5% CO_2. Cells were then strained with a 70 μm and 40 μm prior to cryopreservation.

Renal cell carcinoma samples were processed and stored as described by Siska, et al (*372*).

Human Induced Pluripotent Stem Cells (iPCSs)

Reprogramming of fibroblasts was induced by transduction with CytoTune Sendai virus (Life Technologies). All experiments were performed under the supervision of the Vanderbilt Institutional Human Pluripotent Cell Research Oversight (VIHPCRO) Committee. Induced pluripotent stem cells were grown in feeder-free conditions in plates coated with Matrigel (BD Biosciences) and maintained in mTESR1 media (Stem Cell Technologies) at 37°C with 5% CO_2. Cells were checked daily for differentiation and were passaged every 3-4 days using Gentle dissociation solution (Stem Cell Technologies). iPSCs were treated with 0.5% EDTA prior to staining with mass cytometry antibody panel as described below.

Mass Cytometry

Thawed samples were first incubated with viability reagent, cisplatin (25 μmol/L, Enzo Life Sciences) (*230*). After incubation with viability reagent, cells were washed in PBS containing 1% BSA. Staining occurred in 50 μL PBS/1% BSA for 30 minutes at room temperature using the antibodies listed in Supplemental Table 6.2. Cells were then washed twice with PBS/1% BSA and fixed with a final concentration of 1.6% paraformaldehyde (PFA, Electron Microscopy Sciences). Cells were washed again, using PBS, and then resuspended in iced cold methanol to permeabalize. Cells were incubated at -20° C overnight before being washed twice in PBS and stained with iridium DNA intercalator (Fluidigm Sciences). Purified, carrier free antibodies were purchased from the listed provider and labeled with the listed metal using the protocol provided

by Fluidigm. Stained samples were collected at Vanderbilt University Flow Cytometry Shared Resource on a CyTOF 1.0 mass cytometer (Fluidigm Sciences). All events were normalized prior to analysis using Fluidigm normalization beads.

CyTOF data preprocessing: Data (FCS files) were collected and stored in the online, analysis platform Cytobank (*229*). Data analysis was performed in Cytobank and statistical programming environment R (version 3.4.0) via Rstudio.

Earth Mover's Distance: The Earth Mover's Distance (EMD) was calculated between each pair of populations using the "transport" library for R (*319, 351*) (https://cran.r-project.org/web/packages/transport/citation.html). Parent population (e.g. live CD45+ events) were gated in Cytobank, followed by the creation of a viSNE map in Cytobank. A viSNE analysis with two output dimensions was performed, equally sampling 5000 events per file, with 1000 iterations, perplexity equal to 30, and theta equal to 0.5. The events with their viSNE axes were then downloaded from Cytobank, and the Earth Mover's Distance (EMD) was calculated between each pair of files using the "transport" library for R. The "wpp" object was used to represent each set of points in the two viSNE axes, and the "wasserstein" function was called on each pair of point sets to produce a distance matrix. Each point was assigned unit weight.

Because calculating a matrix with the EMD between each set of 5000 events from the viSNE analysis is computationally expensive, four optimizations were performed. (1) Each file was further downsampled to 1000 out of the original 5000 events per file in the viSNE analysis. Each event was still assigned unit weight, and each point set therefore still had an equal total mass of 1000. (2) The "shortsimplex" method was used for the "wasserstein" function in the "transport" library, which accepted no other parameters besides the pair of weighted point sets (*373*). (3) Each population was automatically assigned a zero EMD compared to itself, and EMD scores already computed across the diagonal were simply copied, since EMD is a metric. (4) The "parallel" library was used to parallelize the computation of each row of the matrix in addition to

the above, using the number of cores detected from the "detectCores" function in the "parallel" library.

EMD values computed by ‘emdist’ were compiled in a CSV file and used to create a heatmap for visualization. Statistical comparisons of EMD values between groups were done in Excel using a Student’s *t*- test. CSV file and heatmap are each produced as an output.

Change in population equation. The frequency of immune populations was determined in Cytobank and exported into CSV files prior to re-organization. For Data Sets 1 and 3, populations were identified by traditional biaxial gating (Figure S6.1). For Data Set 2, populations were identified by first running a viSNE on nucleic acid expressing events from all patients at all time points and then running a SPADE on the tSNE axes (Figure 6.5B). Fifteen nodes (15) were identified with 5% down sampling. The following equation was used to determine the change in frequency for all data sets where $FREQ_t$ is equal to the frequency of a population at a given time point and $FREQ_{pre}$ is the frequency of that same population prior to the start of therapy. The addition of 0.01 to both the numerator and the denominator is to account for the appearance of new populations over the course of therapy.

$$\text{Change in frequency} = \ln((FREQ_t + 0.01)/(FREQ_{pre} + 0.01))$$

R was used to conduct a paired Student’s *t*- test to compare samples from the same patient at different time points of treatment. R script provided by Carr, *et al* was used to create boxplots in R (*197*). In the case of Data Set 1, a Bonferroni correction was used for multiple hypothesis testing.

MEM. MEM creates a quantitative label of cell identity for given populations (*348*). The MEM equation is implemented in R. MEM labels were either created for indicated populations using the bulk, non-population as the reference (Figures 6.3, 6.5D, and 6.6C), using iPSCs stained and run on mass cytometry as the common reference (Figures 6.4 and 6.6D), or using hematopoietic

stem cells stained and run on mass cytometry as the common reference (Figure 6.5E) (*348*). Median MEM labels were created by taking the median MEM score of each marker for each population. Standard deviation is shown. ΔMEM scores are calculated by subtracting the MEM score of the pre-therapy sample from the MEM score of the indicated time point.

Similarity of MEM labels. Root mean square deviation (RMSD) and hierarchical clustering were used to compare MEM labels, as previously described (*348*). The MEM vectors for each non-reference population were calculated over phenotype channels which were shared across all non-reference populations and the single reference population. Each MEM vector contained the population's MEM score, calculated for each of the common phenotype channels, in reference to the single reference population. The MEM RMSD between pairs of non-reference populations was then calculated using the Euclidean distance between these MEM vectors.

Heatmaps representing population similarity were generated from each distance matrix using the "heatmap.2" function of the "gplots" library for R. The distance matrix was normalized by the maximum non-normalized distance d_max between any pair of populations, then multiplied by 100, then subtracted from 100. The result was that zero entries in the original distance matrix would receive a similarity score of 100, while the pair of populations with greatest distance in the original distance matrix would receive a similarity score of 0. Thus, two populations with the exact same enrichment score would have 100% similarity (*348*). To compare populations, median RMSD scores were compared using a two-tailed, student’s T test.

Code availability. Original data sets are provided as FCS files in Flow Repository and as Excel files. Software for calculating EMD and displaying it as a heat map is available as Supplementary Software. Software for generating MEM scores is available in the Supplementary Software of Diggins, *et al* (*348*) (http://mem.vueinnovations.com/).

Data availability

Data Set 1

Peripheral blood from melanoma patients treated with αPD-1 and healthy peripheral blood controls, is available as FCS files in Flow Repository. SNaPshot genotyping was done in the clinic on tumors resected from each patient. Forty-eight mutations in NRAS, BRAF, KIT, CTNNB1, and GNAQ were monitored (*374*).

Data Set 2

Peripheral blood from AML patients treated with chemotherapy, shown in Figure 6.5, was generated by CyTOF analysis as described by Ferrell, *et al. (328)* and is available as FCS files in Flow Repository (http://flowrepository.org/id/FR-FCM-ZZMC). Patient characteristics and treatment details are available in Ferrell, *et al*.

Data Set 3

Serially biopsied melanoma tumors from patients treated with BRAFi and MEKi were generated in separate mass cytometry experiments. Patients MP-034, MP-029, MP-031, MP-032, MP-055, and MP-059 were stained with the mass cytometry panel described in Supplemental Table 6.2. Patients MP-019, MP-023, MP-054, MP-052, and MP-062 were stained with the panel described by Doxie, *et al* (in preparation). FCS files are available in Flow Repository. SNaPshot genotyping was done as described above.

Additional Data

Data for Figure 6.4 were generated by us in separate mass cytometry studies characterizing untreated melanoma tumors, glioblastoma tumors, and non-malignant tonsil and adenoid. FCS files are available in Flow Repository. Renal cell carcinoma tumors RC-29, RC-37, and RC-52 were published by Siska *et al* (*372*) and SEB stimulated PBMC were published by Nicholas *et al* (*327*).

Data sets used in the RMSD heatmap are described by Diggins, et al (*348*).

Supplementary Table 6.1. Patient Information for Blood and Tissue Donors, Related to Figures 1-4, and 6

Patient ID	Timepoint	Age	Gender	Malignancy	Sample Type	Tumor Site	Genotype	Prior Treatment	Ongoing Treatment	Citation
MP-019	Baseline	43	M	Melanoma	Tumor	Axillary LN	$BRAF^{V600E}$	None	Untreated	Doxie, et al. *Under review*
	Week 4					Axillary LN			Dabrafenib + Trametinib	
MP-054	Baseline	62	M	Melanoma	Tumor	Neck, Back	$BRAF^{V600E}$	None	Untreated	
	Week 4					Neck, Back			Dabrafenib + Trametinib	
MP-023	Baseline	69	M	Melanoma	Tumor	Cervical LN	$BRAF^{V600E}$	None	Untreated	
	Week 4					Cervical LN			Dabrafenib + Trametinib	
MP-029	Baseline	41	F	Melanoma	Tumor	Axillary LN	$BRAF^{V600E}$	None	Untreated	
	Week 4					Axillary LN			Dabrafenib + Trametinib	
MP-031	Baseline	28	F	Melanoma	Tumor	Axillary LN	$BRAF^{V600E}$	None	Untreated	
	Week 4					Axillary LN			Untreated	
MP-032	Baseline	47	F	Melanoma	Tumor	Chest	$BRAF^{V600E}$	None	Dabrafenib + Trametinib	
	Week 4					Chest			Untreated	
MP-034	Baseline	63	F	Melanoma	Tumor	Groin, thigh	$BRAF^{V600E}$	None	Untreated	
	Week 4					Groin, thigh			Dabrafenib + Trametinib	
MP-055	Baseline	53	F	Melanoma	Tumor	Neck, scalp	$BRAF^{V600E}$	None	Untreated	
	Week 4					Neck, scalp			Untreated	
MP-052	Baseline	37	M	Melanoma	Tumor	LN, groin	$BRAF^{V600E}$	None	Dabrafenib + Trametinib	
	Week 4					LN, groin			Untreated	
MP-059	Baseline	75	F	Melanoma	Tumor	Thigh	$BRAF^{V600E}$	None	Dabrafenib + Trametinib	
	Week 4					Thigh			Untreated	
MP-062	Baseline	79	M	Melanoma	Tumor	Neck, scalp	$BRAF^{V600E}$	None	Dabrafenib + Trametinib	
	Week 4					Neck, scalp			Untreated	
MP-004	n/a	52	M	Melanoma	Tumor	LN	$BRAF^{V600E}$	None	n/a	
MP-013	n/a	69	M	Melanoma	Tumor	Axillary LN	WT	None	n/a	n/a
MP-015	n/a	41	F	Melanoma	Tumor	Cervical LN	$NRAS^{Q61R}$	Chemotherapy	n/a	n/a
MP-039	n/a	37	M	Melanoma	Tumor	LN	$NRAS^{Q61R}$	None	n/a	n/a
MP-049b	n/a	60	M	Melanoma	Tumor	Small bowel	$NRAS^{Q61R}$	None	n/a	n/a
MB-004	Baseline	70	M	Melanoma	PBMC	n/a	$BRAF^{V600R}$	Vemurafenib, Dabrafenib+ Trametinib	None	n/a
	Week 3					n/a			Pembrolizumab	n/a
	Week 12					n/a			Pembrolizumab	n/a
	Month 6					n/a			Pembrolizumab	n/a
MB-005	Baseline	66	M	Melanoma	PBMC	n/a	NF1 (FM)	Ipilimumab	None	n/a

	Week 3					n/a			Pembrolizumab	n/a
	Week 12					n/a			Pembrolizumab	n/a
	Month 6					n/a			Pembrolizumab	n/a
MB-006	Baseline	59	M	Melanoma	PBMC	n/a	$NRAS^{Q61}$ (FM)	None	None	n/a
	Week 5					n/a			Pembrolizumab	n/a
	Week 12					n/a			Pembrolizumab	n/a
	Month 6					n/a			Pembrolizumab	n/a
MB-007	Baseline	77	M	Melanoma	PBMC	n/a	$BRAF^{V600E}$ (FM)	Ipilimumab, Dabrafenib+ Trametinib	None	n/a
	Week 3					n/a			Pembrolizumab	n/a
MB-008	Baseline	49	F	Melanoma	PBMC	n/a	$NRAS^{Q61R}$	Ipilimumab, Palbociclib+ Trametinib	None	n/a
	Week 3					n/a			Pembrolizumab	n/a
	Week 12					n/a			Pembrolizumab	n/a
	Month 6					n/a			Pembrolizumab	n/a
MB-009	Baseline	74	F	Melanoma	PBMC	n/a	TET2 subclonal, TP53 R110P, RB1 splice	Ipilimumab	None	n/a
	Week 3					n/a			Pembrolizumab	n/a
	Week 12					n/a			Pembrolizumab	n/a
	Month 6					n/a			Pembrolizumab	n/a
MB-010	Baseline	63	M	Melanoma	PBMC	n/a	$BRAF^{L597}$ (FM)	Ipilimumab	None	n/a
	Week 3					n/a			Pembrolizumab	n/a
	Week 12					n/a			Pembrolizumab	n/a
	Month 6					n/a			Pembrolizumab	n/a
MB-012	Baseline	62	F	Melanoma	PBMC	n/a	NF1 (FM)	Ipilimumab	None	n/a
	Week 3					n/a			Pembrolizumab	n/a
	Week 12					n/a			Pembrolizumab	n/a
	Month 6					n/a			Pembrolizumab	n/a
MB-013	Baseline	75	M	Melanoma	PBMC	n/a	NF1, $BRAF^{G593I}$ (FM)	Trametinib	None	n/a
	Week 6					n/a			Pembrolizumab	n/a
	Month 6					n/a			Pembrolizumab	n/a
MB-041	Baseline	41	M	Melanoma	PBMC	n/a	$BRAF^{V600E}$	Ipilimumab	None	n/a
	Week 3					n/a			Pembrolizumab	n/a
LC-04B	n/a	65	n/a	Glioblastoma	Tumor	Brain	*IDH* wt	Steroids	n/a	n/a
LC-06B	n/a	41	n/a	Glioblastoma	Tumor	Brain	*IDH* wt	Steroids	n/a	n/a
W-5	n/a	60	n/a	Glioblastoma	Tumor	Brain	*IDH* wt	Steroids	n/a	n/a
RC-29	n/a	72	M	Renal Cell Carcinoma	Tumor	Kidney	n/a	n/a	n/a	Siska, et al. (*372*)
RC-37	n/a	54	M	Renal Cell Carcinoma	Tumor	Kidney	n/a	n/a	n/a	
RC-52	n/a	45	M	Renal Cell Carcinoma	Tumor	Kidney	n/a	n/a	n/a	
VUK006	n/a	n/a	n/a	none	PBMC	n/a	n/a	n/a	n/a	Diggins, et al. (*348*)
VUK007	n/a	n/a	n/a	none	PBMC	n/a	n/a	n/a	n/a	
VUK008	n/a	n/a	n/a	none	PBMC	n/a	n/a	n/a	n/a	
VUK026	n/a	n/a	n/a	none	PBMC	n/a	n/a	n/a	n/a	
VU10	n/a	n/a	n/a	none	PBMC	n/a	n/a	n/a	n/a	
VU11	n/a	n/a	n/a	none	PBMC	n/a	n/a	n/a	n/a	
VU14	n/a	n/a	n/a	none	PBMC	n/a	n/a	n/a	n/a	

VU17	n/a	n/a	n/a	none	PBMC	n/a	n/a	n/a	n/a	
VU18	n/a	n/a	n/a	none	PBMC	n/a	n/a	n/a	n/a	
VU11A	n/a	n/a	n/a	none	Adenoid	n/a	n/a	n/a	n/a	n/a
VU19T	n/a	n/a	n/a	none	Tonsil	n/a	n/a	n/a	n/a	n/a
Ad18	n/a	n/a	n/a	none	Adenoid	n/a	n/a	n/a	n/a	n/a
Ad19	n/a	n/a	n/a	none	Adenoid	n/a	n/a	n/a	n/a	n/a

Supplementary Table 6.2. Staining Panels for Mass Cytometry					
Metal	**Antibody**	**Melanoma and iPSC**	**GBM**	**Clone**	**Company**
103	Rhodium (viability)		x	n/a	Fluidigm
141	ICOS	x	x	C398.43	Biolegend
142	CD19	x	x	HIB19	Fluidigm
143	TIM3	x	x	F38-2E2	Biolegend
144	CCR5	x		NP-6G4	Fluidigm
144	CD11b		x	ICRF44	Fluidigm
145	CD4	x	x	RPA-T4	Fluidigm
146	CD64	x	x	10.1	Fluidigm
147	CD20	x	x	2H7	Fluidigm
148	CD38	x	x	HIT2	Biolegend
149	CCR4	x	x	205410	Fluidigm
150	CD43	x	x	84-3C1	Fluidigm
151	CD14	x	x	M5E2	Fluidigm
152	TCRγδ	x	x	11F2	Fluidigm
153	CD45RA	x	x	HI100	Fluidigm
154	CD45	x	x	HI30	Fluidigm
156	CXCR3	x	x	G025H7	Fluidigm
158	CD33	x	x	WM53	Fluidigm
159	CCR7	x	x	G034H7	Fluidigm
160	CD28	x	x	CD28.2	Fluidigm
161	CD32	x	x	RUO	Biolegend
162	CD69	x	x	FN50	Fluidigm
163	HLA-DR	x	x	L243	Biolegend
164	CD45RO	x	x	UCHL1	Fluidigm
165	CD16	x	x	3G8	Fluidigm
166	CD44	x	x	BJ18	Fluidigm
167	CD27	x	x	O323	Fluidigm
168	CD8	x	x	SKI	Fluidigm
169	CD25	x	x	2A3	Fluidigm
170	CD3	x	x	SP34-2	Fluidigm
171	CXCR5	x	x	J252D4	Biolegend
172	CD57	x	x	HCD57	Fluidigm
174	PD-1	x	x	EH12.2H7	Biolegend
175	PD-L1	x	x	29E.2A3	Fluidigm
176	CD56	x	x	CMSSB	Fluidigm
Ir 191/193	Iridium intercalator	x	x	n/a	Fluidigm
195	Cisplatin (viability)	x		n/a	Fluidigm

Chapter VII

CONCLUSIONS AND FUTURE DIRECTIONS

Summary and Significance

The systems wide impact of immunotherapy is not well understood. Given the complex and temporal nature of the immune system, a single cell, systems immune monitoring approach is needed to understand the biological and clinical impact. In this thesis, I describe the development of a biological and computational approach for systems immune monitoring in clinical samples. My work represents a foundation for analysis of and discovery within clinical data sets. When applied to a cohort of melanoma patients receiving anti-PD-1 therapy, the ensemble analysis approach automatically identified a unique case where a patient experienced bone barrow failure. Additionally, when applied to melanoma tumors sequentially biopsied during small molecule inhibitor therapy, this ensemble identified and described a novel T cell type that exists across human cancers, but not in healthy tissue.

In Chapter II (*327*), I worked with Dr. Katherine Vowell to develop a single, high dimensional, mass cytometry panel that faithfully recapitulates 5 flow cytometry panels in its ability to characterize activated T cells. Mass and fluorescence cytometry are quantitative single cell flow cytometry approaches that are powerful tools for characterizing diverse tissues and cellular systems. Here mass cytometry was directly compared with fluorescence cytometry by studying phenotypes of healthy human PBMC in the context of superantigen stimulation. One mass cytometry panel and five fluorescence cytometry panels were used to measure 20 well-established lymphocyte markers of memory and activation. Comparable frequencies of both common and rare cell subpopulations were observed with fluorescence and mass cytometry using biaxial gating. The unsupervised high-dimensional analysis tool viSNE was then used to analyze data sets generated from both mass and fluorescence cytometry. viSNE analysis effectively

characterized PBMC using eight features per cell and identified similar frequencies of activated CD4+ T cells with both technologies. These results suggest combinations of unsupervised analysis programs and extended multiparameter cytometry will be indispensable tools for detecting perturbations in protein expression in both health and disease.

In Chapter III (Greenplate, et al. *accepted JCO Precision Oncology*, November 2017), I apply the mass cytometry panel developed in Chapter II to a clinically relevant and long-studied disease case in order to better understand the systemic immune response to anti-cancer therapy. The promise of precision oncology is that identifying genomic and proteomic alterations will direct the rational use of molecularly targeted therapy. This approach is particularly applicable to neoplasms that are resistant to standard cytotoxic chemotherapy like T-cell leukemias and lymphomas. In this study, we tested the feasibility of targeted next generation sequencing in profiling diverse T-cell neoplasms and focused on the therapeutic utility of targeting activated JAK1 and JAK3 in an index case. Using FoundationOne® and FoundationOne® Heme assays, we performed genomic profiling on 91 consecutive T-cell neoplasms for alterations in 405 genes. An index case of T-PLL is presented which was analyzed by targeted next generation sequencing. The index case of a patient with T-PLL with a clonal JAK1 V658F mutation that responded to ruxolitinib therapy. On relapse, an expanded clone harboring downregulation of the phosphatase, CD45, was identified using mass cytometry. We demonstrate the JAK missense mutations were activating and caused pathway hyperactivation and conferred cytokine hypersensitivity. The results underscore the utility of profiling cases resistant to standard regimens and support JAK enzymes as rational therapeutic targets for T-cell leukemias and lymphomas.

Given the success of systems immune monitoring with mass cytometry in leukemia patients, in Chapter IV (*312*), I move into dissecting systems wide immune response to anti-PD-1 therapy in a melanoma patient. Antibodies aimed at blocking the interaction between PD-1 and its ligands have shown impressive efficacy in a variety of malignancies and are generally well

tolerated. Research has focused intensely on T cells and their interaction with cells within melanoma tumors, while relatively little is understood about the systems immunology of the cells in the blood during checkpoint inhibitor therapy. Longitudinal cytomic analysis using mass cytometry can characterize all the cells in a small sample of blood and has the potential to reveal key shifts in the cellular milieu occurring during treatment. I reported a case of advanced melanoma in which mass cytometry detected abnormal myeloid cells resulting from myelodysplastic syndrome (MDS) in the blood following treatment with an anti-PD-1 agent. Myeloid blasts comprised <1% of peripheral blood mononuclear cells (PBMC) one month after the start of treatment. By 6 months after starting therapy, myeloid blasts comprised 5% of PBMC and a bone marrow biopsy confirmed refractory anemia with excess blasts-2 (RAEB-2). Longitudinal mass cytometry immunophenotyping comprehensively characterized blast phenotype evolution and revealed elevated PD-1 expression on the surface of non-blast myeloid cells. These findings highlight the clinical significance of cytomic monitoring, indicate that the myeloid compartment should be monitored during checkpoint inhibitor therapy, and emphasize the value of systems immunology in medicine.

With increased ability to monitor dozens of proteins simultaneously on a single cell comes the challenge of accurately assigning cellular identity. Proteins once thought to be lineage restricted now appear on a wide variety cells, confounding traditional naming practices. To solve this problem, Dr. Kirsten Diggins developed Marker Enrichment Modeling (MEM), an algorithm that objectively describes cells by quantifying contextual feature enrichment and reporting a human and machine-readable text label (*348*). MEM outperforms traditional metrics in describing immune and cancer cell subsets from fluorescence and mass cytometry. MEM provides a quantitative language to communicate characteristics of new and established cytotypes observed in complex tissues. To this study, I contributed dozens of primary human samples characterized

by mass cytometry, data analysis of classical T cell subsets, and an immunologist's view of cell identity.

In Chapter VI (Greenplate, et al. under review January 2018), I use the tools, methodology, and philosophy developed in previous chapters to characterize and dissect the peripheral blood of melanoma patients treated with anti-PD-1 and sequential human, melanoma tumors treated with small molecule inhibitors. Advances in single cell biology have enabled measurements of >40 protein features on millions of immune cells within clinical samples. However, the data analysis steps following cell population identification are susceptible to bias, time-consuming, and challenging to compare across studies. In Chapter VI, an ensemble of unsupervised tools was developed to evaluate four essential types of immune cell information, incorporate change over time, and address diverse immune monitoring challenges. The four complementary properties characterized were: 1) systemic plasticity, 2) change in population abundance, 3) change in signature population features, and 4) novelty of cellular phenotype. Three systems immune monitoring studies were selected to challenge this ensemble approach. In serial biopsies of melanoma tumors undergoing targeted therapy, the ensemble approach revealed enrichment of double-negative (DN) T cells. Melanoma tumor resident DN T cells were abnormal and phenotypically distinct from those found in non-malignant lymphoid tissues, but similar to those found in glioblastoma and renal cell carcinoma. Overall, ensemble systems immune monitoring provided a robust, quantitative view of change in both the system and cell subsets, allowed transparent review by human experts, and revealed abnormal immune cells present across multiple human tumor types.

In summary, this thesis advances our understanding of cellular identity, systems immune monitoring, and the biology of immune response in melanoma patients receiving anti-cancer therapy. I showed that high dimensional, single cell techniques combined with advanced analysis tools were able to identify cell types that lacked canonical identity markers. Specifically, mass

cytometry and analysis tools viSNE and SPADE were able to group activated T cells lacking CD3 with other T cells. These results open the door to identification of novel and unexpected cell types in heterogeneous, human samples. In fact, applying this panel and analysis, I was able to identify unexpected cell types in two different clinical settings, each with actionable medical treatment. In a patient with melanoma, the identification of immature myeloid blats led to the diagnosis of myelodysplastic syndrome and subsequent change in therapy. I was able to identify an increase in myeloid cells expressing PD-1 at the start of therapy and an increase of activated monocytes over the course of therapy. The implication here is multifaceted. The first implication is that monitoring the immune system over time is far more powerful than a static view of only one time point. It was the change in the peripheral immune milieu that indicated the impact of therapy. The second implication is that immunotherapies, like anti-PD-1, can act on many cell types with unintended clinical consequences. Thus, it is critical to monitor multiple cell types and multiple time points. The discovery of unexpected and evolving cells over the course of therapy led to the development of a quantitative cell identity labeling method, incorporated into an ensemble of analysis tools. I propose 4 key features that must be measured and quantified when executing systems immune monitoring. This is the first ensemble to include quantification of systems plasticity, subset abundance, and population phenotype and novelty. To quantify systems plasticity, I developed a novel method whereby Earth Mover's Distance (EMD) is applied to the axes of a viSNE plot to quantify change and stability. This ensemble is the first step in automated systems immune monitoring in the clinic. It provides multiple views of the immune system and can be used to compare systems across platforms and institutions. When applied to my own systems immune monitoring projects, it revealed remarkable stability in the peripheral blood of melanoma patients receiving anti-PD-1 therapy. Importantly, it revealed an expansion of a novel cell type, T cells lacking CD4 and CD8, in melanoma tumors treated with small molecule inhibitors. These DN T cells were shown to be present across human cancers and phenotypically distinct

from healthy. These cells represent a new path towards understanding anti-tumor immunity and novel target of immunotherapy.

Double negative T cells in human cancer

A major finding in this body of work is the discovery of T cells expressing CD3, but lacking CD4, CD8, and TCRγδ, termed double negative (DN) T cells. They were found to be expanded in the tumors of melanoma patients who received BRAF and MEK inhibitors and were also present in smaller numbers in renal cell carcinoma and glioblastoma tumors. DN T cells found in the tumors had a memory phenotype, expressing high levels of CD45RO and CD44, but lacking expression of CCR7 and CD45RA (Figure 6.6C). As part of the future directions, I propose a thorough investigation of the phenotype, function, and origin of these cells. Below, I will detail what is currently known about DN T cells in human health and disease followed by a hypothesis and experimental plan designed to dissect their function in human cancers.

As described in the thesis introduction, DN T cells are first seen during T cell development in the thymus, where they are first DN then DP before committing to a single positive expression of CD4 or CD8. It is generally thought that only SP T cells expressing either CD4 or CD8 leave the thymus, fully mature. However, it is also known that 1-4% of healthy, human PBMCs is composed of TCRαβ+ DN T cells (*375*). Little is known about these DN T cells and whether they leave the thymus, having never expressed CD4 or CD8 or if they lose expression of their co-receptor after having once expressed it. Studies in mice lend credence to the idea that TCRαβ+ DN T cells found in the periphery are primitive cells that escaped from the thymus during development (*376, 377*) or underwent a rare, alternative development track (*378*). However, recent work with mouse and human cells suggests that DN T cells arise in the periphery from either CD4 or CD8 T cells after intense stimulation (*362, 364, 379*). To address this question, Fischer, et al. performed QRT-PCR analysis on T cell receptor excision circles (TRECs) to assess

whether peripheral DN T cells from humans had the same intrathymic maturation pathway as CD4 and CD8 T cells. During V(D)J recombination during thymic development, extrachromosomal DNA excision products, known as TRECs, are generated. The products are not replicated along with nuclear DNA and are thus diluted as the cells divide (*380*). In 4 of their 7 donors, DN T cells had fewer TRECs, corresponding to 1-4 times more cell divisions than either CD4s or CD8s. This suggests that these cells are not thymic emigrants, but instead, T cell subsets that have expanded in the periphery (*361*). There is no clear cut answer as to where DN T cells originate and it is likely that the origin of DN T cells differs depending on the physiological state of the host. The ability to definitely determine the origin of these cells is hampered by the lack of specific, defining surface markers, transcription factors, or mRNA that mark DN T cells specifically.

Little is known about the phenotype of TCRαβ DN T cells. They are "negatively" characterized, meaning they are characterized by the lack of certain markers. These T cells lack CD4 and CD8, differentiating them from SP TCRαβ DN T cells. They have polyclonal TCRs and lack expression of CD56, separating them from NK T cells (*381*). Preliminary work in mice shows that these DN T cells are indeed TCRαβ+ and express CD44, CD69, and CD28 (*364*). My results using mass cytometry reveal similar results with expression of CD45RO and CD44 being the most distinguishing markers. However, given the novelty of this population, it's possible that these cells express non-canonical T cell markers not commonly measure. In addition to their ill-defined function and phenotype in the healthy mouse and human, almost nothing is known about the role of DN T cells in human cancer. Given that human melanoma, glioblastoma, and renal cell carcinoma tumors are populated by these cells, understanding their development, phenotype, and function can significantly impact the understanding of tumor immunology and the treatment of cancer patients.

The function of DN T cells is also under debate, with some postulating that DN T cells are regulatory and another suggesting that they are effectors, able to kill target cells (*382*). Supporting

the notion that DN T cells are effectors, able to exert killing functions, is the high number of these cells found in the peripheral blood of patients with autoimmune disorders, like myasthenia gravis (MG) or systemic lupus erythematosus (SLE) (*383, 384*). DN T cells in SLE patients were shown to secrete high levels of IL-17, a pro-inflammatory cytokine (*384*). In healthy individuals, gene expression profiling of DN T cells from the peripheral blood show high levels of overlap with expression profiles of CD8 effector T cells. High expression of inflammatory cytokines *IL1b*, *IL8*, and others were also seen (*379*). Strong evidence suggesting the killing power of DN T cells was recently shown when donor-derived DN T cells were able to effectively kill host AML cells *in vitro* and in a patient xenograft model (*385*). In support of a suppressor phenotype, *in vitro* studies have shown that DN T cells are able to suppress CD8 and CD4 T cells (*386*), B cells (*387*), and dendritic cells (*388*). This suppression is almost always cell contact mediated and is executed through granzyme/perforin or trogocytosis of MHC molecules by the DN T cells (*386, 389, 390*). As with the origin debate, it is likely that these cells have different functions depending on the setting.

The wide range of functions of DN T cells and clinical implications in other diseases suggest that DN T cells represent an important, novel target in cancer immunotherapy. DN T cells may represent a new population of effector T cells able to kill tumor cells or they could join other regulatory cells, like MDSCs, as cells that suppress anti-tumor activities. Based on the known biology of DN T cells and the results obtained in Chapter VI, I hypothesize that DN T cells were CD4 expressing T cells that lost expression of their co-receptor through external stimulation and are suppressor cells. In the following paragraphs, I propose experiments to 1) characterize protein surface expression and transcriptomics of DN T cells, 2) dissect the function of tumor-resident DN T cells, and 3) dissect a mechanism through which DN T cells become abundant in tumors.

The first step to understanding the role of DN T cells in cancer patients is to better characterize their phenotype. This first step is similar to the work recently published on the

phenotypic characterization of MDSCs. Identifying a high dimensional phenotype in vitro better enabled tracking and identification in human patients with melanoma (*391*). I propose that DN T cells from human cancer samples and healthy human tissue be characterized using mass cytometry. I have begun some of this work, using the mass cytometry panel developed in this thesis. This preliminary work shows that the DN T cells found in tumor and healthy tissue do not express the TCRγδ receptor (Figure 7.1-a-b). Preliminary fluorescence flow experiments indicate that these cells do indeed express TCRαβ, however future mass cytometry panels should contain this antibody for confirmation. In addition to lacking expression of TCRγδ, DN T cells from cancer patients are largely CD45RO positive, indicating a memory phenotype. They are also positive for CD44, CD43, CD69, and CCR5 (Figure 7.1-c-d). While these markers are positively expressed, they do not distinguish DN T cells from CD8 or CD4 T cells. Despite their activated, memory phenotype, DN T cells are much less likely to express PD-1 on their surface than CD8 T cells found in the same tumor (Figure 7.1-e). This is of interest because, as discussed extensively throughout this thesis, PD-1 expressing T cells are the target for multiple immunotherapies currently used in the clinic. The lack of PD-1 expression on these DN T cells indicates that they are poor targets for the drug and may represent an escape mechanism for the tumor. Further work will need to be done to characterize the inhibitory receptor expression on these cells. I propose that future mass cytometry panels contain key inhibitory markers like TIGIT, Lag3, and Tim-3. Additionally, future phenotypic analysis should look at expression of NK-associated proteins like NKG2D. If DN T cells are able to kill tumor cells, it could be through non-antigen specific mechanisms, similar to NK cells (*392*). Finally, I suggest that transcription factors T-bet, EOMES, and BCL-2 be included in order to properly assess proliferative potential and effector state (*393*).

The next step towards characterization of DN T cells that I propose is genetic profiling. While mass cytometry provides an extensive view of surface and internal proteins, it is unable to

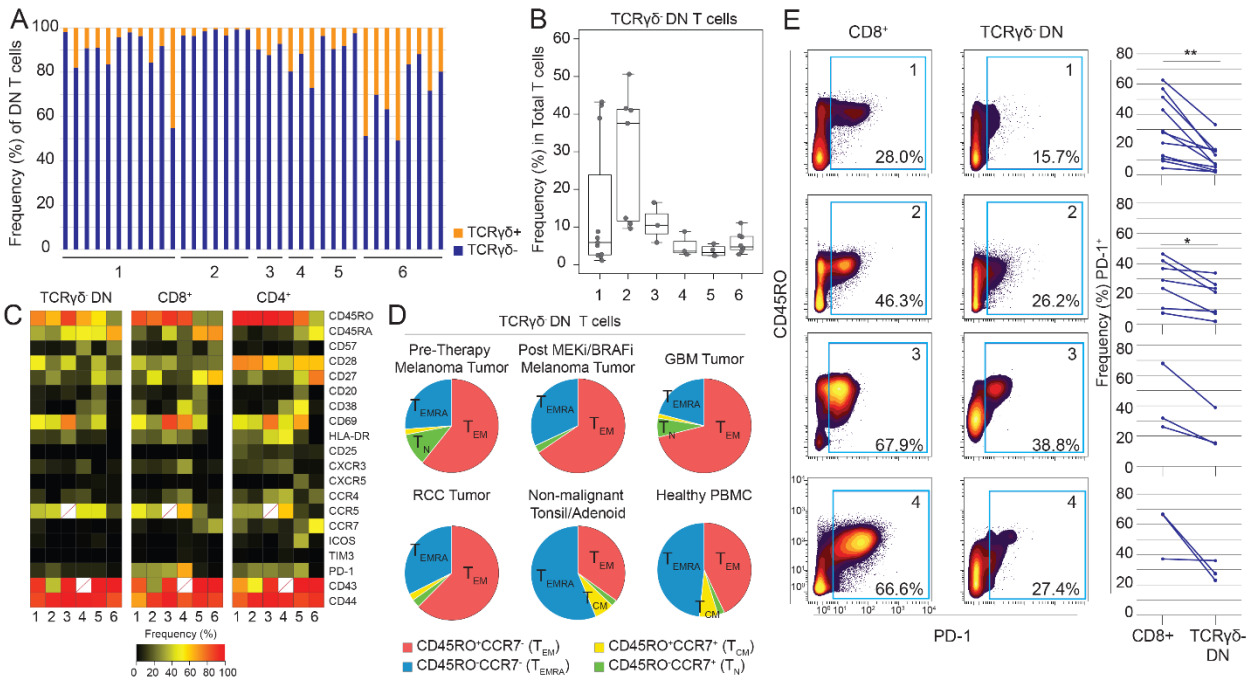

Figure 7.1: Double negative T cells across cancers have a memory phenotype with reduced levels of PD-1. Mass cytometry was used to characterize immune cells from melanoma, GBM, RCC, and healthy control tonsil/adenoid and peripheral blood. a) Bar graphs show the frequency of DN T cells that are TCRγδ+ (orange) or TCRγδ- (blue). Each bar represents an individual patient sample. Numbers indicate sample type. [1. melanoma tumor biopsy prior to therapy, N=11; 2. melanoma tumor biopsy after 4 weeks of treatment with BRAFi and 2 weeks of MEKi, N=6; 3. GBM, N=3; 4. RCC, N=3; 5. non-malignant tonsil or adenoid, N=4; 6. healthy donor PBMC, N=8] b) Frequency of TCRγδ- DN T cells as a percentage of all T cells. c) Heatmaps show the median frequency of positive expression for each marker on the right. d) Pie charts show the median frequency of T cell memory populations (indicated in the legend). e) Biaxial plots show representative plots of PD-1 expression for each tumor type. Frequency of PD-1 expressing CD8+ and TCRγδ- DN T cells is shown (right). Student's two-tailed, paired t-test. *p<0.05, **p<0.01

characterize TCR clonality or mRNA transcript. First, DN T cells from patient samples would need to be sorted to separate them from CD4 and CD8 T cells. I would use CD4, CD8, TCRαβ, and CD19 to produce 4 different aliquots; DN T cells ($TCR\alpha\beta^{+}CD4^{-}CD8^{-}CD19^{-}$), CD4 T cells ($TCR\alpha\beta^{+}CD4^{+}CD8^{-}CD19^{-}$), CD8 T cells ($TCR\alpha\beta^{+}CD4^{-}CD8^{+}CD19^{-}$), and negative control B cells ($TCR\alpha\beta^{-}CD4^{-}CD8^{-}CD19^{+}$). I propose two different techniques that can be used to assess whether or not the DN T cells consist of clonally amplified T cells. The first technique is described by Fischer,et al and involves TCR Vβ gene segment usage on the sorted cell populations (*361*). If a large fraction of the cells used the same TCR Vβ gene segment, it would indicate clonality. CD4

and CD8 T cells would make appropriate internal controls for clonality. B cells would act as a negative control. For a more in depth, single cell approach, the emulsion PCR based technology, like 10x Genomics, could be used to interrogate TCR clonality. If clonality is revealed in the DN T cells, it would indicate an antigen-specific response. It would suggest that a specific, antigen-specific TCR was being triggered, resulting in clonal expansion. If this was the case, it would be critical to 1) assess for shared TCR sequences across cancers, suggesting a shared antigen and 2) take steps to reconstruct the antigenic target. A lack of clonality would suggest a bystander effect of T cells trafficking into or resident in the tumor microenvironment. If this were the case, it would be imperative to dissect the tumor microenvironment for soluble or cell-bound factors that could attack DN T cells from the blood, induce DN T cell expansion, or induce downregulation of CD4 and CD8 on SP T cells.

The final step in characterization of DN T cells is gene expression profiling. This step will provide a more comprehensive view of DN T cells and could provide insight as whether these cells are derived from CD4 of CD8 T cells. Work from Crispin, et al used microarray analysis to show that DN T cells from healthy individuals had a large overlap of gene expression with CD8, but not CD4, T cells (*379*). This could provide evidence that DN T cells seen in the tumor are producing transcript for CD4 or CD8, but are unable to translate it into protein, providing evidence of their origin. I, again, propose the use of single-cell transcript technology, like 10x genomics. Because it requires small amounts of DNA, it is better suited for use with clinical samples. The single cell aspect of this technology would also reveal any heterogeneity within the DN T cell population. Based on the biaxial flow plots in Figure 6.6F, that show low expression of CD4 on T cells prior to therapy and low to no expression post-therapy, I hypothesize that these cells were once CD4 T cells that have been stimulated to lose CD4 expression. Because of this, I believe that gene expression profiling with reveal a large overlap in gene expression between intratumoral CD4 and DN T cells. The results of the gene expression profile will provide direction for functional

analysis and insights into the origin of these cells as transcripts for effector molecules, like cytokine, would also be measured.

I hypothesize that these tumor resident DN T cells are suppressor cells that negatively impact clinical outcome. I would use the results of the characterization assays to inform the next phase of experiments where I would determine the function of these DN T cells. To determine whether DN T cells are killers or suppressors, I would first measure intracellular cytokines, granzyme B, and perforin levels after stimulation. To accomplish this, I would use plate bound antibodies against CD3 and CD28 to stimulate single cell mixtures from human tumors and tonsils for three hours in the presence of brefeldin A and/or monensin. I would then use a mass cytometry panel, focused on intracellular cytokines and effector molecules to measure the production of functional proteins. The specific cytokines chosen will be influenced by the results of the transcriptional analysis. For example, high levels of *IL2* transcript would cause me to include IL-2 in my mass cytometry panel. Using a fluorescence flow approach, it was shown that DN T cells from the blood of healthy humans can be induced to express IL-1, IL-10, and IL-8 (*379*). This mixture of inflammatory, IL-1, and anti-inflammatory, IL-10, cytokines within the same cells indicates the complex nature of their biology and is evidence of the need for high dimensional analysis techniques. I hypothesize that DN T cells in tumors will produce anti-inflammatory cytokines, like IL-10, but also effector molecules like granzyme B and perforin.

Because it is likely that DN T cells could produce both suppressive and killing molecules after stimulation, it will be important to assess their ability to suppress target cells directly. To do this, I would perform an allogenic, 3-way mixed lymphocyte reaction (MLR) experiment. The goal is to assess the ability of DN T cells to suppress T cells proliferation in the presence of allogenic DCs. To conduct this experiment, I would purify T cell from PBMCs using magnetic bead isolation. I would then derive DCs from allogenic PBMCs as previously described (*391*). These T cells and DCs would be cultured with sorted DN T cells from tumors, along with sorted $CD8^+$ and

$CD4^+CD25^+$ T cells as negative and positive controls, respectively. The reaction would go on for 5 days with proliferation measured by thymidine uptake. If just the PBMC-derived T cells and DCs were mixed together, the recognition of foreign MHC by T cells would result in T cell proliferation. However, if the DN T cells were suppressor cells, their presence in the culture would reduce the PBMC-derived T cell proliferation. If the cells were suppressors, the next step would be to determine whether suppression is mediated by cell:cell contact or through soluble factors. To address this, the 3-way MLR would be conducted in a transwell plate where the DN T cells were either present with the PBMC-derived T cells and DCs or on the separated from them via a membrane that allows the passage of soluble proteins. I hypothesize that in the 3-way MLR, DN T cells would act as suppressors and that this suppressive behavior is cell contact dependent.

By increasing our depth of knowledge of the phenotype and function of these cells, it will be possible to target them to improve immunotherapy and patient outcome. For example, if the cells are indeed suppressive, the knowledge gained from the phenotypic characterization could produce a new target for mAb therapy designed to deplete these cells. If they are suppressive via soluble factors, drugs designed to block or inhibit the function of these soluble factors could be developed. If DN T cells in the tumor microenvironment are not suppressors, it will be critical to understand whether they are exhausted or still able to exert effector functions. Phenotypic profiling of inhibitory receptors like PD-1 and Tim-3, along with transcription factors T-bet and Eomes, will provide a clearer understanding of the functional state. If these cells are exhausted, it will be important to target expressed inhibitory receptors with antibody blockade. Because these cells were seen across human cancers, it is possible that proposed therapeutics could be tested against a wide range of diseases.

Machine learning for human health

The work done in this thesis combined investigation of clinical biology and the development of computational tools required to analyze the high dimensional data produced by large study cohorts that monitor patients over time. Since the start of my thesis research, the mass cytometry field and computational tools that accompany it have expanded greatly. Prior to 2013, few mass cytometry studies were performed outside of Stanford University and Vanderbilt was the 17th institution to acquire a mass cytometer. Metal conjugated antibodies were limited and normalization beads were not commercially available. As mass cytometry became better understood and more broadly applied, computational tools raced to catch up. Of note, viSNE was not introduced to the immunology community until 2013 and at that time, the algorithm was only able to analyze 100,000 events (*231*). In only a few short years, mass cytometry has become a fixture in the immunologists' toolkit. Mass cytometry has revealed clinical correlates to drug response (*343, 394*) and begun to populate atlases of human and mouse cell identity (*219, 366, 395*). I have been a part of this advancement of mass cytometry and data analysis through my work developing mass cytometry for solid tumors (*396, 397*) and the development of tools designed to quantitatively provide cell identity (*348*). As the technology advances, so do the complexity of problems that can be addressed. Mass cytometry has now been adapted for imaging, resulting in quantitative, 30 parameter images that contain positional identity (*398*). Groups have been working towards simultaneous measurement of both protein and RNA in the same cell (*399*). High-dimensional, single-cell technologies and their associated analysis platforms will continue to advance given additional time, funding, and effort. The impact of these single cell technologies is not simply in the database of information they generate, but how that database is harnessed to improve human health.

Machine learning algorithms designed to harness the data generated by mass cytometry and other high dimensional techniques have also drastically improved over the last few years. Tools like Phenograph (*400*), DensVM (*219*), ACCENSE (*334*), and CellCNN (*349*) have been

created to automatically subset cells into populations. MEM, described in Chapter V, produces a vector of information that can be used to compare cell subsets across platforms and research centers (*348*). The value of this vector was shown in Chapter VI where DN T cells were compared across different human tumors and tissues even though they did not share the same mass cytometry panels. This work provides the foundation for a data base of cell identity where users can compare their subset of interest to thousands of subsets generated and published on by researchers around the world. The idea of using both the spread and magnitude of the data to create an enrichment label applies not only to cells, but to patients and their data as well. In and out of the hospital, humans are generating hundreds of thousands of data points from nutrition and walking steps logged into fitness devices to music listened to through streaming applications to data compiled in electronic medical records (*401, 402*). With all of this data on so many humans, high dimensional data analysis and machine learning is poised to revolutionize patient care and outcome in medical facilities. In Chapter IV, I describe the identification of a melanoma patient who develops MDS during treatment with anti-PD-1 therapy. This discovery was made after I poured over the mass cytometry data and clinicians poured over her medical charts for months. This human, expert driven analysis was time consuming and in Chapter VI I use EMD on the tSNE axes to identify this patient within a matter of seconds. Its cases like these that are ripe for machine learning. As the technology progresses, it's likely that mass cytometry will integrate into the clinic (Figure 7.2). I envision mass cytometry will be used to monitor the systemic immune response in patients receiving therapy. Algorithms designed to clusters cells, like FlowSOM (*403*), will segment cells into populations and MEM will be run with a common reference population to generate an enrichment label. That label could then be compared to a database of enrichment labels and given a similarity score to help diagnose and monitor the patient. In the case of my MDS patient, this work flow could have automatically identified a small population of cells with high degrees of similarity to MDS blasts. This would have informed the doctor and impacted her

therapy immediately, instead of within the 8 month time window in which the disease was actually caught. In addition to quickly monitoring and adjusting patient care regimens, the data generated in real time will be able to accelerate the scientific discovery process (Figure 7.2).

It's highly unlikely that a single technology will revolution patient care. Instead, the sum of all useful technology creates an ecosystem of useful art, termed the technium, which pushes the world forward (*404*). The technium, populated by high dimensional, single cell technologies and their accompanying data analysis platforms is ever growing and poised to greatly impact medical care.

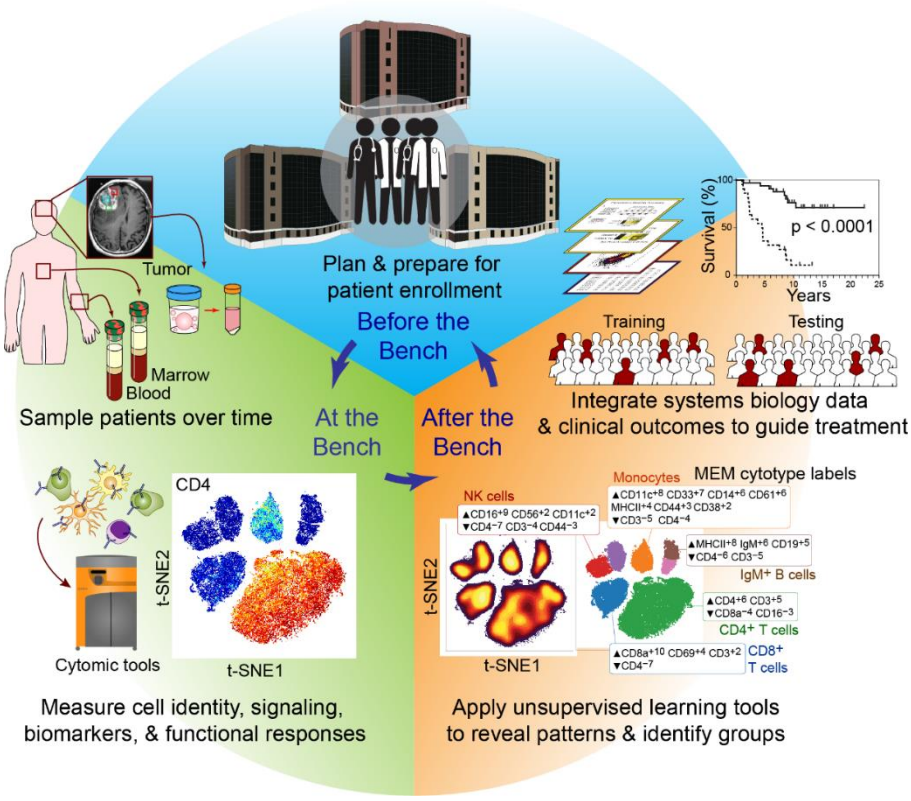

Figure 7.2. Overview of clinical mass cytometry research. Clinical mass cytometry studies consist of multiple steps. At the bedside, physicians determine study questions by choosing when to sample patients, which tissues to sample, and by identifying control groups. In collaboration between the bedside and bench, patients are sampled over time and live single cells are isolated and viably cryopreserved. At the Bench, researchers use cytomic technologies like mass cytometry and choose key cellular features to test biomarkers and test basic and translational research hypotheses. After the Bench, computational biologists use combinations of machine learning tools, expert knowledge, and mathematical modeling to identify clinically and biologically relevant cell types and to characterize changes in tissues. Between the bench and the bedside, systems approaches are used to integrate bench and clinical research information to reveal patient groups, stratify risk, and match treatments to cellular features observed in patient samples. *Diggins, et al. Under review*

Appendix A

DISSECTING COMPLEX CELLULAR SYSTEMS WITH HIGH DIMENSIONAL SINGLE CELL MASS CYTOMETRY

Authors: Mikael Roussel, Allison R. Greenplate, and Jonathan M. Irish

This work appears in manuscript form as published in *The Human innate Immunity Handbook* 2016 (Roussel, et al. 2016).
http://www.worldscientific.com/doi/abs/10.1142/9789814678735_0002

Introduction

Analysis at the single cell level is crucial for characterizing cells within complex, heterogeneous populations (*208*). This chapter explores the history of single cell biology in the mononuclear phagocyte system and the contributions that new measurement and analysis tools have made to describe these cells. Mononuclear phagocytes represent a particular challenge due to the large number of phenotypes that these cells adopt after maturation and infiltration into tissues. The ability of fluorescent flow cytometry to interrogate individual cells has driven the modern era of immunology and revealed the details of the innate immune system. However, spectral overlap constrains the number of parameters that are routinely measured. Mass cytometry is a high dimensional, quantitative, single cell flow cytometry approach that uses time of flight mass spectrometry as a detection tool (*9*). By coupling antibodies to metal isotopes instead of fluorophores, mass cytometry using a Cytometry by Time of Flight (CyTOF) instrument circumvents limitations of fluorescent spectral overlap and endogenous cellular auto-fluorescence and enables simultaneous measurement of more than 35 cellular features. The quantitative, high-throughput nature of mass cytometry has sparked a new era of comprehensive single cell biology studies of complex cellular systems (*202, 405*) .

The mononuclear phagocyte system

Early observations

From the start, phagocytes were described using light microscopy as cells that could engulf other particles, such as pathogens (Figure A.1). With the development of the cluster of differentiation system (*406*), great strides were made in tracking and characterizing heterogeneous populations of mononuclear phagocytes (*407-409*). A consensus emerged that monocytes could be divided into key subsets using surface markers, and three functional subsets were termed “classical”, “intermediate”, and “non-classical” based on contrasting expression of CD14 and CD16 (Figure A.1) (*410, 411*). However, these definitions were recognized as incomplete from the start, and much effort has been put into identifying additional markers of cell subsets. For example, CCR2 and Tie-2 have been associated with contrasting polarization roles in down- and up- regulating the inflammatory phenotype, respectively (*412, 413*).

Phenotype and function vs. lineage identity

In contrast with adaptive immune cells, mononuclear phagocytes are not defined by lineage-restricted cell surface signaling complexes. Intracellular signaling and signals received do play crucial roles in polarization, but signaling receptors are not thought to specifically define monocyte or macrophage subsets. Many markers that are closely associated with myeloid cell function and identity are expressed on other cells, including CD14 on endothelial and epithelial cells (*414*) and HLA-DR on B cells, activated T cells, and cancer cells of diverse origins, including neural origin melanoma cells (*415*). The cells known as “mononuclear phagocytes” include monocytes, dendritic cells, and tissue resident macrophages (*416*). The main difference between this term and “myeloid cells” is the implication of lineage origin; some mononuclear phagocytes originate from outside the myeloid lineage (*408*). The apparent convergent development of mononuclear phagocytes from different lineages raises the fundamental question: are cell populations defined by lineage ancestry or by phenotype and function (*416, 417*)?

Complexity in biology and nomenclature: polarization subsets, M1 vs. M2, TAMs, and MDSCs

Reference panels for blood monocyte evaluation include three core markers, HLA-DR, CD14, and CD16 (*410, 418-420*). Other commonly used markers include CD13, CD33, and CD11b, which have been proposed to decipher monocyte maturation and differentiation in bone marrow and blood (*421*). During infection, monocytes migrate through tissues where they can differentiate in dendritic cells or macrophages.

Within tissues, CD68 and CD163 are frequently proposed to characterize macrophage types (*422*). These cell populations, which are involved in tissue homeostasis and host defense, were historically split into classically-activated or “M1” and alternatively-activated or “M2”. M1 polarization occurs in response to IFNγ or LPS stimulation and is associated with an increase of inflammatory cytokines and tumoricidal capabilities. In contrast, IL-4, IL-10, or IL-13 stimulation polarizes macrophages to an M2 associated with tissue repair, pro-angiogenesis, and a lack of effective tumor immunity. In fact, these two types capture functions that are part of a wide spectrum of overlapping polarization states that depend largely on programming from external stimuli (*422, 423*).

Tumor-associated myeloid cells can exhibit immunosuppressive properties mediated by soluble or membrane-bound factors such as TNF, IL-10 or CD163. The identification of the mechanisms responsible for the selective recruitment and acquisition of an immunosuppressive phenotype is the subject of intense research (*424*). Indeed, manipulating locally the immune microenvironment by blocking recruitment of precursors or altering the suppressor cells *in situ* may improve antitumor immune responses. One approach to this is to selectively reprogram macrophages to promote anti-tumor immunity (*425*). In most cancers, macrophages are the most abundant tumor-infiltrating immune cells. Tumor-associated macrophages (TAM) are immunosuppressive and often exhibit M2 characteristics that include expression of immunoregulatory molecules (e.g. B7-H4), an IL-12^{low} IL-10^{high} secretion profile, and the capacity

to inhibit effector T cell functions. TAMs thus represent an attractive target for immunotherapies directed at the tumor microenvironment. An improved understanding of macrophage phenotype would greatly aid in selectively targeting functionally distinct macrophage subsets.

Human myeloid derived suppressor cells (MDSCs) can also exhibit anti-tumor activity, but are distinct from TAMs in that they include myeloid cells other than macrophages and function in healthy regulatory contexts and diseases other than cancer. MDSCs are generally divided into two groups: monocytic and granulocytic MDSCs (*426, 427*). MDSCs suppress both innate and adaptive anti-tumor immunity through mechanisms including: T_{reg} development, deprivation of essential amino acids, and release of oxidizing molecules(*428*). In cancer, MDSCs are recruited and activated by soluble factors secreted both by cancerous and host stromal cells within the tumor microenvironment (*426, 428*). MDSCs are a major contributor to immune dysfunction of patients with significant solid tumor burdens (*426*). The relationships between MDSCs observed in cancer and TAMs are not well understood, and it is not known to what extent cancers of the myeloid lineage depend on distinct properties of TAMs and MDSCs.

While phenotypically distinct subsets of monocytes, macrophages, TAMs, and MDSCs have focused functional roles (*429-432*), it remains clear that the mononuclear phagocyte system is a broad *continuum* of phenotypes and that the classification systems are partially overlapping. Recently, mouse innate immune cells were comprehensively characterized using a 38-antibody mass cytometry panel (*219*). A comparable high dimensional mass cytometry and machine learning study of human mononuclear phagocytes could help to bring clarity to this system.

Revisiting the mononuclear phagocyte system with high dimensional single cell analysis

Mass cytometry and machine learning

The ~5 to 10 fold increase in the number of per-cell features routinely measured in mass cytometry experiments has resulted in a massive increase in data complexity and revealed unexpected phenotypic patterns on well-studied cell populations. Traditionally, flow cytometry

data are analyzed manually using biaxial gates. This type of analysis is highly susceptible to bias and requires prior knowledge of phenotype – a major limitation in the setting of disease. Additionally, traditional biaxial gating is impractical, since a routine CyTOF experiment measuring 32 features would produce 496 possible biaxial combinations that might still incompletely represent multidimensional phenotypic continuums. This problem has been extensively researched in the field of machine learning, where multidimensional analysis, clustering, and trajectory analysis are common themes (*194, 219, 411, 433-436*). Advances in computational biology have helped power high dimensional single cell biology and have provided researchers with powerful dimensionality reduction and cell classification tools.

SPADE and viSNE are unsupervised tools that can reduce high-dimensional data to a 2D map. Spanning-tree progression analysis of density-normalized events (SPADE) and is an unsupervised machine learning tool that clusters cells into nodes based on selected features (*407-409, 433*). SPADE clusters cells into groups (represented by a circle) and organizes those groups into a hierarchy of related phenotypes (*202, 410, 411, 434*). Statistics are displayed for each group (*412, 413, 433*). More recently, Amir and colleagues adapted the t-stochastic neighbor embedding (t-SNE) algorithm to create a tool called visualization of t-SNE (viSNE) (*416, 435*). viSNE software arranges single cells on a 2 dimensional 'map' based on their phenotypic similarity to each other in high-dimensional space, where 'islands' on the map are comprised of phenotypically similar cells (*410, 418-420, 435*). A heatmap where color represents protein expression on cells can be used to characterize the results of both viSNE and SPADE. Cellular abundance is represented by the size of the population in SPADE, whereas viSNE represents cellular abundance with a separate density map, comparable to that of a contour plot. Both of these tools analyze data in an unsupervised fashion, reducing individual bias and allowing for identification of cell populations with unusual or novel phenotypes (*208, 421*). The use of tools

like SPADE and viSNE in combination with mass cytometry has resulted in better characterization of many cell types, including the cells of the myeloid system (*219, 422*).

Mass cytometry's contributions to myeloid biology

Recent papers have shed light on the myeloid compartment by using mass cytometry to characterize human and mice cell populations (*194, 219, 429-432, 436*). Bodenmiller et al. profiled the dynamic response and crosstalk among immune cells from 14 blood populations (*194, 219*). Altogether, on 14 non-overlapping PBMC subsets, 12 phosphorylated proteins were analyzed upon 12 different stimuli at 8 time points. This resulted in more than 18,000 conditions tested per sample. After 15 min of LPS stimulation, NFκB phosphorylation was activated on a subset of monocytes expressing $CD14^{pos}$ $HLA\text{-}DR^{int}$. Of note, at 60 min of stimulation, STAT3 became phosphorylated in $CD4^{high}$ T-cells (which are not thought to be able to directly respond to LPS as they lack CD14 / TLR4), suggesting intercellular crosstalk (*194, 426, 427*). The same approach was applied to analyzed the clinical relevance of surgery-induced immune perturbations (*426, 428, 436*). After surgery, a specific $CD33^{pos}$ $CD11b^{pos}$ $CD14^{pos}$ $HLA\text{-}DR^{low}$ subset of monocyte was found expanded with differential phosphorylation of STAT4, CREB, and NFκB (*426, 436*). Interestingly, single cell network profiles were correlated with the patient's clinical recovery (*208, 436*). Thus, these concordant results show the potential of CyTOF to analyze a large number of subsets arising from a heterogeneous population such as myeloid cells, as well as analyze a time-course response with a large number of conditions.

Myeloid complexity also results from the tissue specialization of monocytes into various populations of macrophages (*9, 437, 438*). To decipher the mouse myeloid system across different tissues, Becher et al. used a 38-antibody panel associated with computational tools to build a framework of reference (Figure A.1) {Bendall, 2014 #415;Bendall, 2014 #415;Di Palma, 2015 #414;Becher, 2014 #402}. By using an automated computational method for population identification, they observed known populations of tissue-resident macrophages. Strikingly, innate

immune cell subsets that were not expected to be well defined by their panel turned out to be phenotypically distinct, even though the markers were chosen specifically for myeloid cells. These results point out both an advantage of a high dimensional single cell approach and the fact that much of our knowledge of protein expression is based on focused analysis panels and gating that restricts the view to known, well-described cell populations. Altogether, these results highlight the potential benefits by using CyTOF for in depth studies on the mononuclear phagocyte system heterogeneity.

Future Directions

Over the past 100 years our knowledge of the mononuclear phagocyte system has expanded in tandem with improvements in measurement tools (Figure A.1). Flow cytometry has recently made a leap forward due to the combination of machine learning tools and high dimensional mass cytometry. Critically, this advance may help to resolve the differences in the field around population identity, especially within the area of suppressor cell phenotypes that may represent different descriptions of a largely overlapping population base. Alternatively, the increase in makers and sensitivity for rare cell populations defined by multiple markers may further fracture the identities of mononuclear phagocytes into more and more functionally distinct subsets. Either way, it seems we stand at the start of a new era where population identities within complex cellular systems can be automatically defined, quantified, and compared.

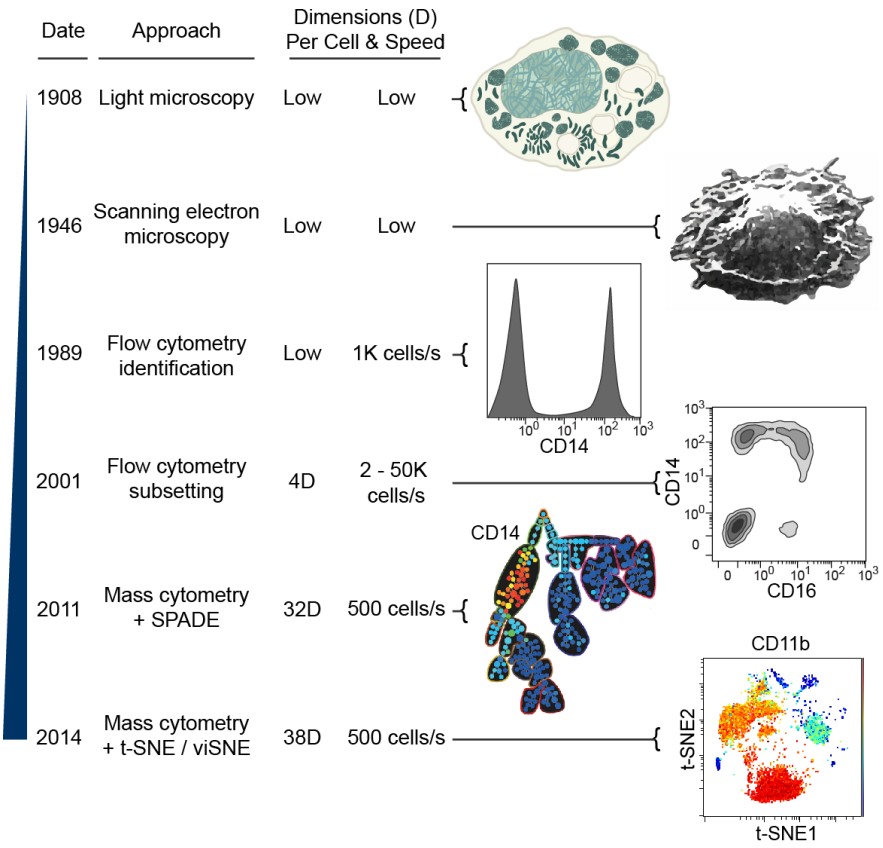

Fig. A.1: Macrophages through the ages: from microscopy to mass cytometry

The first observations of mononuclear phagocytes were made by microscopy in 1908 and noted the presence of lysosomes and the engulfment and destruction of bacteria. In the 1940s, electron microscopy provided a clear view of macrophage shape and the pseudopods that seek extracellular particles and help direct macrophage movement. In 1983, the 3C10 antibody for CD14 and other myeloid lineage antibodies were developed. By 1989, CD14 had become standard in flow cytometry studies of mononuclear phagocytes, but multidimensional analysis was not yet widespread. At the start of the new millennium, multidimensional analysis was becoming mainstream and 2-laser cytometers capable of routine 4-dimensional analysis were widespread. Multidimensional dimensional analysis revealed additional complexity within cells known to be mononuclear phagocytes, and terms like 'classical' $CD14^{pos}$ $CD16^{neg}$ cells, 'intermediate' $CD14^{pos}$ $CD16^{pos}$ cells, and 'non-classical' $CD14^{neg}$ $CD16^{pos}$ were developed based on apparent clusters in 2D flow cytometry. In 2011, mass cytometry characterized all human bone marrow cells with a single 32-antibody panel. Key to this work was the use of the unsupervised clustering tool SPADE, which infers a phenotypic tree of cell population clusters identified in high-dimensional data [34]. In 2014, mass cytometry measurements of eight mouse tissues using a 38-antibody panel developed for the myeloid system created a comprehensive reference map of the myeloid system. This study was also powered by unsupervised dimensionality reduction tools developed for machine learning, including t-SNE and ISOMAP. The 2011 and 2014 studies both relied on unsupervised tools that revealed *cyto incognito* – hidden cells with unexpected phenotypes that would have been overlooked in traditional analysis.

Appendix B

MASS CYTOMETRY DEEP PHENOTYPING OF HUMAN MONONUCLEAR PHAGOCYTES AND MYELOID DERIVED SUPPRESSOR CELLS FROM HUMAN BLOOD AND BONE MARROW

Authors: Mikael Roussel, P. Brent Ferrell, Jr., Allison R. Greenplate, Faustine Lhomme, Simon Le Gallou, Kirsten E. Diggins, Douglas B. Johnson, and Jonathan M. Irish

This work appears in manuscript form as published in *Journal of Leukocyte Biology* 2017 (Roussel, et al. 2017).
http://onlinelibrary.wiley.com/doi/10.1189/jlb.5MA1116-457R/full
License number: 4279380226460, Issued on January 31, 2018

Abstract

The monocyte phagocyte system (MPS) includes numerous monocyte, macrophage, and dendritic cell (DC) populations that are heterogeneous both phenotypically and functionally. In this study, we sought to characterize these diverse MPS phenotypes with mass cytometry (CyTOF). To identify a deep phenotype of monocytes, macrophages, and dendritic cells, a panel was designed to measure 38 identity-, activation-, and polarization- markers including CD14, CD16, HLA-DR, CD163, CD206, CD33, CD36, CD32, CD64, CD13, CD11b, CD11c, CD86, and CD274. MPS diversity was characterized for (1) circulating monocytes from healthy donors, (2) monocyte-derived macrophages further polarized *in vitro* (i.e. M-CSF, GM-CSF, IL-4, IL10, IFN©, or LPS long-term stimulations), (3) monocyte-derived DCs, and (4) myeloid-derived suppressor cells (MDSCs), generated *in vitro* from bone marrow and/or peripheral blood. Known monocyte subsets were detected in peripheral blood to validate the panel and analysis pipeline. Then, by using various culture conditions and stimuli before CyTOF analysis, a multidimensional framework for the MPS compartment was constructed and registered against historical M1- or M2-macrophages, monocyte subsets, and DCs. Notably, MDSCs generated *in vitro* from bone

marrow expressed more S100A9 than when generated from peripheral blood. Finally, to test the approach *in vivo*, peripheral blood from melanoma patients (n = 5) was characterized and observed to be enriched for MDSCs with a phenotype of CD14posHLA-DRlowS100A9high (3% of PBMC in healthy donors, 15.5% in melanoma patients, $p < 0.02$). In summary, mass cytometry comprehensively characterized phenotypes of human monocyte, MDSC, macrophage, and DC subpopulations in both *in vitro* models and patients.

Introduction

The monocyte phagocyte system (MPS) is a complex cellular compartment that includes phenotypically and functionally heterogeneous cells, including monocyte, macrophage, and dendritic cells (DC) populations {Guilliams, 2014 #529}. MPS cells belong to the innate immune system, whose activities can include infection defense, tissue homeostasis and controlling T cell immunity (*439-441*). Phenotypic definition of myeloid cells is variable because of the lack of consistency between markers first identified in mice and humans. For example, while macrophages and myeloid-derived suppressor cells (MDSCs) are typically defined as F4/80high and Gr1pos respectively in mice (*442*), in humans EMR1 (the human F4/80 homolog) is expressed on eosinophils instead of macrophages (*443*), and Gr1 has no human homolog (*444*). Furthermore, there are few unique marker of cell identity, as most of the markers of interest (e.g. CD14, CD11b, CD33, HLA-DR, CD64) are shared by various myeloid cells and none is lineage-specific. Finally, myeloid cells, particularly monocytes and macrophages, are highly plastic with respect to phenotype and function and depend upon various surrounding signals for differentiation/polarization. In the context of cancer or sepsis, an altered myelopoiesis can give rise to suppressive myeloid cells with poor phagocytic activity (*445*). Overall, this complexity of phenotype is highlighted by the growing literature on monocyte, DC, or macrophage nomenclature {Bronte, 2016 #456;Guilliams, 2014 #529;Ancuta, 2015 #457;Ziegler-Heitbrock, 2010

#458;Murray, 2014 #459}. In particular, monocytes are classified in 4 phenotypic subsets (CD14posCD16neg, CD14posCD16pos, CD14dimCD16posSlanlow, and CD14dimCD16posSlanhigh) (*411, 446*), however, within these traditional phenotypes, additional functional subsets have been discovered, such as Tie2-expressing monocytes (TEMs), involved in angiogenesis, or monocytic-MDSCs, involved in T5 cell immune suppression (*445, 447*). Moreover, the paradigm of macrophage polarization has dramatically evolved in the last decade from a binary polarization (classically activated [M1, IFN©- or LPS- driven] vs. alternatively-activated [M2, IL4- or IL10- driven]) to a much more complicated landscape (*448-450*). Recently, Xue and colleagues assessed the transcriptional landscape of multiple activated human macrophage subpopulations generated by numerous *in vitro* stimuli (*451*). At least nine clusters were found to recapitulate macrophage polarization status, in particular an already described regulatory macrophage (M_TPP) associated with tumor necrosis factor (TNF), prostaglandin E2 and TLR2-ligand stimuli (*451-453*). At the protein level, characterization of these heterogeneous cell types has been largely accomplished with "low resolution" approaches (e.g., morphological evaluation and immunohistochemistry), wherein only one or a few proteins were used to identify populations, as an example, CD68 and CD163 are frequently proposed to characterize macrophage types (*422*). High-resolution approaches such as mass cytometry (also known as cytometry by time-of-flight, or CyTOF) are valuable in order to better understand their diversity, function and identify potential targets for novel therapies {Engblom, 2016 #450;Ginhoux, 2016 #463;Greenplate, 2016 #548}. CyTOF combined with high-dimensional analysis, in particular visualization of t-distributed stochastic neighbor embedding (viSNE), spanning-tree progression analysis of density-normalized events (SPADE), and marker enrichment modeling (MEM), are robust methods to identify numerous and novel subsets from heterogeneous populations (*9, 210, 231, 310, 348, 454*). Indeed, several studies using CyTOF have explored the immune compartment including B-, T-, NK-, or myeloid cells either from peripheral blood or from tissues

(*9, 200, 219, 220, 222, 316, 327, 455-460*). In particular, Becher and colleagues developed a myeloid dedicated panel to characterize myeloid cells across eight mice tissues, which revealed previously unidentified populations in mice tissues using an unsupervised approach of CyTOF data (*208, 456*). We hypothesized that human MPS complexity would benefit from a high dimensional single cell approach {Irish, 2014 #209;Greenplate, 2016 #548;Roussel, 2016 #475}. Here, a single mass cytometry panel comprised of 38 antibodies was combined with high dimensional analysis methods with the aim of deciphering the human MPS compartment in primary samples including peripheral blood mononuclear cells (PBMCs) from healthy donors and from patients with melanoma. Results from primary cells were compared to observations from *in vitro* models of myeloid differentiation using human blood and bone marrow cells exposed to established polarizing inflammation factors. Unsupervised analysis tools, including viSNE, SPADE, and MEM, were used to create and describe a comprehensive reference framework for the MPS compartment and to characterize an abnormal abundance of MDSCs in the peripheral blood of melanoma patients.

Materials and Methods

Samples and mononuclear cells preparation

Peripheral blood from healthy donors (HDs) or from melanoma patients was obtained in accordance with the Declaration of Helsinki following protocols approved by Vanderbilt University Medical Center (VUMC) Institutional Review Board. Bone marrow from HDs was obtained under French legal guidelines and fulfilled the requirements of the University Hospital of Rennes institutional ethics committee. Peripheral blood was drawn by venipuncture into heparinized tubes. Bone marrow was obtained by aspiration after sternotomy for cardiac surgery and cells were kept in sodium heparin bags. Mononuclear cells were isolated using Ficoll-Paque PLUS (GE Healthcare Bio-sciences, Uppsala, Sweden) centrifugation. Freshly isolated mononuclear cells

were immediately cryopreserved in FBS (Life Technologies, Grand Island, NY, USA) containing 12% DMSO (Fischer Scientific, Fair Lawn, NJ, USA). For *in vitro* monocyte-derived cells experiments, buffy coats from HDs were obtained according to protocols accepted by the institutional review board at the university hospital from Rennes. After collection, monocytes were purified from PBMC by elutriation before cryopreservation (plate-forme DTC, CIC Biotherapie 0503, Nantes, France). Monocytes represented more than 85% of the cells.

***In vitro* culture and stimulation**

For *in vitro* differentiations, cells were cultured in 6-wells plates at 2x106 cells/mL in a humidified atmosphere at 37°C, 5% CO2 in RPMI 1640 (Mediatech Inc, Manassas, VA) enriched with FCS 10% (Gibco, Life technologies) and supplemented with 1% PenStrep solution (Gibco, Life technologies). MDSCs were derived from 8 peripheral blood- or bone marrow- mononuclear cells. Cells were cultured for 4 days and activations were performed with GM-CSF (40 ng/mL; Peprotech, Rocky Hill, NJ) and G-CSF (40 ng/mL; Peprotech) and, for bone marrow cells, GM-CSF and IL-6 (40 ng/mL; Peprotech) as previously described (*461, 462*). Immature DCs were generated from monocytes by GM-CSF and IL-4 (40 ng/mL; EMD Millipore, Billerica, MA) for 6 days, media were changed at 3 days. Then for terminal differentiation, TNF (10 ng/mL; EMD Millipore) was added in culture for 2 days. Macrophage at baseline (M_b) was generated from monocytes by stimulation by M-CSF (50 ng/mL; Cell Signaling, Danvers, MA) for 3 days, as previously described [16]. Then M_b were further polarized during 3 days, by IL-4, IL-10 (10 ng/mL; Peprotech), IL-6 (10 ng/mL; Peprotech), IFNg (10 ng/mL; Cell Signalling), LPS (10 ng/mL; Sigma-Aldrich, St Louis, MO), or TPP (TNF〈 [10 ng/mL; EMD Millipore]; Pam3CSK4 [100 ng/mL; Invivogen, San Diego, CA]; prostaglandine E2 [1 ⌈g/mL, Sigma]). At the end of each condition culture, except for DCs, wells were treated with Accutase (Sigma Aldrich) prewarmed at 37°C, for 30 sec, before collection, washing and staining.

Allogeneic three-way Mixed Lymphocyte Reaction assay

Suppressive capacities of *in vitro* PBMC- and bone marrow- derived MDSCs were determined in an allogeneic three-way mixed lymphocyte reaction (MLR) assay. T cells were purified from PBMCs from a healthy donor using the Pan T Cell isolation kit (Miltenyi Biotec, Bergisch Gladbach, Germany). DCs and MDSCs were obtained by culture conditions described above. DCs were derived from PBMCs obtained from an allogeneic donor. MDSCs were obtained from 3 donors for PBMCs and 2 for bone marrows. After 4 days of *in vitro* differentiation, CD14posCD33posCD11bposHLA-DRlow

MDSC from bone marrow and monocytes were sorted using a FACS ARIA cell sorter

(BD Biosciences). For MLRs reaction, 1 x 105 T cells of one donor were seeded in culture media with 2,000 allogeneic DCs and different MDSC:T ratio (1:8, 1:4, 1:2). The MLR assays were carried out during 5 days in round-bottomed 96-well plates to ensure efficient DC/T cell contact. T cell proliferation was measured by thymidine uptaking (1 µCi/well) during the last 16 h.

Antibodies, cell labeling and mass cytometry analysis

Purified antibodies from Biolegend (San Diego, CA, USA) or Immunotech (Marseille, France) were labeled using MaxPar DN3 labeling kits (Fluidigm, San Francisco, CA), titrated and stored at 4°C in antibody stabilization buffer (Candor Bioscience GmbH, Wangen, Germany). Antibodies from Miltenyi Biotech (Bergisch Gladbach, Germany) or R&D systems (Minneapolis, MN) were labeled with FITC, PE or APC (Table S1). Antibodies metal-tagged were from Fluidigm. Cell labeling and mass cytometry analysis was performed as previously described {Greenplate, 2016 #548;Ferrell, 2016 #331}. Briefly, cells were incubated with a viability reagent (cisplatin, 25 µM; Enzo Life Sciences, Farmingdale, NY, USA) as previously described (*230*). Then, 3x106 cells were washed in phosphate buffered saline (PBS, HyClone Laboratories, Logan, UT) containing

1% bovine serum albumin (BSA, Fisher Scientific, Fair Lawn, NJ) and stained in 50 µL PBS and BSA 1% containing antibody cocktail. Cells were stained for 30 minutes at room temperature using antibodies listed (Table S1). Cells were washed twice in PBS and BSA 1% and then fixed with 1.6% paraformaldehyde (PFA, Electron Microscopy Sciences, Hatfield, PA, USA). Cells were washed once in PBS and permeabilized by resuspending in ice cold methanol. After incubating overnight at - 20°C, cells were washed twice with PBS and BSA 1% and stained with iridium DNA intercalator (Fluidigm) for 20 minutes at room temperature. Finally, cells were washed twice with PBS and twice with diH2O before being resuspended in 1x EQTM Four Element Calibration Beads (Fluidigm) and collected on a CyTOF 1.0 mass cytometer (Fluidigm) at the Vanderbilt Flow Cytometry Shared Resource. Events were normalized as previously described (*270*).

Data processing and analysis

Data analysis was performed using the workflow already described (*207*). Raw median intensity values were transformed to a hyperbolic arcsine (arcsinh) scale with a cofactor of 5. Analysis was performed on Cytobank using published techniques including SPADE, viSNE and hierarchical clustering (*229, 231*). Each file was pre-gated on singlets and viable cells as defined by cisplatin and iridium gating. The analysis pipeline was as follows: after gating on nucleated cells (Iridiumpos), the labeling was assessed on biaxial plots on CD45pos cells. Then, a viSNE analysis was performed. On the viSNE map, B-, T-, and NK- cells were distinguished, and then the remaining cells were engulfed in a MPS gate, and were further clustered with SPADE. Heat maps were performed using the marker enrichment modeling (MEM) algorithm (*348*).

Statistical analysis

Statistical analyses were performed with GraphPad Prism 5.0 software (GraphPad Software, San Diego, CA, USA) using Wilcoxon or Mann-Whitney tests as appropriate.

Results

CyTOF delineates four monocyte subsets in peripheral blood from HDs

In order to recapitulate the diversity and heterogeneity of monocyte subsets, a CyTOF panel using 38 parameters was designed (Table B.S1). Based on literature profiling, proteins in this panel were expected to be expressed at different levels for MPS cell types and associate with

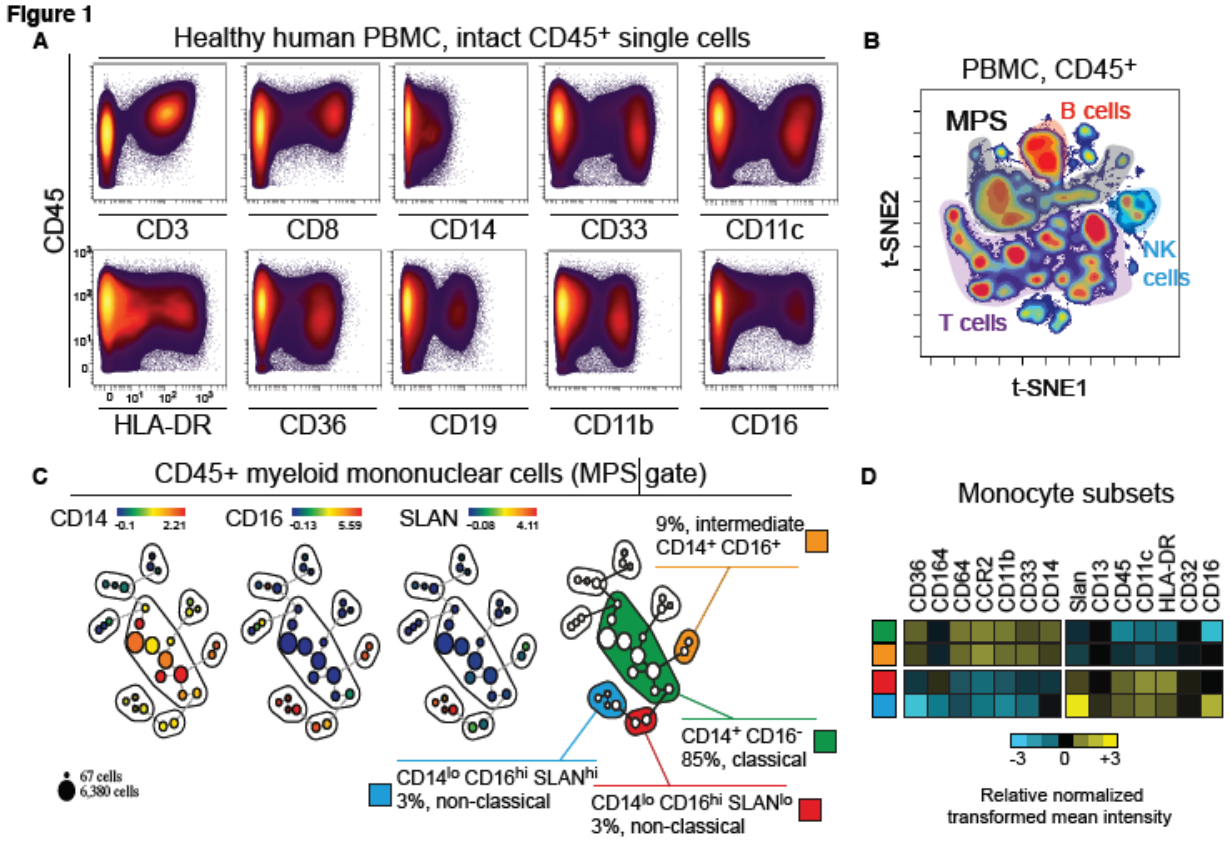

Figure B.1: CyTOF panel and workflow analysis delineates four monocyte subsets in peripheral blood. (**A**) Biaxial plots showing the expression of markers on $Ir^{pos}CD45^{pos}$ PBMC measured by mass cytometry. A representative healthy donor is shown. An arcsinh scale (-5.0 to 104) with a cofactor of 5 was used. (**B**) By mass cytometry analysis >100,000 IrposCD45pos cells were defined on a biaxial plot, before classification on a viSNE algorithm. MPS (>20,000 cells) was gated as remaining cells after the exclusion of B- (CD19pos), T- (CD3pos), and NK- ($CD3^{neg}CD16^{pos}CD45RA^{pos}$) lymphocytes and doublets. (**C**) Events in the MPS gate were then parsed with SPADE into 30 nodes using all clustering markers except CD19 and CD3. $CD14^{pos}$-, $CD16^{pos}$-, and Slanpos- SPADE groups were observed to match classical- ($CD14^{pos}CD16^{neg}$), intermediate- ($CD14^{pos}CD16^{pos}$), non-classical $Slan^{low}$- ($CD14^{dim}CD16^{pos}Slan^{low}$), and non-classical $Slan^{pos}$- ($CD14^{dim}CD16^{pos}Slan^{high}$) monocytes. A representative healthy donor is shown. % represents the frequency among PBMC. (**D**) On the 4 monocyte subsets previously described in (B), heat maps showing the relative normalized transformed mean intensity for various markers tested by mass cytometry, for a representative healthy donor.

differentiation, polarization, and activation states. PBMCs from HDs were first tested and the MPS gate defined with the analysis pipeline (Figure B.1A, B).

To characterize known and expected monocyte sub-populations in peripheral blood (*i.e.* classical, intermediate, and non-classical), the analysis was initially defined to seek 30 nodes representing populations of phenotypically distinct cells. In manual review of the features distinguishing the identified nodes, four groups were apparent. The four phenotypically similar groups of clusters aligned closely with canonical monocyte populations in peripheral blood, namely CD14posCD16neg, CD14posCD16pos, CD14dimCD16posSlanlow, and CD14dimCD16posSlanhigh. These subsets comprised 85%, 9%, 3%, and 3% of monocytes respectively, as expected (*411*) (Figure B.1C). Dendritic cell population SPADE nodes were recognized within the MPS gate as HLA-DRhighCD123high (pDC) or HLA-DRhighCD11chigh (cDC), whereas polynuclear basophils (Pnb) were recognized as HLA-DRlowCD123pos. Finally, the relative expression of additional markers across the monocyte subsets as obtained by mass cytometry was compared (Figure B.1D). Both Slanhigh and Slanlow subsets of non-classical monocytes expressed lower level of CD36, CD64, CCR2, and CD14, consistent with previously published data (*411, 463*). These observations confirmed that the panel design and analysis strategy captured well-established monocyte subtypes.

DCs-, MDSCs- and macrophages- derived *in vitro* from monocyte are profiled by CyTOF

Given that CD14 and CD16, the two central markers used to delineate monocyte subsets in the established nomenclature, show a continuous gradient of expression, we hypothesized that a high-dimensional approach would enhance the characterization of monocytic myeloid-derived suppressor cells (M-MDSC) and macrophage polarization subtypes. *In vitro* derived DCs, MDSCs, and macrophage subsets (M_b, M_LPS, M_IFNγ, M_IL4, M_IL10, M_IL6, and M_TPP)

from peripheral blood monocytes were characterized as a comparison point for *in vivo* studies (Figure B.2A). In vitro subsets were derived according to best practices for characterizing myeloid cell

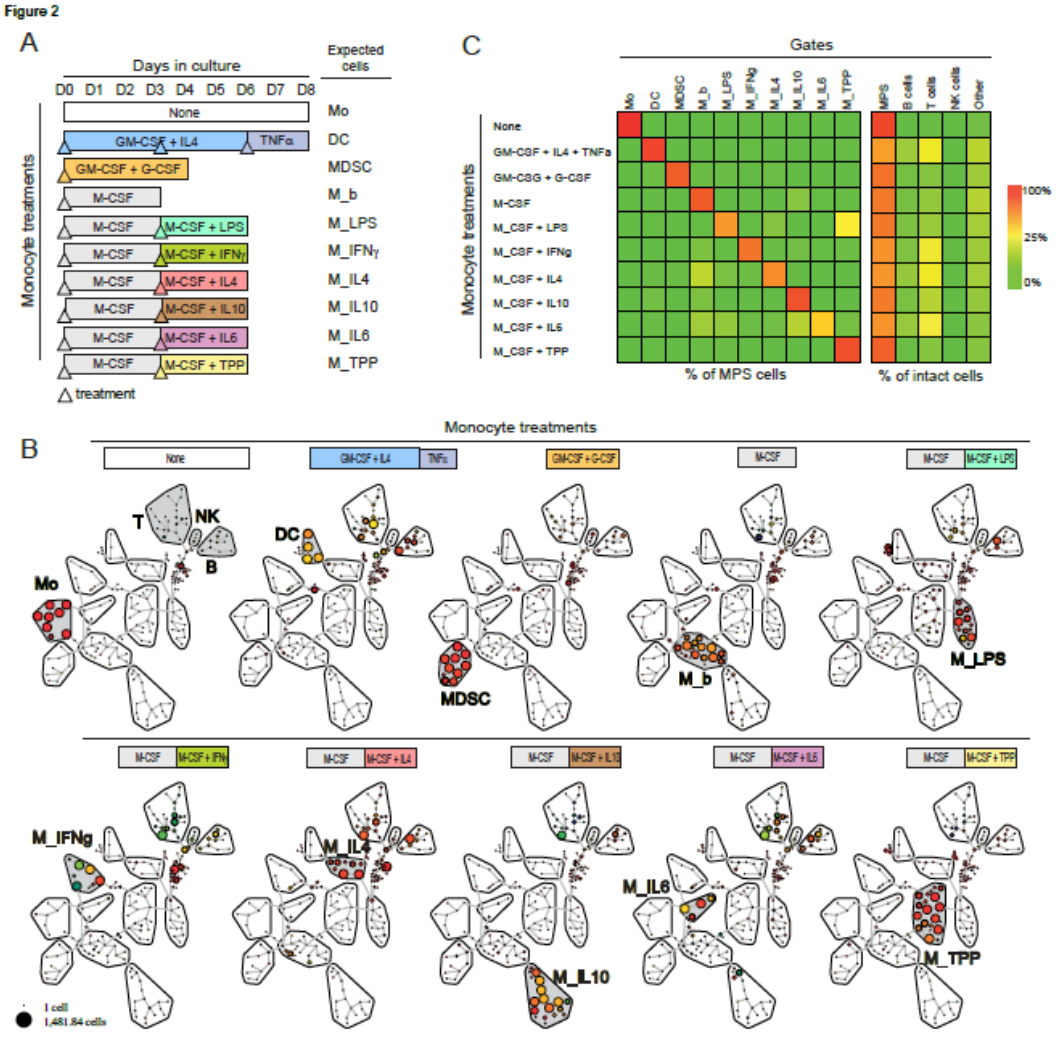

Figure B.2: CyTOF profiles DCs-, MDSCs- and macrophages- derived *in vitro* from monocyte (**A**) Experimental procedure to derived DC, MDSC, and macrophage at baseline (M_b) or polarized under various stimuli (M_LPS, M_IFNγ, M_IL4, M_IL10, M_IL6, and M_TPP [a cocktail including TNFα, PGE2, and Pam3]). Peripheral blood monocytes were obtained from blood donors and purified by elutriation. Expected cells from the stimuli condition are indicated on the right. Days of treatment (colored up-pointing triangle) or of collection (black down-pointing triangle) were specific to the culture condition. (**B**) After CyTOF analysis, cells were defined as IrposCD45pos. Then, a SPADE analysis with 200 nodes and downsampling at 10% was performed. Adjacent nodes with an increase in cells abundance and phenotypic similarity were labeled in red with the name of expected cells from the culture condition. Mo, DC, MDSC, M_b, M_LPS, M_IFNγ, M_IL4, M_IL10, M_IL6, and M_TPP gates are positive for myeloid markers whereas T-, NK-, and B- gates expressed CD3, CD16/CD45RA, CD19, respectively. Nodes outside gates were considered as unclassified (**C**) *Left*- Cell abundance in gate (Mo, DC, MDSC, M_b, M_LPS, M_IFNγ, M_IL4, M_IL10, M_IL6, and M_TPP) reported to MPS gate and related to each condition of stimulation. *Right*- Cell abundance in Mo, DC, MDSC, M_b, M_LPS, M_IFNγ, M_IL4, M_IL10, M_IL6, and M_TPP gates (sum in MPS) and B-, T-, NK gate or unclassified, reported to intact cells (IrposCD45pos) and related to each condition of stimulation. Average percentage of 2 independent experiments.

polarization (*448, 451, 462*). After a SPADE analysis (Figure B.2B), variation of cell abundance under stimulation in each node was summarized (Figure B.2C). Before stimulation, monocytes

comprised 98.6% of the MPS. Under appropriate stimulation, DC, MDSC, and M_b were increased from 0.1% to 76%, 87%, and 78%, respectively, in the MPS gate. After polarization, M_LPS, M_IFNg, M_IL4, M_IL10, M_IL6, and M_TPP were increased from less than 10% to 52%, 66%, 56%, 80%, 40%, and 81%, respectively. Interestingly, some conditions polarized monocytes to more than just one main population. For instance, M-CSF + LPS increased the percentage of cells in the both LPS gate from (0.9% to 53%) and TPP gate (from 3.2% to 22%) (Figure B.2C). Finally, unclassified cells (i.e., those not included in any gate) were below 10% in all conditions. Of note, T cells were increased under IL-4, IFN©, or IL-6 treatments (from 4% in the control to approximately 22% after culture).

MDSCs and polarized macrophages have specific phenotypes

Next, the phenotype of cells types obtained after differentiation of monocytes and polarization of macrophages was examined. To broadly assess the modulation of protein expression, median expression was assessed for each population (Figure B.3A). Average transformed median expression was then calculated from nodes included in each gate identity (Figure B.3B). Monocytes (Mo) were distinguished by high expression of CD33, CD36, and CCR2 and low CD163 and CD274 expression. DCs were CD11chigh and HLA-DRhigh. M_b were CD14, CD206, and HLA-DR positive. Statistical differences between all conditions are summarized in. In particular, various polarized macrophages were compared to M_b (Figure B.3C). M_LPS was distinguished by high levels of CD13 and CD86 and low level of CD163 and CD206 ($P < .01$). M_IL4 was CD274high and CD64low (P<.01). M_TPP expressed CD14high and HL-DRlow ($P < .001$). M_IFNg was CD64high and CD86high ($P < .001$). M_IL10 was CD14high, CCR2high, and

CD163high ($P < .01$), of note CD163 was significantly more expressed in M_IL10 than in M_b ($P < .01$). Finally, M_IL6 was CD11chigh and CD33high ($P < .05$). Then, MDSCs were compared to monocytes (Mo), DCs, and M_b (Figure B.3C). MDSC showed higher expression of CD32, CD206, and CD13 ($P < .05$), and a lower expression of CD36, CD163, S100A9, CD33, and HLA-DR ($P < .05$), when compared to monocytes. Compared to DC, MDSC expressed higher amounts of CD32, CD206, CD64, CCR2, CD14 ($P < .05$) and lower amounts of CD13, CD274,

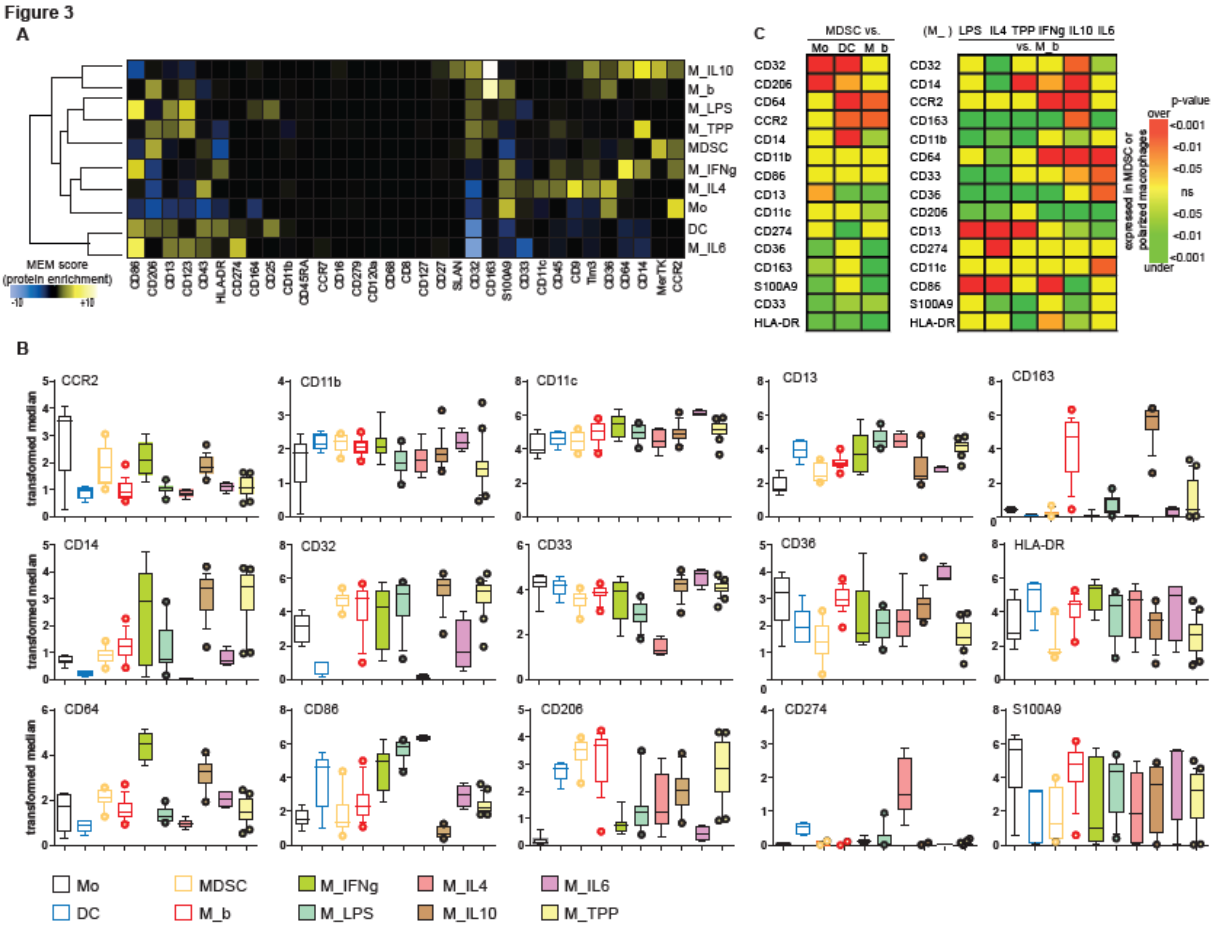

Figure B.3: MDSC and polarized macrophages derived *in vitro* have specific phenotypes
(**A**) For Mo, DC, MDSC, M_b, M_LPS, M_IFNγ, M_IL4, M_IL10, M_IL6, and M_TPP gates, transformed median expression for each marker was averaged from all nodes included in the gate. After normalization, results are shown on heat map after hierarchical clustering. (**B**) Comparison of markers for each node (each dot represents a node). Box and Whisker plots with the 10-90 percentiles and the outliers are shown. Nodes from 2 or 3 different experiments are shown. (**C**) *Left*- Comparison of p-values between MDSC and monocyte (Mo), dendritic cells (DC), and M_b and *Right*- comparison of various polarized macrophage (M_IFNg, M_LPS, M_IL4, M_IL10, M_IL6, M_TPP) to M_b. Rows and columns were arranged after hierarchical clustering (not shown). Only markers at least once statistically different are shown. Unpaired t-tests (parametric or nonparametric as appropriate after normality test) were performed. Yellow: non-significant (ns); Light to dark green: significantly underexpressed in MDSC or polarized macrophages; Orange to red: significantly overexpressed in MDSC or polarized macrophages.

CD33, and HLA-DR ($P < .05$). Finally, comparing MDSC to M_b, higher expression of CD64 and CCR2 was observed ($P < .05$) and lower expression of CD14, CD13, CD11c, CD36, CD163, S100A9, CD33, and HLA-DR was observed ($P < .05$). Peripheral blood derived MDSC were distinguished by the expected low expression of HLA-DR and by an unexpectedly low expression

of S100A9, in contrast to other peripheral blood mononuclear myeloid cell populations, with the exception of DCs.

MDSCs derived from bone marrow are S100A9pos

Published protocols have established methods to derive MDSC, including combining cytokines or culturing peripheral blood or bone marrow. We derived MDSCs from bone marrow to investigate their phenotype following the protocol published by Marigo and colleagues (*461*). As published, we cultured human bone marrow for 4 days with GM-CSF+G-CSF or GM-CSF+IL6 before CyTOF analysis (Figure B.4A). Median protein expression is shown on hierarchically clustered heatmaps (Figure B.4B). A first group of nodes (in green) was mainly CD11cpos, CD11bpos, CD36pos, CD14pos CD13pos, CD64pos, and HLA-DRpos but also CD274pos and CD86pos. These cells displayed heterogeneous expression of S100A9, in particular node #7 (S100A9low) was increased only with GM-CSF+G-CSF. One group of cells (in purple) displayed the expected MDSC phenotype (i.e. S100A9high, CD33pos, CD14pos and HLA-DRlow), in addition, these cells were also CD64pos, CD11bpos, CCR2pos, CD36pos, CD13pos, and CD32pos. Of note, node #24 was only increased under GM-CSF and G-CSF and was characterized by a very high expression of CD32. Finally, a third group of nodes was found (in orange) in which cells were CD123pos and HLA-DRpos, while CD14, CD11b, CD36, CD64, and S100A9 were not expressed; thus, these cells were labeled DC (Figure B.4B). The increase in abundance for these cells was assessed in 3 different human bone marrow samples. All three phenotypes (i.e. monocytes that were CD86pos and CD274pos, MDSC, and DC) were significantly increased after GM-CSF+G-CSF or GM-CSF+IL6 culture when compared to the vehicle (Figure B.4C). No difference in cell frequency was found between both conditions (Figure B.4C). Finally, due to the phenotypic differences observed between MDSCs derived from PBMC and bone marrow, and to demonstrate their suppressive capabilities, an allogeneic three-way MLR assay was performed (Figure B.5).

MDSCs obtained were suppressive at ratio of 1:8, 1:4, and 1:2 when derived from bone marrows and 1:4 and 1:2 when derived from PBMCs (p<.05).

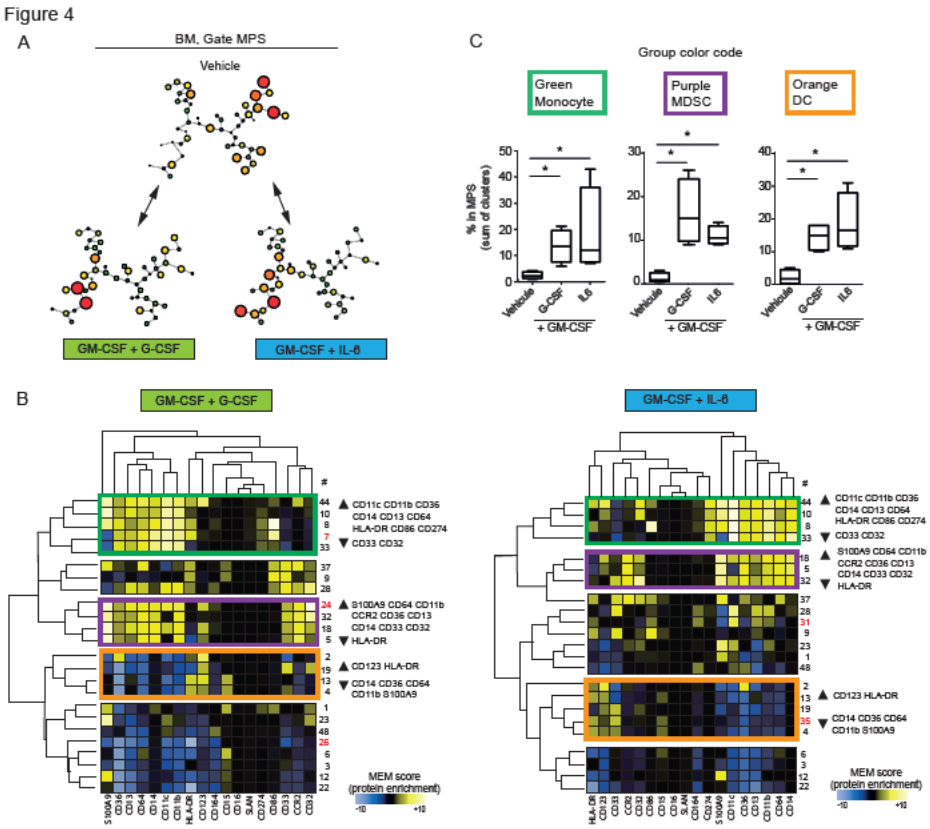

Figure B.4: MDSCs obtained from bone marrow are S100A9pos (**A**) Human bone marrow was cultured for 4 days with GM-CSF+IL6 or GM-CSF+GCSF or with the vehicle. By mass cytometry analysis >100,000 IrposCD45pos cells were defined on a biaxial plot, before classification on a viSNE algorithm. MPS 35 (>20,000 cells) was gated as remaining cells after the exclusion of B- (CD19pos), T- (CD3pos), and NK- (CD3negCD16posCD45RApos) lymphocytes and doublets. Events in the MPS gate were then parsed with SPADE arbitrary restricted to 50 nodes using all clustering markers but CD19 and CD3. Then comparisons were made between each culture conditions and cells treated with vehicle. Nodes with a 2 fold increase in cell abundance (percentage FC>1) between GM-CSF+G-CSF and vehicle or between GM-CSF+IL6 were retained for further analysis (**B**) Transformed median expression for each markers was averaged from each nodes (percentage FC>1). After normalization, results are shown on heat map after hierarchical clustering. *Left*- Nodes with an increase in cell abundance after GM-CSF+G-CSF culture. *Right*- Nodes with an increase in cell abundance after GM-CSF+IL6 culture. #nodes ID; in red: nodes increased in only one condition. Rectangles in green, purple, or orange indicate various phenotype of interest. A representative experiment is shown. (**C**) Abundance of cells in the MPS gate for each phenotype of interest with or without GM-CSF+G-CSF or GM-CSF+IL6 (n = 4). **P*<.05.

Figure 5

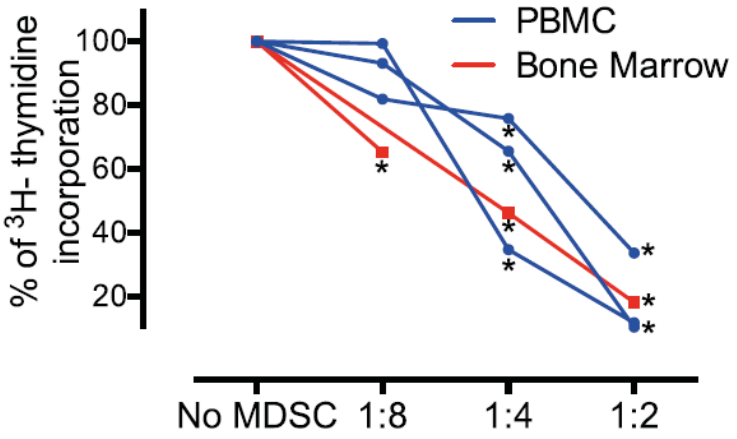

Figure B.5: MDSCs derived from PBMC or bone marrow are both suppressive. An allogeneic three-way MLR was performed on MDSCs derived from PBMCs or bone marrows. APCs and T-cells were cultured with no MDSCs and various ratios of MDSCs to T-cells (1:8, 1:4, and 1:2). The inhibition of 3H- thymidine incorporation was evaluated. Results are represented as percentage of inhibition where 100% is the condition without MDSCs. Replicates (3 to 5) wells were performed for each condition. *P<.05, indicates significant difference when compared to the condition without MDSCs.

Mass cytometry identifies phenotypic MDSCs in the peripheral blood of melanoma patients

The mass cytometry panel, unsupervised analysis approach, and myeloid cell definitions were finally evaluated in clinical samples. MDSCs have previously been reported to be increased in peripheral blood from solid tumor patients irrespective of the disease stage, including melanoma patients (*464-468*). Here, an abundance of cells with an MDSC phenotype including high S100A9 protein expression were observed in the peripheral blood of melanoma patients (Figure B.6A). This cell type was significantly increased in 8 samples from 4 patients compared to HD, with abundance at 3% and 15.5% from the MPS gate, respectively (P = .019) (Figure B.6B).

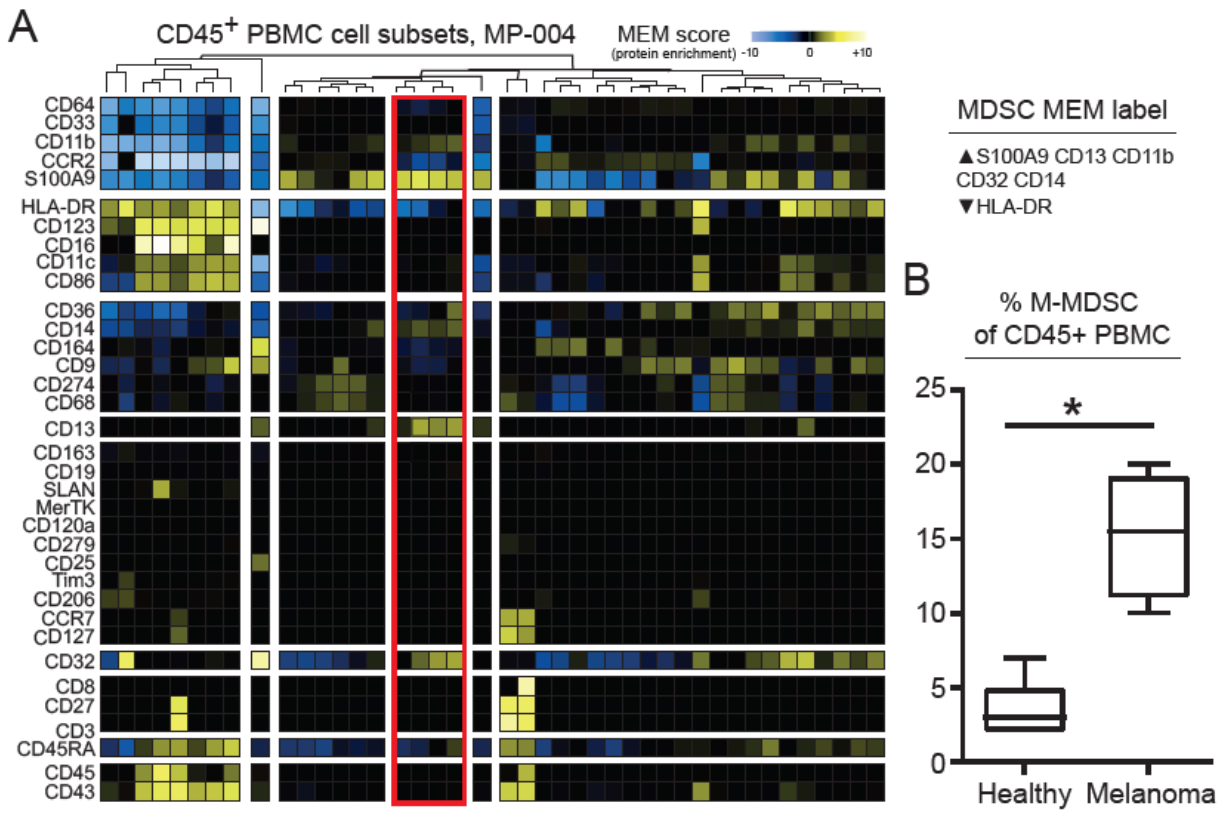

Figure B.6: MDSC accumulated in melanoma patient peripheral blood revealed by mass cytometry (A) By mass cytometry analysis, >100,000 IrposCD45pos cells were defined on a biaxial plot before viSNE analysis. MPS cells (>20,000 cells) were gated as remaining cells after the exclusion of B- (CD19pos), T- (CD3pos), and NK- (CD3negCD16posCD45RApos) lymphocytes and doublets. Events in the MPS gate were then parsed with SPADE arbitrary restricted to 50 nodes using all clustering markers but CD19 and CD3. After normalization, transformed median expression for each markers and each node are shown on heat map after hierarchical clustering; in red: nodes increased with an increase of CD14pos S100A9pos cells. (**B**) Abundance of CD14pos S100A9pos cells in the MPS gate in PBMC from healthy donor (n=4) and melanoma patients (n=5). *P<.05.

Discussion

The MPS compartment includes monocyte, DCs and macrophages, cells that are extremely heterogeneous in their phenotypes and functions. Recently, their nomenclature has been extensively revised and clarified {Guilliams, 2014 #529;Bronte, 2016 #456;Ziegler-Heitbrock, 2010 #458;Murray, 2014 #459}. As there are no unique identity markers and an overlap in their phenotype, their definition at the protein level still debated. Here, we hypothesized that mass cytometry data parsed by high dimensional approaches such as SPADE, viSNE, and hierarchical clustering, will clarify at the protein level the human spectrum of the MPS compartment. To this

aim, various *in vitro* culture conditions and peripheral blood from cancer patients were compared to build a reference data framework including 1) monocyte subsets and MDSCs, 2) DCs, and 3) macrophages under basal conditions or treated with various canonical polarization stimuli. To date, mass cytometry analyses have been performed on a limited number of myeloid populations. In human, peripheral blood, bone marrow, or tissues from HDs (*9*), inflammatory or septic patients (*225, 316, 456, 469*), or patients suffering from acute myeloid leukemia (AML) (*314, 328, 344, 470*) have been analyzed for myeloid cells. Noteworthy, except in AML, panels employed, were not dedicated specifically for in deep analysis of the myeloid compartment. Markers used in these studies included mostly CD13, CD33, CD36, CD14, CD16, HLA-DR, CD11b, CD11c, and CD123. In a recent comprehensive panel dedicated to the monitoring of immunomodulatory therapies on PBMCs, CD14, CD15, HLA-DR, CD11c, CD36, CD16, CD169, CD123, CD303, Siglec-8, and CD1c were proposed to delineate neutrophils, monocytes, basophils, eosinophils, as well as DC subsets (*471*). In mice, more complete myeloid targeted panels have been published, in particular with the use of the specific myeloid markers F4/80, Ly6C, and Ly6G (*219, 335*). The panel was built by including 1) canonical markers from prior studies of the human MPS (*472*), 2) markers know to be modulated in specific monocyte subsets or macrophages polarization stages (viz. CCR2, CD163, CD206, CD32, and CD64), and 3) markers differentially expressed during monocyte/DC activation (viz. CD86, CD274, CD45RA). The panel was validated on PBMC in recognizing in HDs, the 4 already described monocytes subsets (CD14posCD16neg, CD14posCD16pos, CD14dimCD16posSlanlow, and CD14dimCD16posSlanhigh) (*411, 446, 448*). Then, to explore the full spectrum of the MPS compartment, we took advantage of recent nomenclature papers (*448*), resource work refining the macrophage transcriptomic landscape (*451*), and studies on MDSCs (*462*)or on DCs (*473, 474*). In particular, Xue and colleagues described 9 different clusters of transcription networks (*451*). We decided to align as much as possible with these conditions and thus derived from monocyte, M_b, M_IL4, M_IL10, M_LPS,

M_IFN©, M_IL6, and M_TPP, but also DCs and MDSCs given that their phenotypes are overlapping. Regarding macrophages, each stimulation condition gave rise to a specific phenotype of polarized macrophage (Figure B.2B, C). There was no or little overlap between M_IFNg and M_LPS (both previously known as M1) and M_IL4 an M_IL10 (both previously known as M2). M_TPP also represented a separate cluster of nodes. This was in agreement with previous findings at the transcriptomic level, where macrophages polarized by IL4, IL10, IFN©, and LPS clustered separately based on RNA expression profiles (*451*). Novel patterns of phenotype within MPS were discovered and remarkable. CD32, CD14, CCR2, CD163, CD64, and CD33 were highly expressed in M_IL10. CD274 and CD86 were highly expressed, whereas CD14, CD32, and CD33 were expressed at low level in M_IL4 (Figure B.2B, C and S2). Surprisingly, phenotype pattern of M_LPS and M_IL4 were separated only by CD32 and CD33, more expressed in M_LPS, whereas CD274 was less express, and CD163 was not differently expressed. CD163 is considered as a key marker of tumor-associated macrophages (TAM) and sometimes by extension for the historical M2 macrophages, however a higher expression in M_IL10 than in M_IL4 has been shown (*475*). M_TPP expressed high levels of CD14 and CD13, whereas HLA-DR was expressed at low level and M_TPP were shown to be immuno-suppressive [16]. MDSCs were also clearly separated from M_b, DCs, and monocytes (Figure B.2B-C) by especially high levels of CD32, CD206, CD64, CCR2, and CD14 and low levels of CD33 and HLA-DR. MDSCs were also phenotypically different form M_IL4, M_IL10, and M_TPP, three polarized macrophages with anti-inflammatory functions, due to higher expression of CCR2 and CD206 and lower expression of CD13. Because HLA-DR expression is continuous across myeloid cells, M-MDSCs have been challenging to distinguish from monocytes in peripheral blood. Based on observations here, we propose using CD32, CD206, and S100A9 in addition to CD14 and HLA-DR (Figure B.3C).

Surprisingly, S100A9, a highly expressed protein marker of MDSCs (*308, 445, 476, 477*), was expressed at low levels in MDSCs generated from peripheral blood (Figure B.3B, C). Despite lower S100A9 than other MDSCs, peripheral blood derived MDSCs were functional and effective at suppressing T cell proliferation (Figure B.5). In previous works, human MDSCs were derived either from peripheral blood or from bone marrow (*461, 462*). Thus we hypothesized that MDSC derived from bone marrow would have a different phenotype. Monocytes, DCs, and MDSCs were increased in abundance when bone marrow were cultured with GM-CSF + G-CSF or with GMCSF + IL6 (Figure B.4C). This observation has not been reported in published protocols to derive MDSCs and would have been difficult to identify without the single cell high-dimensional mass cytometry approach. In agreement, it has been shown recently that GM-CSF cultured murine bone marrow generated both macrophage and DC (*474*). We also found that MDSCs derived from human marrow expressed a more consistent phenotype, highly expressing S100A9, CD14, CD64, CD11b, CCR2, CD32 while remaining HLA-DRlow, making BM MDSCs an ideal, if less practical to obtain, reference point. Finally, this approach was employed to characterize clinical samples from melanoma patients because in this cancer high level of circulating MDSC have been described across grades (*464, 468*). MDSCs with the same phenotype as those derived from bone marrow were enriched in the blood of melanoma patients.

In summary, a broad phenotypic analysis of the human MPS compartment characterizes know cell populations and brings increased clarity to the definitions of cell types including MDSC and polarized mononuclear phagocytes. In particular, the multidimensional approach at the protein level might constitute the first step of efforts in unifying transcriptomic to proteomic and functional approaches in a multi-OMICs era (*478*). It would be interesting to expand the panel in order to have a clear view of signaling pathways involved. Finally, this study also highlights the potential value of mass cytometry in system immune monitoring of the myeloid compartment for patients in clinical trials.

Table B.S1: Table of antibodies or parameters used for mass cytometry analysis

Metal / Parameter	Antibody / Compound	Clone	Company	Custom conjugate (C) / Indirect staining (I)	Description or cell target
141Pr	CD11b	ICRF44	Biolegend	C	Antigen presenting cell
142Nd	CD19	HIB19	Fluidigm	-	B-lymphocyte
143Nd	CD366 Tim3	F38-2E2	Biolegend	C	T-cells, DC-, and monocyte subsets
144Nd	Slan-FITC / anti-FITC	DD-1	Miltenyi Biotech / Fluidigm	I	Monocyte subsets
145Nd	MerTK-PE / anti-PE	125518	R&D systems / Fluidigm	I	Macrophages
146Nd	CD64	10.1	Fluidigm	-	Monocyte subsets
147Sm	CD36	5-271	Biolegend	C	Monocyte subsets
148Nd	CD164	67D2	Biolegend	C	Monocyte subsets
149Sm	CCR2	K036C2	Biolegend	C	Chemokine receptor involved in monocyte migration
150Nd	CD43	84-3C1	Fluidigm	-	Myeloid subsets
151Eu	CD123	6H6	Fluidigm	-	Basophils, DC
152Sm	CD13	WM15	Fluidigm	-	Myeloid cells
153Eu	CD45RA	HI100	Fluidigm	-	NK and monocyte subsets
154Sm	CD163	GHI/61	Fluidigm	-	Monocyte subsets
155Gd	CD27	L128	Fluidigm	-	T-lymphocyte subsets
156Gd	CD86	IT2.2	Fluidigm	-	Costimulatory molecule, B-, T-cells, DC
158Gd	CD33	WM53	Fluidigm	-	Myeloid cells
159Tb	CD11c	Bu15	Fluidigm	-	DC, T- and NK-subsets
160Gd	CD14	M5E2	Fluidigm	-	Monocyte, Macrophages
161Dy	CD32	FUN-2	Biolegend	C	FCγRII, myeloid-, B- cells
162Dy	S100A9-APC / anti-APC	MRP-14	Biolegend / Fluidigm	I	Regulate neutrophil and macrophage recruitment
163Dy	HLA-DR	L243	Biolegend	C	Antigen presenting cell
164Dy	CD206	3.29B1.10	Beckman Coulter	C	Mannose receptor, macrophages, immature DCs
165Ho	CD16	3G8	Fluidigm	-	NK and monocyte subsets
166Er	CD120a	80M2	Beckman Coulter	C	Tumor necrosis factor receptor
167Er	CCR7	G043H7	Fluidigm	-	Expressed on activated DCs
168Er	CD8	SK1	Fluidigm	-	T-lymphocyte subsets
169Tm	CD25	2A3	Fluidigm	-	IL-2 receptor, T-, B- cells and myeloid precursors
170Er	CD3	SP34-2	Fluidigm	-	T-lymphocyte
171Yb	CD68	Y1/82A	Fluidigm	-	Macrophages
172Yb	CD9	SN4 C3-3A2	Fluidigm	-	Tetraspanin, expressed on monocytes subsets
173Yb	CD45	2D1	Biolegend	C	Pan-leukocyte
174Yb	CD279	EH12.2H7	Biolegend	C	PD-1: immunologic checkpoint
175Yb	CD274	29E.2A3	Fluidigm	-	PD-L1: immunologic checkpoint
176Yb	CD127	A019D5	Fluidigm	-	IL-7R
191Ir	Iridium	-	Fluidigm	-	DNA tag. Cell identifier
193Ir	Iridium	-	Fluidigm	-	DNA tag. Cell identifier
195Pt	Cisplatin	-	Enzo Life Sciences	-	Viability stain
Cell length	-	-	-	-	-

Appendix C

MELANOMA-SPECIFIC MHC-II EXPRESSION REPRESENTS A TUMOR-AUTONOMOUS PHENOTYPE AND PREDICTS RESPONSE TO ANTI-PD-1/PD-L1 THERAPY

Authors: Douglas B. Johnson, Monica V. Estrada, Roberto Salgado, Violeta Sanchez, Deon B. Doxie, Susan R. Opalenik, Anna E. Vilgelm, Emily Feld, Adam S. Johnson, Allison R. Greenplate, Melinda E. Sanders, Christine M. Lovly, Dennie T. Frederick, Mark C. Kelley, Ann Richmond, Jonathan M. Irish, Yu Shyr, Ryan J. Sullivan, Igor Puzanov, Jeffrey A. Sosman & Justin M. Balko

This work as published from the manuscript published in *Nature Communications* 2016 (Johnson, et al. 2016).
https://www.nature.com/articles/ncomms10582

Abstract

Anti-PD-1 therapy yields objective clinical responses in 30–40% of advanced melanoma patients. Since most patients do not respond, predictive biomarkers to guide treatment selection are needed. We hypothesize that MHC-I/II expression is required for tumor antigen presentation and may predict anti-PD-1 therapy response. In this study, across 60 melanoma cell lines, we find bimodal expression patterns of MHC-II, while MHC-I expression was ubiquitous. A unique subset of melanomas are capable of expressing MHC-II under basal or IFNγ-stimulated conditions. Using pathway analysis, we show that MHC-II+ cell lines demonstrate signatures of 'PD-1 signaling', 'allograft rejection' and 'T-cell receptor signaling', among others. In two independent cohorts of anti-PD-1-treated melanoma patients, MHC-II positivity on tumor cells is associated with therapeutic response, progression-free and overall survival, as well as CD4+ and CD8+ tumor infiltrate. MHC-II+ tumors can be identified by melanoma-specific immunohistochemistry using commercially available antibodies for HLA-DR to improve anti-PD-1 patient selection.

Introduction

Monoclonal antibodies blocking the programmed death-1 (PD-1) receptor or its ligand (PD-L1) relieve the suppression of anti-tumor immune responses in a variety of cancers. Durable

remissions occur in sizable fractions of patients with melanoma (30–40%) (*215, 295, 296, 300, 479, 480*), non-small cell lung cancer (15–20%) (*295, 300, 481-483*), renal cell carcinoma (20–30%) (*295, 300, 484*), bladder urothelial carcinoma (30%) (*485*), Hodgkin's lymphoma (80–90%) (*309*), and others including head and neck squamous-cell carcinoma and triple-negative breast cancer (*171, 300, 486, 487*). Accurate predictive markers of therapeutic efficacy are needed to optimize patient selection, improve treatment decision-making and minimize costs. To date, several candidate approaches have been identified in melanoma. These include tumor or immune cell expression of PD-L1 (*295, 300*), identification of neoantigens through next-generation sequencing techniques (*488, 489*) and T-cell receptor clonality profiling (*490*). While quite promising, these assays are technically challenging and require specialized tissue processing.

Tumors evade immune surveillance by immune checkpoint expression (PD-L1 and others), immunosuppressive cytokine profiles, tolerogenic immune cell recruitment (regulatory T-cells and others) and cancer-specific cell signaling (*138, 491, 492*). In addition, cancer cells can lose the ability to present tumor antigens, thus avoiding recognition by cytotoxic T cells and antigen presenting cells, thus avoiding recognition by cytotoxic T cells and antigen presenting cells (APCs) (*493*). Downregulation of major histocompatibility complex class-I and -II (MHC-I and MHC-II) has been linked to immune suppression, metastatic progression and a poor prognosis in numerous malignancies (*493-497*).

Despite the established importance of tumor-specific antigen expression, the influence of MHC-I and MHC-II expression on response to new immune therapies, particularly anti-PD-1/PDL1, has not been explored. Specifically, HLA-DR is frequently expressed on melanoma and has unclear functional and prognostic significance (*498-500*). We hypothesized that MHC-I and MHC-II expression, particularly HLA-DR, are required for anti-PD-1/PD-L1 activity and serve as technically and clinically feasible predictive biomarkers for therapeutic efficacy. In this study, we find that melanoma-specific expression of HLA-DR marks tumors with unique inflammatory

signals that are more responsive to PD-1-targeted therapy. On the basis of this, we propose use of tumor-specific HLA-DR expression as a potential biomarker of high likelihood of response to these agents in clinical trials.

Results

MHC-I and MHC-II expression in melanoma cell lines.

On the basis of the known biological interactions of PD-1/PD-L1- signaling, antigen presentation by tumor or professional APCs is hypothesized to be a requirement for immune recognition of the malignant cell. MHC-I presents antigen to CD8+ cytotoxic T lymphocytes (CTL) and is ubiquitously expressed by most cells. Loss of MHC-I is typically thought to trigger natural-killer cell checkpoints, resulting in natural-killer cell-mediated cytotoxicity. In contrast, MHC-II, which presents antigen to CD4+ T-helper cells, is typically restricted to professional APCs such as dendritic cells and B cells. HLA-DR, the primary antigen-presenting molecule of the MHC-II pathway is expressed in some cancers, particularly in response to CTL-secreted interferon-gamma (IFNγ). Some data suggest that non-immune cells, including cancer cells, can function as MHC-II+ APCs (*501-503*). Given the heterogeneity of the tumor milieu, we asked whether MHC-I and II were expressed in in vitro cell line models of melanoma (rather than in resected melanoma tumors), where the contribution of stromal and infiltrating immune cells could be excluded.

Using the Cancer Cell Line Encyclopedia (CCLE) melanoma panel of 60 cell lines, we determined that MHC-I mRNA expression (using HLA-A as the prototype) was ubiquitously high across almost all melanoma cell lines (Figure C.1a). In contrast, HLA-DRA, the prototype MHC-II molecule, demonstrated a strong bimodal distribution pattern, and appeared absent in ~50% of cell lines (Figure C.1a). The remaining cell lines demonstrated intermediate-to-high mRNA levels. When cell lines were factored according to HLA-DRA mRNA (using an arbitrary cutoff of 6 (RMA log2 signal intensity), there was a signature of 159 genes which were significantly altered (up or

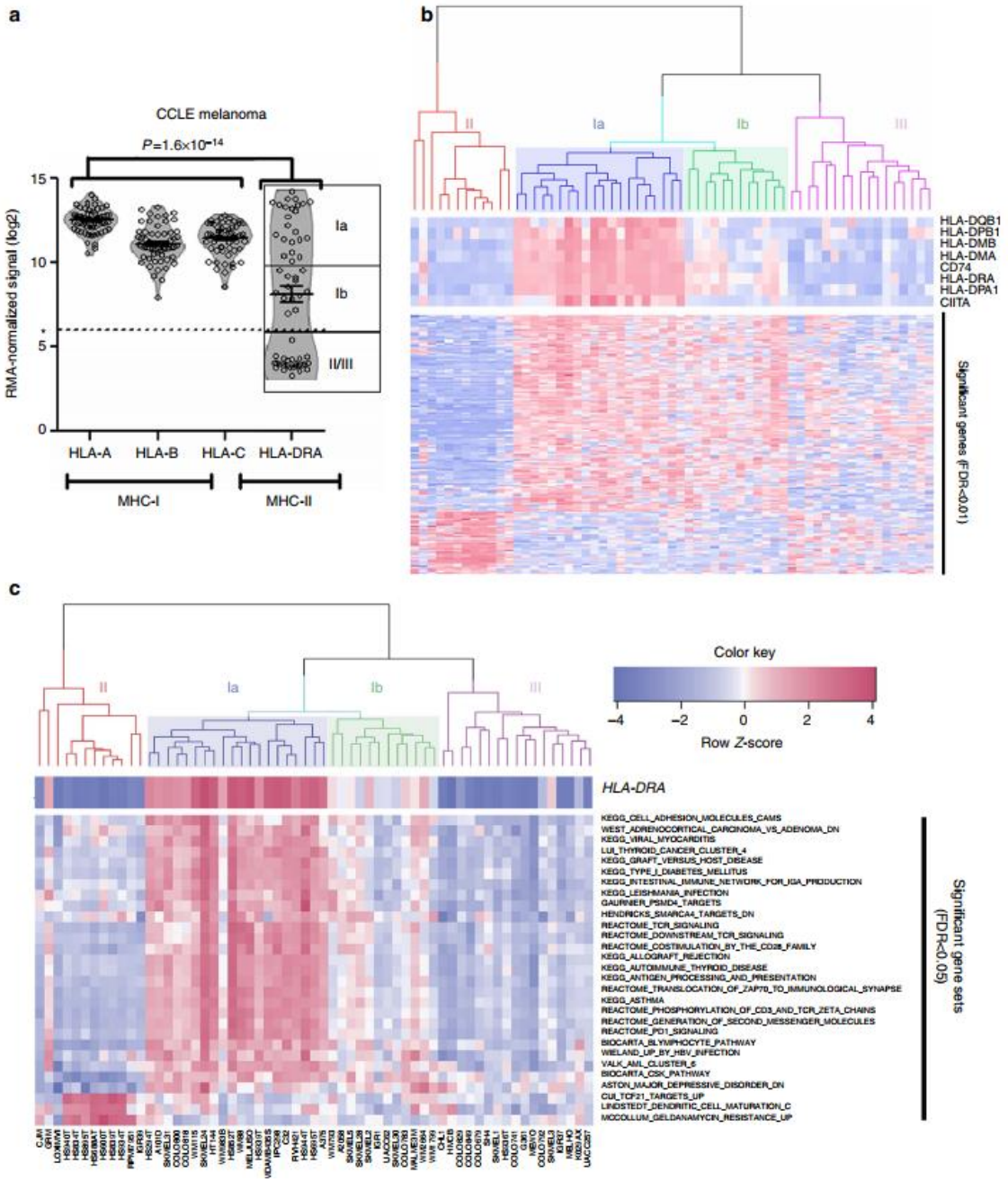

Figure C.1: A unique subtype of melanoma expresses MHC-II. (a) Microarray data from 60 melanoma cell lines in the CCLE48 were analysed for MHC-I (HLA-A/B/C and MHC-II (HLA-DRA) expression. Bars represent the mean±s.d. P value is the result of the Kolmogorov–Smirnov test comparing the distribution of MHC-I (HLA-A, HLA-B, HLA-C) expression with MHC-II expression (HLA-DRA). *represents the cutoff for defining MHC-II(+). (b) Gene-expression data from HLA-DRA(+) cell lines (Clusters Ia/Ib) were compared with HLA-DRA( ) cell lines (Clusters II and III) by an FDR-corrected row t-test. An ad hoc heat map is shown at the top, highlighting classical MHC-II genes. (c) Normalized microarray data were analyzed by GSA47 using the curated Molecular Signatures Database, and the resulting gene set scores are presented as a hierarchical clustered heat map.

downregulated, false-discovery rate (FDR) <1%) in HLA-DRA-expressing cells compared with

those cell lines lacking HLA-DRA mRNA (Figure C.1b). Clustering on these genes suggested four clusters of expression patterns, which we identified as clusters Ia and Ib (predominantly HLA-DR-expressing) and clusters II and III (predominantly HLA-DR-negative). Gene set analysis (GSA) of the CCLE based on MHC-II classification yielded 27 gene sets with upregulated scores and 1 with a downregulated score at an FDR≤5% in the Ia/Ib subtype. Bioinformatics analysis of the enriched gene sets suggested that HLA-DRA-expressing cell lines harbored expression signatures of 'PD-1 signaling', 'T-cell receptor signaling', 'graft-versus-host disease' and 'allograft rejection' (Figure C.1c). These findings suggested that there were tumor-cell autonomous signaling pathways driving MHC-II expression consistent with a pro-immune/ anti-tumor response. The presence of a high mutational burden and resulting neoantigens has been shown to predict response to PD-L1 therapy in lung cancer (*504*). HLA-DR-expressing melanoma lines had a higher total nonsynonymous mutational load by targeted next-generation sequencing of 1,561 genes, although this was not statistically significant (Wilcoxon rank sum test $P < 0.056$).

Since mRNA expression does not imply functional protein expression, and because micro-environmental IFNγ is known to influence MHC-I, MHC-II and PD-L1 expression, we characterized representative cell lines from HLA-DRA-expressing (cluster Ia and Ib, Figure C.1b) and HLA-DRA-deficient (cluster II, Figure C.1b) subgroups by flow cytometry under basal and stimulated (IFNγ) conditions. Cell-surface expression mirrored mRNA-expression patterns; MHC-I (HLA-A/B/C) expression was detected in all cell lines under both basal and stimulated conditions. However, the antibody utilized to assess MHC-I expression is reactive with all class-I alleles and haplotypes and specific class-I allele expression was not assessed in this study. In contrast, MHC-II (HLA-DR) was present only on the intermediate/Ib (SKMEL5 and SKMEL28) and high/Ia cell lines (WM115 and A375; Figure C.2a–c). No significant increase in HLA-DR expression was

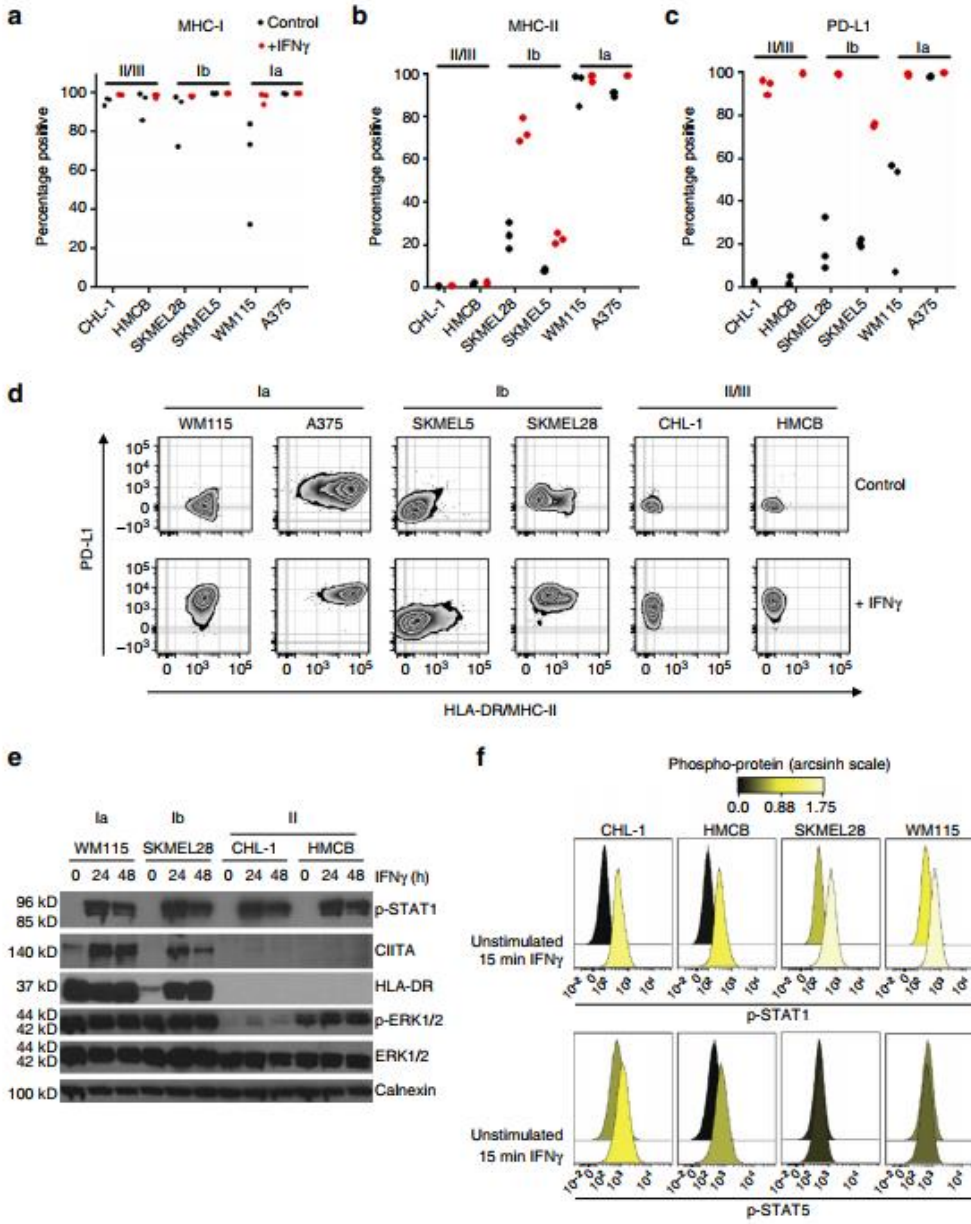

Figure C.2: Characterization of MHC-II(+) melanoma cell lines. Melanoma cell lines were treated with IFNγ for 24 h before collection and live-cell staining and flow cytometry analysis for MHC-I/HLA-A/B/C (a), MHC-II/HLA-DR (b) and PD-L1 (c). Bars represent mean±s.e.m. for at least three experiments (d) Representative flow plots from c. (e) Western blot analysis of melanoma cell lines after 24 or 48 h of IFNγ stimulation. (f) Phosphorylation of STAT1 (top row) and STAT5 (bottom row) in melanoma cell lines at 15 min after IFNγ stimulation. Histograms were colored according to the arcsinh transformed ratio or MFI medians relative to the table minimum value.

observed with either CHL-1 or HMCB even after 72 h of IFNγ treatment. Notably, the intermediate/Ib cell line SKMEL28 had a unique population (25%) of cells that was constitutively

HLA-DR-expressing at baseline, and was potently induced by IFNγ (Figure C.2d). The high (Ia) WM115 cell line was essentially 100% positive for HLA-DR at both basal and stimulated conditions.

Interestingly, PD-L1 expression was potently induced with stimulation in all cell lines, though the HLA-DR+ cell lines exhibited greater populations of cells that were PD-L1 positive in the absence of IFNγ (Figure C.2c,d). Consistent with this, STAT1 was robustly activated with IFNγ stimulation in all cell lines, whereas CIITA expression, a master regulator of MHC-II transcription, was only induced in HLA-DR+ Ia/Ib cells (Figure C.2e). Phospho-flow analysis demonstrated that while STAT1 was activated robustly with short-term (15 min) IFNγ stimulation, STAT5 was preferentially activated by IFNγ in MHC-II cell lines (Figure C.2f), consistent with the observations of others that STAT5 can contribute to resistance to interferon signaling and phenotypes (*505*). Together, these results suggest that there is a tumor-cell autonomous inflammatory signal present in a subset of melanomas that may predispose the tumor to enhanced MHC-II expression, antigen presentation (direct or cross presentation via exosomes (*506*)) to CD4 T-helper cells and immune recognition, coinciding with higher PD-L1 expression. Furthermore, these data suggest that STAT5 activation may contribute to suppression of this inflammatory signal. Thus, we reasoned that the HLA-DR-expressing subtype of melanoma can be unmasked to the immune system by therapeutic inhibition of the PD-1/PD-L1 axis.

HLA-DR expression by genotype.

HLA-DRA expression was specifically enriched in cell lines harboring NRAS mutations (Figure C.3a). Notably, studies by our group and others have suggested that patients harboring NRAS mutations experience improved response rates to PD-1 axis therapy and other immune therapies (*507, 508*). Although the biological basis of this correlation remains to be elucidated, these results were intriguing and compatible with our hypothesis. To test whether the same association could

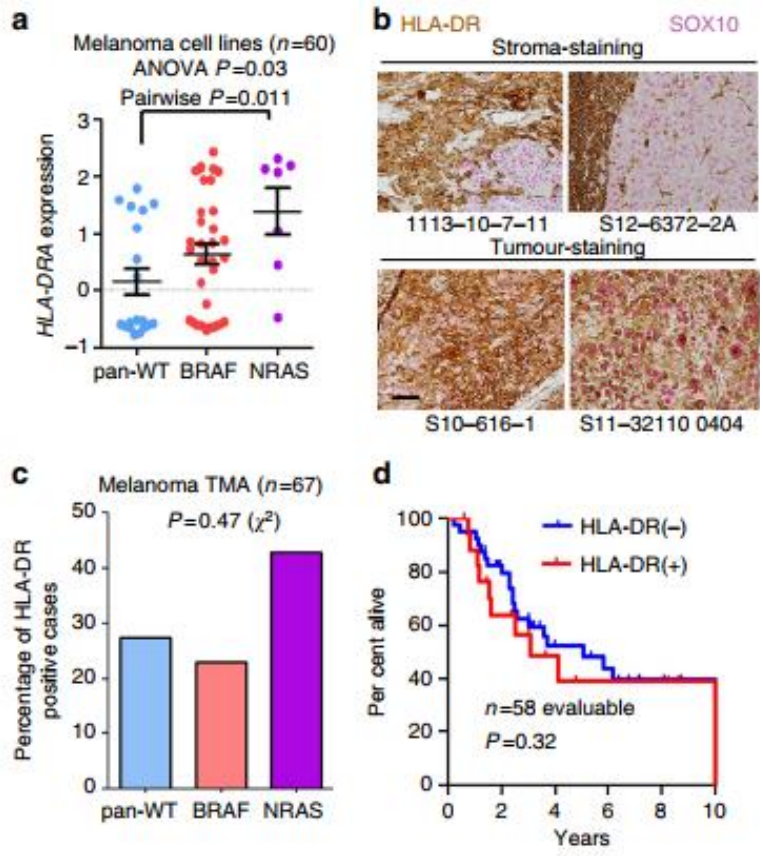

Figure C.3: MHC-II-positive melanoma cell lines associate with NRAS mutations. (a) HLA-DRA mRNA expression in melanoma cell lines (n ¼ 60; one cell line lacked mRNA expression data) from the CCLE compared by genotype. P value (Po0.05) represents result of Tukey's post hoc analysis comparing pan-WT with NRAS-mutant cell lines, following a significant ANOVA (P ¼ 0.03) performed among all groups. Bars represent mean±s.e.m. (b) Representative IHC for HLA-DR (brown) and SOX10 (pink) in cases with isolated stromal positivity (top) and with tumor specific staining (bottom). Both HLA-DR and SOX10 immunostaining is present in all four sections. Scale bar, 50 mm. (c) Analysis of HLA-DR IHC in a melanoma TMA (n ¼ 67 evaluable) by genotype. P value represents result of a w2-test. (d) Overall survival of patients (n ¼ 58 evaluable) within the TMA by HLA-DR status (left censored at time of diagnosis). The remaining patient samples were included from outside institutions and follow-up data were not available from those institutions. P value is the result of the log-rank test.

be observed in clinical samples, we investigated MHC-II/HLA-DR expression by IHC in a tissue microarray (TMA) of melanoma patient samples (n < 67) with known BRAF and NRAS genotypes who largely had not received immune therapy. Dual-color IHC was performed with HLA-DR and SOX10 to distinguish tumor versus stromal expression of HLA-DR (Figure C.3b). We observed HLA-DR+ tumor expression in 20/67 (30%) evaluable samples. HLA-DR was expressed more frequently in the NRAS mutated cohort (43%, 6 of 14) than in BRAF-mutated (23%, 3 of 13) and BRAF/NRAS wild-type populations (28%, 11 of 39; Figure C.3c), but this was not statistically significant (χ^2-test P < 0.47). Thus, NRAS genotype seems to trend with HLA-DR positivity, but this association does not appear to be a significant. A larger sample size would be needed to conclusively determine whether this association is apparent or absent in patients. Importantly, in this unselected population of patients, expression of HLA-DR was not associated with overall

survival (log-rank P < 0.32), suggesting that HLA-DR expression may not be generally prognostic in advanced melanoma (Figure C.3d).

HLA-DR expression in patients receiving anti-PD-1 or PD-L1.

We previously observed that in a diverse collection of melanoma cell lines, patterns of HLA-DR expression were (i) constitutively high, (ii) heterogeneous, but inducible by IFNγ, or (iii) constitutively off. Similar patterns were observed in a cohort of unselected melanoma tumors, and thus we hypothesized that these patterns may be predictive of benefit to immunotherapy.

To test this hypothesis, we used the patient-derived xenograft (PDX) models from the tumor resections of two melanoma patients who subsequently received anti-PD-1 therapy; patient 1 (PT1; non-responder, 0% HLA-DR-positive, class II/III) and patient 2 (PT2; partial responder, heterogeneous 15% HLA-DR positive, class Ib; Figure C.4a). In PT2, the HLA-DR-staining pattern was clearly positive at the invasive interface, suggesting immunereactivity in this particular tumor, in contrast to other tumors identified in the TMA study which were MHC-II+ throughout the tumor. The resected tumors from PT1 and PT2 were serially transplanted to athymic nu/nu mice, which are highly deficient in functional T cells (*509*), ruling out a possible source of IFNγ (Figure C.4b). Immunohistochemistry analysis of both PDX models, grown in nude mice, demonstrated no detectable HLA-DR expression.

However, when PDX tumors were freshly resected, sectioned and grown ex vivo as cultured tissue slices, in the presence or absence of IFNγ, only the PT2 PDX model (anti-PD-1 responder) upregulated HLA-DR (Figure C.4d). Thus, HLA-DR may be a marker of IFNγ activity in the microenvironment of some (but not all) tumors. Furthermore, this experiment supports the notion that the IFNγ response varies significantly among melanomas, and demonstrates tumor autonomous features. Furthermore, these data suggest that HLA-DR expression in melanoma

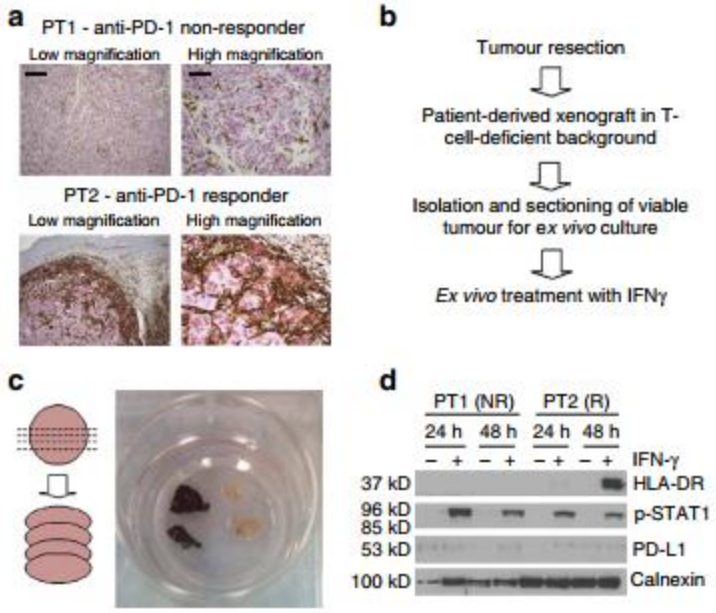

Figure C.4: Ex vivo culture of tumors derived from anti-PD-1-responding and non-responding patients identifies heterogeneity in interferon response. (a) Patient tumor blocks stained for HLA-DR (brown) and SOX10 (pink) at low (scale bar, 500 um) and high magnification (scale bar, 200 mm); PT1: anti-PD-1 non-responder and PT2: anti-PD-1 responder. (b) Experimental schema. (c) Schema and images of PDX tissue sections (ex vivo organotypic culture). (d) Western blot analysis of tissue sections cultured in the presence or absence of IFNγ for 24–48 h.

cells may be a biomarker for tumors primed with activated T-cells and an appropriate IFNγ response to mediate sensitivity to PD-1/PD-L1 blockade. Importantly, however, these data do not rule out the existence of melanomas constitutively expressing HLA-DR in the absence of IFNγ stimulation, as is observed in a significant number of melanoma cell line models (Figure C.1).

In order to determine whether MHC-II expression on melanoma tumors is associated with clinical response to PD-1/PD-L1-targeted therapy, we obtained archival pre-treatment biopsy or resection specimens from 30 patients treated with anti-PD-1 (nivolumab, pembrolizumab) or anti-PD-L1 (MPDL3280A; n < 2). The median age was 56 years, the median number of prior therapies was 1, and 14 (47%) had failed ipilimumab (Table C.1). Twenty-three patients (77%) had stage IV M1c disease and 12 (40%) had elevated serum lactate dehydrogenase (LDH).

We chose to differentiate MHC-II+ from MHC-II samples using a cutoff of 45% of tumor (SOX10+) membranes showing staining. Tumor HLA-DR staining strongly correlated with response to therapy. Among 14 patients with positive HLA-DR staining (45% estimation of positive tumor membranes in the entire tissue section), 11 patients (79%) had complete (n < 3) or partial (n < 8) response (Figure C.5a). Clinical activity was inferior in HLA-DR non-expressing

Table 1 | Clinical characteristics of patients treated with anti-PD-1/PD-L1*.

	Number	Percentage
Age	56 (median)	27-81 (range)
Gender		
Male	16	53
Female	14	47
Stage		
M1a	3	10
M1b	4	13
M1c	23	77
LDH elevated	12	40
Mutation		
BRAF V600	6	20
NRAS Q61	7	23
BRAF/NRAS wild type	17†	57
Prior therapies	1 (median)	0-3 (range)
IL-2	5	20
Ipilimumab	14	47
BRAF ± MEK inhibitor	4	13
Cytotoxic chemotherapy	5	17

*Discovery cohort, $n = 30$.
†NRAS status unknown in two patients.

melanomas; 6 of 16 patients (38%) responded to therapy (overall response rate 79 versus 38%, Fisher's exact test $P < 0.033$). Clinical benefit (including mixed responses) was similarly superior in MHCII+ patients (Fisher's exact test $P < 0.007$). Importantly, this finding was confirmed in a second independent data set of 23 melanoma patients treated with anti-PD-1 therapy (single agent or concurrently with other immunotherapies). Of these 23 additional patients, 6/8 (75%) of HLA-DR+ tumors responded (PR or CR), while only 4/15 (27%) HLA-DR- responded (Fisher's exact test $P < 0.025$; Figure C.5b). Rapid objective clinical responses were observed in HLA-DR+ tumors, even in patients with other negative prognostic features, including a patient with bulky disease, elevated LDH, impaired functional status and failure of both ipilimumab and dabrafenib/trametinib, and a patient with a 410 cm liver mass and LDH4500 U l 1 following failure of interleukin-2 and ipilimumab (Figure C.5c).

We also compared progression-free survival (PFS) between patient groups in both data sets, when survival data were available. The median PFS was superior in the HLA-DR+ group (median not reached versus 3.2 months, log-rank $P < 0.02$; Figure C.5d). Overall survival was also superior for the HLA-DR+ cohort (median not reached versus 27.5 months, log-rank $P < 0.003$; Figure C.5d). We excluded the three patients with mixed responses from the PFS analysis (given difficulties specifying time of clinical progression), but not the OS analysis. Importantly,

statistical significance or a trend toward significance was retained at other cut-points as well, including 1, 10 and 20% (PFS log-rank P < 0.01, P < 0.08 and P < 0.03, respectively, and OS log-rank P < 0.002, P < 0.01 and P < 0.11, respectively). Notably, we did not observe an association with HLA-DR expression and response among 13 patients treated with ipilimumab alone, although the sample size is too small to make definitive conclusions.

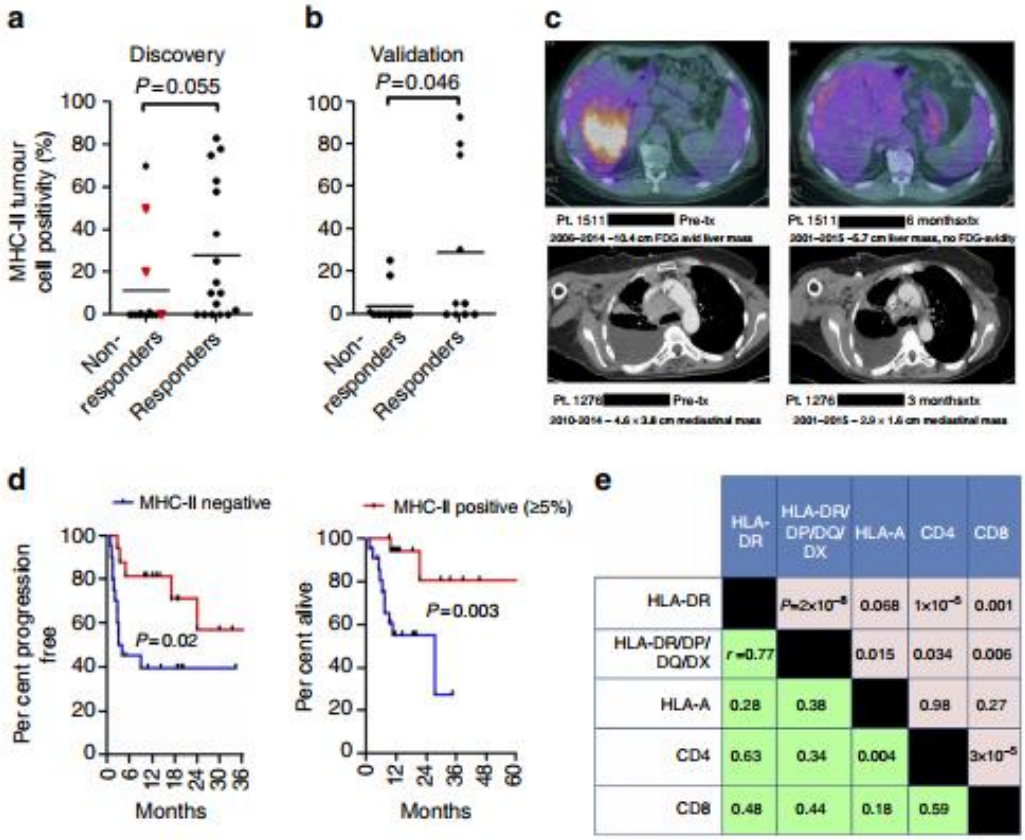

Figure C.5: MHC-II(+) melanomas have improved response rates and clinical benefit to PD-1/PD-L1 inhibition. (a) HLA-DR positivity by IHC plotted versus response to PD-1/PD-L1-targeted therapy in the discovery set (n=30). Responders include partial and complete responders; non-responders include mixed responders and progressive disease patients. Mixed responders (n = 3) are noted by a red triangle. P value is the result of the Wilcoxon's rank sum test. (b) HLA-DR positivity by IHC in the validation set (n = 23) plotted versus response to PD-1/PD-L1-targeted therapy. P value is the result of the Wilcoxon's rank sum test (c) Representative images of scans from anti-PD-1 therapy-treated MHC-II(+) patients (d) Progression-free survival (left) and overall survival (right) in anti-PD-1/PD-L1-treated patients, stratified by HLA-DR/MHC-II positivity (5% total tumor cells staining on entire tissue section used as cut point). Data from both the initial and validation cohorts were included, when available. P value is the result of the log-rank test. (e) Correlation matrix of IHC markers. P values for the Pearson's correlation appear above the diagonal and correlation coefficients (r) appear below the diagonal.

MHC-II antibody specificity and concordance of assessment.

To investigate the possibility of alternative MHC class II molecule expression, we performed IHC using a second monoclonal antibody targeting a common epitope to HLA-DR, -DP, -DQ and -DX (pan-MHC-II) on all samples. Results largely correlated with HLA-DR (Figure C.5e), supporting high specificity of the HLA-DR antibody. No additional cases were identified as MHC-II+ by use of the pan-MHC-II antibody. Pan-MHC-II positivity was also associated with objective clinical response (Mann–Whitney's $P < 0.02$) as well as PFS and OS using a 5% cut-point (log-rank $P < 0.04$ and $P < 0.009$, respectively). Concordance in HLA-DR positivity assessment between two independent blinded pathologists was 77%. After web-mediated discussion of the discordant cases, a final consensus was reached.

Other clinical correlates.

To investigate the impact of MHC-I expression on response to anti-PD-1/PD-L1, we performed HLA-A IHC on the same pre-treatment samples. As observed in melanoma cell line models, HLA-A expression was nearly ubiquitous across all tumors and expression level was not statistically associated with response to therapy. However, HLA-B and HLA-C protein expression were not assessed in this study. CD4+ and CD8+ T-cell infiltration was also assessed by IHC. CD4 was not statistically associated with therapy response, while a trend towards significance was detected with CD8 (Mann–Whitney's $P < 0.077$), as has been previously described (*490*). The lack of statistical association in our study may be due to scoring method, as the invasive front of the tumor was not detectable in all biopsies or resection specimens. Thus, the total per cent positivity of CD8+ T cells invading into the tumor was calculated. Interestingly, the percentage of infiltrating CD4+ T cells were more strongly correlated with HLA-DR expression (Pearson's $r < 0.63$; $P < 1\ 10\ 5$), while CD8+ infiltrate was more weakly correlated (Pearson's $r < 0.48$; $P < 0.001$; Figure C.5e). Although HLA-DR and CD4+ infiltrate are biologically connected, association of

HLA-DR with CD8 infiltrate may be suggestive evidence that enhanced CD4+ Th infiltrate could support the continued accumulation of CD8+ CTLs in the tumor microenvironment. In our cohort, PD-L1 immunostaining in the tumor compartment was rare, occurring in 4/24 (17%) tested patients and showed no correlation with response to PD-1/PD-L1-targeted therapy.

Discussion

Targeting the PD-1/PD-L1-signaling axis produces durable responses in a subset of melanoma patients. Although a genetic basis for clinical response to CTLA-4 inhibition in melanoma has recently been suggested (*488*), so far few studies have suggested a tumor-cell autonomous basis for response to PD-1/PD-L1 monoclonal antibodies. Herein, we have identified a unique inflammatory transcriptional signature in melanoma cell lines that can be identified by tumor cell-specific MHC-II/HLA-DR expression. Interestingly, heterogeneity in MHC-II expression among panels of melanoma lines has been previously noted (*510*). We hypothesize that MHC-II expression is either (i) a functional antigen-presenting molecule that can promote CD4 T-helper cell aid to the anti-tumor milieu or (ii) a non-functional marker of the inflammatory state of the cell or tumor milieu. The presence of heterogeneity among cell lines grown ex vivo argues against the latter. Yet another alternative hypothesis is that MHC-II Ta expression on melanoma cells could be instrumental in promoting Treg differentiation in a process that requires PD-1/PD-L1 interaction; thus interruption of this signaling could be beneficial in MHC-II+ tumors. Although we did not assess different CD4 subsets (Th1, Th2, Th17, Treg), we nonetheless observed superior clinical outcomes with anti-PD-1/PD-L1 therapy in patients harboring melanomas with MHC-II expression.

In a bioinformatics analysis of MHC-II expression in melanoma cell lines, which rules out contaminating stromal and immune contribution, we found a number of gene-expression pathways to be upregulated in melanoma cell lines expressing MHC-II (Figure C.1c). The majority

of these pathways suggested the presence of an inflammatory signature and reflected gene sets found to be upregulated in response to viral (WIELAND UP BY HBV INFECTION), parasitic infections (KEGG LEISHMANIA INFECTION) and autoimmune disease (KEGG GRAFT VERSUS HOST DISEASE, KEGG ALLOGRAFT REJECTION, KEGG ASTHMA and KEGG AUTOIMMUNE THYROID DISEASE). Biologically, these pathways reflected stimulation of T-cell receptors (REACTOME TCR SIGNALING and COSTIMULATION BY THE CD28 FAMILY) and B-cell activation (BIOCARTA BLYMPHOCYTE PATHWAY and KEGG INTESTINAL IMMUNE NETWORK FOR IGA PRODUCTION). Although several gene sets were statistically downregulated in MHC-II+ cell lines, visual inspection of the heatmap suggested that these associations were primarily driven by high expression of target genes in a subset of MHC-II- cell lines, specifically Cluster II (Figure C.1c).

Although MHC-I is ubiquitously expressed in most cell types, MHC-II is typically restricted to the immune system, as the MHC-II pathway is thought to utilize extracellular antigens (released from apoptotic or necrotic cells and engulfed by professional APCs). However, tumor-specific MHC-II expression has been noted in a number of malignancies, including breast (*496*), colon (*494*) and melanoma (*495*). Experimentally, MHC-II+ epithelial cells can present antigen to CD4+T-helper cells (*502*) and enforced expression of MHC-II in tumor cells can promote anti-tumor immunity and tumor rejection in vivo (*503*). Collectively these data support a role for aberrant HLA-DR/ MHC-II expressing tumors as being a uniquely immunogenic subtype (with the ability to stimulate CD4+T-helper cells) which may adapt by expressing PD-L1. Thus, although some MHC-II- tumors may express PD-L1, this alone may not permit anti-tumor immunity through PD-1/PD-L1 inhibition. In our study, HLA-DR expression strongly correlated with response to anti-PD-1. Critically, other relevant variables also co-occurred with HLA-DR expression, demonstrated through in silico cell line analysis (GSA), flow cytometry of well characterized melanoma cell lines (PD-L1 expression and CIITA expression) and pre-treatment melanoma samples (CD4 and CD8

T-cell infiltration). Together, these data strongly argue that HLA-DR plays a causal or correlative role in anti-PD-1/PD-L1 responses. Interestingly, HLA-A expression did not statistically correlate with CD8 expression in our study (Figure C.5e). This could be due to more ubiquitous expression of HLA-A among the tumors, and it could be that the spectrum of MHC-I neo-antigen may be the rate-limiting step in this association. MHC-II expression on the tumor did correlate with CD4 infiltrate, though the nature or composition of these CD4 þ cells is not yet understood (Th1, Th2, Th17 or Tregs). Furthermore, in this study, only HLA-A was assessed for MHC-I. Additional contributing effects of HLA-B and HLA-C as well as non-classical MHC-I proteins were not assessed in this study due to limitations in robust antibodies and amount of tissue available for analysis.

Although our data point towards a functional role of MHC-II expression as contributing to sensitivity to PD-1/PD-L1 axis inhibition, it is important to note that some tumors responded to PD-1-targeted therapy, despite having no detectable MHC-II expression. There are several possible explanations for this observation: (i) that tumor sampling heterogeneity limited our ability to detect HLA-DR in the tumor and/or (ii) that these tumors may be similar to the Ib (interferon-inducible) group and PD-1 inhibition in these patients may increase CD8 infiltration and local IFNγ secretion, inducing HLA-DR, which could be detected by an on-treatment assessment. Of course, this is hypothetical, and also assumes that HLA-DR is a functional biomarker, rather than a surrogate, which remains to be experimentally proven. Yet a third hypothesis would be that other inflammatory/antigenic factors mediated by MHC-I (such as mutational burden and neo-antigen presence) could be sufficiently high in some cases to circumvent or abrogate an MHC-II requirement. Nonetheless, the potential role of MHC-II as a surrogate biomarker for response cannot be overlooked.

In order to demonstrate a functional role of MHC-II in promoting response to PD-1/PD-L1 therapy, we overexpressed Ciita in B16/F0 melanoma cells to determine whether constitutive

tumor-cell MHC-II expression would enhance response to PDL1 mAB in vivo. Despite previous reports(*506*) of successful constitutive MHC-II (IA/IE) expression by lentivirus-mediated Ciita overexpression, we were unable to establish a stable population of MHC-II+ cells in culture, despite repeated rounds of selection and flow sorting. Expansion of the positive population in cell numbers sufficient for the experiment routinely caused the MHC-II+ population to degrade to ~1–2% after 3–5 passages. The reason for this selection is presently unclear but is a matter of current investigation. Possible explanations are silencing of the lentiviral promoter or cell-mediated internalization of MHC-II.

Nonetheless, we injected either control (*LacZ*-expressing) or *Ciita*/MHC-II+ B16 cells (ranging from 10 to 30% MHC-II þ at the time of injection) into the flank of C57/Bl6 mice and monitored tumor growth and survival with either IgG (isotype) control or anti-PD-L1 mAB, given twice weekly, beginning on day + 1 following tumor-cell challenge. The subgroup of Ciita þ B16 melanoma cells with the highest degree of MHC-II positivity (30%) at the time of injection, treated with anti-PD-L1, had slower tumor formation and prolonged survival, although the effect was marginal. We believe the observed effect may not have been robust due to unstable expression and rapid selection of *Ciita*-transduced cells *in vitro* and *in vivo*. Interestingly, there appears to be an MHC-II+ dose–effect response to PD-L1 mAB (that is, 30% MHC-II+ responded better than 10 or 20%). While these results are difficult to interpret due to difficulty in establishing a pure cell line, we believe they do support a potential functional role of MHC-II expression in immunotherapy response.

Conflicting reports of stromal versus tumor PD-L1 staining, coupled with the lack of standardization, proprietary nature and the difficulties associated with PD-L1 as an IHC antigen have precluded the routine use of this marker in the clinic. In our study, a relatively low number of samples stained positively for PD-L1, despite appropriate positive controls (human placenta). The low proportion of samples with PD-L1 staining and lack of correlation of positivity with patient

benefit reinforce the problems of using PD-L1 as a clinical biomarker. In contrast, HLA-DR can be robustly identified on tumor cells through use of dual-color IHC using well-established commercially available antibodies. We propose that with additional validation, melanoma HLA-DR expression may be a rapidly translatable biomarker for patient stratification of PD-1/PD-L1 immunotherapy which can easily be performed in standard pathology laboratories at most institutions at low cost. This marker, if validated, could be envisioned to stratify patients towards anti-PD-1 monotherapy and away from the more toxic but potentially more clinically active combination of ipilimumab and nivolumab (*511-513*). Furthermore, understanding the biological basis for differential MHC-II expression among melanomas may identify agents that induce MHC-II positivity and can be used in combination with PD-1/PD-L1-targeted therapy to enhance response rates.

Methods

*Immunoblotting***.** Immunoblotting was performed as previously described (*514, 515*). Briefly, cells were washed in cold phosphate-buffered saline, collected and lysed in 1x RIPA buffer (50 mM Tris (pH 7.4), 1% NP-40, 150 mM NaCl, 1 mM EDTA, 0.1% SDS, 0.25% sodium deoxycholate, 5 mM NaF, 5 mM Na3VO4, 10% glycerol, 1 M phenylmethyl-sulphonylfluoride and protease inhibitors) for 30 min on ice. Lysates were sonicated for 2–3 s to shear DNA and cleared by centrifugation at 13,200 r.p.m. for 15 min. Protein concentrations of the lysates were determined by BCA assay (Bio-Rad, Hercules, CA). Samples were separated by SDS-PAGE and transferred to nitrocellulose membrane. Membranes were blocked with 5% non-fat dry milk or 5% bovine serum albumin in tris-buffered saline with 0.1% Tween-20 for 1 h at room temperature and then incubated overnight at 4° C with the appropriate antibody as indicated. Following incubation with appropriate horseradish peroxidase-conjugated secondary antibodies, proteins were visualized using an enhanced chemiluminescence detection system. This study was performed using the following antibodies: p-STAT1 (Cell Signaling Technology, #7649, 1:5,000) STAT1 (Santa Cruz

Biotechnology, #SC592, 1:5,000), p-ERK1/2 (Cell Signaling Technology,#9101, 1:5,000), ERK1/2 (Cell Signaling Technology #9102, 1:5,000), CIITA (Cell Signaling Technology #3793, 1:1,000) HLA-DR (Santa Cruz Biotechnology, sc-53319, 1:5,000).

Standard flow cytometry. Flow cytometry was performed using the following antibodies: HLA-DR/PE-Cy7 (Biolegend, clone L243, 1:20), CD274/PD-L1/APC (Biolegend, clone 29E.2A3, 1:200) and HLA-A/B/C –Alexa Fluor488 (1:100, Biolegend, clone W6/32) mouse MHC-II (I-A/I-E, 1:20, Biolegend, clone M5/114.15.2). DAPI was used as a viability dye. Samples were analyzed on an Aria III laser system (BD Biosciences).

Phospho-flow cytometry. Melanoma cell lines were treated with Accutase (EMD Millipore, #SCR005) for 10 min at 37° C to dissociate them from the plate. Dissociated cell lines were rested at 37° C in a CO2 incubator for 30 min before stimulation. After resting, cells were stimulated by adding IFNγ (Cell Signaling Technology) at a final concentration of 100 ng ml 1. During signaling, cells were kept in a 37° C CO_2 incubator. After 15 min of signaling, cells were fixed for 10 min at room temperature with a final concentration of 1.6% paraformaldehyde (Electron Microscopy Services). Cells were then pelleted, and permeabilized by resuspension in 2 ml of methanol and stored over night at -20° C. Flow cytometry was performed using the following antibodies: HLA-DR/BV421 (BD Horizon, clone G46-6, 1:40), p-STAT5/PE-Cy7 pY694 (BD Phosflow, clone 47, 1:10) and p-STAT1/PerCP-Cy5.5 pY701(BD Phosflow, clone 4A, 1:10). Samples were analyzed on a LSRII system (BD Biosciences).

Immunohistochemistry. For HLA-DR (Santa Cruz Biotechnology (sc-53319), 1:1,000)/SOX10 (LsBio (LS-C312170), 1:30), HLA-DR-DP-DQ-DX (Santa Cruz Biotechnology (sc-53302), 1:1,000)/SOX10, HLA-A (Santa Cruz Biotechnology (sc-365485), 1:1,300)/SOX10 and PD-L1 (Cell Signaling Technology #13684,1:500)/SOX10 dual IHC, tumor sections were stained overnight at 4° C with both antibodies. Antigen retrieval was performed using Citrate Buffer (pH6)

using a Biocare Decloaking Chamber. The visualization system utilized was MACH2 (Biocare) using DAB (Dako) and Warp Red (Biocare), and counterstained with hematoxylin. For CD4 and CD8 staining, slides were placed on a Leica Bond Max IHC stainer. All steps besides dehydration, clearing and coverslipping are performed on the Bond Max. Heat-induced antigen retrieval was performed on the Bond Max using their Epitope Retrieval 2 solution for 20 min. Slides were incubated with anti-CD4 (PA0427, Leica, Buffalo Grove, IL) or anti-CD8 (MS-457-R7, ThermoScientific, Kalamazoo, MI) for 1 h. The Bond Polymer Refine detection system was used for visualization. CD4 and CD8 were scored as per cent of infiltrating CD4(+) or CD8(+) cells in the tumor area.

HLA-DR scoring determination. Two pathologists (M.V.E. and R.S.) who were unaware of clinical response data made independent visual estimations of the percentage of tumor membrane-specific positivity for HLA-DR, in SOX10(+) nuclei areas, in the whole-tumor section focusing at the tumor hot spots. For all staining batches positive and negative controls (human tonsil; HLA-DR is positive in germinal and non-germinal center cells and negative in squamous epithelial cells) were included and stained appropriately and reproducibly in all cases. Furthermore, nearly all cases had positive-staining stromal cells (presumably B-cells and macrophages) as an internal control. In concordant cases (both investigators scored as ‘negative’ (<5% of all tumor cells in the entire tissue section staining positive; that is, all analyzable fields of view) or ‘positive’ (≥5% of tumor cells in the entire tissue section staining positive; that is, all analyzable fields of view), the result was averaged. For discordant cases (that is, positive versus negative interpretation, or any concerns on evaluable nature of the specimen) the investigators reviewed the case together to reach a final conclusion or consensus. If no consensus could be agreed upon, the sample was listed as non-evaluable.

CCLE analysis. Gene-expression data (Affymetrix hg133plus2) from the CCLE were downloaded from the Broad Institute (http://www.broadinstitute.org) and analyzed in R (http://www.r-

project.org/)(*516*). RMA-normalized melanoma cell line data were collapsed to the gene level and filtered using the 'genefilter' package. Differentially expressed genes were identified using a t-test with a FDR correction (*517*). Hierarchical clustering was performed using 1-Spearman's rank correlation and complete linkage. GSA was performed using the GSA package in R and the maxmean statistic (*518*). Gene sets in the molecular signatures database curated gene sets C2 collection (version 3.0) were utilized for GSA.

*Cell and tumor culture***.** SKMEL28 and WM115 cell lines were obtained from Dr Kimberly Dahlman (Vanderbilt University), CHL-1 and HMCB melanoma cell lines were obtained from the laboratory of William Pao (Vanderbilt University). Cell line nature was not directly authenticated, but protein-marker expression was consistent with published *HLA-DRA* mRNA expression patterns (CCLE). Cell lines were confirmed mycoplasma-free and cultured in DMEM containing 10% FBS. Stimulation with recombinant human IFNγ (R&D Systems) was performed at 100 ng ml^{-1}. For PDX models and *ex vivo* organotypic culture, tumors were freshly resected and sectioned using an Alto tissue matrix sectioner (Roboz Surgical, Gaithersburg, MD).

Patients. Patient samples and data were procured based on availability of tissue and were not collected according to a pre-specified power analysis. All patients provided informed written consent on IRB-approved protocols (Vanderbilt IRB #030220 and #100178). Tumor samples for the TMA and for the HLA-DR staining cohort were obtained from tumor biopsies or tumor resections obtained for clinical purposes. Samples were obtained within 2 years of start of anti-PD-1/ PD-L1 therapy (nivolumab, pembrolizumab and MPDL3280a). Only patients with available tumor samples and evaluable responses were included. In cases where multiple tissues were available for the same patient, the evaluable sample collected closest to PD-1 therapy was used for scoring. Clinical characteristics and objective response data were obtained by retrospective review of the electronic medical record. All responses were investigator assessed, RECIST

defined responses or (in a single case) prolonged stable disease with clinical benefit lasting >3 years.

For the validation set, all patients were consented to an IRB-approved tissue banking protocol (for MGH patients as part of either Dana Farber Harvard Cancer Center protocols 02-017 and 11-181). Samples were obtained before therapy with anti-PD-1/PD-L1 monoclonal antibodies for research (as opposed to clinical) purposes. A linked database was prospectively maintained and regularly updated with clinical characteristics, response to therapy, date of progression (if applicable) and date of death or last follow-up visit.

Statistical analysis. The tests of hypotheses concerning between two groups comparisons were completed using either two-sample Student's t-test or nonparametric Wilcoxon's rank sum test for continuous variables of interest. The analysis of variance with Tukey's multiple comparison adjustment was used for comparisons of more than two independent groups. Dichotomous data were compared using the χ^2-test with the Yates correction or Fisher's exact test when appropriate. The Kolmogorov–Smirnov test (KS-test) was used to determine if the distribution of the data sets differed significantly. For PFS analysis, the survival curves were estimated using the Kaplan–Meier method with the log-rank test to examine the statistically significant differences between study groups. For gene analysis, the FDR-adjusted Student's t-test was used to identify the 'winner genes' then followed by the complete linkage cluster analysis based on 1-Spearman's correlation. Statistical analyses were performed using R or GraphPad Prism. All P values reported were two-sided.

Appendix D

SINGLE CELL ANALYSIS OF HUMAN TISSUES AND SOLID TUMORS WITH MASS CYTOMETRY

Authors: Nalin Leelatian, Deon B. Doxie, Allison R. Greenplate, Bret C. Mobley, Jonathan M. Lehman, Justine Sinnaeve, Rondi M. Kauffmann, Jay A. Werkhaven, Akshitkumar M. Mistry, Kyle D. Weaver, Reid C. Thompson, Pierre P. Massion, Mary A. Hooks, Mark C. Kelley, Lola B. Chambless, Rebecca A. Ihrie, and Jonathan M. Irish

This work appears in manuscript form as published in *Cytometry Part B* 2016 (Leelatian, et al. 2016).
http://onlinelibrary.wiley.com/doi/10.1002/cyto.b.21481/full

License 4278960631682, Issued January 30, 2018

Abstract

Background: Mass cytometry measures 36 or more markers per cell and is an appealing platform for comprehensive phenotyping of cells in human tissue and tumor biopsies. While tissue disaggregation and fluorescence cytometry protocols were pioneered decades ago, it is not known whether established protocols will be effective for mass cytometry and maintain cancer and stromal cell diversity.

Methods: Tissue preparation techniques were systematically compared for gliomas and melanomas, patient derived xenografts of small cell lung cancer, and tonsil tissue as a control. Enzymes assessed included DNase, HyQTase, TrypLE, collagenase (Col) II, Col IV, Col V, and Col XI. Fluorescence and mass cytometry were used to track cell subset abundance following different enzyme combinations and treatment times.

Results: Mechanical disaggregation paired with enzymatic dissociation by Col II, Col IV, Col V, or Col XI plus DNase for 1 hour produced the highest yield of viable cells per gram of tissue. Longer dissociation times led to increasing cell death and disproportionate loss of cell subsets. Key markers for establishing cell identity included CD45, CD3, CD4, CD8, CD19, CD64, HLA-

DR, CD11c, CD56, CD44, GFAP, S100B, SOX2, nestin, vimentin, cytokeratin, and CD31. Mass and fluorescence cytometry identified comparable frequencies of cancer cell subsets, leukocytes, and endothelial cells in glioma (R = 0.97), and tonsil (R = 0.98).

Conclusions: This investigation establishes standard procedures for preparing viable single cell suspensions that preserve the cellular diversity of human tissue microenvironments.

Introduction

In preparing single cell suspensions of healthy and malignant tissue, a common goal is to preserve viability while maintaining cellular diversity and preserving rare subsets. Multidimensional cytometry is well suited to this challenge because it can simultaneously characterize known cell types and reveal novel cell subsets (*175, 208*). Mass cytometry uses antibodies to quantify features of individual cells in primary tissues (*218, 320*) and has been applied to characterize cell subsets in human bone marrow, blood, and germinal center tissues as well as diverse murine tissues (*9, 231, 314*). However, mass cytometry remains relatively untested in the context of solid tumors. Fluorescence flow cytometry and fluorescence activated cell sorting (FACS) have been used to prospectively isolate functionally distinct cell subsets and suggest that mass cytometry analysis could help to further characterize solid tumors (*175*). A key goal of this study was to evaluate the suitability of different cell preparation techniques for mass cytometry and to develop standard procedures and quality controls that do not require measuring light scatter. An additional goal was to use the multidimensionality of mass cytometry to characterize preservation of cellular diversity under different solid tumor cell preparation techniques.

In this study, mechanical and enzymatic dissociation protocols were systematically tested on multiple types of fresh human solid tumors and tissues to develop an efficient, reliable method for dissociation and single-cell analysis by mass cytometry. Human tonsils and lymphoma tumors reliably dissociate with mechanical force alone and we have previously established protocols for

their study by fluorescence cytometry (*192, 272*) and mass cytometry (*223*). Preparation techniques for tissue samples derived from intraoperative resections of gliomas (grades II-IV), melanomas, and patient derived xenografts (PDX) of small cell lung cancer (SCLC) were compared. As a control, the same techniques were applied to human tonsillar tissue. The abundance of different cell types, such as leukocytes, endothelial cells, epithelial cells, fibroblasts, and cancer cell subsets, was tested under these conditions. Established protein markers for expected cell types in tissues tested in this study were used in fluorescence cytometry (Table S1) and mass cytometry (Table S2, Table S4). The common markers were selected so that both rare and abundant cell types could be compared between mass and fluorescence cytometry. The additional markers in the mass cytometry panel provided a more comprehensive analysis of cell diversity.

Six enzymes for cell separation were selected to compare in solid tumor preparation protocols for mass cytometry analysis: HyQTase, TrypLE, collagenase (Col) II, Col IV, Col V, and Col XI. Enzyme choice was based in part on prior use in several solid tumor types and preparation of single cell suspensions containing cancer cell and immune subsets for FACS (*519-524*). DNase was also tested to determine its ability to enhance live cell yield from dissociation. Dissociation kinetics for enzyme combinations in distinct tissue types were also characterized. Finally, specific enzymes and dissociation duration times were selected based on optimal viable cell yield and representation of expected cell populations.

Materials and Methods

Tissue Sample Collection – All samples were obtained with patient consent, with Vanderbilt institutional review board (IRB) approval, in accordance with the Declaration of Helsinki, and were de-identified. Gliomas were intraoperative specimens from WHO grade II, III, or IV tumors (IRB #131870), collected in sterile normal saline. Melanomas were cutaneous and lymph node

resections (IRB #030220), collected in MEM (Corning/Mediatech, Corning, NY) with 10% FBS + 1X Pen/Strep (GE Healthcare, Pittsburgh, PA). Small-cell lung cancer (SCLC) patient derived xenograft (PDX) samples were obtained as a gift from the Rudin laboratory (LX-22, (*525*)) and propagated solely as patient-derived xenografts in female athymic nude mice (HSD:Athymic Nude-Foxn1$^{nu/nu}$) obtained from Envigo with Vanderbilt institutional animal care and use committee (IACUC) approval. SCLC PDX were collected in RPMI 1640 (Corning/Mediatech, Corning, NY) plus 10% FBS+ 1X Pen/Strep. Glioma, melanoma, and SCLC PDX samples were transported at room temperature without delay to the laboratory and processing began within 30 minutes of collection from patients. Human tonsillar tissue was obtained from routine tonsillectomies (IRB #121328), collected in RPMI 1640 (Corning/Mediatech, Corning, NY) plus 10% FBS+ 1X Pen/Strep, transported on ice, and processed within 4 hours of collection.

Mechanical and Enzymatic Dissociation – Sequential dissociation steps are described in detail in the main text. “Coarse mincing” indicates no additional mechanical dissociation of tissues (i.e. tissues were left as obtained intraoperatively). “Fine mincing” indicates additional mechanical dissociation using scalpels. Conventional mechanical dissociation of tonsils included fine mincing and immediate filtration of tissue through a 70 µm cell strainer without additional enzymatic dissociation, as previously established (*192, 223, 272*). Dissociation enzymes were obtained from Sigma Aldrich (Darmstadt, Germany) (collagenase II, IV, V, and XI), ThermoFisher (Waltham, MA) (TrypLE-Express), and GE Healthcare (PA) (HyQTase). Collagenases were used at 1 mg/mL. HyQTase and TrypLE-Express were used at 1X according to the manufacturer’s recommendations. DNase I (Sigma Aldrich) was used at a final concentration of 0.25 mg/mL. For conditions involving collagenases and no enzyme, cells were resuspended in recommended media for specific tissue types prior to adding indicated enzymes (gliomas, DMEM/F12+Glutamax, (Gibco/Life Technologies, MA) with a defined hormone and salt mix (*526*) and 50 µg/mL gentamicin; melanomas, MEM with 10% FBS + 1X Pen/Strep; Tonsils and SCLC

PDXs, RPMI 1640 + 10% FBS + 1X Pen/Strep. For dissociation conditions with HyQTase or TrypLE, tissues were dissociated in working concentrations of enzymes (with or without DNase), without addition of cell culture media, according to the manufacturer's recommendations. Enzymatic dissociations were performed in a 37°C incubator with 5% CO_2, with constant rocking on a nutating platform mixer at 18 rpm. Cells were then strained with 70 µm and 40 µm cell strainers prior to further analysis.

Quantification of cell viability – Cell suspensions obtained from different dissociation protocols were resuspended in corresponding cell culture media at volumes proportional to initial tissue weight (1 mL per 100 mg of tissue). Viable cells were quantified using Trypan Blue staining, normalized to the initial tissue weight, and reported as millions of live cells per gram of tissue.

Statistical testing – Enzyme conditions were compared as groups (horizontal lines) using a Student's t-test. The relationship between cell subset abundance measured by fluorescence or mass cytometry was compared using Pearson's correlation R and Spearman's rank correlation ρ (rho).

Cell line and cell culture – Jurkat cells were obtained from Utpal Dave at Vanderbilt, and were grown in RPMI 1640 + 10% FBS + 1X Pen/Strep as recommended. MeWo cells were obtained from Kimberly Dahlman and Jeffery Sosman with permission of Antoni Ribas (UCLA) and were grown in MEM + 10% FBS + 1X Pen/Strep, as recommended.

Flow cytometry - Cell suspensions were evenly divided for parallel phenotyping with fluorescence and mass cytometry according to the protocols below. Conditions were identical between mass and fluorescence cytometry with the exception of an additional staining step including saponin for mass cytometry analyses of glioma and melanoma that include SOX2. This type of saponin step has been established to have no significant impact on subsequent mass cytometry staining (*436*).

Fluorescence flow cytometry – For fluorescence cytometry, live surface staining was performed for surface marker detection (Supplemental Table S1). After washing with PBS and pelleting twice (at 200 x *g* for 5 min each time), cells were fixed with 1.6% paraformaldehyde (Electron Microscopy Services, Fort Washington, PA) for 10 min at room temperature, washed with PBS (HyClone Laboratories, Logan, UT), pelleted at 800 × *g,* and permeabilized with 100% ice-cold methanol (Fisher Scientific, Waltham, MA) at −20°C overnight following established protocols (*272, 527*). Cells were washed twice with cell staining media composed of PBS plus 1% BSA (Fisher Scientific, Waltham, MA) and pelleted at 800 *x g*. For each comparison, cells were stained in 100 µL staining media for 30 minutes at room temperature. All antibodies are listed in Supplemental Tables. Note that some antibodies that detect cell surface antigens (CD45-BV786, CD44-PE, and CD31-PE-Cy7) were used after fixation and methanol permeabilization due to concerns for stabilization of fluorochromes after methanol exposure. After staining, cells were washed twice with PBS, pelleted at 800 *x g*, and resuspended in PBS for analysis on a 5-laser LSRII (BD Biosciences, San Jose, CA) at the Vanderbilt Flow Cytometry Shared Resource.

Mass cytometry – Solid tissue cells obtained from the same dissociation conditions as those analyzed by fluorescence flow cytometry were stained live for cell surface markers, fixed, permeabilized, and washed as for fluorescence flow cytometry above and in concordance with established mass cytometry protocols (*320*). Permeabilization with 0.02% Saponin (Millipore, Darmstadt, Germany) in PBS was also included before methanol permeabilization of gliomas and melanomas as part of an optimized multi-step protocol that included detecting SOX2, which was not included in the fluorescence panel. Metal-tagged antibodies were used to stain cells in 100 µL cell staining media for 30 minutes at room temperature (Supplemental Table S4). After staining, cells were washed once with PBS, once with deionized water, pelleted at 800 *x g*, and resuspended in deionized water containing normalization beads (Fluidigm). Standard bead-based normalization was used as previously described (*270*). Cells were collected on a CyTOF 1.0 at

the Vanderbilt Flow Cytometry Shared Resource. Original data were normalized with MATLAB normalization software prior to further analysis using Cytobank (*229*) and established mass cytometry analysis methods (*207*). viSNE analysis was performed using 60,000 cCasp3^{-}HH3^{+} cells per sample. For glioma G-LC-15, the following markers were used for viSNE analysis: CD31, CD64, CD45RO, S100B, CD45, PDGFRα, SOX2, CD24, CD44, CD3, GFAP, αSMA, HLA-DR, and CD56. For tonsil T02-23, the following markers were used for viSNE analysis: CD4, IgD, CD16, CD45RO, CD45RA, CD45, CD27, CD86, CD33, CD11c, CD14, CD19, CD38, CD8, CD3, IgM, HLA-DR, and CD56. Samples of the same tissue type dissociated with different types of collagenase were analyzed simultaneously by viSNE.

Histone H3 testing – Healthy peripheral blood mononuclear cells (PBMCs) were used as controls in testing histone H3 as a nucleated cell marker for multiple flow cytometry platforms. PBMCs were stained live for detection of cell surface markers (Supplemental Table S2). After being washed twice with PBS, cells were then fixed with 1.6% paraformaldehyde and permeabilized with 100% ice-cold methanol for intracellular staining. Stained PBMCs were then evenly divided and half of the cells were stained with iridium at a final concentration of 0.25 μM in PBS for 15 minutes at room temperature. Cells were then washed once with PBS, once with deionized water, pelleted at 800 *x g*, and resuspended in deionized water containing normalization beads. Cells were collected as described above.

Results

Tissue dissociation with collagenase and DNase improved live cell yield

A matrix of dissociation conditions was tested to identify optimal protocols for multiple solid tumor types and tonsil controls (Figure D.1). The mechanical dissociation protocol (*see Materials and Methods*) was first compared to fine mincing of tonsil tissue followed by a 2-hour enzymatic dissociation with combinations of collagenase and DNase. For tonsils, a combination of fine

mincing, collagenase, and DNase resulted in superior live cell yield per gram of tissue compared to conventional dissociation methods ($p < 0.05$). Additionally, fine mincing of tonsils did not adversely affect cell viability when compared to coarse mincing (left as obtained intraoperatively).

Since freshly resected tissues and tumors frequently differ in size, fine mincing was selected as an initial mechanical dissociation step for all tissue types. To determine the optimal enzymes for disaggregation of human gliomas, seven different enzymatic conditions were tested for their ability to yield live, single cells (Figure D.1A, N = 3). Intraoperative samples of gliomas were finely minced and incubated with a cocktail of DNase plus one enzyme (either HyQTase, TrypLE, Col II, Col IV,

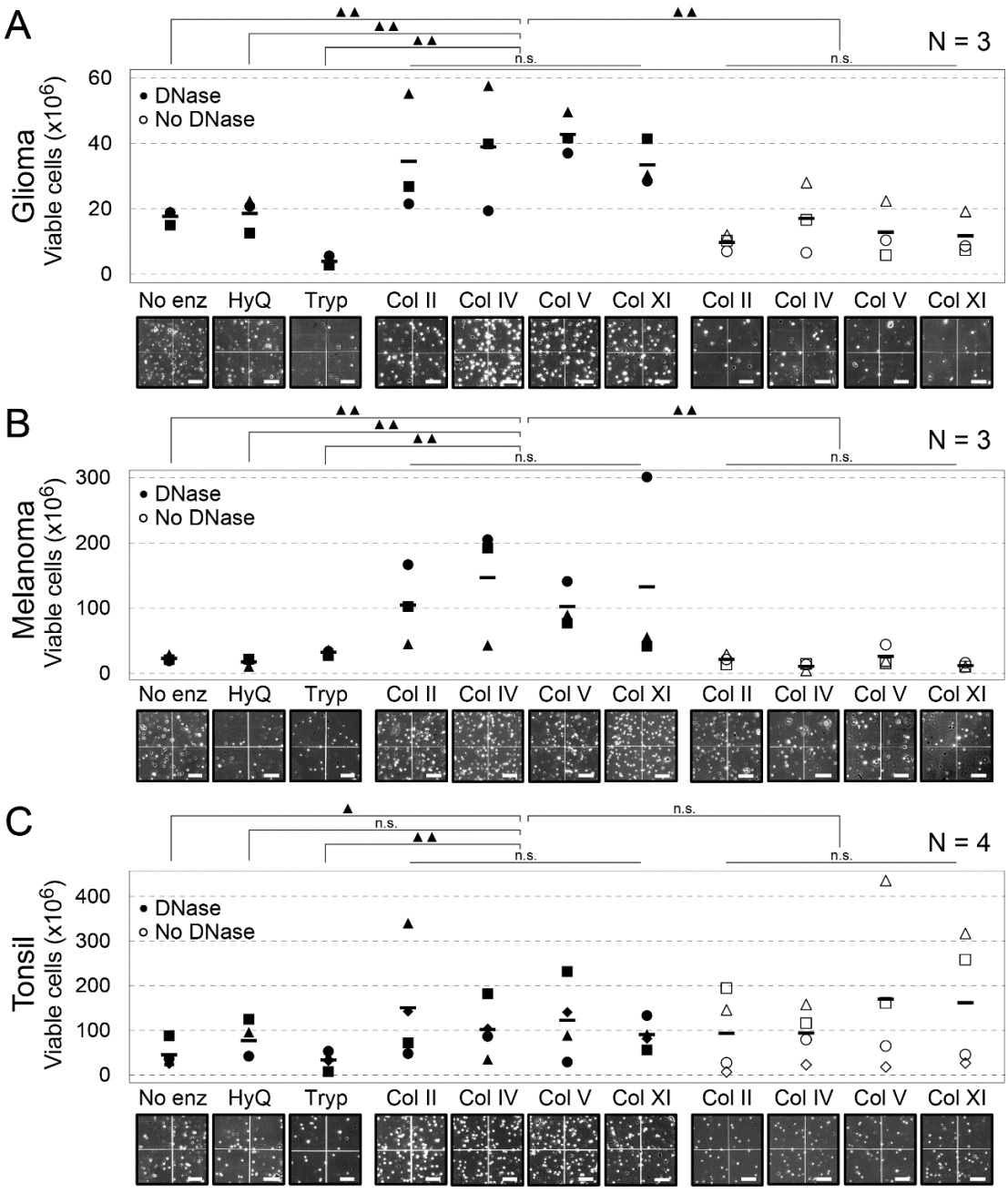

Figure D.1 - Collagenase plus DNase treatment provides better yield of live cells from three human tissues than no enzyme, TrypLE, HyQTase, or collagenase treatment alone. Graphs show millions of viable cells per gram yielded by different tissue preparation conditions following fine mincing for (A) gliomas, (B) melanomas, and (C) tonsil tissue. In addition to DNase (closed symbols), preparation enzymes tested included no additional enzyme (No enz), recombinant trypsin TrypLE (Tryp), HyQTase (HyQ), and collagenase (Col) II, IV, V, or XI. Average live cell yield is indicated for each condition by the thick horizontal line. Individual tissues or tumors are represented by different symbols. Representative trypan blue stained images are depicted under each condition. Scale bars = 100 µm. Symbols denote not significant (n.s.), $p < 0.05$ (♦), or $p < 0.01$ (♦♦). N indicates number of separate individual sample donors tested under each condition for each tissue type.

Col V, or Col XI) or DNase alone for 2 hours at 37°C, with continuous rocking. Increased live cell yield per gram of tissue was seen in conditions containing collagenase and DNase as compared to other conditions ($p < 0.01$). Additionally, DNase plus collagenase improved live cell yield for glioma compared to collagenase alone ($p < 0.01$). No significant differences were observed in live cell yield per gram of glioma tissue between conditions using different types of collagenases plus DNase.

The same matrix of conditions was tested on intraoperative samples of human melanomas (Figure D.1B, N = 3). As with glioma, no significant difference in live cell yield was observed between different types of collagenases, and viable cell yields were highest in conditions containing collagenases and DNase ($p < 0.01$). In freshly resected tonsils (Figure D.1C, N = 4), collagenases with DNase gave a higher live cell yield than either DNase alone ($p < 0.05$) or TrypLE plus DNase ($p < 0.01$). However, collagenases with DNase did not significantly differ from HyQTase with DNase, and addition of DNase did not result in higher or lower live cell yield, in tonsil dissociation.

Enzymatic dissociation with collagenase and DNase for 1-2 hours provided superior live cell yields

While incubation in enzyme solutions enhanced tissue disaggregation (Figure D.1), excessive incubation might adversely affect cell viability. A dissociation time course was performed on intraoperative glioma specimens to determine the optimal time point for highest live single cell yield (Figure D.2A). Gliomas were finely minced and incubated in collagenases plus DNase for 30 minutes, 1 hour, 2 hours, 4 hours, or 6 hours (Figure D.2A, N = 3). Live cell yield per gram of glioma tissue significantly decreased after 4 hours of enzymatic dissociation with Col II, Col V, or Col XI plus DNase compared to earlier time points (Col II and Col XI, $p < 0.001$; Col V, $p < 0.05$), whereas it significantly decreased after 6 hours of dissociation with Col IV plus DNase (Figure D.2A, $p < 0.001$).

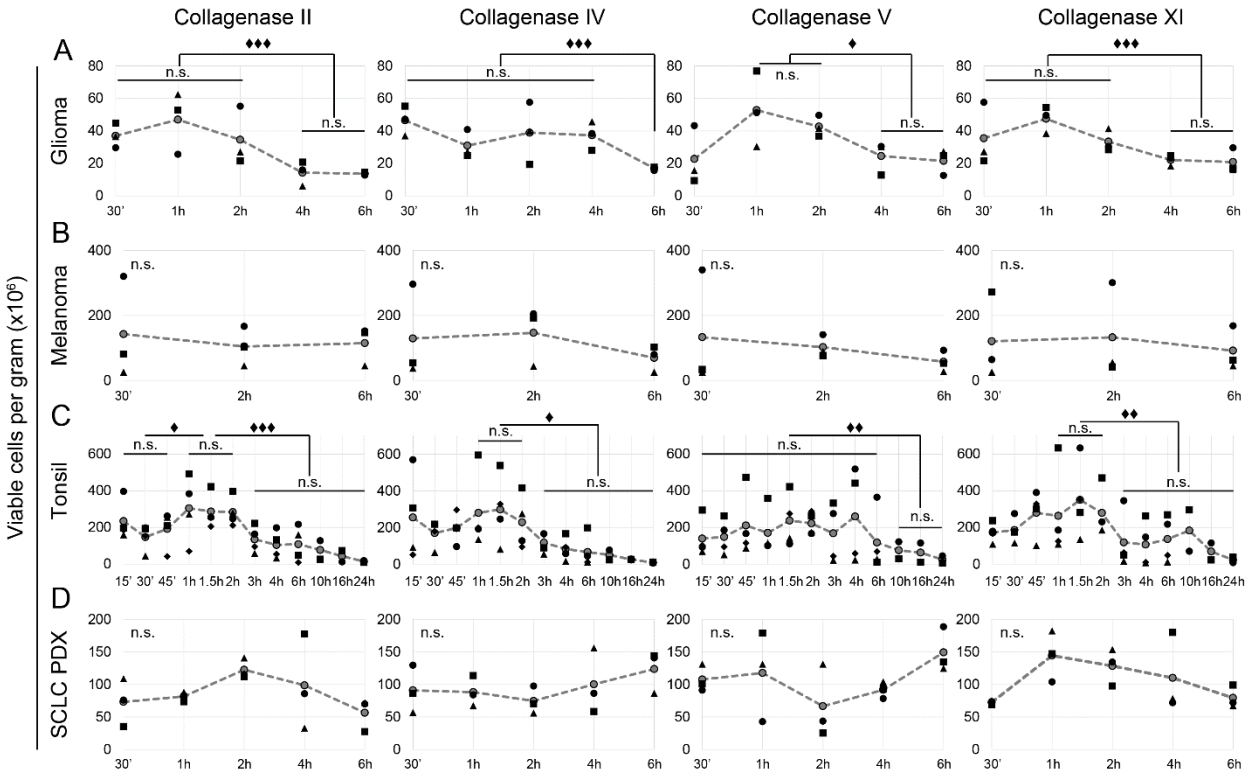

Figure D.2 - Collagenase and DNase treatment for 1 or 2 hours provided better overall live cell yield than other times. (A) Gliomas (N = 3) were finely minced and treated for varying times with DNase and either Col II, Col IV, Col V, or Col XI. Yield of live single cells (x10^6) per gram was quantified from Trypan blue images after 30 minutes (’), 1 hour (h), 2h, 4h, and 6h (filled symbols). Individual tissues or tumors are represented by different symbols. Grey circles mark average yield and are connected with dashed lines to indicate dissociation kinetics. Dissociation kinetics were similarly assessed for (B) melanomas (N = 3), (C) tonsil tissue (N = 4, except for 10h, 16h, 24h where N = 2), and (D) SCLC PDX tumors (N = 3) (D). Symbols denote not significant (n.s.), $p < 0.05$ (♦), $p < 0.01$ (♦♦), or $p < 0.001$ (♦♦♦).

Dissociation kinetics of tonsils were also characterized for time points ranging from 15 minutes to 24 hours (Figure D.2C). Finely minced tonsils dissociated with Col II plus DNase for 1-2 hours gave higher live cell yield when compared to earlier time points ($p < 0.05$) as well as later time points ($p < 0.001$). Similarly, viable cell yield decreased significantly after 1-2 hours when tonsils were dissociated with either Col IV or Col XI plus DNase (IV, $p < 0.05$; IX, $p < 0.01$). Live cell yield from the combination of Col V and DNase also decreased after 6 hours ($p < 0.01$). Live cell yield from intraoperative melanoma specimens and SCLC patient-derived xenografts (PDXs) did not

significantly decrease after 6 hours of dissociation, regardless of the type of collagenase (Figure D.2B and 2D).

Testing histone H3 as a nucleated cell marker compatible with mass and fluorescence cytometry

An anti-Histone H3 (HH3) monoclonal antibody was next tested as a potential marker of nucleated cells that would function equivalently in fluorescence and mass cytometry. Jurkat T leukemia cells gated as intact cells were 98.9% positive for HH3 in fluorescence cytometry. Similarly, when Jurkat cells were gated first as $HH3^+$, they were observed to be >99.8% intact cells when gated using light scatter in fluorescence cytometry. Peripheral blood mononuclear cells (PBMCs) were used to further test HH3 because PBMC have well-studied cell subsets that have been extensively characterized by both fluorescence and mass cytometry (*194, 196, 320*). PBMCs from a healthy donor were stained with a panel of 16 mass-tagged antibodies. Frequencies of known cell subsets identified by biaxial gating were closely correlated in the same mass cytometry dataset gated using HH3 or established iridium-based gating (Pearson correlation R = 1.00, Spearman rank of subset abundance rho (ρ) = 1.00), supporting the use of HH3 as nucleated cell marker across multiple flow cytometry platforms.

Assessment of cell subset diversity in solid tumor following collagenase and DNase treatment

Two- to seven-dimensional fluorescence flow cytometry has been used extensively to characterize presence and abundance of cell subsets in patient-derived tissues. Glioma cell subsets consistent with those documented in prior studies were present after a 1-hour dissociation with DNase plus Col II using fluorescence flow cytometry (Figure D.3A, Col II). In glioma sample G-RT-06, 55.4% of all events were identifiable as intact nucleated cells based on HH3 staining. $CD45^+$ immune cells comprised 59.7% of live intact cells, which included $CD3^+$ T cells (26.7%) as well as other immune cell types (71.8%). Presence of immune cell subsets was confirmed with immunohistochemistry (IHC) staining of formalin-fixed paraffin-embedded (FFPE) sections of the

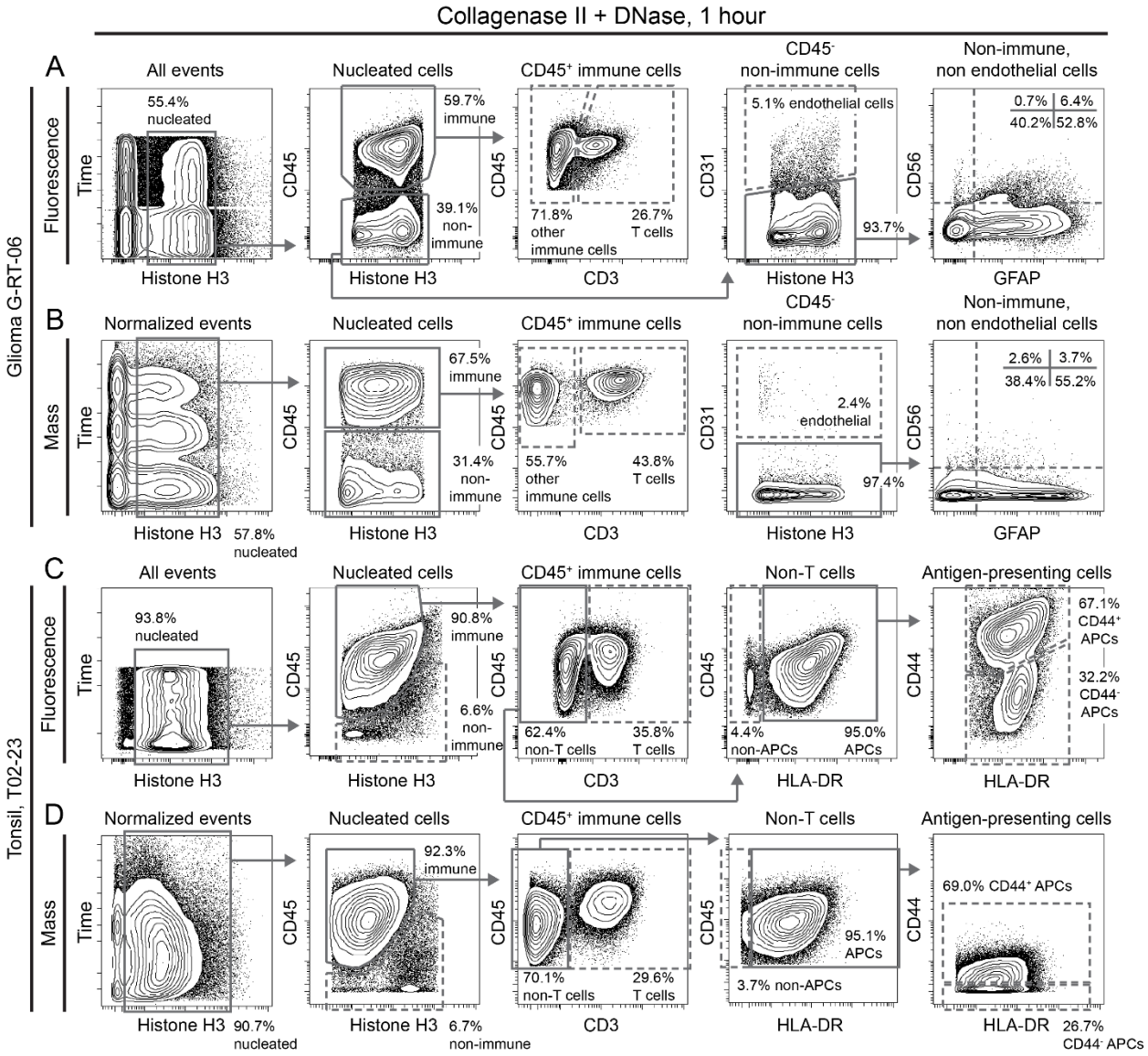

Figure D.3 – Frequency of cell types in glioma, and tonsil tissue quantified by fluorescence and mass cytometry. Biaxial plots show gating for established cell types in human tumors and tissues prepared using Col II plus DNase for 1 hour. Nucleated cells ($HH3^+$) were identified. Immune cells ($CD45^+$), T cells ($CD45^+$ $CD3^+$), APCs ($CD45^+$ $CD3^-$ $HLA\text{-}DR^+$), endothelial cells ($CD31^+$ $CD45^-$), and non-immune non-endothelial cells ($CD45^-$ $CD31^-$) were also found. (A) In fluorescence cytometry analysis of glioma from an individual patient (G-RT-06), CD56 (NCAM) and GFAP expression are shown for $CD45^-$ $CD31^-$ cells. (B) A similar gating scheme was applied to mass cytometry data from G-RT-06. In tonsil tissue from donor T02-23, CD44 and HLA-DR are shown for $CD45^+$ $CD3^-$ $HLA\text{-}DR^+$ cells, for both fluorescence (C) and mass cytometry analysis (D). Frequency of terminal populations (dashed gates) was compared between fluorescence and mass cytometry in Table 1.

same sample. Additionally, $CD31^+$ endothelial cells were detected (5.1% of non-immune cells), as were cell subsets that differentially expressed CD56 (NCAM) and GFAP. The abundance of nucleated cells and other known cell subsets was similar between different collagenase types.

To determine if cells derived from dissociations using collagenase and DNase were suitable for mass cytometry analysis, cells obtained from intraoperative glioma resections (G-RT-06) were stained with 16 isotope-labelled antibodies (Table S4). Histone H3 was used to identify intact nucleated cells. A biaxial analysis sequence similar to that used for fluorescence flow cytometry analysis was used for comparison of subset abundance identified by these two cytometry platforms (Figure D.3B). A strong correlation of cell subset abundance between the two methods was observed and quantified (Table 1; Pearson's R = 0.97, Spearman's rank ρ = 0.93). Similar comparisons were performed in tonsils (Figure D.3D). Strong correlations of subset abundance between the two different cytometry platforms was also observed in tonsil (Table 1; Pearson's R = 0.98, Spearman's rank ρ = 0.90).

Subsets of immune cells in tonsils were also identified by fluorescence flow cytometry, including $CD3^+$ T cells, $CD44^+$ antigen-presenting cells (APCs), $CD44^-$ APCs, and additional immune and non-immune cell types, as expected (Figure D.3C, Col II). Abundance of tonsil cell subsets was similar between dissociations using different collagenase types. Single cells obtained from resected melanomas (MP-04) and a melanoma cell line, MeWo, were analyzed by fluorescence flow cytometry and were observed to have intrinsic auto-fluorescence on some channels, whereas glioma and tonsil samples studied here showed no auto-fluorescence. Mass cytometry was next used to study melanoma tumors. $CD45^+$ immune subsets, including $CD45^+$HLA-DR^+ antigen-presenting cells, $CD45^+CD3^+$ T cells ($CD8^+$ and $CD8^-$, and $CD45RO^+$ memory and $CD45RO^-$ non-memory), as well as $CD31^+$ endothelial cells were identified in melanoma. Additionally, among the non-immune, non-endothelial cells, other cell subsets were identifiable by nestin, SOX2, CD44, HLA-ABC, vimentin, and cytokeratin.

To characterize the effects of different types of collagenase on the presence of cell subsets, mass cytometry analysis of cells derived from glioma dissociation at one hour with DNase plus either Col II, Col IV, Col V, or Col XI was performed (Figure D.4). This time point was selected based

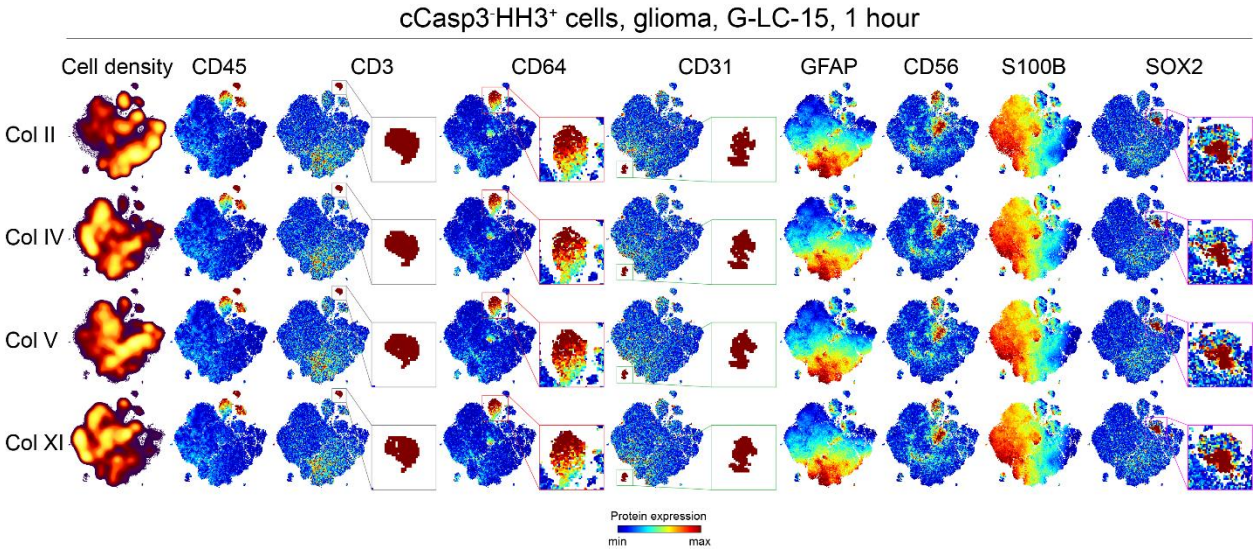

Figure D.4 – Treatment of a glioma with different collagenases yielded comparable cell subset frequencies. viSNE plots show non-apoptotic nucleated cells (cCasp3$^-$HH3$^+$) from glioma G-LC-15 obtained following 1-hour treatment with DNase plus either Col II, VI, V, or XI. Heat plots indicate cell density (first column) or expression of 8 proteins indicating cell type (CD45, CD3, CD64, CD31, GFAP, CD56, S100B, and SOX2). viSNE mapping was run together. Color-coded inserts next to the complete map highlight cell subsets (grey = CD45$^+$CD3$^+$ T cell, 0.9 ± 0.1%; red = CD45$^+$CD64$^+$ microglia, 3.9 ± 1.0%; green = CD45$^-$CD31$^+$ endothelial cells, 0.7 ± 0.2%; fuchsia = SOX2$^+$ stem-like cells, 1.2 ± 0.5%).

on its highest live cell yield across multiple tissue types, shown above. viSNE analysis (*231*) was used to compare cell subsets in the different dissociation conditions. Known cell subsets in gliomas were present in all conditions, including CD45$^+$ immune cells (CD3$^+$ T cells, and CD64$^+$ microglia), CD45$^-$CD31$^+$ endothelial cells, GFAP$^+$ glial cells, S100B$^+$ astrocyte-like cells, and SOX2$^+$ stem-like cells. Established cell subsets were also observed in tonsil specimens dissociated for one hour in all types of collagenase. As expected, the majority of cells were CD45$^+$ immune cells. Additionally, known immune subsets, including CD3$^+$CD4$^+$ helper T cells, CD3$^+$CD8$^+$ cytotoxic T cells, CD19$^+$IgD$^+$ naïve B cells, and CD19$^+$CD27$^+$ memory B cells, were identified. These findings suggest that both mass cytometry and fluorescence cytometry identify key cell subsets in glioma and tonsil dissociated with collagenase plus DNase.

Longer dissociation times led to disproportionate cell death and loss of cellular diversity

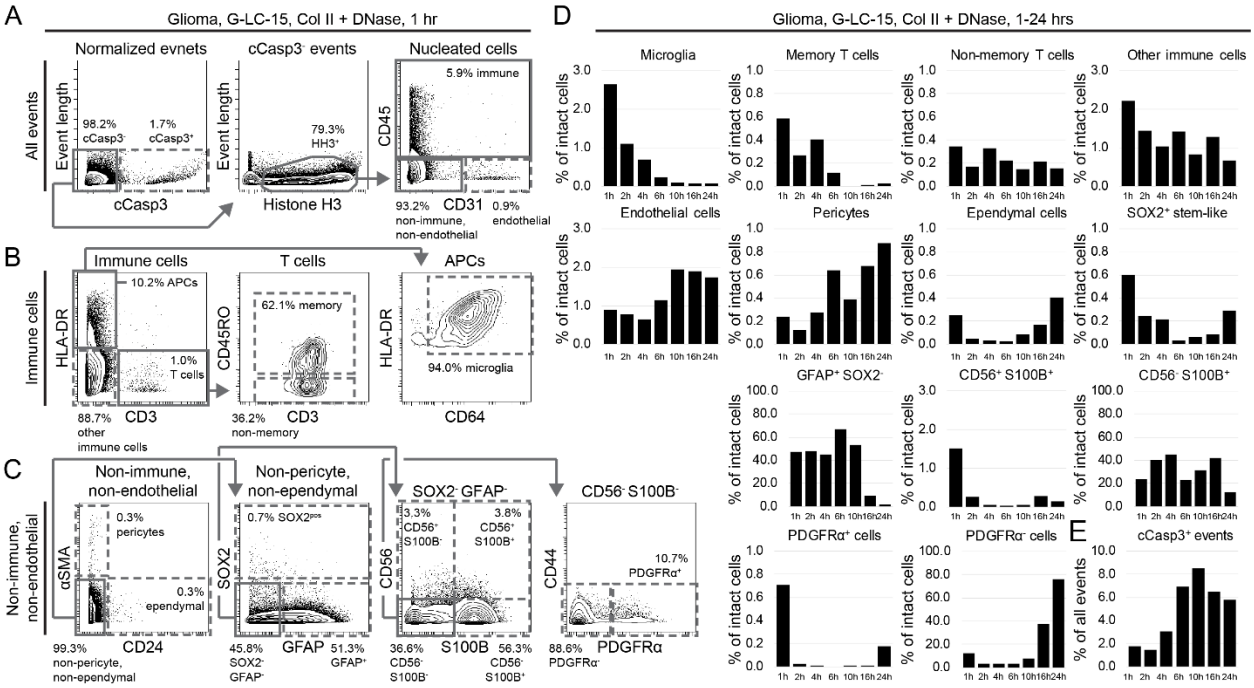

Figure D.5 – Enzymatic treatment times longer than one hour differentially impact glioma tumor cell subsets. Biaxial plots and bar graphs quantify cell subsets measured in mass cytometry analysis of glioma G-LC-15 after varying treatment times with collagenase II and DNase. (A) Gating for apoptotic cells (cCasp3$^+$) and live immune cells (cCasp3$^-$CD45$^+$), endothelial cells (cCasp3$^-$CD31$^+$), and non-immune, non-endothelial cells (cCasp3$^-$CD45$^-$CD31$^-$). (B) Subsets of glioma tumor-infiltrating immune cells were identified, including microglia (HLA-DR$^+$CD64$^+$), CD45RO$^+$ and CD45RO$^-$ subsets of CD3$^+$ T cells, and other immune cells. (C) Pericytes (CD45$^-$CD31$^-$αSMA$^+$), ependymal cells (CD45$^-$CD31$^-$CD24$^+$), SOX2$^+$ stem-like cells (CD45$^-$CD31$^-$SOX2$^+$), GFAP$^+$ cells (CD45$^-$CD31$^-$GFAP$^+$), and astrocyte-like cells (CD45$^-$CD31$^-$S100B$^+$) were quantified as subsets of G-LC-15. (D) Gating for cell types as in (A-C) was applied to mass cytometry analysis of cells from G-LC-15 treated with collagenase II plus DNase for 1, 2, 4, 6, 10, 16, or 24 hours. (E) Percentage of apoptotic cells as in (A) was measured for each dissociation time, as in (D).

To determine if the abundance of cell subsets changed over time with enzymatic dissociation, time course dissociations of glioma sample, G-LC-15 (Figure D.5), and tonsil sample, T02-23 , with DNase plus Col II were performed. Cell subsets were identified using sequential biaxial analysis and given the indicated labels following expert review. Apoptotic cells, defined by high cCasp3 signal, were excluded from subsequent cell subset quantification (Figure D.5A). Within the population of HH3$^+$ nucleated cells, marker analysis identified CD45$^+$ immune cells and CD31$^+$ endothelial cells. Known subsets of immune cells were present within the CD45$^+$ population, including microglia (HLA-DR$^+$CD64$^+$), memory T cells (CD3$^+$CD45RO$^+$), and non-memory T cells (CD3$^+$CD45RO$^-$) (Figure D.5B). Within the CD45$^-$CD31$^-$ population, pericytes (αSMA$^+$) and

ependymal cells ($CD24^+$) were seen, as well as rare $SOX2^+$ stem-like cells, $GFAP^+$ glial cells, $PDGFR\alpha^+$ cells, and $S100B^+$ astrocyte-like cells (Figure D.5C). Quantification of these cell subsets was performed in samples obtained from different dissociation durations to characterize maintenance and enrichment of cell subsets over time (Figure D.5D). Among immune cells, a decrease in microglia (after 1 hour) and memory T cells (after 4 hours) was noted, whereas the proportion of non-memory T cells appeared to remain constant over the full range of times tested. $SOX2^+$ stem-like cells were most abundant after 1 hour of dissociation and decreased thereafter. Even though the proportion of $SOX2^+$ stem-like cells increased at 24 hours after dissociation, the overall decrease in viable cells after 4-6 hours of glioma dissociation (Figure D.2A) suggested an overall loss in total viable stem-like cells at later time points. Additionally, the abundance of $GFAP^+$ glial-like cells (known to be present in most gliomas) remained constant during the initial 10 hours of dissociation and showed a decrease after 16 hours. This suggested that longer dissociation depletes key cell subsets in glioma. Most of the nucleated, non-apoptotic cells that remained after 24 hours of dissociation lacked expression of the key cell identity markers used in this study. Moreover, the abundance of $cCasp3^+$ apoptotic events also increased over time (Figure D.5E).

A similar time course strategy was applied to tonsil specimen dissociation. A decrease in the abundance of most immune cell subsets was observed at all time points greater than 1 hour of dissociation with Col II plus DNase. This decrease affected all T cell subsets, plasma cells/blasts, germinal center B cells, class-switched memory B cells, and unswitched memory B cells. Notably, abundance of naïve B cells remained constant during the initial 6 hours of dissociation and only decreased after 10 hours. $CD27^-IgD^-$ B cells increased in abundance at time points extending to 6 hours, followed by a decrease at 10 hours. Dendritic cells were the only immune cell subsets that continued to increase in abundance at 24 hours of dissociation. As expected, longer dissociation times likewise led to an increase in apoptotic cells.

Discussion

A common protocol of collagenase II plus DNase for 1 hour was identified as effective for preparing viable and mass cytometry compatible single cell suspensions of all tested human solid tumors and healthy tissues. Multiple types and combinations of enzymes and dissociation kinetics were compared in freshly resected patient-derived tissues and patient-derived xenografts. Unexpectedly, collagenase also resulted in greater viable cell yield from tonsils when compared to the conventional dissociation method (Figure D.1), indicating that the protocol for preparation of tonsil and lymphoma tumors could be further refined. DNase clearly improved live cell yield from gliomas and melanomas and is strongly recommended for tissues where there may be ongoing cell death. Even though DNase was not observed to improve tonsil dissociation, DNase also did not adversely affect tonsil cell viability. Live cell yield from glioma dissociation began to decrease after 4-6 hours. However, live cell yields from melanoma and SCLC PDX were constant throughout the dissociation duration tested (6 hours) for all types of collagenase. In contrast, live cell yield from tonsils was maximal during the initial 2 hours of dissociation, except for collagenase V, which significantly decreased only after 6 hours.

Critically, dissociation of tissue using combined collagenase and DNase preserved cellular diversity, as seen by mass cytometry and standard fluorescence flow cytometry (Figure D.3 and Figure D.4). At one hour after dissociation, known cell subsets were present as expected in each of the tested tissue types. These included immune cells in tonsil, infiltrating immune cells in glioma and melanoma, and tissue-specific cell subsets, such as cancer cell subsets, endothelial cells, glial cells, pericytes, and stem-like cells in gliomas. A difference in abundance of T cells observed between fluorescence and mass cytometry was determined to be due to use of different anti-CD3 antibody clones, as has been previously reported (*196, 199*). While immune cells and $GFAP^+$ cells in glioma were confirmed with IHC stains and observed to be in relatively close agreement between IHC and flow cytometry, small tissue sections and sections that do not sample all tumor

regions may over- or under-represent cell subsets or overlook rare cells. The quantitative analysis of a large number of whole cells by multidimensional flow cytometry (10^5 to 10^7) provides a strong complement to the location information provided by imaging cytometry (*454*).

Longer dissociation times led to increased cell death and disproportionate depletion of cell subsets in both gliomas and healthy tonsil. Additionally, the abundance of glial/astrocyte-like cells, as well as rare stem-like cells in glioma, decreased over time. Even though the proportions of some cell subsets increased at later time points (endothelial cells, pericytes, $SOX2^+$ stem-like cells in gliomas, and dendritic cells and $CD27^-IgD^-$ B cells in tonsils), the significant increase in cell death over a long period of dissociation would result in an overall decrease in total yield of those cell types. Comparison of the results from gliomas, melanomas, SCLC xenografts, and tonsil tissue indicates that different tissues may be sensitive to prolonged enzymatic digestion. Dissociation conditions should be evaluated closely and carefully matched to tissue type and study goals. However, based on the results here, no more than 1 hour of dissociation is recommended unless the protocol is being optimized for a specific purpose. In future single-cell-level studies of other complex solid tissues, it will be critical to identify conditions that efficiently generate single-cell suspensions while preserving rare subpopulations of interest. Additionally, cell viability stains such as Cisplatin can be included in future mass cytometry experiments that aim to test cell functions like signaling, proliferation, viability, or cytokine production (*230*).

REFERENCES

1. D. S. Chen, I. Mellman, Oncology meets immunology: the cancer-immunity cycle. *Immunity* **39**, 1-10 (2013).

2. T. L. Darrow, C. L. Slingluff, Jr., H. F. Seigler, The role of HLA class I antigens in recognition of melanoma cells by tumor-specific cytotoxic T lymphocytes. Evidence for shared tumor antigens. *J Immunol* **142**, 3329-3335 (1989).

3. S. L. Topalian *et al.*, Human CD4+ T cells specifically recognize a shared melanoma-associated antigen encoded by the tyrosinase gene. *Proc Natl Acad Sci U S A* **91**, 9461-9465 (1994).

4. P. P. Lee *et al.*, Characterization of circulating T cells specific for tumor-associated antigens in melanoma patients. *Nat Med* **5**, 677-685 (1999).

5. D. T. Alexandrescu *et al.*, Immunotherapy for melanoma: current status and perspectives. *J Immunother* **33**, 570-590 (2010).

6. D. R. Leach, M. F. Krummel, J. P. Allison, Enhancement of antitumor immunity by CTLA-4 blockade. *Science* **271**, 1734-1736 (1996).

7. F. S. Hodi *et al.*, Improved Survival with Ipilimumab in Patients with Metastatic Melanoma. *The New England journal of medicine* **363**, 711-723 (2010).

8. S. L. Topalian *et al.*, Safety, activity, and immune correlates of anti–PD-1 antibody in cancer. *N Engl j Med* **2012**, 2443-2454 (2012).

9. S. C. Bendall *et al.*, Single-cell mass cytometry of differential immune and drug responses across a human hematopoietic continuum. *Science* **332**, 687-696 (2011).

10. S. C. Bendall, G. P. Nolan, M. Roederer, P. K. Chattopadhyay, A deep profiler's guide to cytometry. *Trends in immunology* **33**, 323-332 (2012).

11. A. Bhandoola, A. Sambandam, From stem cell to T cell: one route or many? *Nature Reviews Immunology* **6**, 117-126 (2006).

12. F. Radtke *et al.*, Deficient T cell fate specification in mice with an induced inactivation of Notch1. *Immunity* **10**, 547-558 (1999).

13. Y. Takahama, Journey through the thymus: stromal guides for T-cell development and selection. *Nature Reviews Immunology* **6**, 127-135 (2006).

14. D. I. Godfrey, J. Kennedy, T. Suda, A. Zlotnik, A developmental pathway involving four phenotypically and functionally distinct subsets of CD3-CD4-CD8-triple-negative adult mouse

thymocytes defined by CD44 and CD25 expression. *The Journal of Immunology* **150**, 4244-4252 (1993).

15. R. N. Germain, T-cell development and the CD4–CD8 lineage decision. *Nature Reviews Immunology* **2**, 309-322 (2002).

16. P. Mombaerts *et al.*, RAG-1-deficient mice have no mature B and T lymphocytes. *Cell* **68**, 869-877 (1992).

17. N. Van Oers, H. Von Boehmer, A. Weiss, The pre-T cell receptor (TCR) complex is functionally coupled to the TCR-zeta subunit. *Journal of Experimental Medicine* **182**, 1585-1590 (1995).

18. E. Robey, B. Fowlkes, Selective events in T cell development. *Annual review of immunology* **12**, 675-705 (1994).

19. H. Takaba, H. Takayanagi, The mechanisms of T cell selection in the thymus. *Trends in immunology*, (2017).

20. T. K. Starr, S. C. Jameson, K. A. Hogquist, Positive and negative selection of T cells. *Annual review of immunology* **21**, 139-176 (2003).

21. M. A. Santana, F. Esquivel-Guadarrama, Cell biology of T cell activation and differentiation. *International review of cytology* **250**, 217-274 (2006).

22. G. J. Randolph, in *Seminars in immunology*. (Elsevier, 2001), vol. 13, pp. 267-274.

23. A. Lanzavecchia, F. Sallusto, Regulation of T cell immunity by dendritic cells. *Cell* **106**, 263-266 (2001).

24. B. Moser, M. Wolf, A. Walz, P. Loetscher, Chemokines: multiple levels of leukocyte migration control☆. *Trends in immunology* **25**, 75-84 (2004).

25. J. G. Cyster, Chemokines and the homing of dendritic cells to the T cell areas of lymphoid organs. *Journal of Experimental Medicine* **189**, 447-450 (1999).

26. F. Sallusto, A. Lanzavecchia, Understanding dendritic cell and T-lymphocyte traffic through the analysis of chemokine receptor expression. *Immunological reviews* **177**, 134-140 (2000).

27. V. N. Ngo, H. L. Tang, J. G. Cyster, Epstein-Barr virus–induced molecule 1 ligand chemokine is expressed by dendritic cells in lymphoid tissues and strongly attracts naive T cells and activated B cells. *Journal of Experimental Medicine* **188**, 181-191 (1998).

28. R. F. Bargatze, E. C. Butcher, Rapid G protein-regulated activation event involved in lymphocyte binding to high endothelial venules. *J Exp Med* **178**, 367-372 (1993).

29. P. A. Giblin, S. T. Hwang, T. R. Katsumoto, S. D. Rosen, Ligation of L-selectin on T lymphocytes activates beta1 integrins and promotes adhesion to fibronectin. *J Immunol* **159**, 3498-3507 (1997).

30. C. Berlin-Rufenach *et al.*, Lymphocyte migration in lymphocyte function-associated antigen (LFA)-1-deficient mice. *J Exp Med* **189**, 1467-1478 (1999).

31. C. R. Monks, B. A. Freiberg, H. Kupfer, N. Sciaky, A. Kupfer, Three-dimensional segregation of supramolecular activation clusters in T cells. *Nature* **395**, 82-86 (1998).

32. B. A. Freiberg *et al.*, Staging and resetting T cell activation in SMACs. *Nat Immunol* **3**, 911-917 (2002).

33. N. D. Pennock *et al.*, T cell responses: naive to memory and everything in between. *Adv Physiol Educ* **37**, 273-283 (2013).

34. F. A. Harding, J. G. McArthur, J. A. Gross, D. H. Raulet, J. P. Allison, CD28-mediated signalling co-stimulates murine T cells and prevents induction of anergy in T-cell clones. *Nature* **356**, 607-609 (1992).

35. F. Pages *et al.*, Two distinct intracytoplasmic regions of the T-cell adhesion molecule CD28 participate in phosphatidylinositol 3-kinase association. *J Biol Chem* **271**, 9403-9409 (1996).

36. M. F. Krummel, J. P. Allison, CD28 and CTLA-4 have opposing effects on the response of T cells to stimulation. *Journal of Experimental Medicine* **182**, 459-465 (1995).

37. J. M. Curtsinger, D. C. Lins, M. F. Mescher, Signal 3 determines tolerance versus full activation of naive CD8 T cells: dissociating proliferation and development of effector function. *J Exp Med* **197**, 1141-1151 (2003).

38. M. Kubin, M. Kamoun, G. Trinchieri, Interleukin 12 synergizes with B7/CD28 interaction in inducing efficient proliferation and cytokine production of human T cells. *J Exp Med* **180**, 211-222 (1994).

39. A. D. Wells, H. Gudmundsdottir, L. A. Turka, Following the fate of individual T cells throughout activation and clonal expansion. Signals from T cell receptor and CD28 differentially regulate the induction and duration of a proliferative response. *J Clin Invest* **100**, 3173-3183 (1997).

40. G. Suzuki *et al.*, Antigen-induced suppression of the proliferative response of T cell clones. *J Immunol* **140**, 1359-1365 (1988).

41. M. K. Jenkins, C. A. Chen, G. Jung, D. L. Mueller, R. H. Schwartz, Inhibition of antigen-specific proliferation of type 1 murine T cell clones after stimulation with immobilized anti-CD3 monoclonal antibody. *J Immunol* **144**, 16-22 (1990).

42. S. Gallucci, P. Matzinger, Danger signals: SOS to the immune system. *Current opinion in immunology* **13**, 114-119 (2001).

43. J. Lieberman, The ABCs of granule-mediated cytotoxicity: new weapons in the arsenal. *Nature reviews. Immunology* **3**, 361 (2003).

44. S. S. Metkar *et al.*, Cytotoxic cell granule-mediated apoptosis: perforin delivers granzyme B-serglycin complexes into target cells without plasma membrane pore formation. *Immunity* **16**, 417-428 (2002).

45. A. J. Darmon, D. W. Nicholson, R. C. Bleackley, Activation of the apoptotic protease CPP32 by cytotoxic T-cell-derived granzyme B. *Nature* **377**, 446-448 (1995).

46. E. Rouvier, M. F. Luciani, P. Golstein, Fas involvement in Ca(2+)-independent T cell-mediated cytotoxicity. *J Exp Med* **177**, 195-200 (1993).

47. P. E. Fields, S. T. Kim, R. A. Flavell, Cutting edge: changes in histone acetylation at the IL-4 and IFN-gamma loci accompany Th1/Th2 differentiation. *J Immunol* **169**, 647-650 (2002).

48. A. C. Mullen *et al.*, Role of T-bet in commitment of TH1 cells before IL-12-dependent selection. *Science* **292**, 1907-1910 (2001).

49. A. W. Taylor-Robinson, R. S. Phillips, Functional characterization of protective CD4+ T-cell clones reactive to the murine malaria parasite Plasmodium chabaudi. *Immunology* **77**, 99-105 (1992).

50. C. G. Vinuesa, M. A. Linterman, D. Yu, I. C. MacLennan, Follicular Helper T Cells. *Annu Rev Immunol* **34**, 335-368 (2016).

51. V. Dardalhon *et al.*, IL-4 inhibits TGF-beta-induced Foxp3+ T cells and, together with TGF-beta, generates IL-9+ IL-10+ Foxp3(-) effector T cells. *Nat Immunol* **9**, 1347-1355 (2008).

52. P. R. Mangan *et al.*, Transforming growth factor-beta induces development of the T(H)17 lineage. *Nature* **441**, 231-234 (2006).

53. S. Eyerich *et al.*, Th22 cells represent a distinct human T cell subset involved in epidermal immunity and remodeling. *The Journal of clinical investigation* **119**, 3573 (2009).

54. W. Chen *et al.*, Conversion of peripheral CD4+CD25- naive T cells to CD4+CD25+ regulatory T cells by TGF-beta induction of transcription factor Foxp3. *J Exp Med* **198**, 1875-1886 (2003).

55. S. C. Meuer *et al.*, Clonotypic structures involved in antigen-specific human T cell function. Relationship to the T3 molecular complex. *J Exp Med* **157**, 705-719 (1983).

56. J. Borst *et al.*, The delta- and epsilon-chains of the human T3/T-cell receptor complex are distinct polypeptides. *Nature* **312**, 455-458 (1984).

57. L. E. Samelson, M. D. Patel, A. M. Weissman, J. B. Harford, R. D. Klausner, Antigen activation of murine T cells induces tyrosine phosphorylation of a polypeptide associated with the T cell antigen receptor. *Cell* **46**, 1083-1090 (1986).

58. E. K. Barber, J. D. Dasgupta, S. F. Schlossman, J. M. Trevillyan, C. E. Rudd, The CD4 and CD8 antigens are coupled to a protein-tyrosine kinase (p56lck) that phosphorylates the CD3 complex. *Proc Natl Acad Sci U S A* **86**, 3277-3281 (1989).

59. A. C. Chan, M. Iwashima, C. W. Turck, A. Weiss, ZAP-70: a 70 kd protein-tyrosine kinase that associates with the TCR zeta chain. *Cell* **71**, 649-662 (1992).

60. J. Bubeck Wardenburg *et al.*, Phosphorylation of SLP-76 by the ZAP-70 protein-tyrosine kinase is required for T-cell receptor function. *J Biol Chem* **271**, 19641-19644 (1996).

61. W. Zhang, J. Sloan-Lancaster, J. Kitchen, R. P. Trible, L. E. Samelson, LAT: the ZAP-70 tyrosine kinase substrate that links T cell receptor to cellular activation. *Cell* **92**, 83-92 (1998).

62. Q. Liu *et al.*, Structural basis for specific binding of the Gads SH3 domain to an RxxK motif-containing SLP-76 peptide: a novel mode of peptide recognition. *Mol Cell* **11**, 471-481 (2003).

63. D. Yablonski, T. Kadlecek, A. Weiss, Identification of a phospholipase C-gamma1 (PLC-gamma1) SH3 domain-binding site in SLP-76 required for T-cell receptor-mediated activation of PLC-gamma1 and NFAT. *Mol Cell Biol* **21**, 4208-4218 (2001).

64. D. Beach, R. Gonen, Y. Bogin, I. G. Reischl, D. Yablonski, Dual role of SLP-76 in mediating T cell receptor-induced activation of phospholipase C-gamma1. *J Biol Chem* **282**, 2937-2946 (2007).

65. J. P. Roose, M. Mollenauer, V. A. Gupta, J. Stone, A. Weiss, A diacylglycerol-protein kinase C-RasGRP1 pathway directs Ras activation upon antigen receptor stimulation of T cells. *Mol Cell Biol* **25**, 4426-4441 (2005).

66. J. Schulze-Luehrmann, S. Ghosh, Antigen-receptor signaling to nuclear factor kappa B. *Immunity* **25**, 701-715 (2006).

67. R. Medzhitov, P. Preston-Hurlburt, C. A. Janeway, A human homologue of the Drosophila Toll protein signals activation of adaptive immunity. *Nature* **388**, 394-397 (1997).

68. H. W. Virgin, E. J. Wherry, R. Ahmed, Redefining chronic viral infection. *Cell* **138**, 30-50 (2009).

69. S. M. Kaech, E. J. Wherry, Heterogeneity and cell-fate decisions in effector and memory CD8+ T cell differentiation during viral infection. *Immunity* **27**, 393-405 (2007).

70. A. Alcami, U. H. Koszinowski, Viral mechanisms of immune evasion. *Immunol Today* **21**, 447-455 (2000).

71. L. G. Guidotti, F. V. Chisari, Immunobiology and pathogenesis of viral hepatitis. *Annu Rev Pathol* **1**, 23-61 (2006).

72. E. J. Wherry, J. N. Blattman, K. Murali-Krishna, R. van der Most, R. Ahmed, Viral persistence alters CD8 T-cell immunodominance and tissue distribution and results in distinct stages of functional impairment. *J Virol* **77**, 4911-4927 (2003).

73. A. J. Zajac *et al.*, Viral immune evasion due to persistence of activated T cells without effector function. *J Exp Med* **188**, 2205-2213 (1998).

74. C. M. Bucks, J. A. Norton, A. C. Boesteanu, Y. M. Mueller, P. D. Katsikis, Chronic antigen stimulation alone is sufficient to drive CD8+ T cell exhaustion. *J Immunol* **182**, 6697-6708 (2009).

75. M. E. Keir, M. J. Butte, G. J. Freeman, A. H. Sharpe, PD-1 and its ligands in tolerance and immunity. *Annu Rev Immunol* **26**, 677-704 (2008).

76. H. Nishimura, M. Nose, H. Hiai, N. Minato, T. Honjo, Development of lupus-like autoimmune diseases by disruption of the PD-1 gene encoding an ITIM motif-carrying immunoreceptor. *Immunity* **11**, 141-151 (1999).

77. H. Nishimura *et al.*, Autoimmune dilated cardiomyopathy in PD-1 receptor-deficient mice. *Science* **291**, 319-322 (2001).

78. D. L. Barber *et al.*, Restoring function in exhausted CD8 T cells during chronic viral infection. *Nature* **439**, 682-687 (2006).

79. Y. Agata *et al.*, Expression of the PD-1 antigen on the surface of stimulated mouse T and B lymphocytes. *Int Immunol* **8**, 765-772 (1996).

80. G. J. Freeman *et al.*, Engagement of the PD-1 immunoinhibitory receptor by a novel B7 family member leads to negative regulation of lymphocyte activation. *J Exp Med* **192**, 1027-1034 (2000).

81. Y. Latchman *et al.*, PD-L2 is a second ligand for PD-1 and inhibits T cell activation. *Nat Immunol* **2**, 261-268 (2001).

82. T. Okazaki, A. Maeda, H. Nishimura, T. Kurosaki, T. Honjo, PD-1 immunoreceptor inhibits B cell receptor-mediated signaling by recruiting src homology 2-domain-containing tyrosine phosphatase 2 to phosphotyrosine. *Proc Natl Acad Sci U S A* **98**, 13866-13871 (2001).

83. J. M. Chemnitz, R. V. Parry, K. E. Nichols, C. H. June, J. L. Riley, SHP-1 and SHP-2 associate with immunoreceptor tyrosine-based switch motif of programmed death 1 upon primary human T cell stimulation, but only receptor ligation prevents T cell activation. *J Immunol* **173**, 945-954 (2004).

84. K. A. Sheppard *et al.*, PD-1 inhibits T-cell receptor induced phosphorylation of the ZAP70/CD3zeta signalosome and downstream signaling to PKCtheta. *FEBS Lett* **574**, 37-41 (2004).

85. R. V. Parry *et al.*, CTLA-4 and PD-1 receptors inhibit T-cell activation by distinct mechanisms. *Mol Cell Biol* **25**, 9543-9553 (2005).

86. N. Patsoukis *et al.*, Selective effects of PD-1 on Akt and Ras pathways regulate molecular components of the cell cycle and inhibit T cell proliferation. *Sci Signal* **5**, ra46 (2012).

87. L. Chen, D. B. Flies, Molecular mechanisms of T cell co-stimulation and co-inhibition. *Nat Rev Immunol* **13**, 227-242 (2013).

88. S. D. Blackburn *et al.*, Coregulation of CD8+ T cell exhaustion by multiple inhibitory receptors during chronic viral infection. *Nat Immunol* **10**, 29-37 (2009).

89. N. Nakamoto *et al.*, Synergistic reversal of intrahepatic HCV-specific CD8 T cell exhaustion by combined PD-1/CTLA-4 blockade. *PLoS Pathog* **5**, e1000313 (2009).

90. H. T. Jin *et al.*, Cooperation of Tim-3 and PD-1 in CD8 T-cell exhaustion during chronic viral infection. *Proc Natl Acad Sci U S A* **107**, 14733-14738 (2010).

91. A. Nakao *et al.*, Identification of Smad7, a TGFbeta-inducible antagonist of TGF-beta signalling. *Nature* **389**, 631-635 (1997).

92. J. Massague, TGFbeta signalling in context. *Nat Rev Mol Cell Biol* **13**, 616-630 (2012).

93. R. Tinoco, V. Alcalde, Y. Yang, K. Sauer, E. I. Zuniga, Cell-intrinsic transforming growth factor-beta signaling mediates virus-specific CD8+ T cell deletion and viral persistence in vivo. *Immunity* **31**, 145-157 (2009).

94. N. Alatrakchi *et al.*, Hepatitis C virus (HCV)-specific CD8+ cells produce transforming growth factor beta that can suppress HCV-specific T-cell responses. *J Virol* **81**, 5882-5892 (2007).

95. M. L. Garba, C. D. Pilcher, A. L. Bingham, J. Eron, J. A. Frelinger, HIV antigens can induce TGF-beta(1)-producing immunoregulatory CD8+ T cells. *J Immunol* **168**, 2247-2254 (2002).

96. D. G. Brooks *et al.*, Interleukin-10 determines viral clearance or persistence in vivo. *Nat Med* **12**, 1301-1309 (2006).

97. R. de Waal Malefyt *et al.*, Interleukin 10 (IL-10) and viral IL-10 strongly reduce antigen-specific human T cell proliferation by diminishing the antigen-presenting capacity of monocytes via downregulation of class II major histocompatibility complex expression. *J Exp Med* **174**, 915-924 (1991).

98. M. Ejrnaes *et al.*, Resolution of a chronic viral infection after interleukin-10 receptor blockade. *J Exp Med* **203**, 2461-2472 (2006).

99. M. A. Curotto de Lafaille, J. J. Lafaille, Natural and adaptive foxp3+ regulatory T cells: more of the same or a division of labor? *Immunity* **30**, 626-635 (2009).

100. T. Veiga-Parga, S. Sehrawat, B. T. Rouse, Role of regulatory T cells during virus infection. *Immunol Rev* **255**, 182-196 (2013).

101. E. M. Shevach, Mechanisms of foxp3+ T regulatory cell-mediated suppression. *Immunity* **30**, 636-645 (2009).

102. A. Kinter *et al.*, Suppression of HIV-specific T cell activity by lymph node CD25+ regulatory T cells from HIV-infected individuals. *Proc Natl Acad Sci U S A* **104**, 3390-3395 (2007).

103. T. Boettler *et al.*, T cells with a CD4+CD25+ regulatory phenotype suppress in vitro proliferation of virus-specific CD8+ T cells during chronic hepatitis C virus infection. *J Virol* **79**, 7860-7867 (2005).

104. S. M. Rushbrook *et al.*, Regulatory T cells suppress in vitro proliferation of virus-specific CD8+ T cells during persistent hepatitis C virus infection. *J Virol* **79**, 7852-7859 (2005).

105. M. R. Young, M. Newby, H. T. Wepsic, Hematopoiesis and suppressor bone marrow cells in mice bearing large metastatic Lewis lung carcinoma tumors. *Cancer Res* **47**, 100-105 (1987).

106. C. Goh, S. Narayanan, Y. S. Hahn, Myeloid-derived suppressor cells: the dark knight or the joker in viral infections? *Immunol Rev* **255**, 210-221 (2013).

107. R. S. Tacke *et al.*, Myeloid suppressor cells induced by hepatitis C virus suppress T-cell responses through the production of reactive oxygen species. *Hepatology* **55**, 343-353 (2012).

108. S. Kusmartsev, D. I. Gabrilovich, STAT1 signaling regulates tumor-associated macrophage-mediated T cell deletion. *J Immunol* **174**, 4880-4891 (2005).

109. E. J. Wherry, T cell exhaustion. *Nat Immunol* **12**, 492-499 (2011).

110. J. N. Blattman, E. J. Wherry, S. J. Ha, R. G. van der Most, R. Ahmed, Impact of epitope escape on PD-1 expression and CD8 T-cell exhaustion during chronic infection. *J Virol* **83**, 4386-4394 (2009).

111. D. Moskophidis, F. Lechner, H. Pircher, R. M. Zinkernagel, Virus persistence in acutely infected immunocompetent mice by exhaustion of antiviral cytotoxic effector T cells. *Nature* **362**, 758-761 (1993).

112. M. J. Fuller, A. J. Zajac, Ablation of CD8 and CD4 T cell responses by high viral loads. *J Immunol* **170**, 477-486 (2003).

113. D. G. Brooks, L. Teyton, M. B. Oldstone, D. B. McGavern, Intrinsic functional dysregulation of CD4 T cells occurs rapidly following persistent viral infection. *J Virol* **79**, 10514-10527 (2005).

114. A. Oxenius, R. M. Zinkernagel, H. Hengartner, Comparison of activation versus induction of unresponsiveness of virus-specific CD4+ and CD8+ T cells upon acute versus persistent viral infection. *Immunity* **9**, 449-457 (1998).

115. E. J. Wherry *et al.*, Molecular signature of CD8+ T cell exhaustion during chronic viral infection. *Immunity* **27**, 670-684 (2007).

116. S. D. Blackburn, H. Shin, G. J. Freeman, E. J. Wherry, Selective expansion of a subset of exhausted CD8 T cells by alphaPD-L1 blockade. *Proc Natl Acad Sci U S A* **105**, 15016-15021 (2008).

117. D. Hanahan, R. A. Weinberg, Hallmarks of cancer: the next generation. *Cell* **144**, 646-674 (2011).

118. M. Maio, Melanoma as a model tumour for immuno-oncology. *Ann Oncol* **23 Suppl 8**, viii10-14 (2012).

119. R. D. Schreiber, L. J. Old, M. J. Smyth, Cancer immunoediting: integrating immunity's roles in cancer suppression and promotion. *Science* **331**, 1565-1570 (2011).

120. L. J. Old, E. A. Boyse, IMMUNOLOGY OF EXPERIMENTAL TUMORS. *Annu Rev Med* **15**, 167-186 (1964).

121. O. Stutman, Tumor development after 3-methylcholanthrene in immunologically deficient athymic-nude mice. *Science* **183**, 534-536 (1974).

122. D. H. Kaplan *et al.*, Demonstration of an interferon gamma-dependent tumor surveillance system in immunocompetent mice. *Proc Natl Acad Sci U S A* **95**, 7556-7561 (1998).

123. V. Shankaran *et al.*, IFNgamma and lymphocytes prevent primary tumour development and shape tumour immunogenicity. *Nature* **410**, 1107-1111 (2001).

124. G. P. Dunn, L. J. Old, R. D. Schreiber, The three Es of cancer immunoediting. *Annu Rev Immunol* **22**, 329-360 (2004).

125. T. Boon, P. van der Bruggen, Human tumor antigens recognized by T lymphocytes. *J Exp Med* **183**, 725-729 (1996).

126. H. T. Khong, Q. J. Wang, S. A. Rosenberg, Identification of multiple antigens recognized by tumor-infiltrating lymphocytes from a single patient: tumor escape by antigen loss and loss of MHC expression. *J Immunother* **27**, 184-190 (2004).

127. P. Matzinger, Tolerance, danger, and the extended family. *Annu Rev Immunol* **12**, 991-1045 (1994).

128. G. P. Sims, D. C. Rowe, S. T. Rietdijk, R. Herbst, A. J. Coyle, HMGB1 and RAGE in inflammation and cancer. *Annu Rev Immunol* **28**, 367-388 (2010).

129. T. A. Ferguson, J. Choi, D. R. Green, Armed response: how dying cells influence T-cell functions. *Immunol Rev* **241**, 77-88 (2011).

130. E. S. Trombetta, I. Mellman, Cell biology of antigen processing in vitro and in vivo. *Annu Rev Immunol* **23**, 975-1028 (2005).

131. K. Franciszkiewicz, A. Boissonnas, M. Boutet, C. Combadiere, F. Mami-Chouaib, Role of chemokines and chemokine receptors in shaping the effector phase of the antitumor immune response. *Cancer Res* **72**, 6325-6332 (2012).

132. L. V. Kalialis, K. T. Drzewiecki, H. Klyver, Spontaneous regression of metastases from melanoma: review of the literature. *Melanoma Res* **19**, 275-282 (2009).

133. L. V. Kalialis, K. T. Drzewiecki, M. Mohammadi, A. B. Mehlsen, H. Klyver, Spontaneous regression of metastases from malignant melanoma: a case report. *Melanoma Res* **18**, 279-283 (2008).

134. R. M. MacKie, R. Reid, B. Junor, Fatal melanoma transferred in a donated kidney 16 years after melanoma surgery. *N Engl j Med* **348**, 567-568 (2003).

135. C. M. Koebel *et al.*, Adaptive immunity maintains occult cancer in an equilibrium state. *Nature* **450**, 903-907 (2007).

136. M. D. Vesely, M. H. Kershaw, R. D. Schreiber, M. J. Smyth, Natural innate and adaptive immunity to cancer. *Annu Rev Immunol* **29**, 235-271 (2011).

137. S. Song *et al.*, Tumour-derived IL-10 within tumour microenvironment represses the antitumour immunity of Socs1-silenced and sustained antigen expressing DCs. *Eur J Cancer* **48**, 2252-2259 (2012).

138. S. Spranger, R. Bao, T. F. Gajewski, Melanoma-intrinsic beta-catenin signalling prevents anti-tumour immunity. *Nature* **523**, 231-235 (2015).

139. T. J. Curiel *et al.*, Blockade of B7-H1 improves myeloid dendritic cell-mediated antitumor immunity. *Nat Med* **9**, 562-567 (2003).

140. E. M. Sotomayor, I. Borrello, E. Tubb, J. P. Allison, H. I. Levitsky, In vivo blockade of CTLA-4 enhances the priming of responsive T cells but fails to prevent the induction of tumor antigen-specific tolerance. *Proc Natl Acad Sci U S A* **96**, 11476-11481 (1999).

141. G. T. Motz, G. Coukos, Deciphering and Reversing Tumor Immune Suppression. *Immunity* **39**, 61-73 (2013).

142. J. K. Min *et al.*, Hepatocyte growth factor suppresses vascular endothelial growth factor-induced expression of endothelial ICAM-1 and VCAM-1 by inhibiting the nuclear factor-kappaB pathway. *Circ Res* **96**, 300-307 (2005).

143. N. Rodig *et al.*, Endothelial expression of PD-L1 and PD-L2 down-regulates CD8+ T cell activation and cytolysis. *Eur J Immunol* **33**, 3117-3126 (2003).

144. F. M. Marincola, E. M. Jaffee, D. J. Hicklin, S. Ferrone, Escape of human solid tumors from T-cell recognition: molecular mechanisms and functional significance. *Adv Immunol* **74**, 181-273 (2000).

145. R. L. Ferris, J. L. Hunt, S. Ferrone, Human leukocyte antigen (HLA) class I defects in head and neck cancer: molecular mechanisms and clinical significance. *Immunol Res* **33**, 113-133 (2005).

146. T. L. Whiteside, Immune suppression in cancer: effects on immune cells, mechanisms and future therapeutic intervention. *Semin Cancer Biol* **16**, 3-15 (2006).

147. J. W. Kim, T. Tsukishiro, J. T. Johnson, T. L. Whiteside, Expression of pro- and antiapoptotic proteins in circulating CD8+ T cells of patients with squamous cell carcinoma of the head and neck. *Clin Cancer Res* **10**, 5101-5110 (2004).

148. H. Dong *et al.*, Tumor-associated B7-H1 promotes T-cell apoptosis: a potential mechanism of immune evasion. *Nat Med* **8**, 793-800 (2002).

149. M. Ahmadzadeh *et al.*, Tumor antigen-specific CD8 T cells infiltrating the tumor express high levels of PD-1 and are functionally impaired. *Blood* **114**, 1537-1544 (2009).

150. K. S. Sfanos *et al.*, Human prostate-infiltrating CD8+ T lymphocytes are oligoclonal and PD-1+. *Prostate* **69**, 1694-1703 (2009).

151. D. M. Pardoll, The blockade of immune checkpoints in cancer immunotherapy. *Nat Rev Cancer* **12**, 252-264 (2012).

152. J. Fourcade *et al.*, Upregulation of Tim-3 and PD-1 expression is associated with tumor antigen-specific CD8+ T cell dysfunction in melanoma patients. *J Exp Med* **207**, 2175-2186 (2010).

153. J. F. Grosso *et al.*, Functionally distinct LAG-3 and PD-1 subsets on activated and chronically stimulated CD8 T cells. *J Immunol* **182**, 6659-6669 (2009).

154. K. Steinbrink *et al.*, Interleukin-10-treated human dendritic cells induce a melanoma-antigen-specific anergy in CD8(+) T cells resulting in a failure to lyse tumor cells. *Blood* **93**, 1634-1642 (1999).

155. R. J. Akhurst, R. Derynck, TGF-beta signaling in cancer--a double-edged sword. *Trends Cell Biol* **11**, S44-51 (2001).

156. A. Facciabene, G. T. Motz, G. Coukos, T-regulatory cells: key players in tumor immune escape and angiogenesis. *Cancer Res* **72**, 2162-2171 (2012).

157. NIH National Cancer Institute, Cancer Stat Facts: Melanoma of the Skin. (2017).

158. A. S. Yang, P. B. Chapman, The history and future of chemotherapy for melanoma. *Hematol Oncol Clin North Am* **23**, 583-597, x (2009).

159. M. B. Atkins *et al.*, High-dose recombinant interleukin 2 therapy for patients with metastatic melanoma: analysis of 270 patients treated between 1985 and 1993. *J Clin Oncol* **17**, 2105-2116 (1999).

160. I. Astsaturov *et al.*, Amplification of virus-induced antimelanoma T-cell reactivity by high-dose interferon-alpha2b: implications for cancer vaccines. *Clin Cancer Res* **9**, 4347-4355 (2003).

161. E. Maellaro *et al.*, Different effects of interferon-alpha on melanoma cell lines: a study on telomerase reverse transcriptase, telomerase activity and apoptosis. *Br J Dermatol* **148**, 1115-1124 (2003).

162. C. M. Fleischmann, G. J. Stanton, W. R. Fleischmann, Jr., Enhanced in vivo sensitivity of in vitro interferon-treated B16 melanoma cells to CD8 cells and activated macrophages. *J Interferon Cytokine Res* **16**, 805-812 (1996).

163. S. A. Rosenberg *et al.*, Immunologic and therapeutic evaluation of a synthetic peptide vaccine for the treatment of patients with metastatic melanoma. *Nat Med* **4**, 321-327 (1998).

164. B. Thurner *et al.*, Vaccination with mage-3A1 peptide-pulsed mature, monocyte-derived dendritic cells expands specific cytotoxic T cells and induces regression of some metastases in advanced stage IV melanoma. *J Exp Med* **190**, 1669-1678 (1999).

165. S. A. Rosenberg *et al.*, Tumor progression can occur despite the induction of very high levels of self/tumor antigen-specific CD8+ T cells in patients with melanoma. *J Immunol* **175**, 6169-6176 (2005).

166. M. E. Dudley *et al.*, Adoptive cell transfer therapy following non-myeloablative but lymphodepleting chemotherapy for the treatment of patients with refractory metastatic melanoma. *J Clin Oncol* **23**, 2346-2357 (2005).

167. R. A. Morgan *et al.*, Cancer regression in patients after transfer of genetically engineered lymphocytes. *Science* **314**, 126-129 (2006).

168. A. van Elsas, A. A. Hurwitz, J. P. Allison, Combination immunotherapy of B16 melanoma using anti-cytotoxic T lymphocyte-associated antigen 4 (CTLA-4) and granulocyte/macrophage colony-stimulating factor (GM-CSF)-producing vaccines induces rejection of subcutaneous and metastatic tumors accompanied by autoimmune depigmentation. *J Exp Med* **190**, 355-366 (1999).

169. Y. Ishida, Y. Agata, K. Shibahara, T. Honjo, Induced expression of PD-1, a novel member of the immunoglobulin gene superfamily, upon programmed cell death. *Embo j* **11**, 3887-3895 (1992).

170. C. Blank *et al.*, PD-L1/B7H-1 inhibits the effector phase of tumor rejection by T cell receptor (TCR) transgenic CD8+ T cells. *Cancer Res* **64**, 1140-1145 (2004).

171. J. R. Brahmer *et al.*, Phase I study of single-agent anti-programmed death-1 (MDX-1106) in refractory solid tumors: safety, clinical activity, pharmacodynamics, and immunologic correlates. *J Clin Oncol* **28**, 3167-3175 (2010).

172. W. H. Fridman, F. Pages, C. Sautes-Fridman, J. Galon, The immune contexture in human tumours: impact on clinical outcome. *Nat Rev Cancer* **12**, 298-306 (2012).

173. N. A. Giraldo *et al.*, The immune contexture of primary and metastatic human tumours. *Curr Opin Immunol* **27**, 8-15 (2014).

174. G. K. Behbehani, S. C. Bendall, M. R. Clutter, W. J. Fantl, G. P. Nolan, Single-cell mass cytometry adapted to measurements of the cell cycle. *Cytometry A* **81**, 552-566 (2012).

175. J. M. Irish, D. B. Doxie, High-dimensional single-cell cancer biology. *Curr Top Microbiol Immunol* **377**, 1-21 (2014).

176. S. P. Patel, R. Kurzrock, PD-L1 Expression as a Predictive Biomarker in Cancer Immunotherapy. *Mol Cancer Ther* **14**, 847-856 (2015).

177. C. L. Sawyers, The cancer biomarker problem. *Nature* **452**, 548-552 (2008).

178. T. F. Gajewski, H. Schreiber, Y. X. Fu, Innate and adaptive immune cells in the tumor microenvironment. *Nat Immunol* **14**, 1014-1022 (2013).

179. U. K. Scarlett *et al.*, Ovarian cancer progression is controlled by phenotypic changes in dendritic cells. *J Exp Med* **209**, 495-506 (2012).

180. M. J. Smyth, N. Y. Crowe, D. I. Godfrey, NK cells and NKT cells collaborate in host protection from methylcholanthrene-induced fibrosarcoma. *Int Immunol* **13**, 459-463 (2001).

181. Z. Qin, T. Blankenstein, CD4+ T cell--mediated tumor rejection involves inhibition of angiogenesis that is dependent on IFN gamma receptor expression by nonhematopoietic cells. *Immunity* **12**, 677-686 (2000).

182. F. Nimmerjahn, J. V. Ravetch, Divergent immunoglobulin g subclass activity through selective Fc receptor binding. *Science* **310**, 1510-1512 (2005).

183. B. Shang, Y. Liu, S. J. Jiang, Y. Liu, Prognostic value of tumor-infiltrating FoxP3+ regulatory T cells in cancers: a systematic review and meta-analysis. *Sci Rep* **5**, 15179 (2015).

184. C. Meyer *et al.*, Chronic inflammation promotes myeloid-derived suppressor cell activation blocking antitumor immunity in transgenic mouse melanoma model. *Proc Natl Acad Sci U S A* **108**, 17111-17116 (2011).

185. F. Balkwill, A. Montfort, M. Capasso, B regulatory cells in cancer. *Trends Immunol* **34**, 169-173 (2013).

186. E. W. Newell, N. Sigal, S. C. Bendall, G. P. Nolan, M. M. Davis, Cytometry by time-of-flight shows combinatorial cytokine expression and virus-specific cell niches within a continuum of CD8+ T cell phenotypes. *Immunity* **36**, 142-152 (2012).

187. L. Strauss, C. Bergmann, W. Gooding, J. T. Johnson, T. L. Whiteside, The frequency and suppressor function of CD4+CD25highFoxp3+ T cells in the circulation of patients with squamous cell carcinoma of the head and neck. *Clin Cancer Res* **13**, 6301-6311 (2007).

188. A. M. Wolf *et al.*, Increase of regulatory T cells in the peripheral blood of cancer patients. *Clin Cancer Res* **9**, 606-612 (2003).

189. K. L. Ling *et al.*, Increased frequency of regulatory T cells in peripheral blood and tumour infiltrating lymphocytes in colorectal cancer patients. *Cancer Immun* **7**, 7 (2007).

190. J. Zhou *et al.*, Enhanced frequency and potential mechanism of B regulatory cells in patients with lung cancer. *J Transl Med* **12**, 304 (2014).

191. Y. Yao *et al.*, CyTOF supports efficient detection of immune cell subsets from small samples. *J Immunol Methods* **415**, 1-5 (2014).

192. J. M. Irish, D. K. Czerwinski, G. P. Nolan, R. Levy, Altered B-cell receptor signaling kinetics distinguish human follicular lymphoma B cells from tumor-infiltrating nonmalignant B cells. *Blood* **108**, 3135-3142 (2006).

193. S. Valitutti, S. Muller, M. Salio, A. Lanzavecchia, Degradation of T cell receptor (TCR)-CD3-zeta complexes after antigenic stimulation. *J Exp Med* **185**, 1859-1864 (1997).

194. B. Bodenmiller *et al.*, Multiplexed mass cytometry profiling of cellular states perturbed by small-molecule regulators. *Nat Biotechnol* **30**, 858-867 (2012).

195. N. P. Restifo, M. E. Dudley, S. A. Rosenberg, Adoptive immunotherapy for cancer: harnessing the T cell response. *Nat Rev Immunol* **12**, 269-281 (2012).

196. K. J. Nicholas *et al.*, Multiparameter analysis of stimulated human peripheral blood mononuclear cells: A comparison of mass and fluorescence cytometry. *Cytometry A*, (2015).

197. E. J. Carr *et al.*, The cellular composition of the human immune system is shaped by age and cohabitation. *Nat Immunol*, (2016).

198. S. P. Perfetto, P. K. Chattopadhyay, M. Roederer, Seventeen-colour flow cytometry: unravelling the immune system. *Nat Rev Immunol* **4**, 648-655 (2004).

199. H. T. Maecker, J. P. McCoy, R. Nussenblatt, Standardizing immunophenotyping for the Human Immunology Project. *Nat Rev Immunol* **12**, 191-200 (2012).

200. S. C. Bendall *et al.*, Single-cell trajectory detection uncovers progression and regulatory coordination in human B cell development. *Cell* **157**, 714-725 (2014).

201. O. Ornatsky *et al.*, Highly multiparametric analysis by mass cytometry. *J Immunol Methods* **361**, 1-20 (2010).

202. M. Angelo *et al.*, Multiplexed ion beam imaging of human breast tumors. *Nat Med* **20**, 436-442 (2014).

203. M. J. Gerdes *et al.*, Highly multiplexed single-cell analysis of formalin-fixed, paraffin-embedded cancer tissue. *Proc Natl Acad Sci U S A* **110**, 11982-11987 (2013).

204. A. J. Simmons *et al.*, Cytometry-based single-cell analysis of intact epithelial signaling reveals MAPK activation divergent from TNF-α-induced apoptosis in vivo. *Mol Syst Biol* **11**, 835 (2015).

205. A. R. Wu *et al.*, Quantitative assessment of single-cell RNA-sequencing methods. *Nat Methods* **11**, 41-46 (2014).

206. O. Stegle, S. A. Teichmann, J. C. Marioni, Computational and analytical challenges in single-cell transcriptomics. *Nat Rev Genet* **16**, 133-145 (2015).

207. K. E. Diggins, P. B. Ferrell, Jr., J. M. Irish, Methods for discovery and characterization of cell subsets in high dimensional mass cytometry data. *Methods* **82**, 55-63 (2015).

208. J. M. Irish, Beyond the age of cellular discovery. *Nat Immunol* **15**, 1095-1097 (2014).

209. E. Mjolsness, D. DeCoste, Machine learning for science: state of the art and future prospects. *Science* **293**, 2051-2055 (2001).

210. P. Qiu *et al.*, Extracting a cellular hierarchy from high-dimensional cytometry data with SPADE. *Nat Biotechnol* **29**, 886-891 (2011).

211. N. C. Institute. (2014).

212. H. Harlin, T. V. Kuna, A. C. Peterson, Y. Meng, T. F. Gajewski, Tumor progression despite massive influx of activated CD8(+) T cells in a patient with malignant melanoma ascites. *Cancer Immunol Immunother* **55**, 1185-1197 (2006).

213. P. A. Prieto *et al.*, CTLA-4 blockade with ipilimumab: long-term follow-up of 177 patients with metastatic melanoma. *Clin Cancer Res* **18**, 2039-2047 (2012).

214. F. S. Hodi *et al.*, Improved survival with ipilimumab in patients with metastatic melanoma. *N Engl j Med* **363**, 711-723 (2010).

215. C. Robert *et al.*, Anti-programmed-death-receptor-1 treatment with pembrolizumab in ipilimumab-refractory advanced melanoma: a randomised dose-comparison cohort of a phase 1 trial. *Lancet* **384**, 1109-1117 (2014).

216. P. K. Chattopadhyay, T. M. Gierahn, M. Roederer, J. C. Love, Single-cell technologies for monitoring immune systems. *Nat Immunol* **15**, 128-135 (2014).

217. S. Di Palma, B. Bodenmiller, Unraveling cell populations in tumors by single-cell mass cytometry. *Curr Opin Biotechnol*, (2014).

218. D. R. Bandura *et al.*, Mass cytometry: technique for real time single cell multitarget immunoassay based on inductively coupled plasma time-of-flight mass spectrometry. *Anal Chem* **81**, 6813-6822 (2009).

219. B. Becher *et al.*, High-dimensional analysis of the murine myeloid cell system. *Nature immunology* **15**, 1181-1189 (2014).

220. A. Horowitz *et al.*, Genetic and environmental determinants of human NK cell diversity revealed by mass cytometry. *Sci Transl Med* **5**, 208ra145 (2013).

221. M. Mingueneau *et al.*, Single-cell mass cytometry of TCR signaling: Amplification of small initial differences results in low ERK activation in NOD mice. *Proc Natl Acad Sci U S A* **111**, 16466-16471 (2014).

222. N. Sen *et al.*, Single-cell mass cytometry analysis of human tonsil T cell remodeling by varicella zoster virus. *Cell Rep* **8**, 633-645 (2014).

223. H. G. Polikowsky, C. E. Wogsland, K. E. Diggins, K. Huse, J. M. Irish, Cutting Edge: Redox Signaling Hypersensitivity Distinguishes Human Germinal Center B Cells. *J Immunol*, (2015).

224. L. Wang *et al.*, Human CD4+ lymphocytes for antigen quantification: characterization using conventional flow cytometry and mass cytometry. *Cytometry A* **81**, 567-575 (2012).

225. B. Gaudilliere *et al.*, Implementing Mass Cytometry at the Bedside to Study the Immunological Basis of Human Diseases: Distinctive Immune Features in Patients with a History of Term or Preterm Birth. *Cytometry A*, (2015).

226. S. Tricot *et al.*, Evaluating the efficiency of isotope transmission for improved panel design and a comparison of the detection sensitivities of mass cytometer instruments. *Cytometry A* **87**, 357-368 (2015).

227. J. M. Irish, D. K. Czerwinski, G. P. Nolan, R. Levy, Kinetics of B cell receptor signaling in human B cell subsets mapped by phosphospecific flow cytometry. *J Immunol* **177**, 1581-1589 (2006).

228. O. I. Ornatsky *et al.*, Study of cell antigens and intracellular DNA by identification of element-containing labels and metallointercalators using inductively coupled plasma mass spectrometry. *Anal Chem* **80**, 2539-2547 (2008).

229. N. Kotecha, P. O. Krutzik, J. M. Irish, Web-based analysis and publication of flow cytometry experiments. *Curr Protoc Cytom* **Chapter 10**, Unit10 17 (2010).

230. H. G. Fienberg, E. F. Simonds, W. J. Fantl, G. P. Nolan, B. Bodenmiller, A platinum-based covalent viability reagent for single-cell mass cytometry. *Cytometry A* **81**, 467-475 (2012).

231. A. D. Amir el *et al.*, viSNE enables visualization of high dimensional single-cell data and reveals phenotypic heterogeneity of leukemia. *Nat Biotechnol* **31**, 545-552 (2013).

232. P. K. Chattopadhyay *et al.*, Quantum dot semiconductor nanocrystals for immunophenotyping by polychromatic flow cytometry. *Nat Med* **12**, 972-977 (2006).

233. J. A. Conrad *et al.*, Antiretroviral therapy reduces the magnitude and T cell receptor repertoire diversity of HIV-specific T cell responses without changing T cell clonotype dominance. *J Virol* **86**, 4213-4221 (2012).

234. D. Meyer-Olson *et al.*, Fluctuations of functionally distinct CD8+ T-cell clonotypes demonstrate flexibility of the HIV-specific TCR repertoire. *Blood* **107**, 2373-2383 (2006).

235. D. Meyer-Olson *et al.*, Clonal expansion and TCR-independent differentiation shape the HIV-specific CD8+ effector-memory T-cell repertoire in vivo. *Blood* **116**, 396-405 (2010).

236. B. C. Simons *et al.*, Despite biased TRBV gene usage against a dominant HLA B57-restricted epitope, TCR diversity can provide recognition of circulating epitope variants. *J Immunol* **181**, 5137-5146 (2008).

237. S. Sadagopal *et al.*, Enhancement of human immunodeficiency virus (HIV)-specific CD8+ T cells in cerebrospinal fluid compared to those in blood among antiretroviral therapy-naive HIV-positive subjects. *J Virol* **82**, 10418-10428 (2008).

238. S. Sadagopal *et al.*, Enhanced PD-1 expression by T cells in cerebrospinal fluid does not reflect functional exhaustion during chronic human immunodeficiency virus type 1 infection. *J Virol* **84**, 131-140 (2010).

239. E. W. Newell, L. L. Yun, Mass cytometry analysis of human T cell phenotype and function. *Methods Mol Biol* **1193**, 55-68 (2014).

240. E. L. Reinherz *et al.*, Clonotypic surface structure on human T lymphocytes: functional and biochemical analysis of the antigen receptor complex. *Immunol Rev* **81**, 95-129 (1984).

241. F. Niedergang *et al.*, The Staphylococcus aureus enterotoxin B superantigen induces specific T cell receptor down-regulation by increasing its internalization. *J Biol Chem* **270**, 12839-12845 (1995).

242. A. Viola, A. Lanzavecchia, T cell activation determined by T cell receptor number and tunable thresholds. *Science* **273**, 104-106 (1996).

243. J. A. Conrad *et al.*, Dominant clonotypes within HIV-specific T cell responses are programmed death-1high and CD127low and display reduced variant cross-reactivity. *J Immunol* **186**, 6871-6885 (2011).

244. E. Coustan-Smith *et al.*, Early T-cell precursor leukaemia: a subtype of very high-risk acute lymphoblastic leukaemia. *The Lancet Oncology* **10**, 147-156 (2009).

245. K. Patrick *et al.*, Outcome for children and young people with Early T-cell precursor acute lymphoblastic leukaemia treated on a contemporary protocol, UKALL 2003. *British Journal of Haematology* **166**, 421-424 (2014).

246. E. J. Yeoh *et al.*, Classification, subtype discovery, and prediction of outcome in pediatric acute lymphoblastic leukemia by gene expression profiling. *Cancer Cell* **1**, 133-143 (2002).

247. S. Chiaretti *et al.*, Gene expression profile of adult T-cell acute lymphocytic leukemia identifies distinct subsets of patients with different response to therapy and survival. *Blood* **103**, 2771-2778 (2004).

248. J. Vose, J. Armitage, D. Weisenburger, T. C. L. P. International, International peripheral T-cell and natural killer/T-cell lymphoma study: pathology findings and clinical outcomes. *J Clin Oncol* **26**, 4124-4130 (2008).

249. D. D. Weisenburger *et al.*, Peripheral T-cell lymphoma, not otherwise specified: a report of 340 cases from the International Peripheral T-cell Lymphoma Project. *Blood* **117**, 3402-3408 (2011).

250. E. R. P. Castellar *et al.*, ALK-negative anaplastic large cell lymphoma is a genetically heterogeneous disease with widely disparate clinical outcomes. *Blood* **124**, 1473-1480 (2014).

251. B. L. Wood *et al.*, T-Lymphoblastic Leukemia (T-ALL) Shows Excellent Outcome, Lack of Significance of the Early Thymic Precursor (ETP) Immunophenotype, and Validation of the Prognostic Value of End-Induction Minimal Residual Disease (MRD) in Children's Oncology Group (COG) Study AALL0434. *Blood* **124**, 1-1 (2014).

252. M. Sakata-Yanagimoto *et al.*, Somatic RHOA mutation in angioimmunoblastic T cell lymphoma. *Nature genetics* **46**, 171-175 (2014).

253. M. McKinney *et al.*, The genetic basis of hepatosplenic T-cell lymphoma. *Cancer Discovery* **7**, 369-379 (2017).

254. J. Choi *et al.*, Genomic landscape of cutaneous T cell lymphoma. *Nature genetics* **47**, 1011-1019 (2015).

255. T. Palomero *et al.*, Recurrent mutations in epigenetic regulators, RHOA and FYN kinase in peripheral T cell lymphomas. *Nature genetics* **46**, 166-170 (2014).

256. K. Kataoka *et al.*, Integrated molecular analysis of adult T cell leukemia/lymphoma. *Nature genetics* **47**, 1304 (2015).

257. E. Chen, L. M. Staudt, A. R. Green, Janus kinase deregulation in leukemia and lymphoma. *Immunity* **36**, 529-541 (2012).

258. C. G. Mullighan *et al.*, JAK mutations in high-risk childhood acute lymphoblastic leukemia. *Proc Natl Acad Sci U S A* **106**, 9414-9418 (2009).

259. L. Y. McGirt *et al.*, Whole-genome sequencing reveals oncogenic mutations in mycosis fungoides. *Blood* **126**, 508-519 (2015).

260. N. Elliott, S. Cleveland, V. Grann, FERM domain mutations induce gain of function in JAK3 in adult T-cell leukemia/lymphoma. (2011).

261. A. K. Bergmann *et al.*, Recurrent mutation of JAK3 in T-cell prolymphocytic leukemia. *Genes, Chromosomes and Cancer* **53**, 309-316 (2014).

262. M. J. Kiel *et al.*, Integrated genomic sequencing reveals mutational landscape of T-cell prolymphocytic leukemia. *Blood* **124**, 1460-1472 (2014).

263. E. G. Jeong *et al.*, Somatic mutations of JAK1 and JAK3 in acute leukemias and solid cancers. *Clinical cancer research* **14**, 3716-3721 (2008).

264. L. P. Yang, G. M. Keating, Ruxolitinib. *Drugs* **72**, 2117-2127 (2012).

265. L. J. Scott, Tofacitinib: a review of its use in adult patients with rheumatoid arthritis. *Drugs* **73**, 857-874 (2013).

266. C. Dearden, How I treat prolymphocytic leukemia. *Blood* **120**, 538-551 (2012).

267. G. M. Frampton *et al.*, Development and validation of a clinical cancer genomic profiling test based on massively parallel DNA sequencing. *Nat Biotechnol* **31**, 1023-1031 (2013).

268. J. H. Layer, C. E. Alford, W. H. McDonald, U. P. Dave, LMO2 Oncoprotein Stability in T-Cell Leukemia Requires Direct LDB1 Binding. *Mol Cell Biol* **36**, 488-506 (2016).

269. Y. Guo, S. Zhao, F. Ye, Q. Sheng, Y. Shyr, MultiRankSeq: Multiperspective Approach for RNAseq Differential Expression Analysis and Quality Control. *BioMed Research International* **2014**, 8 (2014).

270. R. Finck *et al.*, Normalization of mass cytometry data with bead standards. *Cytometry Part A* **83**, 483-494 (2013).

271. J. H. Myklebust *et al.*, High PD-1 expression and suppressed cytokine signaling distinguish T cells infiltrating follicular lymphoma tumors from peripheral T cells. *Blood* **121**, 1367-1376 (2013).

272. J. M. Irish *et al.*, B-cell signaling networks reveal a negative prognostic human lymphoma cell subset that emerges during tumor progression. *Proceedings of the National Academy of Sciences* **107**, 12747-12754 (2010).

273. C. Goodings *et al.*, Enforced expression of E47 has differential effects on Lmo2-induced T-cell leukemias. *Leuk Res* **39**, 100-109 (2015).

274. X. Han *et al.*, Lymphoma survival patterns by WHO subtype in the United States, 1973-2003. *Cancer Causes Control* **19**, 841-858 (2008).

275. C. Boucheix *et al.*, Immunophenotype of adult acute lymphoblastic leukemia, clinical parameters, and outcome: an analysis of a prospective trial including 562 tested patients (LALA87). French Group on Therapy for Adult Acute Lymphoblastic Leukemia. *Blood* **84**, 1603-1612 (1994).

276. S. A. Forbes *et al.*, COSMIC: mining complete cancer genomes in the Catalogue of Somatic Mutations in Cancer. *Nucleic Acids Research* **39**, D945-D950 (2011).

277. C. G. Mullighan *et al.*, Rearrangement of CRLF2 in B-progenitor–and Down syndrome–associated acute lymphoblastic leukemia. *Nature genetics* **41**, 1243-1246 (2009).

278. Y. Yamashita *et al.*, Array-based genomic resequencing of human leukemia. *Oncogene* **29**, 3723-3731 (2010).

279. J. Irie-Sasaki *et al.*, CD45 is a JAK phosphatase and negatively regulates cytokine receptor signalling. *Nature* **409**, 349-354 (2001).

280. G. A. Koretzky, J. Picus, T. Schultz, A. Weiss, Tyrosine phosphatase CD45 is required for T-cell antigen receptor and CD2-mediated activation of a protein tyrosine kinase and interleukin 2 production. *Proceedings of the National Academy of Sciences* **88**, 2037-2041 (1991).

281. J. H. Myklebust *et al.*, Distinct patterns of B-cell receptor signaling in non-Hodgkin lymphomas identified by single-cell profiling. *Blood* **129**, 759-770 (2017).

282. D. Vallois *et al.*, Activating mutations in genes related to TCR signaling in angioimmunoblastic and other follicular helper T-cell-derived lymphomas. *Blood*, blood-2016-2002-698977 (2016).

283. R. L. Boddicker *et al.*, Integrated mate-pair and RNA sequencing identifies novel, targetable gene fusions in peripheral T-cell lymphoma. *Blood*, blood-2016-2003-707141 (2016).

284. C. Haan *et al.*, Jak1 has a dominant role over Jak3 in signal transduction through γc-containing cytokine receptors. *Chemistry & biology* **18**, 314-323 (2011).

285. S. Degryse *et al.*, JAK3 mutants transform hematopoietic cells through JAK1 activation, causing T-cell acute lymphoblastic leukemia in a mouse model. *Blood* **124**, 3092-3100 (2014).

286. E. Losdyck *et al.*, Distinct Acute Lymphoblastic Leukemia (ALL)-associated Janus Kinase 3 (JAK3) Mutants Exhibit Different Cytokine-Receptor Requirements and JAK Inhibitor Specificities. *Journal of Biological Chemistry* **290**, 29022-29034 (2015).

287. R. Chiarle *et al.*, Stat3 is required for ALK-mediated lymphomagenesis and provides a possible therapeutic target. *Nat Med* **11**, 623-629 (2005).

288. M. E. Flanagan *et al.*, Discovery of CP-690,550: a potent and selective Janus kinase (JAK) inhibitor for the treatment of autoimmune diseases and organ transplant rejection. *Journal of medicinal chemistry* **53**, 8468-8484 (2010).

289. A. Quintás-Cardama *et al.*, Preclinical characterization of the selective JAK1/2 inhibitor INCB018424: therapeutic implications for the treatment of myeloproliferative neoplasms. *Blood* **115**, 3109-3117 (2010).

290. P. S. Changelian *et al.*, The specificity of JAK3 kinase inhibitors. *Blood* **111**, 2155-2157 (2008).

291. M. W. Karaman *et al.*, A quantitative analysis of kinase inhibitor selectivity. *Nat Biotech* **26**, 127-132 (2008).

292. J. R. Girton, K. M. Johansen, Chromatin structure and the regulation of gene expression: the lessons of PEV in Drosophila. *Adv Genet* **61**, 1-43 (2008).

293. S. M. Cleveland *et al.*, LMO2 induces T-cell leukemia with epigenetic deregulation of CD4. *Exp Hematol* **42**, 581-593 e585 (2014).

294. M. Porcu *et al.*, Mutation of the receptor tyrosine phosphatase PTPRC (CD45) in T-cell acute lymphoblastic leukemia. *Blood* **119**, 4476-4479 (2012).

295. S. L. Topalian *et al.*, Safety, activity, and immune correlates of anti-PD-1 antibody in cancer. *N Engl j Med* **366**, 2443-2454 (2012).

296. O. Hamid *et al.*, Safety and tumor responses with lambrolizumab (anti-PD-1) in melanoma. *N Engl j Med* **369**, 134-144 (2013).

297. A. Ribas *et al.*, Pembrolizumab versus investigator-choice chemotherapy for ipilimumab-refractory melanoma (KEYNOTE-002): a randomised, controlled, phase 2 trial. *Lancet Oncol*, (2015).

298. S. M. Ansell *et al.*, PD-1 Blockade with Nivolumab in Relapsed or Refractory Hodgkin's Lymphoma. *N Engl j Med*, (2014).

299. D. T. Le *et al.*, PD-1 Blockade in Tumors with Mismatch-Repair Deficiency. *N Engl j Med* **372**, 2509-2520 (2015).

300. R. S. Herbst *et al.*, Predictive correlates of response to the anti-PD-L1 antibody MPDL3280A in cancer patients. *Nature* **515**, 563-567 (2014).

301. P. Brodin *et al.*, Variation in the human immune system is largely driven by non-heritable influences. *Cell* **160**, 37-47 (2015).

302. J. M. Taube *et al.*, Association of PD-1, PD-1 ligands, and other features of the tumor immune microenvironment with response to anti-PD-1 therapy. *Clin Cancer Res* **20**, 5064-5074 (2014).

303. D. Brohee, N. Higuet, In vitro stimulation of peripheral blood mononuclear cells by phytohaemagglutinin A induces CD45RA expression on monocytes. *Cytobios* **71**, 105-111 (1992).

304. K. Ogata *et al.*, Clinical significance of phenotypic features of blasts in patients with myelodysplastic syndrome. *Blood* **100**, 3887-3896 (2002).

305. M. Ishida *et al.*, Differential expression of PD-L1 and PD-L2, ligands for an inhibitory receptor PD-1, in the cells of lymphohematopoietic tissues. *Immunol Lett* **84**, 57-62 (2002).

306. S. Y. Kordasti *et al.*, IL-17-producing CD4(+) T cells, pro-inflammatory cytokines and apoptosis are increased in low risk myelodysplastic syndrome. *Br J Haematol* **145**, 64-72 (2009).

307. S. Y. Kordasti *et al.*, CD4+CD25high Foxp3+ regulatory T cells in myelodysplastic syndrome (MDS). *Blood* **110**, 847-850 (2007).

308. X. Chen *et al.*, Induction of myelodysplasia by myeloid-derived suppressor cells. *J Clin Invest* **123**, 4595-4611 (2013).

309. S. M. Ansell *et al.*, PD-1 blockade with nivolumab in relapsed or refractory Hodgkin's lymphoma. *N Engl j Med* **372**, 311-319 (2015).

310. Y. Saeys, S. V. Gassen, B. N. Lambrecht, Computational flow cytometry: helping to make sense of high-dimensional immunology data. *Nat Rev Immunol* **16**, 449-462 (2016).

311. A. P. Patel *et al.*, Single-cell RNA-seq highlights intratumoral heterogeneity in primary glioblastoma. *Science* **344**, 1396-1401 (2014).

312. A. R. Greenplate, D. B. Johnson, P. B. Ferrell, J. M. Irish, Systems immune monitoring in cancer therapy. *Eur J Cancer* **61**, 77-84 (2016).

313. J. M. Irish *et al.*, Single cell profiling of potentiated phospho-protein networks in cancer cells. *Cell* **118**, 217-228 (2004).

314. J. H. Levine *et al.*, Data-Driven Phenotypic Dissection of AML Reveals Progenitor-like Cells that Correlate with Prognosis. *Cell* **162**, 184-197 (2015).

315. A. R. Greenplate *et al.*, Myelodysplastic Syndrome Revealed by Systems Immunology in a Melanoma Patient Undergoing Anti–PD-1 Therapy. *Cancer Immunology Research* **4**, 474-480 (2016).

316. B. Gaudilliere *et al.*, Clinical recovery from surgery correlates with single-cell immune signatures. *Sci Transl Med* **6**, 255ra131-255ra131 (2014).

317. I. T. Young, Proof without prejudice: use of the Kolmogorov-Smirnov test for the analysis of histograms from flow systems and other sources. *J Histochem Cytochem* **25**, 935-941 (1977).

318. D. Kim, V. S. Donnenberg, J. W. Wilson, A. D. Donnenberg, The use of simultaneous confidence bands for comparison of single parameter fluorescent intensity data. *Cytometry A* **89**, 89-97 (2016).

319. D. Y. Orlova *et al.*, Earth Mover's Distance (EMD): A True Metric for Comparing Biomarker Expression Levels in Cell Populations. *PLoS One* **11**, e0151859 (2016).

320. N. Leelatian, K. E. Diggins, J. M. Irish, in *Single Cell Protein Analysis*. (Springer, 2015), pp. 99-113.

321. N. Leelatian *et al.*, Single cell analysis of human tissues and solid tumors with mass cytometry. *Cytometry B Clin Cytom*, (2016).

322. Nomenclature for clusters of differentiation (CD) of antigens defined on human leukocyte populations. IUIS-WHO Nomenclature Subcommittee. *Bull World Health Organ* **62**, 809-815 (1984).

323. C. I. Civin *et al.*, Antigenic analysis of hematopoiesis. III. A hematopoietic progenitor cell surface antigen defined by a monoclonal antibody raised against KG-1a cells. *J Immunol* **133**, 157-165 (1984).

324. S. Doulatov, F. Notta, E. Laurenti, J. E. Dick, Hematopoiesis: a human perspective. *Cell Stem Cell* **10**, 120-136 (2012).

325. A. Basit *et al.*, ICAM-1 and LFA-1 play critical roles in LPS-induced neutrophil recruitment into the alveolar space. *Am J Physiol Lung Cell Mol Physiol* **291**, L200-207 (2006).

326. R. C. Furze, S. M. Rankin, Neutrophil mobilization and clearance in the bone marrow. *Immunology* **125**, 281-288 (2008).

327. K. J. Nicholas *et al.*, Multiparameter analysis of stimulated human peripheral blood mononuclear cells: A comparison of mass and fluorescence cytometry. *Cytometry A* **89**, 271-280 (2016).

328. P. B. Ferrell, Jr. *et al.*, High-Dimensional Analysis of Acute Myeloid Leukemia Reveals Phenotypic Changes in Persistent Cells during Induction Therapy. *PLoS One* **11**, e0153207 (2016).

329. F. Hahne *et al.*, flowCore: a Bioconductor package for high throughput flow cytometry. *BMC Bioinformatics* **10**, 106 (2009).

330. B. B. Gregory R. Warnes, Lodewijk Bonebakker, Robert Gentleman, Wolfgang Huber Andy Liaw, Thomas Lumley, Martin Maechler, Arni Magnusson, Steffen Moeller, Marc Schwartz, Bill Venables, gplots: Various R Programming Tools for Plotting Data. (2015).

331. H. F. Lo K, Brinkman R and Gottardo R FlowClust: a Bioconductor package for automated gating of flow cytometry data. *BMC Bioinformatics* **10**, (2009).

332. T. R. Mosmann *et al.*, SWIFT-scalable clustering for automated identification of rare cell populations in large, high-dimensional flow cytometry datasets, Part 2: Biological evaluation. *Cytometry A*, (2014).

333. R. V. Bruggner, B. Bodenmiller, D. L. Dill, R. J. Tibshirani, G. P. Nolan, Automated identification of stratifying signatures in cellular subpopulations. *Proc Natl Acad Sci U S A* **111**, E2770-2777 (2014).

334. K. Shekhar, P. Brodin, M. M. Davis, A. K. Chakraborty, Automatic Classification of Cellular Expression by Nonlinear Stochastic Embedding (ACCENSE). *Proc Natl Acad Sci U S A* **111**, 202-207 (2014).

335. M. H. Spitzer *et al.*, IMMUNOLOGY. An interactive reference framework for modeling a dynamic immune system. *Science* **349**, 1259425 (2015).

336. N. Leelatian, K. E. Diggins, J. M. Irish, Characterizing Phenotypes and Signaling Networks of Single Human Cells by Mass Cytometry. *Methods Mol Biol* **1346**, 99-113 (2015).

337. C. Cox, J. E. Reeder, R. D. Robinson, S. B. Suppes, L. L. Wheeless, Comparison of frequency distributions in flow cytometry. *Cytometry* **9**, 291-298 (1988).

338. P. Brodin, M. M. Davis, Human immune system variation. *Nat Rev Immunol* **17**, 21-29 (2017).

339. K. J. Kaczorowski *et al.*, Continuous immunotypes describe human immune variation and predict diverse responses. *Proc Natl Acad Sci U S A*, (2017).

340. N. Kotecha *et al.*, Single-cell profiling identifies aberrant STAT5 activation in myeloid malignancies with specific clinical and biologic correlates. *Cancer Cell* **14**, 335-343 (2008).

341. J. S. Tsang *et al.*, Global analyses of human immune variation reveal baseline predictors of postvaccination responses. *Cell* **157**, 499-513 (2014).

342. M. H. Spitzer *et al.*, Systemic Immunity Is Required for Effective Cancer Immunotherapy. *Cell* **168**, 487-502 e415 (2017).

343. A. C. Huang *et al.*, T-cell invigoration to tumour burden ratio associated with anti-PD-1 response. *Nature* **545**, 60 (2017).

344. G. K. Behbehani *et al.*, Mass Cytometric Functional Profiling of Acute Myeloid Leukemia Defines Cell-Cycle and Immunophenotypic Properties That Correlate with Known Responses to Therapy. *Cancer Discov* **5**, 988-1003 (2015).

345. S. Kordasti *et al.*, Deep-phenotyping of Tregs identifies an immune signature for idiopathic aplastic anemia and predicts response to treatment. *Blood*, (2016).

346. M. Roederer *et al.*, The genetic architecture of the human immune system: a bioresource for autoimmunity and disease pathogenesis. *Cell* **161**, 387-403 (2015).

347. H. G. Polikowsky *et al.*, Systems Immune Monitoring with Mass Cytometry Characterizes Altered Peripheral Immune Cell Environments in Patients with Chronic Graft Versus Host Disease. *Blood* **128**, 4572-4572 (2016).

348. K. E. Diggins, A. R. Greenplate, N. Leelatian, C. E. Wogsland, J. M. Irish, Characterizing cell subsets using marker enrichment modeling. *Nat Methods* **14**, 275-278 (2017).

349. E. Arvaniti, M. Claassen, Sensitive detection of rare disease-associated cell subsets via representation learning. *Nat Commun* **8**, 14825 (2017).

350. L. M. Weber, M. D. Robinson, Comparison of clustering methods for high-dimensional single-cell flow and mass cytometry data. *Cytometry A* **89**, 1084-1096 (2016).

351. A. S. Japp *et al.*, Wild immunology assessed by multidimensional mass cytometry. *Cytometry A* **91**, 85-95 (2017).

352. A. Viola *et al.*, Quantitative contribution of CD4 and CD8 to T cell antigen receptor serial triggering. *J Exp Med* **186**, 1775-1779 (1997).

353. J. M. Irish, N. Kotecha, G. P. Nolan, Mapping normal and cancer cell signalling networks: towards single-cell proteomics. *Nat Rev Cancer* **6**, 146-155 (2006).

354. S. C. Wei *et al.*, Distinct Cellular Mechanisms Underlie Anti-CTLA-4 and Anti-PD-1 Checkpoint Blockade. *Cell* **170**, 1120-1133 e1117 (2017).

355. D. Marvel, D. I. Gabrilovich, Myeloid-derived suppressor cells in the tumor microenvironment: expect the unexpected. *J Clin Invest* **125**, 3356-3364 (2015).

356. D. L. DeMets, S. S. Ellenberg, Data Monitoring Committees - Expect the Unexpected. *N Engl j Med* **375**, 1365-1371 (2016).

357. D. Behl *et al.*, Absolute lymphocyte count recovery after induction chemotherapy predicts superior survival in acute myelogenous leukemia. *Leukemia* **20**, 29 (2006).

358. C. L. Mackall *et al.*, Age, Thymopoiesis, and CD4+ T-Lymphocyte Regeneration after Intensive Chemotherapy. *New England Journal of Medicine* **332**, 143-149 (1995).

359. R. Das *et al.*, Combination therapy with anti-CTLA-4 and anti-PD-1 leads to distinct immunologic changes in vivo. *J Immunol* **194**, 950-959 (2015).

360. V. Vallacchi *et al.*, Transcriptional profiling of melanoma sentinel nodes identify patients with poor outcome and reveal an association of CD30(+) T lymphocytes with progression. *Cancer Res* **74**, 130-140 (2014).

361. K. Fischer *et al.*, Isolation and characterization of human antigen-specific TCR alpha beta+ CD4(-)CD8- double-negative regulatory T cells. *Blood* **105**, 2828-2835 (2005).

362. I. V. Grishkan, A. Ntranos, P. A. Calabresi, A. R. Gocke, Helper T cells down-regulate CD4 expression upon chronic stimulation giving rise to double-negative T cells. *Cell Immunol* **284**, 68-74 (2013).

363. J. J. Priatel, O. Utting, H. S. Teh, TCR/self-antigen interactions drive double-negative T cell peripheral expansion and differentiation into suppressor cells. *J Immunol* **167**, 6188-6194 (2001).

364. D. Zhang *et al.*, New differentiation pathway for double-negative regulatory T cells that regulates the magnitude of immune responses. *Blood* **109**, 4071-4079 (2007).

365. P. J. Ebert *et al.*, MAP Kinase Inhibition Promotes T Cell and Anti-tumor Activity in Combination with PD-L1 Checkpoint Blockade. *Immunity* **44**, 609-621 (2016).

366. S. Chevrier *et al.*, An Immune Atlas of Clear Cell Renal Cell Carcinoma. *Cell* **169**, 736-749 e718 (2017).

367. M. T. Wong *et al.*, A High-Dimensional Atlas of Human T Cell Diversity Reveals Tissue-Specific Trafficking and Cytokine Signatures. *Immunity* **45**, 442-456 (2016).

368. I. Tirosh *et al.*, Dissecting the multicellular ecosystem of metastatic melanoma by single-cell RNA-seq. *Science* **352**, 189-196 (2016).

369. A. S. Johnson, H. Crandall, K. Dahlman, M. C. Kelley, Preliminary results from a prospective trial of preoperative combined BRAF and MEK-targeted therapy in advanced BRAF mutation-positive melanoma. *J Am Coll Surg* **220**, 581-593 e581 (2015).

370. N. Leelatian *et al.*, Single cell analysis of human tissues and solid tumors with mass cytometry. *Cytometry B Clin Cytom* **92**, 68-78 (2017).

371. N. Leelatian *et al.*, Preparing Viable Single Cells from Human Tissue and Tumors for Cytomic Analysis. *Curr Protoc Mol Biol* **118**, 25C 21 21-25C 21 23 (2017).

372. P. J. Siska *et al.*, Mitochondrial dysregulation and glycolytic insufficiency functionally impair CD8 T cells infiltrating human renal cell carcinoma. *JCI Insight* **2**, (2017).

373. C. Gottschlich, D. Schuhmacher, The Shortlist Method for fast computation of the Earth Mover's Distance and finding optimal solutions to transportation problems. *PLoS One* **9**, e110214 (2014).

374. C. M. Lovly *et al.*, Routine multiplex mutational profiling of melanomas enables enrollment in genotype-driven therapeutic trials. *PLoS One* **7**, e35309 (2012).

375. F. D'Acquisto, T. Crompton, CD3+ CD4− CD8−(double negative) T cells: saviours or villains of the immune response? *Biochemical pharmacology* **82**, 333-340 (2011).

376. R. C. Halder *et al.*, Intensive generation of NK1.1- extrathymic T cells in the liver by injection of bone marrow cells isolated from mice with a mutation of polymorphic major histocompatibility complex antigens. *Immunology* **102**, 450-459 (2001).

377. M. Johansson, N. Lycke, A unique population of extrathymically derived alpha beta TCR+CD4-CD8- T cells with regulatory functions dominates the mouse female genital tract. *J Immunol* **170**, 1659-1666 (2003).

378. M. Egerton, R. Scollay, Intrathymic selection of murine TCR alpha beta+CD4-CD8- thymocytes. *Int Immunol* **2**, 157-163 (1990).

379. J. C. Crispín, G. C. Tsokos, Human TCR-αβ+ CD4− CD8− T cells can derive from CD8+ T cells and display an inflammatory effector phenotype. *The Journal of Immunology* **183**, 4675-4681 (2009).

380. L. Al-Harthi *et al.*, Detection of T cell receptor circles (TRECs) as biomarkers for de novo T cell synthesis using a quantitative polymerase chain reaction–enzyme linked immunosorbent assay (PCR–ELISA). *Journal of immunological methods* **237**, 187-197 (2000).

381. E. E. Hillhouse, S. Lesage, A comprehensive review of the phenotype and function of antigen-specific immunoregulatory double negative T cells. *Journal of autoimmunity* **40**, 58-65 (2013).

382. S. C. Juvet, L. Zhang, Double negative regulatory T cells in transplantation and autoimmunity: recent progress and future directions. *Journal of molecular cell biology* **4**, 48-58 (2012).

383. C. Reinhardt, A. Melms, Normalization of elevated CD4−/CD8−(double-negative) T cells after thymectomy parallels clinical remission in myasthenia gravis associated with thymic hyperplasia but not thymoma. *Annals of neurology* **48**, 603-608 (2000).

384. J. C. Crispín *et al.*, Expanded double negative T cells in patients with systemic lupus erythematosus produce IL-17 and infiltrate the kidneys. *The Journal of Immunology* **181**, 8761-8766 (2008).

385. J. B. Lee *et al.*, Allogeneic human double negative T cells as a novel immunotherapy for acute myeloid leukemia and its underlying mechanisms. *Clinical cancer research*, clincanres. 2228.2017 (2017).

386. Z.-X. Zhang, L. Yang, K. J. Young, B. DuTemple, L. Zhang, Identification of a previously unknown antigen-specific regulatory T cell and its mechanism of suppression. *Nat Med* **6**, 782-789 (2000).

387. W. Li *et al.*, Ex vivo converted double negative T cells suppress activated B cells. *International immunopharmacology* **20**, 164-169 (2014).

388. J. F. Gao *et al.*, Regulation of antigen-expressing dendritic cells by double negative regulatory T cells. *Eur J Immunol* **41**, 2699-2708 (2011).

389. Z.-X. Zhang *et al.*, Double-negative T cells, activated by xenoantigen, lyse autologous B and T cells using a perforin/granzyme-dependent, Fas-Fas ligand-independent pathway. *The Journal of Immunology* **177**, 6920-6929 (2006).

390. M. S. F. McIntyre, K. J. Young, J. Gao, B. Joe, L. Zhang, Cutting edge: in vivo trogocytosis as a mechanism of double negative regulatory T cell-mediated antigen-specific suppression. *The Journal of Immunology* **181**, 2271-2275 (2008).

391. M. Roussel *et al.*, Mass cytometry deep phenotyping of human mononuclear phagocytes and myeloid-derived suppressor cells from human blood and bone marrow. *Journal of leukocyte biology* **102**, 437-447 (2017).

392. J. C. Sun, L. L. Lanier, NK cell development, homeostasis and function: parallels with CD8+ T cells. *Nature Reviews Immunology* **11**, 645 (2011).

393. A. M. Intlekofer *et al.*, Effector and memory CD8+ T cell fate coupled by T-bet and eomesodermin. *Nature immunology* **6**, 1236 (2005).

394. C. Krieg *et al.*, High-dimensional single-cell analysis predicts response to anti-PD-1 immunotherapy. *Nat Med*, (2018).

395. M. T. Wong *et al.*, A high-dimensional atlas of human T cell diversity reveals tissue-specific trafficking and cytokine signatures. *Immunity* **45**, 442-456 (2016).

396. P. J. Siska *et al.*, Mitochondrial dysregulation and glycolytic insufficiency functionally impair CD8 T cells infiltrating human renal cell carcinoma. *JCI Insight* **2**, (2017).

397. N. Leelatian *et al.*, Single cell analysis of human tissues and solid tumors with mass cytometry. *Cytometry Part B: Clinical Cytometry* **92**, 68-78 (2017).

398. D. Schapiro *et al.*, histoCAT: analysis of cell phenotypes and interactions in multiplex image cytometry data. *nature methods* **14**, 873 (2017).

399. A. P. Frei *et al.*, Highly multiplexed simultaneous detection of RNAs and proteins in single cells. *nature methods* **13**, 269 (2016).

400. J. H. Levine *et al.*, Data-driven phenotypic dissection of AML reveals progenitor-like cells that correlate with prognosis. *Cell* **162**, 184-197 (2015).

401. K. Kelly, Extrapolations. (2016).

402. S. Dieleman, Recommending music on Spotify with deep learning. (2014).

403. S. Van Gassen *et al.*, FlowSOM: Using self-organizing maps for visualization and interpretation of cytometry data. *Cytometry Part A* **87**, 636-645 (2015).

404. K. Kelly, The Next Transitions in the Technium. (2012).

405. S. Di Palma, B. Bodenmiller, Unraveling cell populations in tumors by single-cell mass cytometry. *Curr Opin Biotechnol* **31**, 122-129 (2015).

406. H. Zola *et al.*, CD molecules 2006—human cell differentiation molecules. *Journal of immunological methods* **319**, 1-5 (2007).

407. S. Gordon, P. R. Taylor, Monocyte and macrophage heterogeneity. *Nature Reviews Immunology* **5**, 953 (2005).

408. S. J. Jenkins, D. A. Hume, Homeostasis in the mononuclear phagocyte system. *Trends in immunology* **35**, 358-367 (2014).

409. F. Geissmann, S. Gordon, D. A. Hume, A. M. Mowat, G. J. Randolph, Unravelling mononuclear phagocyte heterogeneity. *Nature Reviews Immunology* **10**, 453 (2010).

410. L. Ziegler-Heitbrock *et al.*, Nomenclature of monocytes and dendritic cells in blood. *Blood* **116**, e74-e80 (2010).

411. J. Cros *et al.*, Human CD14dim monocytes patrol and sense nucleic acids and viruses via TLR7 and TLR8 receptors. *Immunity* **33**, 375-386 (2010).

412. C. Murdoch, S. Tazzyman, S. Webster, C. E. Lewis, Expression of Tie-2 by human monocytes and their responses to angiopoietin-2. *The Journal of Immunology* **178**, 7405-7411 (2007).

413. N. V. Serbina, E. G. Pamer, Monocyte emigration from bone marrow during bacterial infection requires signals mediated by chemokine receptor CCR2. *Nature immunology* **7**, 311 (2006).

414. H. Jersmann, Time to abandon dogma: CD14 is expressed by non-myeloid lineage cells. *Immunology & Cell Biology* **83**, 462-467 (2005).

415. G. D'alessandro, I. Zardawi, J. Grace, T. W. H. McCarthys, P. Hersey, Immunohistological evaluation of MHC class I and II antigen expression on nevi and melanoma: relation to biology of melanoma. *Pathology* **19**, 339-346 (1987).

416. F. Geissmann *et al.*, Development of monocytes, macrophages, and dendritic cells. *Science* **327**, 656-661 (2010).

417. M. Guilliams *et al.*, Dendritic cells, monocytes and macrophages: a unified nomenclature based on ontogeny. *Nature Reviews Immunology* **14**, 571 (2014).

418. M. J. McPhail *et al.*, CD14, CD16 and HLA-DR reliably identifies human monocytes and their subsets in the context of pathologically reduced HLA-DR expression by CD14hi/CD16neg monocytes: Expansion of CD14hi/CD16pos and contraction of CD14lo/CD16pos monocytes in acute liver failure. *Cytometry Part A* **81**, 823-834 (2012).

419. P. Autissier, C. Soulas, T. H. Burdo, K. C. Williams, Evaluation of a 12-color flow cytometry panel to study lymphocyte, monocyte, and dendritic cell subsets in humans. *Cytometry Part A* **77**, 410-419 (2010).

420. J. Bocsi, S. Melzer, I. Dähnert, A. Tárnok, OMIP-023: 10-Color, 13 antibody panel for in-depth phenotyping of human peripheral blood leukocytes. *Cytometry Part A* **85**, 781-784 (2014).

421. E. Van Lochem *et al.*, Immunophenotypic differentiation patterns of normal hematopoiesis in human bone marrow: Reference patterns for age-related changes and disease-induced shifts. *Cytometry Part B: Clinical Cytometry* **60**, 1-13 (2004).

422. S. K. Biswas, P. Allavena, A. Mantovani, Tumor-associated macrophages: functional diversity, clinical significance, and open questions. *Seminars in immunopathology* **35**, 585-600 (2013).

423. J. Xue *et al.*, Transcriptome-based network analysis reveals a spectrum model of human macrophage activation. *Immunity* **40**, 274-288 (2014).

424. A. Mantovani, M. Locati, Tumor-associated macrophages as a paradigm of macrophage plasticity, diversity, and polarization: lessons and open questions. *Arteriosclerosis, thrombosis, and vascular biology* **33**, 1478-1483 (2013).

425. S. S. Yu *et al.*, Macrophage-specific RNA interference targeting via “click”, mannosylated polymeric micelles. *Molecular pharmaceutics* **10**, 975-987 (2013).

426. D. I. Gabrilovich, S. Nagaraj, Myeloid-derived suppressor cells as regulators of the immune system. *Nature Reviews Immunology* **9**, 162 (2009).

427. E. Peranzoni *et al.*, Myeloid-derived suppressor cell heterogeneity and subset definition. *Current opinion in immunology* **22**, 238-244 (2010).

428. D. I. Gabrilovich, S. Ostrand-Rosenberg, V. Bronte, Coordinated regulation of myeloid cells by tumours. *Nature Reviews Immunology* **12**, 253 (2012).

429. M. A. Ingersoll *et al.*, Comparison of gene expression profiles between human and mouse monocyte subsets. *Blood* **115**, e10-e19 (2010).

430. K. L. Wong *et al.*, Gene expression profiling reveals the defining features of the classical, intermediate, and nonclassical human monocyte subsets. *Blood* **118**, e16-e31 (2011).

431. A. M. Zawada *et al.*, SuperSAGE evidence for CD14++ CD16+ monocytes as a third monocyte subset. *Blood*, blood-2011-2001-326827 (2011).

432. F. O. Martinez *et al.*, Genetic programs expressed in resting and IL-4 alternatively activated mouse and human macrophages: similarities and differences. *Blood* **121**, e57-e69 (2013).

433. P. Qiu *et al.*, Extracting a cellular hierarchy from high-dimensional cytometry data with SPADE. *Nat Biotechnol* **29**, 886 (2011).

434. A. Horowitz *et al.*, Genetic and environmental determinants of human NK cell diversity revealed by mass cytometry. *Sci Transl Med* **5**, 208ra145-208ra145 (2013).

435. E.-a. D. Amir *et al.*, viSNE enables visualization of high dimensional single-cell data and reveals phenotypic heterogeneity of leukemia. *Nat Biotechnol* **31**, 545 (2013).

436. G. K. Behbehani *et al.*, Transient partial permeabilization with saponin enables cellular barcoding prior to surface marker staining. *Cytometry A* **85**, 1011-1019 (2014).

437. D. Hashimoto, J. Miller, M. Merad, Dendritic cell and macrophage heterogeneity in vivo. *Immunity* **35**, 323-335 (2011).

438. F. Ginhoux, S. Jung, Monocytes and macrophages: developmental pathways and tissue homeostasis. *Nature Reviews Immunology* **14**, 392-404 (2014).

439. C. Engblom, C. Pfirschke, M. J. Pittet, The role of myeloid cells in cancer therapies. *Nat Rev Cancer* **16**, 447-462 (2016).

440. Y. Lavin, A. Mortha, A. Rahman, M. Merad, Regulation of macrophage development and function in peripheral tissues. *Nat Rev Immunol* **15**, 731-744 (2015).

441. M. Merad, P. Sathe, J. Helft, J. Miller, A. Mortha, The dendritic cell lineage: ontogeny and function of dendritic cells and their subsets in the steady state and the inflamed setting. *Annu Rev Immunol* **31**, 563-604 (2013).

442. P. R. Taylor *et al.*, Macrophage receptors and immune recognition. *Annu Rev Immunol* **23**, 901-944 (2005).

443. J. Hamann *et al.*, EMR1, the human homolog of F4/80, is an eosinophil-specific receptor. *Eur J Immunol* **37**, 2797-2802 (2007).

444. G. A. Rabinovich, D. Gabrilovich, E. M. Sotomayor, Immunosuppressive strategies that are mediated by tumor cells. *Annu Rev Immunol* **25**, 267-296 (2007).

445. V. Bronte *et al.*, Recommendations for myeloid-derived suppressor cell nomenclature and characterization standards. *Nat Commun* **7**, 12150 (2016).

446. L. Ziegler-Heitbrock *et al.*, Nomenclature of monocytes and dendritic cells in blood. *Blood* **116**, e74-80 (2010).

447. M. De Palma *et al.*, Tie2 identifies a hematopoietic lineage of proangiogenic monocytes required for tumor vessel formation and a mesenchymal population of pericyte progenitors. *Cancer Cell* **8**, 211-226 (2005).

448. P. J. Murray *et al.*, Macrophage activation and polarization: nomenclature and experimental guidelines. *Immunity* **41**, 14-20 (2014).

449. F. O. Martinez, S. Gordon, M. Locati, A. Mantovani, Transcriptional profiling of the human monocyte-to-macrophage differentiation and polarization: new molecules and patterns of gene expression. *J Immunol* **177**, 7303-7311 (2006).

450. F. Ginhoux, J. L. Schultze, P. J. Murray, J. Ochando, S. K. Biswas, New insights into the multidimensional concept of macrophage ontogeny, activation and function. *Nat Immunol* **17**, 34-40 (2016).

451. J. Xue *et al.*, Transcriptome-based network analysis reveals a spectrum model of human macrophage activation. *Immunity* **40**, 274-288 (2014).

452. D. M. Mosser, J. P. Edwards, Exploring the full spectrum of macrophage activation. *Nat Rev Immunol* **8**, 958-969 (2008).

453. J. P. Edwards, X. Zhang, K. A. Frauwirth, D. M. Mosser, Biochemical and functional characterization of three activated macrophage populations. *J Leukoc Biol* **80**, 1298-1307 (2006).

454. M. H. Spitzer, G. P. Nolan, Mass Cytometry: Single Cells, Many Features. *Cell* **165**, 780-791 (2016).

455. M. T. Wong *et al.*, Mapping the Diversity of Follicular Helper T Cells in Human Blood and Tonsils Using High-Dimensional Mass Cytometry Analysis. *Cell Rep* **11**, 1822-1833 (2015).

456. V. van Unen *et al.*, Mass Cytometry of the Human Mucosal Immune System Identifies Tissue- and Disease-Associated Immune Subsets. *Immunity* **44**, 1227-1239 (2016).

457. G. M. Mason *et al.*, Phenotypic Complexity of the Human Regulatory T Cell Compartment Revealed by Mass Cytometry. *J Immunol* **195**, 2030-2037 (2015).

458. L. Hansmann *et al.*, Mass cytometry analysis shows that a novel memory phenotype B cell is expanded in multiple myeloma. *Cancer Immunol Res* **3**, 650-660 (2015).

459. D. M. Strauss-Albee, A. Horowitz, P. Parham, C. A. Blish, Coordinated regulation of NK receptor expression in the maturing human immune system. *J Immunol* **193**, 4871-4879 (2014).

460. M. Guilliams *et al.*, Unsupervised High-Dimensional Analysis Aligns Dendritic Cells across Tissues and Species. *Immunity* **45**, 669-684 (2016).

461. I. Marigo *et al.*, Tumor-induced tolerance and immune suppression depend on the C/EBPbeta transcription factor. *Immunity* **32**, 790-802 (2010).

462. M. G. Lechner, D. J. Liebertz, A. L. Epstein, Characterization of cytokine-induced myeloid-derived suppressor cells from normal human peripheral blood mononuclear cells. *J Immunol* **185**, 2273-2284 (2010).

463. T. P. Hofer *et al.*, slan-defined subsets of CD16-positive monocytes: impact of granulomatous inflammation and M-CSF receptor mutation. *Blood* **126**, 2601-2610 (2015).

464. M. Sade-Feldman *et al.*, Clinical Significance of Circulating CD33+CD11b+HLA-DR- Myeloid Cells in Patients with Stage IV Melanoma Treated with Ipilimumab. *Clin Cancer Res* **22**, 5661-5672 (2016).

465. B. M. Rudolph *et al.*, Increased frequencies of CD11b(+) CD33(+) CD14(+) HLA-DR(low) myeloid-derived suppressor cells are an early event in melanoma patients. *Exp Dermatol* **23**, 202-204 (2014).

466. I. Chevolet *et al.*, Clinical significance of plasmacytoid dendritic cells and myeloid-derived suppressor cells in melanoma. *J Transl Med* **13**, 9 (2015).

467. B. Weide *et al.*, Myeloid-derived suppressor cells predict survival of patients with advanced melanoma: comparison with regulatory T cells and NY-ESO-1- or melan-A-specific T cells. *Clin Cancer Res* **20**, 1601-1609 (2014).

468. Y. Mao *et al.*, Melanoma-educated CD14+ cells acquire a myeloid-derived suppressor cell phenotype through COX-2-dependent mechanisms. *Cancer Res* **73**, 3877-3887 (2013).

469. M. Mingueneau *et al.*, Cytometry by time-of-flight immunophenotyping identifies a blood Sjogren's signature correlating with disease activity and glandular inflammation. *J Allergy Clin Immunol* **137**, 1809-1821 e1812 (2016).

470. L. Han *et al.*, Single-cell mass cytometry reveals intracellular survival/proliferative signaling in FLT3-ITD-mutated AML stem/progenitor cells. *Cytometry A* **87**, 346-356 (2015).

471. S. Baumgart, A. Peddinghaus, U. Schulte-Wrede, H. E. Mei, A. Grutzkau, OMIP-034: Comprehensive immune phenotyping of human peripheral leukocytes by mass cytometry for monitoring immunomodulatory therapies. *Cytometry A* **91**, 34-38 (2017).

472. M. Roussel, Greenplate, A.R., Irish, J.M., Dissecting Complex Cellular Systems with High Dimensional Single Cell Mass Cytometry. *Experimental approaches for the investigation of innate immunity*, 15-26 (2016).

473. Y. I. Son *et al.*, A novel bulk-culture method for generating mature dendritic cells from mouse bone marrow cells. *J Immunol Methods* **262**, 145-157 (2002).

474. J. Helft *et al.*, GM-CSF Mouse Bone Marrow Cultures Comprise a Heterogeneous Population of CD11c(+)MHCII(+) Macrophages and Dendritic Cells. *Immunity* **42**, 1197-1211 (2015).

475. M. D. van de Garde *et al.*, Chronic exposure to glucocorticoids shapes gene expression and modulates innate and adaptive activation pathways in macrophages with distinct changes in leukocyte attraction. *J Immunol* **192**, 1196-1208 (2014).

476. P. H. Feng *et al.*, CD14(+)S100A9(+) monocytic myeloid-derived suppressor cells and their clinical relevance in non-small cell lung cancer. *Am J Respir Crit Care Med* **186**, 1025-1036 (2012).

477. F. Zhao *et al.*, S100A9 a new marker for monocytic human myeloid-derived suppressor cells. *Immunology* **136**, 176-183 (2012).

478. S. Gordon, A. Pluddemann, F. Martinez Estrada, Macrophage heterogeneity in tissues: phenotypic diversity and functions. *Immunol Rev* **262**, 36-55 (2014).

479. C. Robert *et al.*, Nivolumab in previously untreated melanoma without BRAF mutation. *N Engl j Med* **372**, 320-330 (2015).

480. C. Robert *et al.*, Pembrolizumab versus Ipilimumab in Advanced Melanoma. *N Engl j Med* **372**, 2521-2532 (2015).

481. N. A. Rizvi *et al.*, Activity and safety of nivolumab, an anti-PD-1 immune checkpoint inhibitor, for patients with advanced, refractory squamous non-small-cell lung cancer (CheckMate 063): a phase 2, single-arm trial. *Lancet Oncol* **16**, 257-265 (2015).

482. E. B. Garon *et al.*, Pembrolizumab for the treatment of non-small-cell lung cancer. *N Engl j Med* **372**, 2018-2028 (2015).

483. S. N. Gettinger *et al.*, Overall Survival and Long-Term Safety of Nivolumab (Anti-Programmed Death 1 Antibody, BMS-936558, ONO-4538) in Patients With Previously Treated Advanced Non-Small-Cell Lung Cancer. *J Clin Oncol* **33**, 2004-2012 (2015).

484. R. J. Motzer *et al.*, Nivolumab for Metastatic Renal Cell Carcinoma: Results of a Randomized Phase II Trial. *J Clin Oncol* **33**, 1430-1437 (2015).

485. T. Powles *et al.*, MPDL3280A (anti-PD-L1) treatment leads to clinical activity in metastatic bladder cancer. *Nature* **515**, 558-562 (2014).

486. R. e. a. Nanda, San Antonio, TX. Abstract S1-09 *Proceedings of the 2014 San Antonio Breast Cancer Symposium;* .

487. T. Y. Seiwert *et al.* (American Society of Clinical Oncology, 2014).

488. A. Snyder *et al.*, Genetic basis for clinical response to CTLA-4 blockade in melanoma. *N Engl j Med* **371**, 2189-2199 (2014).

489. M. Yadav *et al.*, Predicting immunogenic tumour mutations by combining mass spectrometry and exome sequencing. *Nature* **515**, 572-576 (2014).

490. P. C. Tumeh *et al.*, PD-1 blockade induces responses by inhibiting adaptive immune resistance. *Nature* **515**, 568-571 (2014).

491. I. Mellman, G. Coukos, G. Dranoff, Cancer immunotherapy comes of age. *Nature* **480**, 480-489 (2011).

492. M. E. Mikucki *et al.*, Non-redundant requirement for CXCR3 signalling during tumoricidal T-cell trafficking across tumour vascular checkpoints. *Nat Commun* **6**, 7458 (2015).

493. F. Garrido, T. Cabrera, N. Aptsiauri, "Hard" and "soft" lesions underlying the HLA class I alterations in cancer cells: implications for immunotherapy. *Int J Cancer* **127**, 249-256 (2010).

494. M. Warabi, M. Kitagawa, K. Hirokawa, Loss of MHC class II expression is associated with a decrease of tumor-infiltrating T cells and an increase of metastatic potential of colorectal cancer: immunohistological and histopathological analyses as compared with normal colonic mucosa and adenomas. *Pathology-Research and Practice* **196**, 807-815 (2000).

495. M. Bernsen *et al.*, On the biological relevance of MHC class II and B7 expression by tumour cells in melanoma metastases. *British journal of cancer* **88**, 424-431 (2003).

496. S. A. Oldford *et al.*, Tumor cell expression of HLA-DM associates with a Th1 profile and predicts improved survival in breast carcinoma patients. *International immunology* **18**, 1591-1602 (2006).

497. Y. Degenhardt *et al.*, Distinct MHC gene expression patterns during progression of melanoma. *Genes, Chromosomes and Cancer* **49**, 144-154 (2010).

498. M. S. Pollack, S. D. Heagney, P. O. Livingston, J. Fogh, HLA-A, B, C and DR Alloantigen Expression on Forty-Six Cultured Human Tumor Cell Lines 2. *JNCI: Journal of the National Cancer Institute* **66**, 1003-1012 (1981).

499. G. Barbieri, E. Rimini, M. A. Costa, Effects of human leukocyte antigen (HLA)-DR engagement on melanoma cells. *International journal of oncology* **38**, 1589-1595 (2011).

500. P. Colloby, K. West, A. Fletcher, Is poor prognosis really related to HLA-DR expression by malignant melanoma cells? *Histopathology* **20**, 411-416 (1992).

501. P. Gogolak, E. Rajnavölgyi, Genomics and Functional Differences of Dendritic Cell Subsets. *Immunogenomics and Human Disease*, 209-247 (2006).

502. M. Londei, J. R. Lamb, G. F. Bottazzo, M. Feldmann, Epithelial cells expressing aberrant MHC class II determinants can present antigen to cloned human T cells. *Nature* **312**, 639-641 (1984).

503. R. Meazza, A. Comes, A. M. Orengo, S. Ferrini, R. S. Accolla, Tumor rejection by gene transfer of the MHC class II transactivator in murine mammary adenocarcinoma cells. *Eur J Immunol* **33**, 1183-1192 (2003).

504. N. A. Rizvi *et al.*, Mutational landscape determines sensitivity to PD-1 blockade in non–small cell lung cancer. *Science* **348**, 124-128 (2015).

505. C. Wellbrock *et al.*, STAT5 contributes to interferon resistance of melanoma cells. *Current biology* **15**, 1629-1639 (2005).

506. Y. S. Lee, S. H. Kim, J. A. Cho, C. W. Kim, Introduction of the CIITA gene into tumor cells produces exosomes with enhanced anti-tumor effects. *Experimental & molecular medicine* **43**, 281-290 (2011).

507. R. W. Joseph *et al.*, Correlation of NRAS mutations with clinical response to high dose IL-2 in patients with advanced melanoma. *Journal of immunotherapy (Hagerstown, Md.: 1997)* **35**, 66 (2012).

508. D. B. Johnson *et al.*, Impact of NRAS mutations for patients with advanced melanoma treated with immune therapies. *Cancer Immunology Research* **3**, 288-295 (2015).

509. F. Loor, B. Kindred, Differentiation of T-cell precursors in nude mice demonstrated by immunofluorescence of T-cell membrane markers. *Journal of Experimental Medicine* **138**, 1044-1055 (1973).

510. T. Rodriguez *et al.*, Patterns of constitutive and IFN-γ inducible expression of HLA class II molecules in human melanoma cell lines. *Immunogenetics* **59**, 123 (2007).

511. J. D. Wolchok *et al.*, Nivolumab plus ipilimumab in advanced melanoma. *New England Journal of Medicine* **369**, 122-133 (2013).

512. M. A. Postow *et al.*, Nivolumab and ipilimumab versus ipilimumab in untreated melanoma. *New England Journal of Medicine* **372**, 2006-2017 (2015).

513. J. Larkin *et al.*, Combined nivolumab and ipilimumab or monotherapy in untreated melanoma. *New England Journal of Medicine* **373**, 23-34 (2015).

514. J. M. Balko *et al.*, Profiling of residual breast cancers after neoadjuvant chemotherapy identifies DUSP4 deficiency as a mechanism of drug resistance. *Nat Med* **18**, 1052-1059 (2012).

515. J. M. Balko *et al.*, Activation of MAPK pathways due to DUSP4 loss promotes cancer stem cell-like phenotypes in basal-like breast cancer. *Cancer Res* **73**, 6346-6358 (2013).

516. R. C. Team. (2014).

517. Y. Benjamini, Y. Hochberg, Controlling the false discovery rate: a practical and powerful approach to multiple testing. *Journal of the royal statistical society. Series B (Methodological)*, 289-300 (1995).

518. B. Efron, R. Tibshirani, On testing the significance of sets of genes. *The annals of applied statistics*, 107-129 (2007).

519. A. D. Boiko *et al.*, Human melanoma-initiating cells express neural crest nerve growth factor receptor CD271. *Nature* **466**, 133-137 (2010).

520. M. Al-Hajj, M. S. Wicha, A. Benito-Hernandez, S. J. Morrison, M. F. Clarke, Prospective identification of tumorigenic breast cancer cells. *Proc Natl Acad Sci U S A* **100**, 3983-3988 (2003).

521. L. Zimmerlin, V. S. Donnenberg, A. D. Donnenberg, Rare event detection and analysis in flow cytometry: bone marrow mesenchymal stem cells, breast cancer stem/progenitor cells in

malignant effusions, and pericytes in disaggregated adipose tissue. *Methods Mol Biol* **699**, 251-273 (2011).

522. J. O. Richards, J. Treisman, N. Garlie, J. P. Hanson, M. K. Oaks, Flow cytometry assessment of residual melanoma cells in tumor-infiltrating lymphocyte cultures. *Cytometry A* **81**, 374-381 (2012).

523. K. S. Chan *et al.*, Identification, molecular characterization, clinical prognosis, and therapeutic targeting of human bladder tumor-initiating cells. *Proc Natl Acad Sci U S A* **106**, 14016-14021 (2009).

524. V. S. Donnenberg, R. J. Landreneau, M. E. Pfeifer, A. D. Donnenberg, Flow cytometric determination of stem/progenitor content in epithelial tissues: an example from nonsmall lung cancer and normal lung. *Cytometry A* **83**, 141-149 (2013).

525. V. C. Daniel *et al.*, A primary xenograft model of small-cell lung cancer reveals irreversible changes in gene expression imposed by culture in vitro. *Cancer Res* **69**, 3364-3373 (2009).

526. B. A. Reynolds, W. Tetzlaff, S. Weiss, A multipotent EGF-responsive striatal embryonic progenitor cell produces neurons and astrocytes. *J Neurosci* **12**, 4565-4574 (1992).

527. P. O. Krutzik, G. P. Nolan, Intracellular phospho-protein staining techniques for flow cytometry: monitoring single cell signaling events. *Cytometry A* **55**, 61-70 (2003).